Hydrogen Production via Catalytic Steam Reforming of Bio-oil Derived from Agricultural Residue

Doctoral Thesis

by

Piyush Pratap Singh

(2017CHZ0004)

DEPARTMENT OF CHEMICAL ENGINEERING

INDIAN INSTITUTE OF TECHNOLOGY ROPAR

April, 2023

Hydrogen Production via Catalytic Steam Reforming of Bio-oil Derived from Agricultural Residue

A Thesis Submitted

In Partial Fulfillment of the Requirements for the Degree of

DOCTOR OF PHILOSOPHY

by

Piyush Pratap Singh

(2017CHZ0004)

DEPARTMENT OF CHEMICAL ENGINEERING

INDIAN INSTITUTE OF TECHNOLOGY ROPAR

April, 2023

Piyush Pratap Singh: *Hydrogen Production via Catalytic Steam Reforming of Bio-oil Derived from Agricultural Residue*

Copyright © 2023, Indian Institute of Technology Ropar

All Rights Reserved

DEDICATED

TO

SUSTAINABLE SOCIETY

&

MY COUNTRY

Declaration of Originality

I hereby declare that the work which is being presented in the thesis entitled ‘**Hydrogen Production via Catalytic Steam Reforming of Bio-oil Derived from Agricultural Residue’** has been solely authored by me. It presents the result of my own independent investigation/research conducted during the time period from January 2018 to February 2023 under the supervision of Dr. Tarak Mondal, Assistant Professor, and Indian Institute of Technology Ropar and Dr. N. Nirmalkar, Assistant Professor, and Indian Institute of Technology Ropar. To the best of my knowledge, it is an original work, both in terms of research content and narrative, and has not been submitted or accepted elsewhere, in part or in full, for the award of any degree, diploma, fellowship, associateship, or similar title of any university or institution. Further, due credit has been attributed to the relevant state-of-the-art and collaborations (if any) with appropriate citations and acknowledgments, in line with established ethical norms and practices. I also declare thatany idea/data/fact/source stated in my thesis has not been fabricated/ falsified/ misrepresented. All the principles of academic honesty and integrity have been followed. I fully understand that if the thesis is found to be unoriginal, fabricated, or plagiarized, the Institute reserves the right to withdraw the thesis from its archive and revoke the associated Degree conferred. Additionally, the Institute also reserves theright to appraise all concerned sections of society of the matter for their information and necessary action(if any). If accepted, I hereby consent for my thesis to be available online in the Institute’s Open Accessrepository, inter-library loan, and the title & abstract to be made available to outside organizations.

Signature:
Name: Piyush Pratap Singh
Entry Number: 2017CHZ0004
Department: Chemical Engineering
Indian Institute of Technology Ropar
Rupnagar, Punjab 140001
Date: 20-02-2023

Certificate

This is to certify that the thesis entitled '**Hydrogen Production via Catalytic Steam Reforming of Bio-oil Derived from Agricultural Residue'**, submitted by **Piyush Pratap Singh (2017CHZ0004)** for the award of the degree of **Doctor of Philosophy** of Indian Institute of Technology Ropar, is a record of bonafide research work carried out under my (our) guidance and supervision. To the best of my knowledge and belief, the work presented in this thesis is original and has not been submitted, either in part or full, for the award of any other degree, diploma, fellowship, associateship or similar title of any university or institution.

In my (our) opinion, the thesis has reached the standard fulfilling the requirements of the regulations relating to the Degree.

Signature of the Supervisor
Name: Dr. Tarak Mondal
Department: Chemical Engineering
Indian Institute of Technology Ropar
Rupnagar, Punjab 140001
Date: 20-02-2023

Signature of the Co- supervisor
Name: Dr. Neelkanth Nirmalkar
Department: Chemical Engineering
Indian Institute of Technology Ropar
Rupnagar, Punjab 140001
Date: 20-02-2023

Acknowledgements

Firstly, my sincere appreciation goes to my supervisor, Dr. Tarak Mondal, Principal Investigator, Catalysis and Sustainable Energy Research Laboratory (CSERL) at IIT Ropar. His constant guidance and motivation, as well as his exceptional research aptitude, were critical to the success of this work. Without his support, this work would not have been feasible. Dr. Mondal's consistent encouragement and push for high achievement were invaluable, and he was always open to discuss any problems that arose. I acquired valuable insights from him on interpreting experimental data, and his confidence in my work inspired me to strive for better outcomes. It was an incredibly fortunate and unforgettable experience to have the opportunity to work under his reflective and revered guidance. His friendly nature and boundless kindness cannot be fully expressed in words, but I am immensely grateful for his unwavering support throughout our time together.

I would also like to express my gratitude to my co-supervisor, Dr. Neelkanth Nirmalkar, for his unwavering support and encouragement throughout my PhD journey. His motivation to persevere through the challenges of research has been instrumental in my growth as a researcher. During challenging times, especially during COVID-19, his guidance and advice were instrumental in helping me overcome obstacles, and I am deeply grateful for his constant support.

I would also like to thank my Doctoral Committee (DC) members, Dr. Vishwajeet Mehandia, Dr. Swati A Patel, Prof. Rajendra Srivastava, and chairperson Prof. Raj P. Chhabra, and Dr. Himanshu Paliwal, for keep evaluating my performance and their thoughtful discussions and suggestions. I wish to convey my sincere thanks to Dr. Asad Sahir for fruitful academic and non-academic discussions, suggestions, and motivation. I am also thankful to all faculty and staff members of Chemical Engineering department for their constant support during my tenure.

I would like to express my gratitude to CRE Lab (PI- Prof. K. K. Pant), IIT Delhi and Catalysis Research Lab (PI- Prof. Rajendra Srivastava), IIT Ropar for providing characterization facilities for my research. I am thankful to my friends Rajan Singh (IIT Delhi) and Dr. Ashish Kumar Kar (IIT Ropar) for their valuable support. Additionally, I appreciate the support provided by Mr. Ravinder Singh (Research Section), Ms. Sunpreet

Kaur (Chemical Engineering office), and Mr. Maan Singh (Chemical Engineering office). I would also like to acknowledge the Central Research Facilities, IIT Ropar, especially Mr. Amit Kaushal (SEM and XRD) and Mr. Damninder Singh (RAMAN). Finally, I would like to thank the Library, IIT Ropar, for granting me access to research papers and books essential to my work.

I would also like to express my gratitude towards CSERL colleagues Subhashini, Anurag, Akanksha, Ankit, Harikiran, Rajat, Ajay, Amir, Laveena, Ajeet and all Chemical Engineering research scholars and students. It was wonderful to work with Anurag, and especially our discussions on various catalytic biomass conversion processes were very fruitful. I would like to specially thank Ms. Riya Wadhwa for her constant support and listening my professional and non-professional conversations, whether she understood or not. She is constant support in this journey. I would also like to thank Mr. Nazim Ali for discussions in all matters and as a tea companion. I sincerely thankful to my friends Dr. Sadanand, Dr. Amrendra Singh, Priya Verma, Bilal Khan, Ankita Gupta, Arzoo Sharma, Dr. Taranjot, Arzoo Narang, Dr. Vikash Tripathi, Dr. Navneet Singh, Harsh Sharma, Suvansh Bhargava, Mohit Kasaniya, Raghav Verma, Simarpreet, Manik, Mukesh, Tanmay, student council friends, and other B.Tech guys for the joyfull environment during my stay at IIT Ropar. I am also thankful to Mr. Rajendra Bhamisra for providing tasty and healthy food in the cafeteria. I sincerely acknowledge security head Mr. Nand Kishore and his staff members for always being supportive and patient, specifically during the pandemic. I also appreciate the cleaning and maintenance staff for their services.

Above all, I owe my heartfelt gratitude to my parents (Mataji & Pitaji), my sister (Mrs. Omlata Singh), brother-in-law (Mr. Ranjeet Singh), Anshu and Pari for their love and support. I would like to take a moment to honour the memory of my beloved sister, Late Mrs. Ravilata Singh. Her presence is greatly missed, and I will always cherish the time I spent with her. I am thankful to all other members who have directly and indirectly supported me in this journey.

At last, I am thankful to the almighty GOD for making me capable for completing this task successfully.

Piyush Pratap Singh

Lay Summary

The objective of this research was to address two pressing issues: environmental impacts resulting from crop burning and the need for a cleaner fuel source. The hydrogen production from waste materials, particularly agricultural residue, could effectively address both concerns. This approach offers a sustainable route to reduce the environmental impact of agricultural waste by producing hydrogen, a fuel with a higher calorific value than petroleum products and no pollution emissions. The current hydrogen production process involves using fossil fuels, particularly natural gas, but catalytic steam reforming of bio-oil derived from agricultural residue could be a promising alternative.

To achieve this, highly active perovskite catalyst $LaNi_{0.5}Co_{0.5}O_3$ was synthesized, which was then rigorously characterized using various sophisticated techniques (XRD, XPS, SEM, etc.) to ensure its purity and quality. The synthesized catalyst was then used to produce green hydrogen via catalytic steam reforming of bio-oil, obtained by pyrolysis of major agricultural residues such as wheat straw, rice husk, corn cob, and sugarcane bagasse. The produced bio-oil's chemical composition was identified via GCMS, and the resulting products received via steam reforming were analyzed using GC-TCD and FID. The spent catalyst was also analyzed to determine the deactivation mechanism, with results indicating that coke was deposited on the catalyst surface in both graphitic and amorphous forms, along with the formation of carbon nanotubes (CNTs).

Furthermore, the kinetic parameters were also evaluated using a power law model. Finally, the thermodynamics potential of advanced steam reforming processes, including sorption-enhanced, chemical looping, and combined chemical looping and sorption-enhanced steam reforming processes, was performed and compared with conventional steam reforming process.

This research underscores the potential of catalytic steam reforming of bio-oil derived from agricultural residue as a cleaner and more sustainable source of hydrogen production.

Abstract

Continued industrialization and urbanization all around the globe have resulted in equally rapid growth in global energy consumption as well as demand. This massive surge in energy demands has increased our dependence on fossil fuels to the point, where it is resulting in unwarranted consequences. Catalytic steam reforming (SR) of agricultural waste derived bio-oil for hydrogen production is a unique technology, offering twin benefits of waste management as well as sustainable energy production.

The present study aims at developing a stable catalytic system for bio-oil steam reforming process to produce green hydrogen. The bio-oil used in this study was produced in the lab through pyrolysis of blend of agricultural residues. The produced bio-oil was characterized via gas chromatography mass spectrometry (GCMS) and Fourier transform infrared spectroscopy (FTIR). Furthermore, the perovskite catalysts $LaNi_xM_{1-x}O_3$ (M = Co, Cu, and Fe) used for steam reforming process, were synthesized using sol-gel method and their catalytic performance towards hydrogen production and bio-oil conversion was evaluated in a fixed bed tubular reactor. A wide array of techniques such as X-ray diffraction (XRD), Brunauer-Emmett-Teller surface area (BET), NH_3 and CO_2 -TPD (temperature programmed desorption), field emission scanning electron microscopy (FE-SEM), X-ray photoelectron spectroscopy (XPS), thermogravimetric analysis (TGA) and pyridine-FTIR were used to analyze the material properties of the synthesized catalysts. The results of these analyses verified the successful formation of the highly sought-after perovskite structure with good amount of surface oxygen vacancies as well as medium-strength acidic and basic sites.

To establish an efficient catalytic system, process parameter (space-time and reaction temperature) optimization and time on stream (TOS) studies were also conducted. The TOS results displayed that $LaNi_{0.5}Co_{0.5}O_3$ perovskite catalyst is stable up to 12 h at 700 ºC for space-time of 17.4 $kg_{cat}.h/kgmol_{bio\text{-}oil}$. Additionally, the kinetic study of phenol steam reforming process were also performed to study the various kinetic parameters. In-depth characterizations (FE-SEM, TGA, Raman spectroscopy and XRD) of spent catalyst after the reaction not only gave further insights about the excellent activity exhibited by the chosen catalyst but also revealed information about the nature of the coke deposited on the surface.

Furthermore, thermodynamic potential of various advanced steam reforming processes was evaluated and compared with the conventional steam reforming process.

Keywords: Steam reforming; Hydrogen production, Perovskite catalyst, Agricultural biomass; Catalyst deactivation; Kinetic study

TABLE OF CONTENTS

Declaration of Originality i

Certificate ii

Acknowledgments i

Lay Summary iii

Abstract iv

List of figures xiii

List of tables xviii

List of symbols, and abbreviations xx

Chapter 1: Introduction 1

1.1 Background 1

1.2 Biomass as a green feedstock for energy production 4

1.3 Biomass Conversion Strategies 7

1.3.1 Thermochemical routes 7

1.3.1.1 Gasification 8

1.3.1.2 Liquefaction 8

1.3.1.3 Pyrolysis 9

1.3.1.4 Direct Combustion 10

1.3.2 Biochemical routes 10

1.3.2.1 Anaerobic digestion 10

1.3.2.2 Fermentation 10

1.4 Bio-oil upgradation 11

1.4.1 Bio-oil 11

1.4.2 Bio-oil upgradation techniques 13

1.4.2.1 Hydro treating 13

1.4.2.2 Hydro-cracking/ hydrogenolysis 13

1.4.2.3 Supercritical fluid (SCF) 14
1.4.2.4 Steam Reforming 14
1.4.2.5 Chemical extraction 14
1.5 Steam reforming process 16
1.5.1 Reaction mechanism 17
1.5.2 Process conditions for steam reforming process 18
1.5.3 Catalysts used for SR process 19
1.6 Observation and research gaps 24
1.7 Objective 25
1.7.1 Main Objective 25
1.7.2 Specific objectives 25
1.8 Organisation of the thesis 26
Chapter 2: Materials and Methods 29
2.1. Catalyst synthesis 29
2.1.1 Materials used 29
2.1.2 Catalyst preparation 29
2.2 Characterization of catalysts 31
2.2.1 X-ray diffractogram (XRD) 31
2.2.2 BET-surface area 32
2.2.3 Scanning electron microscopy (SEM) 32
2.2.4 Energy-dispersive X-ray spectroscopy (EDX) 32
2.2.5 Diffuse Reflectance infrared Fourier transform spectroscopy (DRIFT) 33
2.2.6 Thermo gravimetric analysis (TGA) 33
2.2.7 Temperature program desorption (TPD) 34
2.2.8 Temperature program reduction (TPR) 34
2.2.9 Raman spectroscopy 35

2.2.10 X-Ray Photon Spectroscopy (XPS) 35

2.3 Thermodynamic assessment of the steam reforming process 36

2.4 Possible Reactions 36

2.4.1 Main reactions 36

2.4.2 Other reactions 37

2.5 Catalytic experiments for steam reforming reaction 37

2.6 Kinetic experiments 39

2.7 Pyrolysis experiments 40

Chapter 3: Simulated bio-oil steam reforming experiments with $LaNi_xCo_{1-x}O_3$ catalysts 43

3.1. Thermodynamic analysis 43

3.1.1 Effect of steam to carbon molar ratio 44

3.1.2 Effect of reaction temperature 45

3.2. Catalyst' characterization 46

3.2.1. X-ray diffraction 46

3.2.2. BET surface area 48

3.2.3. SEM and EDX 49

3.2.4. Temperature Programmed Reduction 50

3.3 Steam reforming of simulated bio-oil (SB1) over $LaNi_xCo_{1-x}O_3$ catalysts 52

3.3.1 Influence of Ni and Co content 52

3.3.2. Effect of reaction temperature 53

3.3.3. Effect of steam to carbon molar ratio (SCMR) 54

3.3.4. Effect of weight hourly space-time 55

3.3.5 Time on stream (TOS) study 56

Chapter 4: Effect of Partial substitution at A and B site of $La_yA_{1-y}Ni_xM_{1-x}O_3$ catalysts 59

4.1 Catalyst characterization 60

4.1.1 X-ray diffraction (XRD)..60

4.1.1.1 B-site substitution..60

4.1.1.2 A-site substitution 63

4.1.2. Temperature programmed reduction (TPR)..65

4.1.2.1. B-site substitution..65

4.1.2.2. A-site substitution 67

4.1.3. Surface Acidity and Basicity..69

4.1.4 X-ray photoelectron spectroscopy (XPS)..71

4.1.4.2 A-site substitution 72

4.1.5 TG Analysis..74

4.1.6. Surface Morphology..75

4.2 Steam reforming of simulated bio-oil (SB2) over $La_yA_{1-y}Ni_xM_{1-x}O_3$ catalysts 76

4.2.1 Effect of partial substitution at A and B – site of perovskite catalyst..................76

4.2.2 Influence of reaction temperature 79

4.2.3 Influence of weight hourly space-time (WHST)..80

4.2.4. Time on stream (TOS) study..81

Chapter 5: Kinetic Study..83

5.1 Process parameter optimization 84

5.1.1 Effect of temperature..84

5.1.2 Effect of SCMR..85

5.1.3 Effect of space time..86

5.1.4 Time on stream study 87

5.2 Development of kinetic model..89

Chapter 6: Catalytic steam reforming of agricultural residue derived bio-oil..........93

6.1 Pyrolysis of agricultural blend to produce bio-oil..93

6.1.1 Effect of temperature..94

6.1.3 Effect of feed stocks........96

6.1.4 Effect of temperature on bio-oil composition........98

6.2 Catalytic steam reforming of raw bio-oil........99

6.3 Comparison of raw bio-oil steam reforming processes........101

Chapter 7: Catalyst deactivation study........103

7.1 Catalyst deactivation study for simulated bio-oil 1 (SB1)........103

7.1.1 Raman spectroscopy........103

7.1.2 Surface morphology........105

7.1.3 Thermogravimetric analysis........106

7.2 Catalyst deactivation study for simulated bio-oil 2 (SB2)........107

7.2.1 RAMAN spectroscopy........107

7.2.2 Surface morphology........108

7.2.3 XRD analysis........109

7.2.4 Thermogravimetric analysis........110

7.3 Catalyst deactivation study for raw bio-oil reforming........111

7.3.1 RAMAN spectroscopy........111

7.3.2 Surface morphology........112

Chapter 8: Advanced steam reforming processes........115

8.1 Simulation Methodology........115

8.1.1 Process description of conventional and advanced reforming processes........117

8.1.2 Methods of data processing........122

8.2 Thermodynamic evaluation of different SR processes........122

8.2.1 Conventional steam reforming (CSR) process........123

8.2.2 Advanced reforming processes........126

8.2.2.1 SESR process........126

8.2.2.2 CLSR process........129

8.2.2.3 SE-CLSR process 132

8.3 Comparing conventional and advanced reforming process 134

8.4.5 Concluding remarks 137

Chapter 9: Conclusion and future recommendations 141

9.1 Conclusions 141

9.2 Future recommendations 143

References: 144

Appendix 159

Fixed bed reactor unit with online GC 160

Pyrolysis Experimental setup 160

Agricultural residue & Bio-oil 161

Gas chromatograph of gas samples 162

List of Publications 163

Journal Publications 163

Book Chapter 164

Conference presentation 165

Biodata 167

List of figures

Fig.1.1 Total primary energy consumption in world by fuel source 1

Fig.1.2 Total primary energy consumption in India by fuel source 2

Fig.1.3 Current hydrogen production sources 3

Fig.1.4 Classifications of biomass 5

Fig.1.5 Various routes for the production of hydrogen from agricultural waste 11

Fig. 2.1 Synthesis of perovskite catalyst 30

Fig.2.2 Schematic diagram of steam reforming experimental setup 39

Fig.2.3 Schematic diagram of pyrolysis experimental setup 41

Fig.3.1 Effect of steam to carbon molar ratio on gaseous products selectivity and bio-oil conversion (T = 700 ºC and P=1 atm) 44

Fig.3.2 Effect of temperature on gaseous products selectivity and bio-oil conversion (SCMR = 2.7 and P=1 atm) 45

Fig.3.3 XRD patterns of (a) $LaCoO_3$ (b) $LaNi_{0.2}Co_{0.8}O_3$, (c) $LaNi_{0.4}Co_{0.6}O_3$, (d) $LaNi_{0.5}Co_{0.5}O_3$, (e) $LaNi_{0.6}Co_{0.4}O_3$, (f) $LaNi_{0.8}Co_{0.2}O_3$ (g) $LaNiO_3$ catalysts 46

Fig.3.4 XRD patterns of (a) fresh and (b) reduced $LaNi_{0.5}Co_{0.5}O_3$ catalysts. 47

Fig.3.5 Morphological (SEM) image for fresh $LaNi_{0.5}Co_{0.5}O_3$ perovskite catalyst 49

Fig.3.6 TPR profiles of (a) $LaCoO_3$ (b) $LaNi_{0.2}Co_{0.8}O_3$, (c) $LaNi_{0.4}Co_{0.6}O_3$, (d) $LaNi_{0.5}Co_{0.5}O_3$, (e) $LaNi_{0.6}Co_{0.4}O_3$, (f) $LaNi_{0.8}Co_{0.2}O_3$ (g) $LaNiO_3$ catalysts. 50

Fig.3.7 Effect of different Ni and Co content on hydrogen yield and bio-oil conversion for $LaNi_xCo_{1-x}O_3$ perovskite catalyst (W/F_{AO} =18.4 kg_{cat}.h/$kgmol_{bio\text{-}oil}$, S/C = 2.7, T=650 ºC and P=1 atm) 53

Fig.3.8 Effect of temperature on gaseous products and bio-oil conversion for $LaNi_{0.5}Co_{0.5}O_3$ perovskite catalyst (W/F_{AO} =18.4 kg_{cat}.h/$kgmol_{bio\text{-}oil}$, S/C= 2.7 and P=1 atm) 54

Fig.3.9 Effect of steam to carbon ratio on gaseous products and bio-oil conversion for $LaNi_{0.5}Co_{0.5}O_3$ perovskite catalyst (W/F_{AO} =18.4 kg_{cat}.h/$kgmol_{bio\text{-}oil}$, T = 650 ºC and P=1 atm) 55

Fig.3.10 Effect of weight hourly space time on gaseous products and bio-oil conversion for $LaNi_{0.5}Co_{0.5}O_3$ perovskite catalyst (S/C=2.7, T = 650 ºC and P=1 atm) 56

Fig.3.11 Effect of time on steam on gaseous products and bio-oil conversion for $LaNi_{0.5}Co_{0.5}O_3$ perovskite catalyst (W/F_{AO} =18.4 $kg_{cat}.h/kmol_{bio\text{-}oil}$, S/C = 2.7 and P=1 atm) (a) Temperature = 700 ºC, (b) Temperature = 650 ºC. 57

Fig.4.1 XRD diffraction patterns of reduced (a) $LaNiO_3$, (b) $LaNi_{0.5}Co_{0.5}O_3$, (c) $LaNi_{0.5}Fe_{0.5}O_3$ and (d) $LaNi_{0.5}Cu_{0.5}O_3$ 61

Fig.4.2 XRD diffraction patterns of fresh (a) $LaNiO_3$, (b) $LaNi_{0.5}Co_{0.5}O_3$, (c) $LaNi_{0.5}Fe_{0.5}O_3$ and (d) $LaNi_{0.5}Cu_{0.5}O_3$ 61

Fig.4.3 XRD patterns of (a) $LaNi_{0.5}Co_{0.5}O_3$, (b) $La_{0.5}Ce_{0.5}Ni_{0.5}Co_{0.5}O_3$, (c) $La_{0.5}Ca_{0.5}Ni_{0.5}Co_{0.5}O_3$ and (d) $La_{0.5}Zr_{0.5}Ni_{0.5}Co_{0.5}O_3$ 63

Fig.4.4 H_2-TPR profiles of $LaNi_{0.5}M_{0.5}O_3$ perovskite catalysts 65

Fig.4.5 H_2-TPR profiles of $La_{0.5}A_{0.5}Ni_{0.5}Co_{0.5}O_3$ perovskite catalysts 67

Fig.4.6 NH_3- TPD profile of $LaNi_{0.5}M_{0.5}O_3$ (M= Ni, Co, Fe, and Cu) perovskite catalysts 69

Fig.4.7 Infrared spectra of Pyridine molecules absorbed on $LaNi_{0.5}Co_{0.5}O_3$ perovskite catalyst surface 69

Fig.4.8 CO_2- TPD profile of $LaNi_{0.5}Co_{0.5}O_3$ perovskite catalysts 70

Fig.4.9 XPS O1s profiles of $LaNi_{0.5}M_{0.5}O_3$ (M= Cu, Fe, Co, and Ni) perovskite catalysts 71

Fig.4.10 XPS O1s profiles of $La_{0.5}A_{0.5}Ni_{0.5}Co_{0.5}O_3$ (A= La, Ce, Ca, and Zr) perovskite catalysts 72

Fig.4.11 TGA plot for mixture of fresh perovskite and carbon (a) $LaNiO_3$, (b) $LaNi_{0.5}Co_{0.5}O_3$, (c) $LaNi_{0.5}Fe_{0.5}O_3$ and (d) $LaNi_{0.5}Cu_{0.5}O_3$ 74

Fig.4.12 FESEM images of fresh perovskite $LaNi_{0.5}Co_{0.5}O_3$ catalyst captured at magnification of (a) 24000x(b) 100,000x 75

Fig.4.13 Effect of different perovskite catalysts $LaNi_{0.5}M_{0.5}O_3$ on gaseous products yield and bio-oil conversion (W/F_{AO} =17.4 $kg_{cat}.h/kgmol_{bio\text{-}oil}$, S/C = 2.7, T=700 ºC and P=1 atm) 76

Fig.4.14 Effect of different perovskite catalysts $La_{0.5}A_{0.5}Ni_{0.5}Co_{0.5}O_3$ on gaseous products yield and bio-oil conversion (W/F_{AO} =17.4 $kg_{cat}.h/kgmol_{bio\text{-}oil}$, S/C = 2.7, T=700 ºC and P=1 atm) 77

Fig.4.15 Influence of reaction temperature on gaseous products yield and bio-oil conversion for $LaNi_{0.5}Co_{0.5}O_3$ perovskite catalyst (W/F_{AO} =17.4 $kg_{cat}.h/kgmol_{bio-oil}$, S/C = 2.7, and P=1 atm) 79
Fig.4.16 Influence of weight hourly space time on gaseous products and bio-oil conversion for $LaNi_{0.5}Co_{0.5}O_3$ perovskite catalyst (S/C=2.7, T = 700 ºC and P=1 atm) 80
Fig.4.17 Influence of time on steam on gaseous products and bio-oil conversion for $LaNi_{0.5}Co_{0.5}O_3$ perovskite catalyst (W/F_{AO} =17.4 $kg_{cat}.h/kgmol_{bio-oil}$, S/C = 2.7, T=700 ºC and P=1 atm) 81

Fig.5.1 Effect of reaction temperature on gaseous products and phenol conversion for $LaNi_{0.5}Co_{0.5}O_3$ perovskite catalyst (W/F_{AO} =30.14 $kg_{cat}.h/kgmol_{phenol}$, S/C = 2.7 and P=1 atm) 84
Fig.5.2 Effect of SCMR on gaseous products and phenol conversion for $LaNi_{0.5}Co_{0.5}O_3$ perovskite catalyst (W/F_{AO} =30.14 $kg_{cat}.h/kgmol_{phenol}$, T = 700 ºC and P=1 atm) 85
Fig.5.3 Effect of space time on gaseous products and phenol conversion for $LaNi_{0.5}Co_{0.5}O_3$ perovskite catalyst (T = 700 ºC, S/C = 2.7 and P=1 atm) 86
Fig.5.4 Time on stream study on gaseous products yield and phenol conversion for $LaNi_{0.5}Co_{0.5}O_3$ perovskite catalyst (W/F_{AO} =30.14 $kg_{cat}.h/kmol_{phenol}$, T = 700 ºC, S/C = 2.7 and P=1 atm) 87
Fig.5.5 Effect of space time on phenol conversion for $LaNi_{0.5}Co_{0.5}O_3$ perovskite catalyst (W/F_{AO} =30.14 $kg_{cat}.h/kmol_{phenol}$, S/C = 2.7 and P=1 atm) 91
Fig.5.6 Arrhenius plot based on power law model for phenol steam reforming using $LaNi_{0.5}Co_{0.5}O_3$ perovskite catalyst 92

Fig.6.1 Effect of temperature on products yield (Ramp Rate = 10 °C/min, N_2 flowrate = 50 mL/min, Feed: Agricultural residues blend) 94
Fig.6.2 Effect of ramp rate on products yield (Temperature = 450 °C/min, N_2 flowrate = 50 mL/min, Feed: Agricultural residues blend) 95
Fig.6.3 Effect of feed stocks on products yield (Ramp Rate = 10 °C/min, N_2 flowrate = 50 mL/min, Temperature = 450 °C/min) 96

Fig.6.4 Effect of temperature on bio-oil composition (Ramp Rate = 10 °C/min, N_2 flowrate = 50 mL/min, Feed: Agricultural residues blend)..98
Fig.6.5 Influence of time on stream on gaseous products and bio-oil conversion for $LaNi_{0.5}Co_{0.5}O_3$ perovskite catalyst (feed flow rate= 12mL/h, S/C = 2.7, T=700 ºC and P=1 atm) 100

Fig.7.1 Raman spectra of (a) fresh and spent $LaNi_{0.5}Co_{0.5}O_3$ perovskite catalyst at (b) 650 ºC and (c) 700 ºC reaction temperature...104
Fig.7. 2 SEM images of spent perovskite $LaNi_{0.5}Co_{0.5}O_3$ catalyst (a) spent catalysts at 650 ºC (b) spent catalyst at 700 ºC...105
Fig.7. 3 TG analysis of spent perovskite $LaNi_{0.5}Co_{0.5}O_3$ catalyst; (a) spent catalyst after 12 h TOS study at 650 ºC, (b) spent catalyst after 6 h TOS study at 700 ºC........................106
Fig.7.4 Raman spectra of spent (a) $LaNiO_3$, (b) $LaNi_{0.5}Co_{0.5}O_3$, (c) $LaNi_{0.5}Fe_{0.5}O_3$ and (d) $LaNi_{0.5}Cu_{0.5}O_3$..107
Fig.7.5 FESEM images of spent perovskite $LaNi_{0.5}Co_{0.5}O_3$ catalyst captured at magnification of (a) 1200x(b) 100,000x..108
Fig.7.6 XRD diffractogram of spent perovskite $LaNi_{0.5}Co_{0.5}O_3$ catalyst 109
Fig.7.7 TG analysis of spent perovskite $LaNi_{0.5}Co_{0.5}O_3$ catalyst....................................110
Fig.7.8 Raman spectra of spent $LaNi_{0.5}Co_{0.5}O_3$ catalyst after raw bio-oil reforming......111
Fig.7.9 FESEM images of spent perovskite $LaNi_{0.5}Co_{0.5}O_3$ catalyst captured at magnification of (a) 1900x(b) 30,000x..112

Fig.8.1 Process flowsheet for the proposed CSR process..120
Fig.8.2 Process flowsheet for the proposed SESR process...120
Fig.8.3 Process flowsheet for the proposed CLSR process 121
Fig.8.4 Process flowsheet for the proposed SE-CLSR process 121
Fig.8.5 Effect of SCMR on (a) product selectivity and (b) energy demands (MJ $kmol_{H2}$-1 and MJ $kmol_{Bio-oil}$-1) and H_2 yield (kg_{H2} $kg_{Bio-oil}$-1) in CSR process..............................124
Fig.8.6 Effect of temperature on (a) product selectivity and (b) energy demands (MJ $kmol_{H2}$-1 and MJ $kmol_{Bio-oil}$-1) and H_2 yield (kg_{H2} $kg_{Bio-oil}$-1) in CSR process...............125

Fig.8.7 Effect of CaO/C MR on (a) product selectivity and (b) energy demands (MJ kmol$_{H2}$-1 and MJ kmolBio-oil-1) and H$_2$ yield (kg$_{H2}$ kg$_{Bio\text{-}oil}$-1) in SESR process 128
Fig.8.8 Effect of temperature on (a) product selectivity and (b) energy demands (MJ kmol$_{H2}$-1 and MJ kmol$_{Bio\text{-}oil}$-1) and H$_2$ yield (kg$_{H2}$ kg$_{Bio\text{-}oil}$-1) in SESR process 129
Fig.8.9 Effect of NiO/C MR on (a) product selectivity and (b) energy demands (MJ kmol$_{H2}$-1 and MJ kmol$_{Bio\text{-}oil}$-1) and H$_2$ yield (kg$_{H2}$ kg$_{Bio\text{-}oil}$-1) in CLSR process 131
Fig.8.10 Effect of temperature on (a) product selectivity and (b) energy demands (MJ kmol$_{H2}$-1 and MJ kmol$_{Bio\text{-}oil}$-1) and H$_2$ yield (kg$_{H2}$ kg$_{Bio\text{-}oil}$-1) in CLSR process 132
Fig.8.11 Effect of temperature on (a) product selectivity and (b) energy demands (MJ kmol$_{H2}$-1 and MJ kmol$_{Bio\text{-}oil}$-1) and H$_2$ yield (kg$_{H2}$ kg$_{Bio\text{-}oil}$-1) in combined SE-CLSR process 134
Fig.8.12 A comparison of the H$_2$ yield (kg$_{H2}$ kg$_{Bio\text{-}oil}$-1) and energy demands (MJ kmol$_{H2}$-1 and MJ kmol$_{Bio\text{-}oil}$-1) for the four processes at their optimum conditions. 137

List of tables

Table 1.1 Ultimate and proximate analysis of some common agricultural residues [8]......6

Table 1.2 Thermochemical conversion routes..8

Table 1.3 Typical parameters and product yield in different modes of pyrolysis process [21] 9

Table 1.4 Physical and chemical characteristics of bio-oil. [30].......................................12

Table1.5 . Composition of pyrolytic Bio-oil from sugarcane bagasse, wheat straw and rice straw [34]...13

Table1.6 Catalytic bio-oil upgrading techniques [39]..15

Table 1.7 Effect of different noble and transition metal catalyst for steam reforming process [43,44]..21

Table 3.1 Textural properties of $LaNi_xCo_{1-x}O_3$ (x=0, 0.2, 0.4, 0.5, 0.6, 0.8 and 1) catalyst samples...48

Table 3.2 Elemental analysis of $LaNi_xCo_{1-x}O_3$ catalyst by EDS analysis 49

Table3.3 Hydrogen consumption for $LaNi_xCo_{1-x}O_3$ during H_2-TPR analysis...................51

Table 3. 4 Properties of Simulated Bio-oil 1 52

Table 4.1 Comparison of simulated bio-oil used for the present work with the literature 59

Table 4.2 Textural properties of $LaNi_{0.5}M_{0.5}O_3$ (M = Ni, Co, Cu, and Fe) catalyst samples 63

Table 5.1 Reaction results at 600 ºC...90

Table 5.2 Reaction results at 650 ºC...90

Table 5.3 Reaction results at 700 ºC...90

Table 6.1 Pyrolysis products yield at different temperature (Ramp Rate = 10 °C/min, N_2 flowrate = 50 mL/min, Feed: Agricultural residues blend) 95

Table 6.2 Pyrolysis products yield at various heating/ramp rate (Temperature = 450 °C/min, N_2 flowrate = 50 mL/min, Feed: Agricultural residues blend)..96

Table 6.3 Pyrolysis products yield for different feed stocks (Ramp Rate = 10 °C/min, N_2 flowrate = 50 mL/min, Temperature = 450 °C/min) 97
Table 6.4 Bio-oil composition at different temperatures...99
Table 6. 5 Comparison of raw bio-oil steam reforming processes 101

Table 8.1 List of model compounds, oxygenates family and their mass fraction used in the present study 116
Table 8. 2 Comparison of H_2 yield and energy demands of the four processes under consideration...137

List of symbols, and abbreviations

BJH	Barrett-Johner-Halenda
BE	binding energy
BET	Brunauer-Emmett-Teller
DTA	differential thermal analysis
ID	inner diameter
FID	flame ionization detector
FTIR	Fourier transform infrared spectroscopy
GHSV	gas hourly space velocity
MRSS	mean residual sum of squares
FE-SEM	Field emission – scanning electron microscopy
GCMS	Gas chromatography mass spectroscopy
TCD	thermal conductivity detector
TGA	thermal gravimetric analysis
TPD	temperature programmed desorption
TPR	temperature programmed reduction
TOS	time-on-stream
W/F	weight of catalyst/molar flow rate of bio-oil
XRD	X-ray diffraction
SR	steam reforming
WGS	water gas shift
Eq	equation
WHST	Weight hourly space time
CNT	Carbon nano tube
XPS	X-ray Photon Spectroscopy
SCMR	Steam to carbon molar ratio
MSW	Municipal solid waste
DRIFT	Diffuse reflectance infrared Fourier transform

Chapter 1: Introduction

1.1 Background

Fossil fuels have been the predominant energy source for humans over the past two centuries. The rapid urbanization and industrialization over the past few years have resulted in a population explosion, which has fuelled a massive surge in global energy demands. As of 2021, the majority of global energy consumption is still derived from non-renewable sources, such as fossil fuels (natural gas, coal, and oil). According to the International Energy Agency (IEA), in 2019, the total primary energy consumption was approximately 158,000 TWh, of which fossil fuels made up about 85%, as displayed in Fig.1.1. Among these, oil is the most prominent contributor to the energy mix, followed by coal and natural gas. Renewable energy sources, including wind, solar, and hydropower, are gaining traction, although they still account for only a small portion of the total global energy mix. In 2019, renewable energy sources constituted about 11% of total primary energy consumption [1].

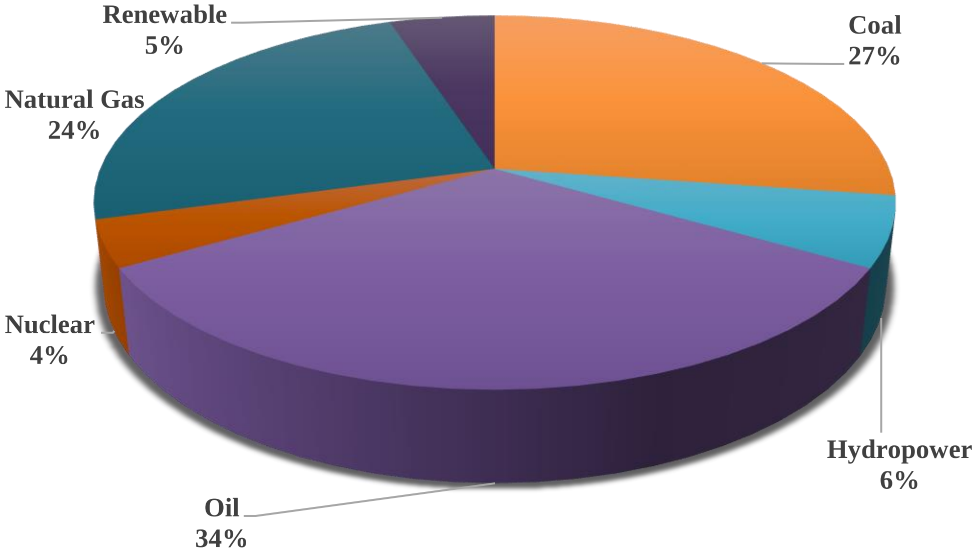

Fig. 1.1 Total primary energy consumption in world by fuel source (source International Energy Agency (IEA), 2019) [1]

In the Indian scenario, primary energy consumption has been increasing rapidly in recent years due to the country's growing population and expanding economy. As of 2020, the total energy consumption in India by fuel source is displayed in Fig. 1.2 according to the 'world energy outlook 2021 Report'. According to this report, the coal remains the largest source of energy in India, accounting for around 45% of the total primary energy consumption. Oil is the second largest contributor, accounting for approximately 24% of the total. Natural gas (6%) and renewables such as hydropower, wind, and solar make up the remaining portion of the energy mix [2]. The Indian government has set ambitious targets to increase the use of renewable energy and reduce the country's dependence on fossil fuels. In recent years, there have been significant investments in renewable energy infrastructure, such as wind and solar power projects, and the government has set a target to achieve 40% of the total installed power capacity from renewable energy sources by 2030.

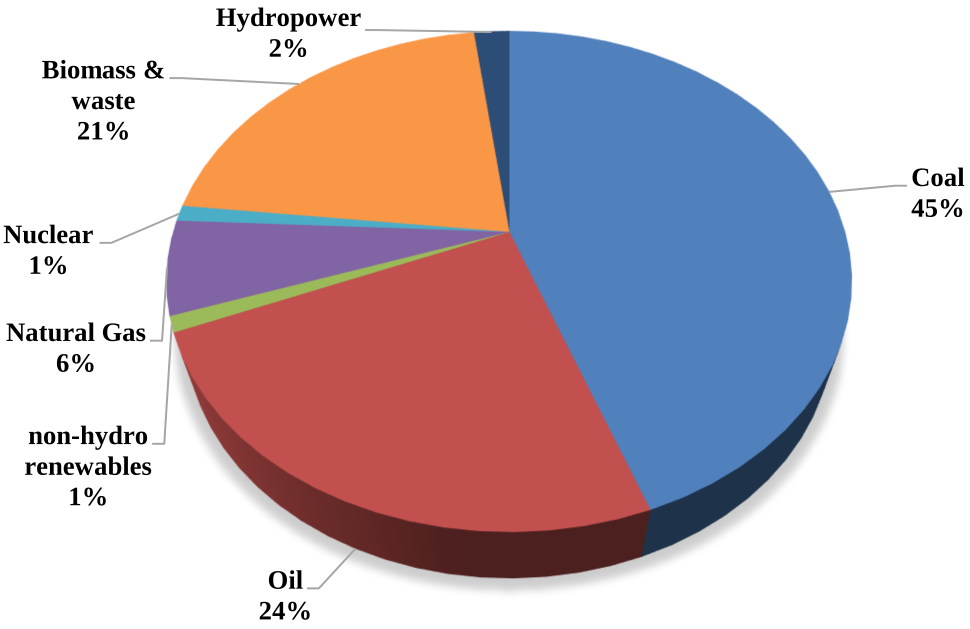

Fig. 1.2 Total primary energy consumption in India by fuel source (Source: world energy outlook 2021 [2])

Moreover, the continued exploitation of fossil fuels brings with it a number of significant challenges. Firstly, fossil fuels are finite resources, and their extraction rates are outpacing their natural replenishment rates. This could result in their exhaustion within the next two to three decades, which could make them too expensive relative to alternative energy sources. Additionally, the combustion of fossil fuels leads to the emission of significant quantities of greenhouse gases, such as carbon dioxide (CO_2) and methane (CH_4), which contribute to global warming and climate change. Finally, the extraction and utilization of fossil fuels have significant environmental consequences. The process of mining coal, drilling for oil, and hydraulic fracturing for natural gas often result in land degradation, air and water pollution, and other forms of environmental harm.

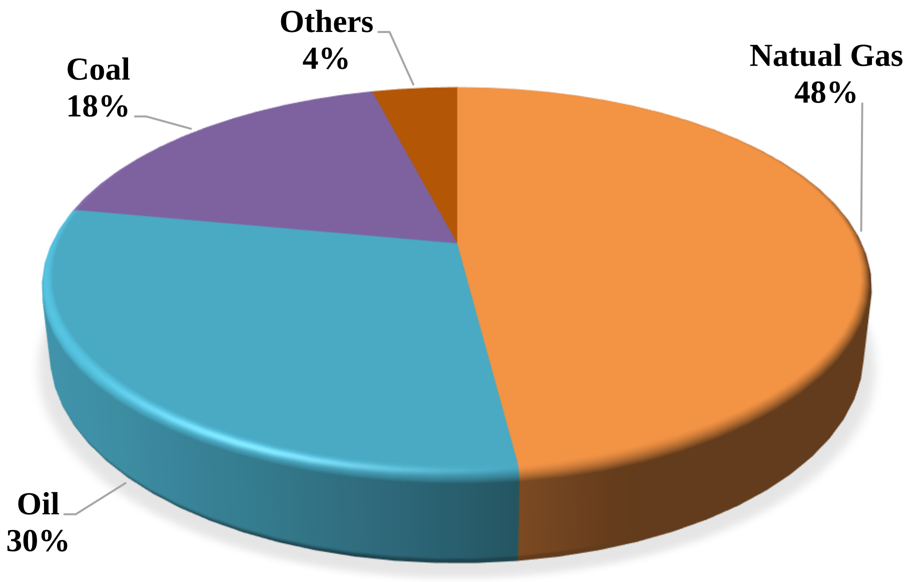

Fig. 1.3 Current hydrogen production sources (Source: BP annual report 2020 [3])

It's essential to recognize that the global energy landscape is constantly changing. While the use of fossil fuels remains prevalent, the trend towards renewable energy is gaining momentum as technology advances and costs decrease. Additionally, many countries and organizations around the world have established targets to increase the use of renewable energy and reduce the dependence on non-renewable sources, which could significantly transform the global energy mix in the years to come.

Therefore, it is crucial to transition towards alternative, renewable sources of energy, such as biomass, solar, wind, and hydropower, to ensure sustainable development and reduce our dependence on finite and environmentally harmful sources of energy. In recent years, hydrogen has received growing attention as a promising green fuel alternative to fossil fuels due to its high energy content, widespread availability in nature, and zero-emission when burned as a fuel. As displayed in Fig.1.3, the current dominant method of producing hydrogen (nearly 96% of global hydrogen production) relies on the reforming of fossil fuels such as natural gas, petroleum crude, and coal gasification, which results in substantial emissions of greenhouse gases and exacerbates the challenge of climate change [3].

Therefore, to meet the sustainability and economic demands of producing hydrogen, research has shifted towards alternative sources such as biomass. The goal is to develop a sustainable and economically viable method for producing hydrogen, reducing reliance on finite and polluting fossil fuels, and mitigating the environmental impacts of energy production. This shift towards alternative sources of hydrogen production has become increasingly important for mitigating the effects of climate change and promoting sustainable energy use.

1.2 Biomass as a green feedstock for energy production

In recent years, the utilization of biomass as a potential substitute for fossil fuels in H_2 production at a commercial scale has been gaining significant attention. Biomass refers to a diverse range of organic materials, including plants, trees, agro-industrial waste, and agricultural residue, that can be obtained or regenerated in a relatively short period of time [4]. Generally, biomass can be categorized as forest waste, energy crops and their by-products, agricultural waste, and municipal solid waste, as depicted in Fig.1.4. The increased interest in biomass as a source of energy can be attributed to several factors, including its abundance, rapid renewability, and carbon-neutrality. Unlike fossil fuels, which are finite and emit carbon dioxide (CO_2) during combustion, biomass captures CO_2 from the atmosphere during its growth process. This makes it a carbon-neutral energy source, which is essential in the context of mitigating the effects of climate change. Furthermore, the diverse nature of biomass materials provides a level of flexibility in terms of the production process and the starting materials used. For example, forest wastes, energy crops, and agricultural waste can all be utilized as starting materials in the production of H_2 [5–7].

Among the various biomass materials available, lignocellulosic biomass, such as agricultural residues, is seen as a promising feedstock for hydrogen production, particularly in countries that have a large agricultural sector, like India. India's agricultural sector covers a large land area of 195 million hectares and produces a variety of crops, including rice, wheat, pulses, and cotton. The production of these crops results in a significant amount of agricultural residues, such as cob, husk, leaves, stubbles, and straws, which can be used as raw material for H_2 production. The current estimated production of dry biomass residues in India's agricultural sector is 683 million tonnes, with projections indicating that this number could rise to 868 million tonnes by 2030 [6,8]. While some of the agricultural residues produced by India's agricultural sector are used for domestic and industrial purposes, a large amount goes unused and is often burned on-farm by farmers to clear the fields for the next crop. This practice has serious consequences for both human health and the environment, as it releases harmful gases like CO_2, CO, CH_4, NOx, and SOx into the air, contributing to air pollution and global warming. Additionally, the burning of crop residues results in the release of smoke and soot particles and a loss of important plant nutrients such as nitrogen, phosphorus, potassium, and sulphur, which negatively affects soil properties [6,8,9].

To address these issues with the disposal and management of agricultural residues, these materials can be converted into industrially valuable products through various thermochemical routes, such as pyrolysis, and further processed into hydrogen via catalytic steam reforming. This transformation process would not only alleviate the environmental impact of agricultural waste disposal but also yield a valuable source of green energy in the form of hydrogen.

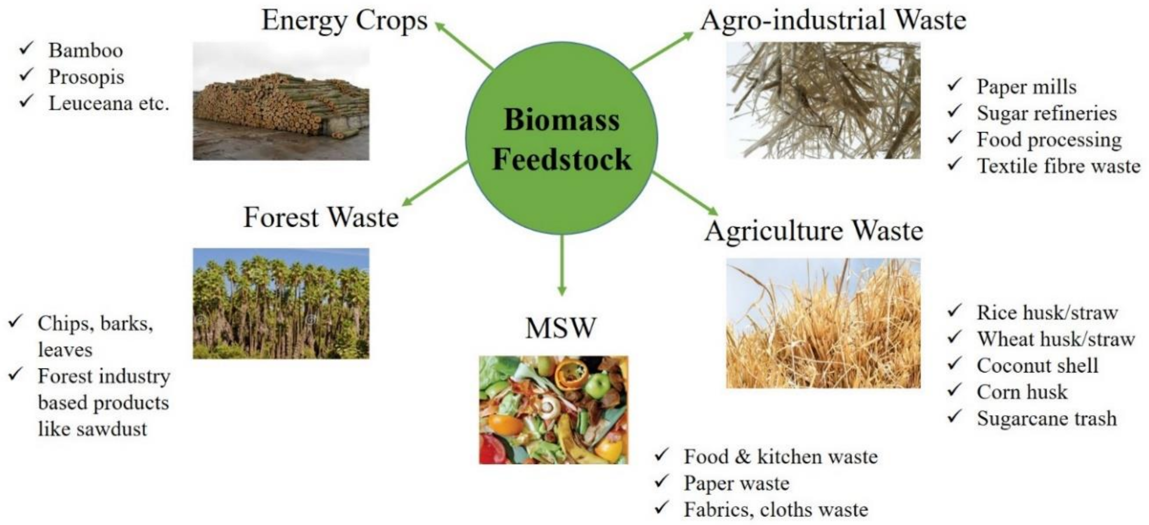
Biomass Feedstock
Energy Crops
✓ Bamboo
✓ Prosopis
✓ Leuceana etc.
Agro-industrial Waste
✓ Paper mills
✓ Sugar refineries
✓ Food processing
✓ Textile fibre waste
Forest Waste
✓ Chips, barks, leaves
✓ Forest industry based products like sawdust
Agriculture Waste
✓ Rice husk/straw
✓ Wheat husk/straw
✓ Coconut shell
✓ Corn husk
✓ Sugarcane trash
MSW
✓ Food & kitchen waste
✓ Paper waste
✓ Fabrics, cloths waste

Fig. 1.4 Classifications of biomass

Table 1.1 Ultimate and proximate analysis of some common agricultural residues [8]

Residue Type	Ultimate analysis (Wt %)					Proximate analysis (Wt%)			
	C	H	O	N	S	Moisture	Ash	Volatile matter	Fixed Carbon
Rice Straw	44.28	6.83	47.9	1.28	0	5.2	6.26	74.47	14.09
Rice Husk	45.18	5.08	48.05	1.62	0.07	7.36	20.07	69.75	2.82
Wheat Straw	48.24	5.64	45.55	0.56	–	7.66	7	78.33	7
Maize Cob	45.27	5.97	47.67	1.09	–	1.88	2.81	77.85	17.46
Corn cob	42.10	5.90	-	0.50	0.48	12.77	2.30	91.16	6.54
Neem seed	54.36	7.36	33.68	3.89	0.70	7.32	3.26	78.20	11.12
Cotton seed	53.10	3.55	37.34	4.47	1.54	10.05	6	67.95	16
Sugarcane leaves	76.83	8.19	14.39	0.59	–	5.67	6.38	77.33	16.33
Banana trunk	33.09	2.94	63.03	0.94	–	6.67	11.67	74.33	7.33
Arhar stalk	36.19	3.64	59.35	0.42	–	7.67	1.67	77.33	16.33
Coconut shell	64.23	6.89	27.61	0.77	0.50	10.1	3.2	75.5	11.2

1.3 Biomass Conversion Strategies

Lignocellulosic biomass, consisting of cellulose, hemicellulose, and lignin, is a complex biopolymer that exhibits variations in composition based on the type of biomass. These components are interlinked and form a three-dimensional network, giving plants their rigidity and strength. The hydrophobic nature of lignin and the crystalline nature of cellulose, combined with the three-dimensional network, make it challenging to degrade lignocellulosic biomass through chemical or microbial processes [10–12].

Because of its complexity, lignocellulosic biomass is challenging to break down, and various strategies have been developed for its efficient conversion. These strategies are classified into two categories: thermochemical and biochemical routes. The following provides a detailed overview of these conversion technologies.

1.3.1 Thermochemical routes

The thermochemical conversion of biomass from agricultural waste into H_2 has been considered a promising approach for green fuel production [13,14]. This method aims to create a greenhouse gas-free ecosystem for long-term sustainability [15]. There are two main thermochemical routes for this process: (a) the conversion of bio-waste into hydrocarbons through gasification and (b) the direct liquefaction of biomass. The type of biomass used as a feedstock has a substantial impact on the efficiency and yield of hydrogen production. The primary thermochemical conversion methods include pyrolysis, combustion, liquefaction, and gasification. Pyrolysis and gasification result in a mixture of CH_4 and CO that can be converted into hydrogen through steam reforming (SR) and the water gas shift (WGS) reactions. Combustion and liquefaction, however, have lower hydrogen yields and can generate toxic by-products. They also require challenging operational conditions such as high pressures [16]. Other advanced thermochemical methods, such as sorption-enhanced steam reforming and integrated technologies (combining pyrolysis and SR), have also been explored for hydrogen production.

Table 1.2 Thermochemical conversion routes

Process	Temperature (ºC)	Oxygen	Products
Gasification	800-1200	Maybe required	Gases, char
Liquefaction	250-370	Not Required	Organic liquid
Pyrolysis	300-600	Not Required	Bio-oil, char, gases
Combustion	700-1400	Required	Heat & Electricity

1.3.1.1 Gasification

Gasification is a thermochemical process that transforms biomass into a gaseous mixture called syngas (H_2 and CO) as main product, whereas the other side products are carbon dioxide, methane, hydrocarbons, and char [13]. The gasification process is achieved by exposing the biomass to high temperatures using steam and oxygen in a regulated environment. The efficiency of gasification depends on various parameters, for instance, the biomass type, catalyst, reactor design, and operating conditions. Suitable biomass for gasification has a moisture level of less than 35% [17]. The gasification process involves various endothermic and exothermic reactions, and the resulting syngas can be further converted into hydrogen. Tar formation is a challenge in the process, but it can be reduced through proper design, management, and use of additives. Biomass sources for gasification include woody trees, plant crops, marine biomass, and composts [18].

1.3.1.2 Liquefaction

The liquefaction method of processing biomass involves the use of low to moderate temperatures, around 250-370 ℃, and high pressure, roughly 10-25 MPa, with the aid of a catalyst [19]. This process is mainly employed when a high hydrogen to carbon ratio is required. The resulting products from liquefaction are highly stable and possess high heating values and low oxygen content. Prior to inputting the biomass into the column for liquefaction, pre-treatment is necessary to remove unwanted woody substances to ensure a stable suspension. After liquefaction, the mixture undergoes spontaneous phase separation to separate the solid, liquid, and gaseous phases. The solid residue can be utilized as a biofuel fertilizer, while the oil can be extracted and used as fuel. The remaining aqueous phase can also be used for further processing. However, this process is not widely used due to its expensive nature and the difficulties associated with handling the lumped mixture produced [20].

1.3.1.3 Pyrolysis

Table 1.3 Typical parameters and product yield in different modes of pyrolysis process [21]

Mode	**Conditions**		**Products**		
	Temperature (°C)	**Residence Time**	**Liquid (wt.%)**	**Char (wt.%)**	**Gas (wt.%)**
Flash	~ 500	~ 1 s	75	12	13
Fast	~600	~ 10 - 15 s	50-70	20	30
Slow	~ 400	Very long	30	35	35

Pyrolysis is a commonly utilized process for the production of hydrogen due to its advantages, such as easy storage and transportation and compatibility with various equipment, including generators, incineration machines, and carriers [14]. This process involves the thermal decomposition of biomass at high temperatures (in excess of 300℃ and up to 700℃) under an inert atmosphere, yielding the production of a gaseous mixture of hydrogen and hydrocarbons, liquid bio-oil, and solid char. Initially, the original purpose of pyrolysis was the production of char, but for hydrogen production, rapid or flash pyrolysis can be used if high temperatures and sufficient residence time are available. This process breaks down complex biomolecules such as cellulose, lignocellulose, proteins, polysaccharides, and lipids into smaller organic molecules, such as gases and vapours. Secondary reactions occur, resulting in the production of hydrogen and other by-products, depending on the process parameters such as decomposition rate, heating rate, feedstock composition, operating pressure, and temperature. Catalyst selection and reactor design also play a significant role by improving the quality and yield of the reaction products. Extensive research has been performed to explore the use of various feedstock materials, including agricultural residue and post-consumer waste, in H_2 production via pyrolysis [22]. The process of pyrolysis can be further categorized into slow or conventional pyrolysis, fast pyrolysis, pyrolyzed derived bio-oil reforming, and flash pyrolysis, as described in Table 1.3 [23].

1.3.1.4 Direct Combustion

Combustion is a process of converting biomass into heat or electrical energy by utilizing the chemical energy stored within the feedstock in the presence of air. The electrical efficiency of this process is low, ranging between 20% and 40%, and can be improved by co-combusting biomass with coal in power plants [24]. However, it is recommended to use biomass with a moisture level of less than 50% for this method to be effective. In some cases, pre-treatment of the feedstock may also be necessary, which results in increased capital investment [25]. Despite its potential for energy generation, combustion has several drawbacks and low hydrogen yield, making it an unappealing option for hydrogen production.

1.3.2 Biochemical routes

The biological conversion of biomass is another sustainable process for hydrogen production. This conversion route involves the decomposition of biomass by bacterial action to produce liquid fuels and gases. Anaerobic digestion and fermentation are the major techniques for biochemical conversion.

1.3.2.1 Anaerobic digestion

This method involves several chemical reactions that break down the macro compounds into simpler compounds that form CH_4, CO, and other gases. The primary stages in this process are acetogenesis, acidogenesis, hydrolysis, and methanogenesis [6]. The overall efficiency of this method is around 21%.

1.3.2.2 Fermentation

The fermentation of organic compounds is a sequence of metabolic processes in which microbes, mainly yeasts, transform simple carbohydrates such as hexoses and pentoses into alcohol and CO_2 under anaerobic conditions. The process quality and yields are affected by various variables, including feedstock, temperature, pH, substrate, and the duration of fermentation [16].

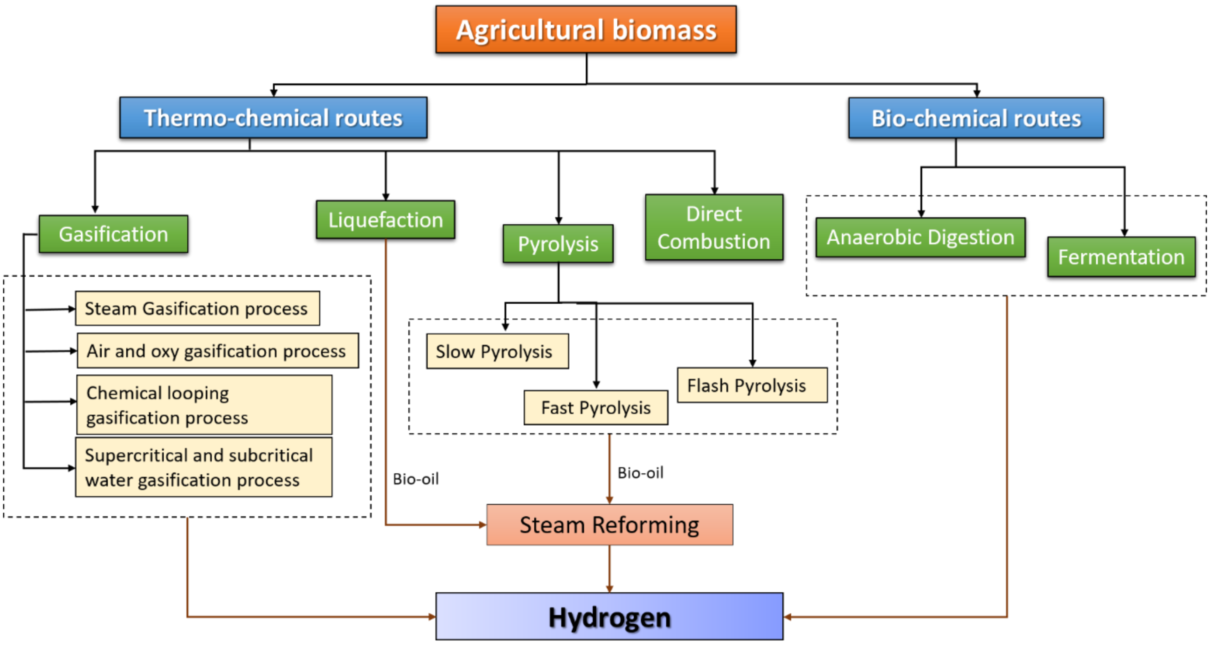
Agricultural biomass
Thermo-chemical routes
Bio-chemical routes
Gasification
Liquefaction
Pyrolysis
Direct Combustion
Anaerobic Digestion
Fermentation
Steam Gasification process
Air and oxy gasification process
Chemical looping gasification process
Supercritical and subcritical water gasification process
Slow Pyrolysis
Fast Pyrolysis
Flash Pyrolysis
Bio-oil
Bio-oil
Steam Reforming
Hydrogen

Fig. 1.5 Various routes for the production of hydrogen from agricultural waste

1.4 Bio-oil upgradation

1.4.1 Bio-oil

Bio-oil, also referred to as pyrolysis oil or pyrolytic oil, is a product obtained from the thermal degradation of biomass through pyrolysis. The resulting bio-oil is a complex mixture of water and a range of oxygenated compounds, including acids, alcohols, aldehydes, esters, ethers, ketones, phenols, and sugars [23,26,27]. The composition and properties of bio-oil are influenced by various factors, including the type of biomass feedstock used and the reaction conditions employed during pyrolysis. For example, factors such as temperature, heating rate, and duration of exposure (residence time) all impact the composition of bio-oil produced [37–39].

Water constitutes a significant portion of bio-oil, accounting for 14-35% of its weight. This is because of the moisture content of the original biomass as well as the dehydration reactions that occur during pyrolysis. The thermal decomposition of the cellulose and hemicellulose fractions leads to the formation of volatile monomeric compounds, while the degradation of the lignin fraction yields the formation of oligomeric compounds in larger quantities.

Additionally, the bio-oil can be divided into two separate phases (aqueous and organic phases) through distillation, followed by condensation, as the main separation method. The aqueous phase is composed of hydrophilic monomeric organics, while the organic phase is comprised of hydrophobic lignin-derived oligomers. The relative proportion of these two phases is dependent on the specific composition of the bio-oil and the methods used for separation [26,28–31].

Table 1.4 Physical and chemical characteristics of bio-oil [30]

Water [wt%]	14-35
ρ [Kg/m^3]	1050-1250
pH	2.5-4
$\mu_{50°C}$ [P]	0.4-10
Specific gravity	1.2
HHV [MJ/Kg]	16-19
C [wt%]	55-65
H [wt%]	5-7
O [wt%]	28-40
S [wt%]	<0.05
N [wt%]	<0.4
Ash [wt%]	<0.2
Solids (char)	0.1-0.2%

Bio-oil differs significantly from crude oil in its chemical composition. While crude oil is predominantly composed of carbon (>80% wt.) and hydrogen and has less than 1% oxygen, bio-oil has a lower carbon content ranging from 55-65% and a much higher oxygen content, ranging from 20-50% and sometimes even reaching 60%. These high oxygen and water levels in bio-oil impart several unfavourable properties, such as a low heating value, low chemical and thermal stability, low volatility, high viscosity, corrosiveness, and poor combustion and ignition characteristics. These properties, along with variations in composition based on feedstock, process conditions, and recovery setup, greatly limit the potential use of bio-oil as a transportation fuel or energy source on a large scale [26,28–33]. As a result, substantial oxygen removal is required prior to any potential utilization of bio-oil.

Table 1.5 . Composition of pyrolytic Bio-oil from sugarcane bagasse, wheat straw and rice straw [34]

Compounds	Composition*		
	Sugarcane Bagasse	Wheat Straw	Rice Straw
Alcohols	-	26.96	27.54
Anhydrous sugars	23.99	0.33	4.58
Ester	3.46	12.38	4.39
Furans	22.75	6.58	16.68
Guaiacol	11.66	8.26	7.04
Phenolics	10.91	10.99	1.38

*GCMS area %

1.4.2 Bio-oil upgradation techniques

1.4.2.1 Hydro treating

Hydrotreating (HDT) is a hydrogenolysis technique used for the upgrading of bio-oil. This process involves the treatment of bio-oil with H_2 in the presence of a catalyst under mild conditions and low pressure. Although this process is relatively cost-effective, its low hydrogen yield and the high coking of the final product are major limitations. As a result, the quality of the fuel obtained is often poor. The use of hydrotreating is still in practice, but efforts are ongoing to improve its efficiency and produce a higher-quality product [35].

1.4.2.2 Hydro-cracking/ hydrogenolysis

Hydrocracking is a process that requires severe conditions, including high pressure (100-2000 psi) and temperature (above 350°C), for its successful execution. The use of a dual-function catalyst and solvents in this process leads to the production of a substantial number of light products. Despite its advantages, hydrocracking is less attractive due to several technical disadvantages, including high cost, clogging of the reactor, and deactivation of the catalyst, among others [26,36].

1.4.2.3 Supercritical fluid (SCF)

The supercritical fluid (SCF) technology is another bio-oil upgradation technique, which employs solvents like acetone, methanol, ethanol, and glycerol. The use of SCF leads to improved bio-oil quality and yield. However, the cost of the solvents used in this process can be substantial, making it an expensive option. As a result, researchers are investigating alternatives to these solvents. One such alternative that has shown potential is glycerol, which is a low-value by-product of biodiesel production. The use of glycerol as a substitute SCF solvent has been shown to produce comparable results to those obtained with other solvents [37].

1.4.2.4 Steam Reforming

Steam reforming is another process to upgrade bio-oil into valuable products. SR process is carried out at high temperatures in the presence of a catalyst and resulting the production of clean and pure H_2. Commercial nickel catalysts have been shown to exhibit excellent activity in the processing of biomass-derived oil. Despite its potential, the SR process is faced with several challenges, such as the deposition of coke on the catalyst surface and the catalyst's degradation over time when used with bio-oil. In addition to this, SR is a complex chemical process that requires a well-developed reactor for its implementation [38].

1.4.2.5 Chemical extraction

Chemical extraction is a technique used to separate valuable chemicals such as phenols, organic acids, and n-alkanes from bio-oil. These chemicals have limited applications in the production of wood flavors or liquid smoke. However, further advancements are necessary to improve the economic viability of this process. This may involve developing more cost-effective methods for extracting these chemicals or finding new applications for these chemicals that can drive demand and increase their economic significance [39].

Table 1.6 Catalytic bio-oil upgrading techniques [39]

Upgradation Method	**Reaction Conditions**	**Pros**	**Cons**
Hydrotreating	$T = 500^{o}C$ P = Low pressure	• Cheaper route • Already commercialized	• High coking, • Poor quality of fuels
Hydro-cracking/ hydrogenolysis	$T > 350^{o}C$ P = High pressure	• Good yield of light products	• Complicated equipment • Expensive • Catalyst deactivation • Reactor clogging
Supercritical fluid	Mild conditions	• Higher oil yield • Better fuel quality	• Expensive solvent required
Steam Reforming	$T = 500\text{-}800^{o}C$ P = 1 atm	• Produces H_2 as a clean energy resource	• Fully developed reactors required • Complicated process
Chemical extraction	Mild conditions	• Good yield of valuable chemicals	• Separation expensive

1.5 Steam reforming process

Steam reforming (SR) is a well-established method for the production of hydrogen, which has been utilized since 1930. The process involves the reaction of hydrocarbons and oxygenates with water vapor in the presence of metal catalysts, resulting in the formation of hydrogen (H_2), carbon monoxide (CO), and carbon dioxide (CO_2). The reaction is endothermic in nature, meaning that it requires the input of heat energy to proceed [5,6,22,40]. The first commercial steam reforming plant was established by Standard Oil Co. in the USA in 1930, using light alkanes as the raw material [42].

Bio-oil is a renewable and sustainable resource that can be used as a feedstock for steam reforming process to produce renewable H_2. Bio-oil is attractive as a reactant due to its high hydrogen content, low sulphur and nitrogen content, which make it a promising alternative to traditional fossil fuels. Steam reforming of bio-oil has the potential to reduce greenhouse gas emissions and dependence on non-renewable fossil fuels. The steam reforming of bio-oil involves mainly two chemical reactions. First, SR (eq.1.1) is a reaction between the bio-oil ($C_nH_mO_k$) and steam (H_2O), which produces hydrogen (H_2), and carbon monoxide (CO). Second, WGS (eq.1.2) is a reaction between carbon monoxide and steam, which results in the production of additional hydrogen and carbon dioxide (CO_2). The overall SR reaction (eq.1.3) is the combination of these two reactions [40,43,44].

Main reactions:

Steam reforming reaction (SR):

$$C_nH_mO_k + (n-k)H_2O \rightarrow n\,CO + \left(n + \frac{m}{2} - k\right)H_2 \qquad (1.1)$$

Water gas shift reaction (WGS):

$$CO + H_2O \leftrightarrow CO_2 + H_2 \qquad (1.2)$$

Overall reaction:

$$C_nH_mO_k + (2n-k)H_2O \rightarrow \left(2n + \frac{m}{2} - k\right)H_2 + nCO_2 \qquad (1.3)$$

Along with these major reactions, several side reactions (eq.1.4-1.11) are also involved during steam reforming process, which are responsible for formation of coke as well as other gaseous products[40].

Other reactions:

Thermal decomposition reaction:

$$C_nH_mO_k \rightarrow C_xH_yO_z + gas(H_2, CO_2, CO, CH_4, CH_q) + coke \qquad (1.4)$$

Methanation reaction:

$$CO + 3H_2 \rightarrow CH_4 + H_2O \qquad (1.5)$$

$$CO_2 + 4H_2 \rightarrow CH_4 + 2H_2O \qquad (1.6)$$

Carbon gasification reaction:

$$C + H_2O \leftrightarrow CO + H_2 \qquad (1.7)$$

$$C + 2H_2O \leftrightarrow CO_2 + 2H_2 \qquad (1.8)$$

Methane steam reforming reaction:

$$CH_4 + H_2O \leftrightarrow CO + 3H_2 \qquad (1.9)$$

Boudouard reaction:

$$2CO \leftrightarrow CO_2 + C \qquad (1.10)$$

Methane decomposition reaction:

$$CH_4 \leftrightarrow C + 2H_2 \qquad (1.11)$$

1.5.1 Reaction mechanism

Since bio-oil contains a large number of oxygenates, some of which are extremely complex in nature, a diverse range of reaction behaviours is observed during the process. Furthermore, the oxygenates are known to exhibit interactions with one another, which results not only in the formation of several by-products but also catalyst deactivation when these by-products get deposited on the catalyst surface [45,46]. This complexity has a significant impact on our understanding of the reaction mechanisms and the development of effective catalysts. The existence of interactions among these oxygenates and the resulting issue of severe coke deposition further adds to the complexity of the process and poses challenges in process development. To mitigate these challenges, researchers often employ a reductionist approach by using simplified model compounds to represent the different families of oxygenates found in bio-oil. This approach helps to establish a stronger understanding of reaction pathways involved in the processing of bio-oil [7].

Studies have recognized the mechanism of bio-oil SR process which includes two major reactions (a bifunctional mechanism) on the supporting metal catalysts. Firstly, oxygenates are disintegrated on the metal surfaces to produce adsorbed carbon species while yielding hydrogen. Secondly, water molecule is adsorbed, and its decomposition (in form of H^+ and OH^-) takes place on the support material and generated –OH groups subsequently move onto the metal and support interfaces or metal particles, where it quickly reacts with carbonaceous species to generate H_2, CO_2, and CO [47]. Water dissociated by the support materials may possibly hinder the catalyst efficiency by significantly oxidizing the active metallic phases [43]. Hence, it is recommended that effective management of the metal/support contact area be in place to encourage the steam reforming process.

1.5.2 Process conditions for steam reforming process

The hydrogen production through steam reforming of bio-oils is influenced by several key process parameters, including temperature, the ratio of steam to carbon, pressure, space time, and the type of catalyst used. The entire process of SR is endothermic, implying that as the temperature rises, the equilibrium shifts to the right, enhancing the production of hydrogen [33,34]. Likewise, the steam-to-carbon ratio has a significant impact on H_2 production. It was noticed that when the temperature and steam to carbon molar ratio (SCMR) surged, H_2 production increased. This was followed by increased carbon conversion, which had been just 15% at 500 °C but had risen to 93 percent at 750 °C [48]. Subsequently, both H_2 yield and carbon conversion increased when SCMR ratio was raised from 1.5 to 6 [49]. Furthermore, studies using a fluidized bed reactor and a fixed bed reactor with CO_2 capture (using CaO and dolomite) at 650 °C and 13,000 h space velocity revealed that H_2 production decreases at high temperatures with CO_2 capture, and the optimal temperature for H_2 production with CO_2 capture is between 550 °C and 650 °C [48]. Contrarily, increasing the SCMR ratio at reduced pressure conditions results in increased H_2 production. The highest H_2 yield was observed for these experimental conditions within the temperature range of 600 and 750 °C. Additionally, bio-oil steam reforming was carried out in a fluidized bed reactor and maximum H_2 yield of 89% was found for space velocity of 830 h^{-1} and SCMR of 9 at 850 °C [50]. Whereas, the SR experiments performed in a fixed bed micro-reactor achieved 80% hydrogen yield and 86% carbon conversion at space velocity of 10,000 h^{-1}, temperature 750 °C, and SCMR>4. A higher selectivity (nearly 100%) of hydrogen was reported in Nozzle fed reactor when experiments were conducted at 800 °C and SCMR of 7.2 [50]. According to the findings, liquid feed rate and reaction temperature are important factors in the catalytic steam reforming process. As the liquid feed rate increases, the residence time reduces, resulting in a decreased H_2 production. On the contrary, greater H_2 yield had been observed which was attributed to the rise in partial pressure in the catalytic reactor bed with increased liquid feed rate. As the reaction rate is directly proportional to the concentration of reactant, a higher partial pressure leads to a greater H_2 yield. By optimizing these process conditions, researchers have examined steam reforming over three different catalysts (12% Ni/γ-Al_2O_3, 1% Pt/γ-Al_2O_3, and C12A7/15% Mg) and maximum H_2 yield of 75% was reported for 1% Pt/γ-Al_2O_3 catalyst at 700 °C [48]. A maximum H_2 yield and carbon conversion of about 80% and 95% at 750 °C, respectively was found which were higher than that obtained while comparing with other hydrocarbons such as methane and naphtha.

1.5.3 Catalysts used for SR process

Catalyst development is an area of intense study in the field of biomass derived bio-oil SR process. Bio-oil consists of a multitude of compounds, primarily acids, aldehydes, alcohols, and cyclic compounds, which makes its composition highly complex [7,32]. The use of model compounds, including acetic acid, is a common practice in the study of bio-oil steam reforming to gain a more comprehensive understanding of the upgrading process. These model compounds allow for systematic investigation and analysis of the bio-oil upgrading process [40]. In the field of bio-oil SR process, researchers have been exploring the use of acetic acid as a reactant to optimize the reaction process. Beyond operating parameters, catalysts also play a critical role in the success of the process. The choice of catalyst, such as metal oxides, zeolites, or acid-base catalysts, can significantly influence the product yield, composition, and reaction kinetics. To obtain the desired product properties, it is crucial to carefully select and optimize the catalyst type, loading, and operating conditions. Moreover, metal oxide catalysts containing noble metals (such as Pd, Rh, Pt, and Ir) and transition metals (such as Co, Ni, Cu, and Fe) have been shown to be effective in the steam reforming process. This is due to their ability to dissociate C-C and C-H bonds, which is an essential aspect of the bio-oil SR process [53,54]. These catalysts have demonstrated promising results, making them an attractive option for researchers in the field. While noble metals have shown promising activity in the bio-oil SR process, their high cost can limit their widespread use. As an alternative, transition metals such as Ni and Co have demonstrated excellent bond-breaking ability, making them a more cost-effective option. These metals are typically impregnated on oxide supports, such as Al_2O_3, to improve their activity. During the SR process, the metal component acts primarily to crack model compounds by dissociating the C-C and C-H bonds, while the oxide support aids in the activation of steam, generation of highly mobile oxygen, and suppression of coking. Overall, the combination of metal and oxide support results in improved performance in the SR process [45,55].

As displayed in Table 1.7, researchers have studied the effect of different noble and transition metal on Al_2O_3 support. For noble metals, Rh has shown promising results towards conversion as well as H_2 selectivity for acetic acid SR process because of its higher C-C bond dissociation capability on comparing with Pt and Pd [55]. On the other hand, Pt has been known to be effective in the WGS reaction, which is beneficial to the acetic acid SR process. Besides noble metals, transition metals especially Co and Ni have also displayed good catalytic activity for acetic acid SR process. Ni and Co both have C-C and C-H bond dissociative property while Fe and Cu have activity only for C-C dissociation and C-H dissociation respectively [7]. In addition, it has been found that Ni/Al_2O_3 is more stable than Co/Al_2O_3 due to its higher resistance to oxidation. Hu et al. [56] has also developed a multi-metal catalyst, made up of Cu, Zn, and Co, in which each of the three metals serves a specific role based on their differing bond-breaking capabilities. This multi-metal catalyst has shown improved performance compared to single metal catalysts, highlighting the potential benefits of using a combination of metals in the bio-oil synthesis reaction process. Cu was intended to help with the WGS process, while Co was meant to help with the acetic acid SR reaction, and Zn was supposed to help with catalytic performance at lower temperatures [53]. Several novel theories using Co-based catalysts were suggested by researchers for the steam reforming process. Moreover, it was found that Co nanoparticles (< 5 nm), have displayed better activity for the decomposition of H_2O, which promotes the oxidation of carbonaceous species during the process. Along with this, the type of supports is also important in regulating reaction routes during SR process. For example, the use of Al_2O_3 (acidic in nature) as a support material in ethanol SR process favours the formation of ethylene by ethanol dehydration route, which subsequently polymerize and promotes coke deposition on the catalyst surface [57,58]. On the other hand, MgO (basic in nature) promotes acetaldehyde formation via ethanol dehydrogenation. Besides acidic and basic support material, reducible support materials were also used in SR process, which promotes acetone formation [59]. The hydrogen yield is definitely influenced by the chemical characteristics of these intermediates. Hence, these studies offer additional insight into the basic understanding of the SR reaction mechanism.

Table 1.7 Effect of different noble and transition metal catalyst for steam reforming process [43,44]

Catalyst	**Temperature (°C)**	**Conversion (%)**	**Selectivity H_2 (%)**	**Remarks**
Fe/Al_2O_3	550°C	45	34	• Active only for cracking of C-C bond
Cu/Al_2O_3	550°C	50	23	• Promote WGS reaction • Active only for cracking of C-H bond
Ni/Al_2O_3	550°C	100	92	• Active for cracking of C-C bond and C-H bond • Promote SR reaction • Coke formation
Co/Al_2O_3	550°C	100	90	• Active for cracking of C-C bond and C-H bond • Promote SR reaction • Coke formation • Less stable than Ni
Rh(0.5 wt%)/Al_2O_3	800°C	97	96	• More active for C-C bond cracking than other noble metals • Expensive • High temp. required
Ru(1 wt%)/Al_2O_3	800°C	38	90	• Expensive • High temp. required
Pt(1 wt%)/Al_2O_3	771°C	80	15	• Efficient for WGS reaction • Coke formation

`1.5.4 Catalyst deactivation in SR process

As mentioned earlier, the steam reforming process is highly intricate, even when focusing on a single model compound. The outcome of the reaction can be influenced by various factors, including the nature of the catalyst used, such as the type of metal, metallic particle size, metal oxidation state, properties of the support/metal oxide promoter as well as the kind of reactants investigated [46,60]. Gaining insight into the steam reforming process, a single model compound can provide valuable insights, but determining the steam reforming reaction mechanism of actual bio-oil is a more complex challenge.

During the steam reforming process, various factors can contribute to the degradation of the catalyst, including sintering of the support material and metal crystallites, as well as coke deposition [7,48,60–62]. To tackle these challenges, recent studies have focused on developing more efficient Ni-based catalytic systems such as bi-metallic, spinel, perovskite etc[63–67]. Different metals' synergistic effects may help to design an effectual catalytic system for bio-oil steam reforming process. Among these, perovskites have emerged as a promising class of catalysts for H_2 production thru reforming, exhibiting exceptional values with both methane and bio-oil model compounds as feedstock [53,67–70]. Perovskite-type oxide catalysts, possessing the general formula ABO_3, are extensively explored in heterogeneous catalysis for various catalytic reactions such as oxidation and/or reduction due to their stability. The A sites are generally occupied by rare-earth (lanthanide) metals and/or alkaline earth metals, whereas the B sites typically house transition metals with 3d, 4d or 5d configurations [71,72]. By changing or partial substituting metals at the A and/or B sites, a large number of perovskite catalysts with different catalysts can be synthesized. Furthermore, this may result in a drastic change in the redox and/or surface properties of the synthesized catalysts, such as the formation of oxygen vacancies, which in turn may also lead to an equally drastic enhancement in catalytic performance [72]. In addition, they can also serve as excellent precursors for the synthesis of supported bimetallic catalysts [72]. Researchers have explored the different catalysts of such combinations for the steam reforming processes. Lanthanum metal has capability of larger oxygen vacancies because of its bigger ionic radius, which is helpful for the in-situ coke oxidation during the reaction. Moreover, the partial substitution of various transition metals at B-site provides the synergistic effect of two metals, resulting the excellent catalyst stability and higher hydrogen gas yield.

Another hindrance in the SR process is the deactivation of the catalyst due to the formation of carbonaceous species on its surface caused by the thermal breakdown of organic molecules (eq.4). In view of this, it is important to understand the nature of the coke deposited on the catalyst surface in order to mitigate its negative effects on the SR process and maintain the efficiency of the catalyst. In this direction, Nogueira et al. [73] reported that, on performing the thermogravimetric analysis (TGA) of spent catalysts (15 Ni/Al and 15Ni5Mg/Al), the initial weight loss was reported in a temperature range of 300-400 °C, which was attributed to oxidation of amorphous coke. While, the second and greatest weight loss was recorded at temperature greater than 500 °C, which was ascribed to oxidation of graphitic/filamentous carbonaceous species formed on catalyst surface.

Moreover, bio-oil oxygenates are more susceptible to polymerization than hydrocarbons (e.g., aldol condensation, and olefin polymerization). Similarly, the severity of polymerization also increases owing to presence of big thermally unstable compounds (e.g., phenols, furans, carbohydrates,) at higher temperatures. Few methods have been suggested to reduce coke deposition on catalyst surface. One is to reduce the surface reactions that contribute to the production of carbonaceous species [46]. Another intends to promote water dissociation in order to assist the gasification of coke precursors and, as a result, inhibit the production of coke. Unfortunately, since water disintegration may oxidize the active site, reducing the number of metallic sites available on the surface, posing an intriguing issue concerning the balance of promoting surface carbonaceous species gasification while preventing active metal site oxidation [43,55].

Furthermore, decreasing the number of metallic sites can be helpful in reducing the deposition of carbonaceous species on the catalyst surface. These factors, if not carefully considered and managed, can negatively impact the stability of the catalyst and hinder its performance during steam reforming operations. It is important to carefully balance the various factors involved in the steam reforming process to achieve optimal results. Hence, catalyst deactivation in bio-oil SR process is mainly due to coke deposition on its surface and sintering of metallic particles at high temperature.

1.6 Observation and research gaps

1. Mainly, the steam reforming of bio-oil model compounds, particularly acetic acid, has been widely studied in the context of SR process. However, simulated bio-oil consist of major organics groups may give better insight for SR process.
2. The use of Ni-based catalysts in steam reforming has been shown to be highly effective in converting acetic acid and producing a high yield of H_2. This makes Ni-based catalysts a promising option for the production of hydrogen from bio-oil and other organic feedstocks.
3. In the context of use of noble metals for SR process, Rh (rhodium) and Pt (platinum) have been found to have excellent catalytic activity, capable of efficiently converting organic feedstocks into hydrogen and carbon monoxide. However, their high cost limits their widespread use in industrial applications.
4. Catalyst deactivation is a significant concern in steam reforming process. Catalyst deactivation refers to the decline in the efficiency and performance of the catalyst over time, leading to a decrease in the yield of hydrogen produced. This can be caused by various factors, such as the accumulation of carbonaceous deposits on the surface of the catalyst, poisoning of the catalyst by impurities in the feedstock, and mechanical failure of the catalyst structure.
5. La-based catalysts have shown promising activity towards steam reforming process due to their ability to suppress the formation of coke and maintain high thermal stability.
6. Perovskite-type oxide catalysts (ABO_3) have shown excellent catalytic activity in various reactions, such as oxidation and reduction, due to their ability to support multiple active sites for reaction. This high activity, combined with their stability at high temperatures, makes perovskite-type oxide catalysts a promising option for steam reforming reactions.
7. Moreover, the partial substitution at A and B position using different metals is also an unique approach to increase the catalytic performance due to an increase in lattice defects.
8. Kinetic studies for the steam reforming process have mainly been focused on acetic acid. However, as bio-oil contains more complex and cyclic molecules, such as phenolics, a kinetic study of the steam reforming process for phenol could provide valuable insights into the steam reforming of bio-oil.

1.7 Objective

The motivation behind this work was to find an alternative source of energy which can fulfil the global energy demand via a sustainable route. In this regard, the present study aims to develop a catalytic system to produce green and renewable hydrogen via steam reforming of bio-oil derived from agricultural residue.

1.7.1 Main Objective

To develop a stable and highly selective catalytic process for hydrogen production from bio-oil, especially from agriculture waste.

1.7.2 Specific objectives

1. Thermodynamic analysis of the overall reaction system.
2. Preparation and characterization of metal-based catalysts based on extensive literature survey.
3. Study the performance of these catalysts to maximize hydrogen production and identify an optimal catalyst for the process.
4. Evaluate the effect of process variables for maximization of hydrogen yield.
5. Kinetic study of the catalytic steam reforming process at optimized parameters.
6. Catalyst deactivation study and coke analysis.
7. Comparative analysis with advanced steam reforming processes.

1.8 Organisation of the thesis

Chapter 1: This chapter consists of the introduction of this dissertation. It includes the motivation behind work. Moreover, a discussion was made about existing energy sources and associated problems in this direction. The detailed discussion is made on alternative energy sources, i.e. green hydrogen produced via catalytic steam reforming. The extensive literature survey in this direction has been also discussed.

Chapter 2: This chapter includes the detailed experimental procedure for the catalyst synthesis, and various characterization techniques for fresh and spent catalysts. Furthermore, the detailed methodology of catalytic steam reforming experiments and biomass pyrolysis is also discussed.

Chapter 3: This chapter contains the thermodynamic potential followed by catalytic activity tests for synthesized $LaNi_xCo_{1-x}O_3$ perovskite catalysts for simulated bio-oil steam reforming experiments. It also includes the process parameter optimization, and catalyst stability test.

Chapter 4: This chapter includes the synergistic effect of various metals at A and B-site elements of perovskite catalyst (ABO_3) for steam reforming of simulated bio-oil to produce green hydrogen.

Chapter 5: This chapter consists of the kinetic study of steam reforming of phenol with the optimum catalyst obtained from the previous studies. The kinetic study parameters were evaluated using the power law model.

Chapter 6: This chapter contains the steam reforming of raw bio-oil using optimum catalyst at optimum process parameters obtained from the previous studies. The raw bio-oil used here is prepared in the lab via pyrolysis of a blend of agricultural residues (rice husk, wheat straw, corn cob and sugarcane bagasse).

Chapter 7: This chapter contains the catalyst deactivation study for the different bio-oil mixture (SB1, SB2, raw bio-oil). The qualitative and quantitative analysis have been discussed in detailed for all cases.

Chapter 8: This chapter comprises the comparative study of various advanced steam reforming processes with the conventional steam reforming of bio-oil. Various aspects of the advanced steam reforming process were discussed to maximize the hydrogen yield and the heat requirement of the process.

Chapter 9: This chapter summarizes the overall conclusion of the thesis.

Chapter 2: Materials and Methods

This chapter presents a comprehensive description of the experimental procedures employed for the synthesis of catalysts, as well as the characterization techniques utilized for both fresh and spent catalysts. Additionally, a detailed experimental methodology for the conduct of catalytic steam reforming experiments and biomass pyrolysis is discussed.

2.1. Catalyst synthesis

2.1.1 Materials used

The reagents $La(NO_3)_2.6H_2O$ (Loba Chemie), $Cu(NO_3)_2.3H_2O$ (Loba Chemie), $Ni(NO_3)_2.6H_2O$ (Hi-Media), $Co(NO_3)_2.6H_2O$ (Hi-Media), $Fe(NO_3)_3.9H_2O$ (CDH India), $Ce(NO_3)_2.6H_2O$ (Hi-Media), $Ca(NO_3)_2.4H_2O$ (Loba Chemie), $Zr(NO_3)_2.6H_2O$ (Loba Chemie) and citric acid (CDH India) were used for the synthesis of different combination of perovskite catalysts.

2.1.2 Catalyst preparation

The perovskite catalysts used throughout this work were synthesized via a sol-gel method, as previously reported in literature [71,74–76]. Firstly, the metal precursors were dissolved in distilled water using a magnetic stirrer. Subsequently, 5% excess (molar) citric acid (gelling agent) was added to the solution, and the mixture was evaporated at 80 ºC until gel formation. The resulting gel was dried at 105 ºC in a hot air oven for 12 h, followed by grinding and calcination at 800 ºC (ramp rate 5 ºC/min) for 6 h in a muffle furnace (Nabertherm "LE6/11/3216").

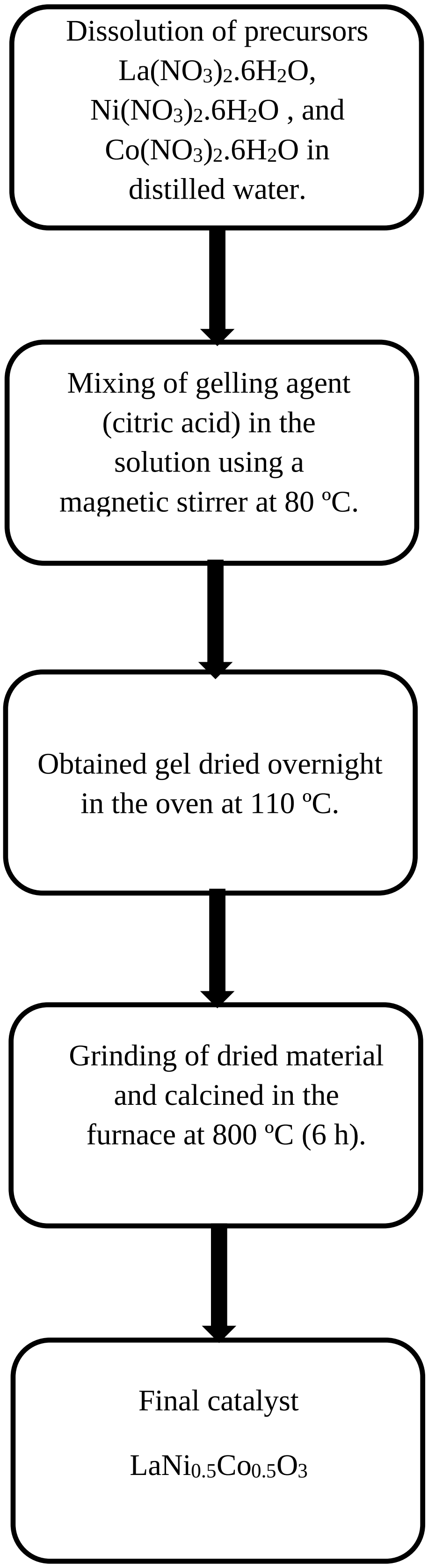
Dissolution of precursors $La(NO_3)_2.6H_2O$, $Ni(NO_3)_2.6H_2O$, and $Co(NO_3)_2.6H_2O$ in distilled water.
Mixing of gelling agent (citric acid) in the solution using a magnetic stirrer at 80 ºC.
Obtained gel dried overnight in the oven at 110 ºC.
Grinding of dried material and calcined in the furnace at 800 ºC (6 h).
Final catalyst
$LaNi_{0.5}Co_{0.5}O_3$

Fig. 2.1 Synthesis of perovskite catalyst

2.2 Characterization of catalysts

The synthesized fresh and spent catalysts were characterized to evaluate their catalytic properties via different characterization techniques as listed below:

1. X-ray diffraction (XRD)
2. BET-surface area
3. Field emission scanning electron microscopy (FESEM)
4. Energy-dispersive X-ray spectroscopy (EDX)
5. Fourier transform infrared spectroscopy (FTIR)
6. Thermo gravimetric analysis (TGA)
7. Temperature program desorption (TPD)
8. Temperature program reduction (TPR)
9. X-Ray Photon Spectroscopy (XPS)
10. RAMAN Spectroscopy

2.2.1 X-ray diffractogram (XRD)

The crystal structure of calcined perovskite catalysts was investigated using X-ray diffraction (XRD) by utilizing a Rigaku Miniflex 600 diffractometer. The instrument was set at 30 kV and 10 mA and utilized Cu Kα radiation (λ=1.5406 Ǻ) within a 2θ range of 10^o to 80^o, with a scanning speed of 4^o/min. Additionally, in-situ XRD analysis of reduced catalyst sample was carried out using a Bruker D8 venture diffractometer. This instrument was equipped with an Anton Paar TCU 2000N temperature control unit, and the analysis was performed at respective reduction temperatures under a H_2/N_2 atmosphere. The identification of crystalline phases was carried out by utilizing the technique of X-ray diffraction, specifically by comparing the 2θ values or d-spacing of the characteristic Bragg reflections of the investigated samples to those of reference samples as listed in the Inorganic crystal structure database (ICSD) database. The average crystallite size (D) of catalyst samples was obtained through the application of the Scherrer equation to the full width at half maximum (FWHM) of the X-ray diffraction peaks, after correcting for the instrumental broadening effect.

$$d = \frac{K * \lambda}{\beta * Cos\theta}$$

Where d is the crystallite size, K is dimensionless shape factor (taken as 0.9, by assuming spherical crystal), λ is wavelength of X-ray, and β represents instrumental broadening of the diffraction line, which corresponds to the Bragg angle (θ), quantitatively represented by the full width at half maximum (FWHM) of the corresponding diffraction peaks.

2.2.2 BET-surface area

The textural properties of the catalysts, such as average pore size, pore volume and BET surface area, were determined using a Belsorp mini X instrument. Prior to analysis, the catalysts were subjected to degassing at 200 ºC for 3 h in a degassing chamber to remove any adsorbed moisture and impurities. Specific surface area and pore size distribution were determined through the application of the Brunauer-Emmett-Teller (BET) equation and the Barrett-Joyner-Halenda (BJH) method, respectively, in a relative pressure range of 0.05 to 0.3. Adsorption-desorption isotherms were also generated for the catalyst samples.

2.2.3 Scanning electron microscopy (SEM)

The scanning electron microscope (SEM) characterization technique utilizes a high-energy, focused electron beam to obtain a variety of signals from the specimen through interactions. The region within the specimen where the primary electron beam interacts with the sample is referred to as the interaction volume. As the electron beam interacts with the sample surface, it produces various signals such as Auger electrons, secondary electrons, backscattered electrons, and X-rays. These signals provide information about the sample's morphology, texture, and chemical composition. A typical SEM signal used to generate a 2D image of the sample's morphology is the secondary electrons. The SEM can achieve magnification levels between 20X and 105X with a spatial resolution of 20nm. The electron gun, consisting of a filament and shield, generates a highly focused and energetic electron beam through thermionic emission in an ultra-high vacuum. In the present work, the surface morphology of fresh and spent catalysts was recorded using a JEOL-JSM-7610FPlus field emission scanning electron microscope (FESEM).

2.2.4 Energy-dispersive X-ray spectroscopy (EDX)

Energy dispersive X-ray spectroscopy (EDX) is a commonly employed analytical method for identifying and determining the distribution of individual elements present in a sample. The method is based on the principle that each element has a unique atomic structure, which results in a distinct elemental peak in the EDX spectra, serving as a fingerprint of the element. An electron beam is produced by an electron gun and directed towards the sample, resulting in the ejection of electrons upon impact. These ejected electrons are replaced by electrons from higher energy levels, which subsequently emit X-rays. The energy or wavelength of these emitted X-rays is used to determine the elemental composition of the sample. The emitted X-rays are detected by a highly sensitive detector, which converts the energy of the X-rays into a voltage pulse through a charge sensitive preamplifier and multichannel analyzer. This voltage measurement is then analyzed by a computer system to determine the elemental composition of the catalyst sample. Bruker make EDX instrument equipped with FESEM instrument was used to record the elemental composition here.

2.2.5 Diffuse Reflectance infrared Fourier transform spectroscopy (DRIFT)

The nature of acidic surface sites of the fresh catalysts was determined by recording the diffuse reflectance infrared Fourier transform (DRIFT) spectrum of adsorbed pyridine (Py-FTIR). A ThermoScientific Nicolet iS50 spectrometer equipped with a Mercury-Cadmium-Tellurium (MCT) detector and a Harrick Praying Mantis cell was used for this purpose. For this analysis, a small amount of catalyst sample was loaded into the DRIFT cell and pre-treated at a temperature of 200 °C for 1h under Argon atmosphere to remove physiosorbed moisture. Subsequently, the sample was cooled down to room temperature and then exposed to pyridine for 30 minutes. After this, the cell was flushed with Argon for 30 minutes to remove the physically adsorbed pyridine on sample surface, following which the spectra (64 scans, and 4 cm^{-1} resolution) was recorded at room temperature. Next, the temperature was raised to 100, 200, and 300 °C at a rate of 10 °C/min and spectra was recorded at each of these temperatures in a similar manner.

2.2.6 Thermo gravimetric analysis (TGA)

The amount of carbon/coke deposited on the catalyst surface was carried out through thermogravimetric analysis (TGA) on a TA SDT 650 thermal analyser. The spent catalyst was obtained by unloading the reactor after the experiments. Each TGA experiment was performed by loading the 15-20 mg of spent catalyst on the 90 µL crucible. After that, spent catalyst samples were heated up to 800 ºC (5 ºC/min ramp rate) with 100 ml/min air flow.

The presence of oxygen mobility/mobile oxygen species in the synthesized perovskite catalysts was also investigated by TGA of a mixture of the catalysts and carbon black (1:1 by weight). The mixture was heated in an inert atmosphere (N_2, 100 mL/min) from 50 °C to 900 °C at a rate of 10 °C/min. Due to its extremely high fixed carbon content (99.6%), carbon black be considered pure carbon and does not lead to any interference during the TGA analysis [71,77]. As a result, any weight loss recorded during the analysis can be attributed to the oxidation of carbon by the mobile oxygen present in the perovskite catalysts, confirming their presence.

2.2.7 Temperature program desorption (TPD)

The acidity of the catalyst was quantitatively determined through the use of Temperature Programmed Desorption (TPD) with ammonia (NH_3) as the probe molecule. The analysis was performed on a Quantachrome CHEMBETTM TPR/TPD instrument. The samples were first preheated at 300 °C at a heating rate of 10 °C/min under continuous helium (He) flows for 30 minutes. Afterwards, the sample cell was cooled to 50 °C and NH_3 gas (10% in He) was adsorbed onto the catalyst surface by flowing through the sample for 1 h at a flow rate of 10 mL/min. The excess or physically adsorbed NH_3 gas was then removed by He flow (50 mL/min) for 30 minutes. Finally, the amount of desorbed gas was determined using an inbuilt temperature-controlled device (TCD) as a function of temperature in the range from 50-500 °C at a rate of 10 °C/min. Similar TPD methodology was used for basic sites of the catalyst using CO_2 as probe molecule.

2.2.8 Temperature program reduction (TPR)

In order to get the reduction temperature for calcined catalyst, temperature programmed reduction (TPR) experiments were carried out using ChemiSoft TPx V1.03 (2750) (Micrometrix). Firstly, pre-treatment of 50-100 mg of catalyst samples were done under an argon atmosphere (Ar flow rate = 30 ml/min) at 250ºC for 1h and then subsequently cooled at room temperature. After pre-treatment, the catalyst samples were reduced under 30 ml/min flow rate of 10% H_2/Ar gas mixture in the temperature range of 25 ºC to 750ºC (ramp rate of 10 ºC/min). The H_2 consumption amount was continuously monitored by a thermal conductivity detector (TCD).

2.2.9 Raman spectroscopy

Raman spectroscopy is a non-invasive technique used to analyze chemical compounds and determine their structural characteristics, phases, and polymorphs. This method is based on how light interacts with the chemical structure of a material, leading to most photons being scattered at the same wavelength as the incident light, known as Rayleigh scattering. A small fraction of photons are scattered at different wavelengths, known as Raman scattering, and the energy difference between the incident and scattered photons is called the Raman shift. Scattered photons with less energy than the incident photons are known as Stokes scattering, while those with more energy are known as Anti-Stokes scattering. In the current study, Raman scattering measurements were conducted using a Renishaw inVia Raman microscope and a LabRam Horiba scientific instrument with 532 nm excitation laser.

2.2.10 X-Ray Photon Spectroscopy (XPS)

X-ray Photoelectron Spectroscopy (XPS) is a widely used analytical technique for surface analysis that provides detailed information on the chemical state and composition of a material. It is a highly surface-sensitive method that can be applied to a wide range of materials. The technique involves the excitation of the sample with Al Kα x-rays, which leads to the emission of photoelectrons from the surface of the material. These emitted electrons are quantized using an electron energy analyzer, and their binding energy and intensity can be used to determine the chemical state and concentration of specific elements. The binding energy (B.E.) of the ejected photoelectrons is given by the equation

$$B.E. = h * \nu - K.E. - \Phi$$

where ϕ, $K.\ E.$, and $h\nu$ represent the work function, kinetic energy, and photon energy, respectively. The average penetration depth for XPS analysis is around 5 nm. In the current study, measurements were carried out using the Versaprobe PHI 5000 (Physical Electronics) scanning system and the ESCALAB XI+ (ThermoFisher Scientific), both under an ultrahigh vacuum analysis chamber and using Al Kα X-rays.

2.3 Thermodynamic assessment of the steam reforming process

Before performing the steam reforming experiments, thermodynamic potential of simulated bio-oil and model oxygenates was tested using Aspen plus software. A thermodynamic analysis was conducted to enhance the comprehension of the suitability of the reaction-product model systems and establish correlations between the process variables, such as temperature, steam to carbon ratio (S/C), and the distribution of products. In order to achieve this, the temperature of the reactor was varied within the range of 400 to 1000 °C at atmospheric pressure, for steam to carbon molar ratio of (1.5-4). The product compositions were estimated by utilizing the standard Gibbs' free energy minimization technique. The species under consideration were hydrogen, carbon monoxide, methane, carbon dioxide, carbon, unreacted simulated bio-oil and water, which were also identified from preliminary experiments.

2.4 Possible Reactions

The steam reforming (SR) and water gas shift (WGS) reactions are the leading reactions involved in the bio-oil SR process. The overall bio-oil SR process is endothermic in nature and produces gaseous products, i.e. H_2, CO_2, and CO[48,78]. However, few other side reactions may also occur during SR process, for instance, thermal decomposition, methanation, Boudouard reactions etc.

2.4.1 Main reactions

Steam reforming reaction (SR):

$$C_nH_mO_k + (n-k)H_2O \rightarrow n\,CO + \left(n + \frac{m}{2} - k\right)H_2 \quad \mathbf{\Delta}\mathrm{H} = +\mathrm{ve} \qquad (2.1)$$

Water gas shift reaction (WGS):

$$CO + H_2O \leftrightarrow CO_2 + H_2 \qquad \mathbf{\Delta}\mathrm{H} = -41\ \mathrm{KJ/mol} \qquad (2.2)$$

Overall reaction:

$$C_nH_mO_k + (2n-k)H_2O \rightarrow \left(2n + \frac{m}{2} - k\right)H_2 + nCO_2 \quad \mathbf{\Delta}\mathrm{H} = +\mathrm{ve} \qquad (2.3)$$

2.4.2 Other reactions

Thermal decomposition reaction:

$C_nH_mO_k \rightarrow C_xH_yO_z + gas(H_2, CO_2, CO, CH_4, CH_q) + coke$ **Δ**H = +ve (2.4)

Methanation reaction:

$CO + 3H_2 \rightarrow CH_4 + H_2O$ **Δ**H = -206 KJ/mol (2.5)

$CO_2 + 4H_2 \rightarrow CH_4 + 2H_2O$ **Δ**H = -165 KJ/mol (2.6)

Carbon gasification reaction:

$C + H_2O \leftrightarrow CO + H_2$ **Δ**H = 131 KJ/mol (2.7)

$C + 2H_2O \leftrightarrow CO_2 + 2H_2$ **Δ**H = 90 KJ/mol (2.8)

Methane steam reforming reaction:

$CH_4 + H_2O \leftrightarrow CO + 3H_2$ **Δ**H = 206 KJ/mol (2.9)

Boudouard reaction:

$2CO \leftrightarrow CO_2 + C$ **Δ**H = -171.5 KJ/mol (2.10)

Methane decomposition reaction:

$CH_4 \leftrightarrow C + 2H_2$ **Δ**H = 74.9KJ/mol (2.11)

2.5 Catalytic experiments for steam reforming reaction

All steam reforming (SR) experiments were conducted in a fixed-bed reactor unit under various process parameters, such as reaction temperature, steam to carbon molar ratio (SCMR), and feed flow rate, at atmospheric pressure as depicted in the schematic diagram (Fig. 2.1). The reactor tube, constructed of Inconel 800 material with an internal diameter of 9.24 mm and a length of 520 mm, was placed inside a furnace with two heating zones. Prior to each SR experiment, the catalyst was in-situ reduced at 650 – 800 °C (as determined from H_2-TPR analysis for various catalyst composition) for 2.5 h under a continuous flow of hydrogen and nitrogen mixture (50 vol% each). The simulated bio-oil/ raw bio-oil/ phenol and water mixture were pumped through an HPLC pump and fed into a pre-mixer heater (temperature 200 °C) to vaporize the feed mixture. The vaporized feed mixed with a carrier gas nitrogen (50 ml/min) was then fed into the reactor tube. The reactor tube was loaded with 1 g of calcined catalyst with inert material silicon carbide (SiC), which was mixed to maintain uniform temperature throughout the bed. All the experiments were conducted by maintaining the plug flow condition, i.e. the ratio of catalyst bed height to particle size and the ratio of internal diameter of the tubular reactor to particle size of catalyst were kept as 50 and 30, respectively. The SR experiments were conducted utilizing various catalysts, at different steam to carbon molar ratios (1.6-3.26), temperatures ranging from 600 to 800 °C and with different space-time conditions. The obtained vapors were condensed using a condenser and then fed into the gas-liquid separator (GLS). The obtained gaseous products were analyzed using Agilent 7820B GC (gas chromatograph)-TCD equipped with Hayesep T, Hayesep Q and Molecular-sieve packed columns installed in series and liquid products were analyzed by an Agilent 7890B GC-FID (gas chromatograph- flame ionization detector) using DB-5 capillary column.

Catalyst performance and optimum parameters were evaluated by quantitative analysis of feed conversion and gaseous products (H_2, CO_2, CH_4, and CO) yield.

The yield of hydrogen was calculated from the following equation:

$$yield\ of\ hydrogen\ gas\ (\%) = \frac{Molar\ flow\ of\ H_2\ in\ gaseuos\ product\ stream}{2.20 \times Molar\ flow\ of\ C\ in\ feed\ stream} \times 100 \qquad (2.12)$$

The yield of other gaseous products was calculated from the following equation:

$$yield\ of\ gaseous\ species\ 'i'\ (\%) = \frac{Molar\ flow\ of\ C\ in\ gaseous\ speices\ 'i'}{Molar\ flow\ of\ C\ in\ feed\ stream} \times 100 \qquad (2.13)$$

Where species *'i'* denotes CO_2, CH_4 and CO gases.

The conversion calculations were done based on the amount of carbon element in the simulated bio-oil mixture using the following formula:

$$Conversion\ (\%)\ = \frac{(Molar\ flow\ of\ C\ in\ feed\ stream - Molar\ flow\ of\ C\ in\ product\ stream)}{Molar\ flow\ of\ C\ in\ feed\ stream} \times 100 \qquad (2.14)$$

The SCMR was calculated by using the following formula:

$$S/_{C} = \frac{no.of\ moles\ of\ water\ fed}{no.of\ moles\ carbon\ fed} \tag{2.15}$$

The weight hourly space-time (WHST) was calculated by

$$\frac{W}{F_{A0}} = \frac{Weight\ of\ catalyst}{Molar\ flow\ rate\ of\ bio-oil}\ (kg_{cat}.h/kgmol_{bio-oil}) \tag{2.16}$$

The amount of coke deposited on catalyst surface was calculated as

$$Coke\ deposition\ rate\ = \frac{weight\ of\ coke\ deposited\ on\ the\ catalyst\ bed\ per\ hour}{weight\ of\ catalyst} \tag{2.17}$$

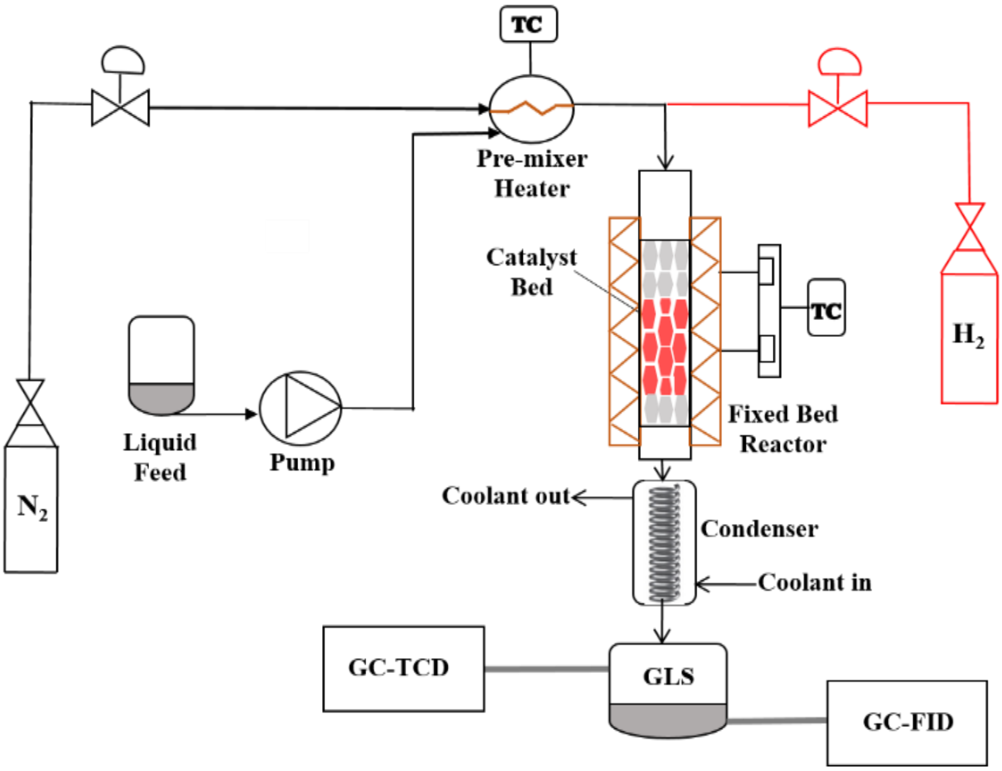
TC
Pre-mixer
Heater
Catalyst
Bed
TC
H$_2$
Liquid
Feed
Pump
Fixed Bed
Reactor
N$_2$
Coolant out
Condenser
Coolant in
GC-TCD
GLS
GC-FID

Fig. 2.1 Schematic diagram of steam reforming experimental setup

2.6 Kinetic experiments

The objective of a kinetic study is to understand the rate of a chemical reaction and to develop a rate equation that is based on the fundamental reaction mechanism. This rate equation is then validated by comparing it to experimentally observed data. This approach allows for the identification of the rate determining step and the determination of the reaction kinetics parameters such as the activation energy and the pre-exponential factor. In the present study, steam reforming experiments were performed to evaluate the kinetic parameters for the phenol steam reforming process with the optimum catalyst. As the phenol was used as a model compound for the kinetic study, all the process parameters were again optimized along with the catalyst stability study. Furthermore, the kinetic experiments were performed under 1 atm pressure and at temperatures of 600, 650, and 700 ºC. The experiments also varied the space time (W/F_{A0}) from 15 to 31 $kg_{cat}.h/kmol_{PhOH}$ and the steam to carbon molar ratio from 1.6 to 3.2 using fresh catalyst samples diluted with an inert material (SiC). The kinetic parameters were then evaluated using a non-linear least-square regression technique to analyze the data. Moreover, the power law model was used to calculate the kinetic parameters.

2.7 Pyrolysis experiments

In order to get the raw bio-oil via pyrolysis process, the experiments were conducted using a tubular fixed bed reactor with an inner diameter of 25.4mm and 1000 mm length as displayed in Fig.2.2. The reactor tube was placed inside a split furnace with two heating zones, and 40g of dried biomass was loaded into it during each experiment. The agricultural residue mainly rice husk, wheat straw, corn cob, and sugarcane bagasse were collected from the villages of Rupnagar district. Before using for the pyrolysis experiment, the agricultural residues were washed properly with the distilled water to remove the impurities present in it. Furthermore, the agricultural residues were dried in an oven to remove the moisture and then the dried biomass was chopped and crushed in a grinder before using in the experiments. After that, the pyrolysis experiments were carried out in a fixed bed reactor by varying temperatures between 400-600 °C, at different heating rates ranging from 5-40 °C/min, and a fixed nitrogen flow rate of 50mL/min. The obtained vapours were passed through a condenser followed by a gas liquid separator to separate the liquid and gaseous. The resulting liquid products were analyzed using an Agilent 7890B GC-MS (gas chromatograph- mass spectroscopy) system equipped with a DB-5 capillary column.

The yields of pyrolysis products have been calculated using following equations:

$$Bio-oil\ yield\ (wt.\%) = \frac{weight\ of\ bio\text{-}oil\ formed}{weight\ of\ feed\ taken} \times 100 \qquad (2.18)$$

$$Biochar\ yield\ (wt.\%) = \frac{\text{weight of biochar formed}}{\text{weight of feed taken}} \times 100 \qquad (2.19)$$

$$Gases\ yield\ (wt.\%) = 100 - (bio - oil\ yield + biochar\ yield) \qquad (2.20)$$

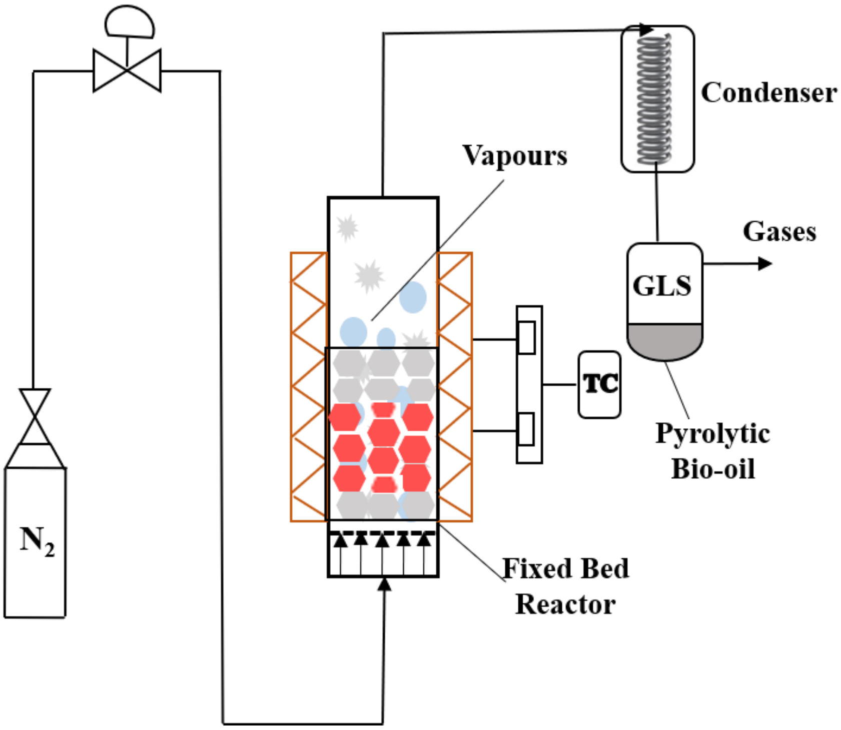
Condenser
Vapours
Gases
GLS
TC
Pyrolytic
Bio-oil
N_2
Fixed Bed
Reactor

Fig. 2.2 Schematic diagram of pyrolysis experimental setup

Chapter 3: Simulated bio-oil steam reforming experiments with $LaNi_xCo_{1-x}O_3$ catalysts

This chapter presents the potential of utilizing simulated bio-oil, which comprises of an elemental composition akin to that of bio-oil obtained from pyrolysis of agricultural waste used by other researchers, for the production of green hydrogen via catalytic steam reforming [76,79,80]. The simulated bio-oil (SB1) used in the study was a mixture of acetic acid (62.3 mol%), phenol (19.9 mol%), and benzaldehyde (17.8 mol%). Prior to conducting catalytic steam reforming (SR) experiments, it was deemed important to assess the thermodynamic potential of the process. This evaluation aimed to gain a deeper understanding of the process parameters, reactions and conditions that impact the reaction's efficacy. The insights gained from this assessment were utilized to fine-tune the conditions for the catalytic experiments and enhance the production of the desired products. Following the evaluation of the thermodynamic potential, a series of perovskite catalysts ($LaNi_xCo_{1-x}O_3$) were synthesized using the sol-gel method. These catalysts were then tested for their activity in steam reforming simulated bio-oil using a tubular fixed bed reactor. The catalysts were characterized using techniques such as BET, XRD, TPR, SEM-EDX, TGA, and Raman spectroscopy. The optimal conditions for the steam reforming process were determined by varying various process parameters such as reaction temperature, weight hourly space-time (WHST), and steam to carbon molar ratio (SCMR) under atmospheric pressure. This was done to determine the most favorable conditions that would result in the highest yield and selectivity of the desired products.

3.1. Thermodynamic analysis

The aim of the thermodynamic analysis was to assess the production and selectivity of hydrogen and to determine how the process variables such as temperature, feed molar ratio, and pressure affect these outcomes. The thermodynamic analysis is critical as it offers a fundamental understanding of the reaction, as the equilibrium conversion is the maximum that can be achieved with any catalyst. This analysis provides valuable insights that can be utilized to optimize the steam reforming process and enhance the production of hydrogen.

3.1.1 Effect of steam to carbon molar ratio

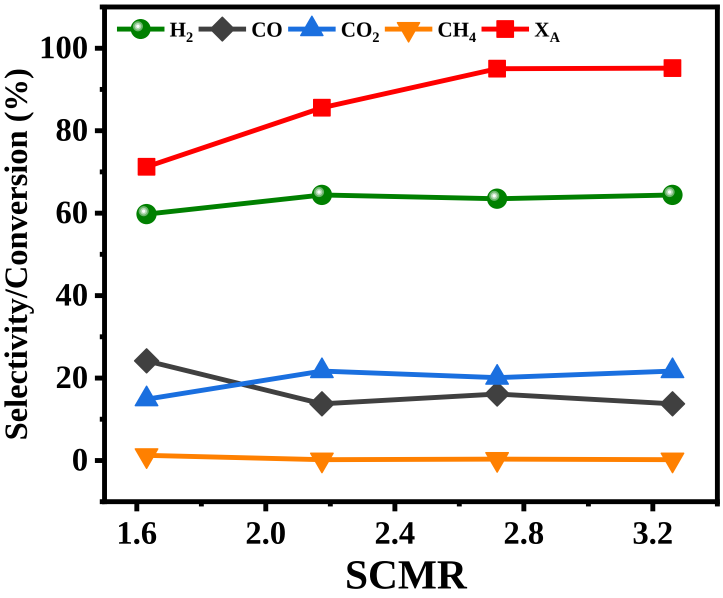

Fig. 3.1 Effect of steam to carbon molar ratio on gaseous products selectivity and bio-oil conversion (T = 700 ºC and P=1 atm)

The study on the impact of steam carbon-to-methane ratio (SCMR) on the steam reforming of simulated bio-oil (SB1) was performed at 700 °C and 1 atm pressure. The results indicate that the addition of water to the feed has a substantial effect on the reaction outcomes. The high water content has been found to suppress the formation of coke and promote the water-gas shift reaction, leading to an increase in hydrogen selectivity.

However, the high water content also requires a high enthalpy for evaporation, which may have implications for the overall energy efficiency of the reaction. Despite this and as displayed in Fig. 3.1, the results demonstrate that the addition of water to the feed results in a more complete steam reforming reaction and the shift towards the water-gas shift and methane reforming reactions.

The study indicates that an increase in water content in the feed leads to a decrease in carbon monoxide (CO) selectivity and an increase in carbon dioxide (CO_2) selectivity, while methane (CH_4) selectivity decreases. This highlights the significant impact that water has on product selectivities in steam reforming reactions for bio-oil and underscores the importance of considering the effect of water in such reactions.

3.1.2 Effect of reaction temperature

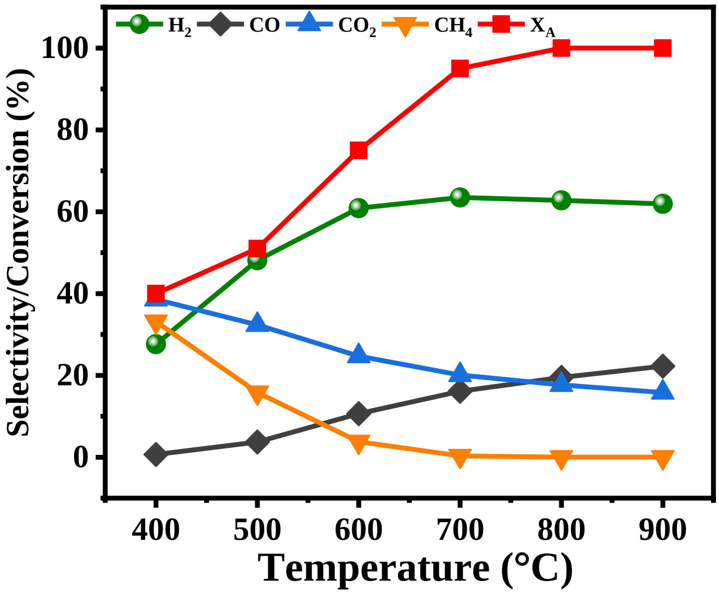

Fig. 3.2 Effect of temperature on gaseous products selectivity and bio-oil conversion (SCMR = 2.7 and P=1 atm)

The temperature has a significant influence on the formation of gaseous products during bio-oil steam reforming and presented in Fig. 3.2. At low temperatures, around 400 °C, the reaction pathway is dominated by decomposition reactions, resulting in high selectivity towards methane formation and low selectivity towards hydrogen production. However, as the temperature increases, the reaction pathway shifts from decomposition to steam reforming reactions, which are more favorable for hydrogen production. As a result, the selectivity towards hydrogen increases, while the selectivity towards methane decreases.

At higher temperatures, above 700 °C, the water gas shift reaction begins to shift in the reverse direction, which is an exothermic reaction. This leads to an increase in the selectivity towards carbon monoxide and a decrease in the selectivity towards carbon dioxide. The reverse water gas shift reaction becomes more significant at high temperatures as the equilibrium constant (K) decreases with increasing temperature. The thermodynamic analysis of the process reveals that the maximum hydrogen production occurs between 600 °C and 700 °C with a steam-to-carbon ratio of 2.7. At this temperature range, the conditions are favorable for both steam reforming and water gas shift reactions to occur in the forward direction, maximizing hydrogen production.

In conclusion, temperature plays a critical role in determining the distribution of gaseous products during bio-oil steam reforming. Understanding the temperature-dependent reaction pathways is important for optimizing the process for maximum hydrogen production and minimizing the formation of unwanted byproducts. Henceforth, these thermodynamics observations were employed for catalytic steam reforming experiments and discussed in the following section.

3.2. Catalyst' characterization

In the study, a series of perovskite catalysts LaNi$_x$Co$_{1-x}$O$_3$ (x= 0, 0.2, 0.4, 0.5, 0.6, 0.8 and 1.0) were synthesized using the sol-gel method. The fresh synthesized catalysts were then examined using various characterization techniques such as BET (Brunauer-Emmett-Teller) surface area analysis, X-ray diffraction (XRD), temperature-programmed reduction (TPR), scanning electron microscopy-energy-dispersive X-ray spectroscopy (SEM-EDX), thermogravimetric analysis (TGA), and Raman spectroscopy. These techniques helped in understanding the structural, textural, compositional, and thermal properties of the catalysts.

3.2.1. X-ray diffraction (XRD)

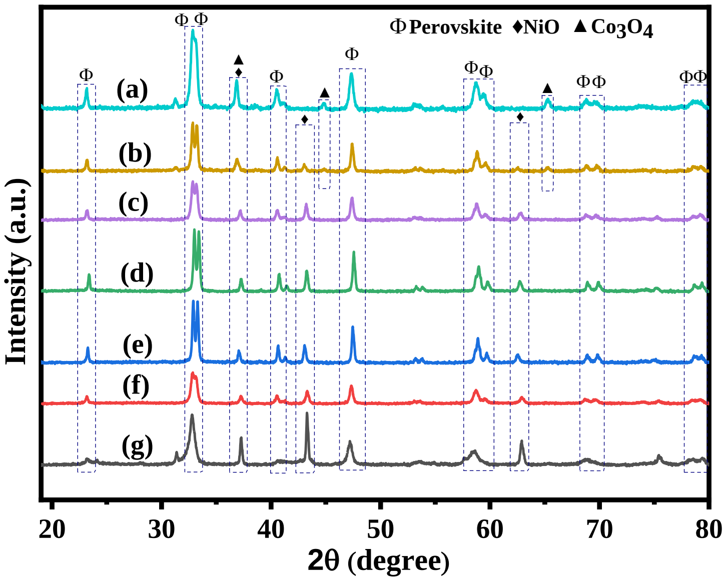

Fig. 3.3 XRD patterns of (a) LaCoO$_3$ (b) LaNi$_{0.2}$Co$_{0.8}$O$_3$, (c) LaNi$_{0.4}$Co$_{0.6}$O$_3$, (d) LaNi$_{0.5}$Co$_{0.5}$O$_3$, (e) LaNi$_{0.6}$Co$_{0.4}$O$_3$, (f) LaNi$_{0.8}$Co$_{0.2}$O$_3$ (g) LaNiO$_3$ catalysts

The obtained XRD spectra (Fig.3.3) exhibits peaks at 2θ values of 23.2°, 32.8°,33.2°, 40.5°, 41.2°, 47.4°, 58.5°, 58.8°, 59.83°, 68.7°, 69.7°, 78.5° and 79.1° were attributed to the (012), (110), (104), (202), (006), (024), (030), (214), (018), (220), (208), (134) and (128) lattices of perovskite structure[77,79,81–83]. The presence of all these characteristic peaks of perovskite in the diffractograms indicates the successful formation of the perovskite crystalline phase in all synthesized catalyst samples. Furthermore, as expected, there was no shifting of the peaks were observed when the loading amounts of Ni and Co were changed in any of the samples because of the fact that Ni and Co have nearly similar ionic radii. Besides these peaks, few additional peaks (displayed in Fig. 3.3) of lesser intensity were observed, which could be attributed to either NiO (ICSD code: 646096) or Co_3O_4 (ICSD code : 56123)[77,81,83]. No peaks attributed to any oxide phase of La was observed in any of the patterns, indicating its successful incorporation into the mixed metal oxide (perovskite) structure. The average crystallite size for fresh catalyst samples is calculated by taking average of five most intense diffraction peaks (2θ = 23.2°, 32.8°,33.2°, 47.4° and 58.5°) which are the main characteristic peaks of perovskite using Scherrer equation and displayed in Table 3.1[84,85].

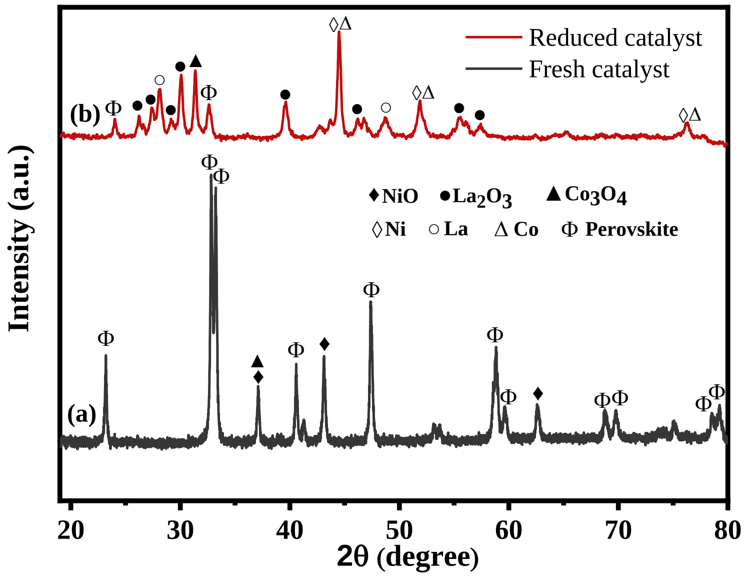

Fig. 3.4 XRD patterns of (a) fresh and (b) reduced $LaNi_{0.5}Co_{0.5}O_3$ catalysts.

Fig.3.4 shows the XRD patterns for the fresh and reduced $LaNi_{0.5}Co_{0.5}O_3$ catalysts. It is observed that all peaks of fresh $LaNi_xCo_{1-x}O_3$ except two located at 2θ = 24.0° and 32.8° disappears, while peaks corresponding to La_2O_3 and Ni-Co alloy (ICSD code: 108308) appears after reducing $LaNi_{0.5}Co_{0.5}O_3$ as displayed in Fig.3.3(b). This signifies that $LaNi_{0.5}Co_{0.5}O_3$ decomposed into La_2O_3 and metallic Ni and Co species (Ni-Co alloy), which get dispersed on La_2O_3 surface [83,86,87]. The most intense peak of reduced sample exhibited at 2θ = 44.5° reveals the signature of Ni-Co alloy formation with crystallite size 44.7 nm [88].

3.2.2. BET surface area

The textural properties of fresh $LaNi_xCo_{1-x}O_3$ catalysts (x=0, 0.2, 0.4, 0.5, 0.6, 0.8 and 1) such as BET specific surface area (SSA), average pore size, pore volume and crystalline size are shown in Table 3.1. The SSA and pore volume were found to be in the range of 3.5-6.1 m^2/g and 0.0092-0.0152 cm^3/g, respectively. The crystalline sizes of the calcined catalysts were calculated by using the Scherrer equation and are displayed in Table 3.1. The calcined catalyst sample $LaNi_{0.5}Co_{0.5}O_3$ had maximum SSA (6.1 m^2/g) and pore volume (0.0152 cm^3/g) among all prepared catalyst samples, while the average pore size and crystalline size were found 10.8 nm and 47.6 nm, respectively.

Table 3.1 Textural properties of $LaNi_xCo_{1-x}O_3$ (x=0, 0.2, 0.4, 0.5, 0.6, 0.8 and 1) catalyst samples

Catalyst	Specific Surface area[a] (m^2/g)	Pore volume[b] (cm^3/g)	Avg. pore size[b] (nm)	Average crystallite size[c] (nm)
$LaNiO_3$	3.8	0.0104	18.2	30.7
$LaNi_{0.8}Co_{0.2}O_3$	4.6	0.0116	15.6	64.8
$LaNi_{0.6}Co_{0.4}O_3$	4.2	0.0108	13.0	62.3
$LaNi_{0.5}Co_{0.5}O_3$	6.1	0.0152	10.8	47.6
$LaNi_{0.4}Co_{0.6}O_3$	3.5	0.0092	17.3	59.5
$LaNi_{0.2}Co_{0.8}O_3$	3.7	0.0101	20.4	42.2
$LaCoO_3$	4.1	0.0108	17.8	32.7

[a] *calculated using BET method*

[b] *calculated using BJH method*

[c] *calculated by the Scherrer equation (2θ = 23.2°, 32.8°,33.2°, 47.4° and 58.5°)*

3.2.3. SEM and EDX

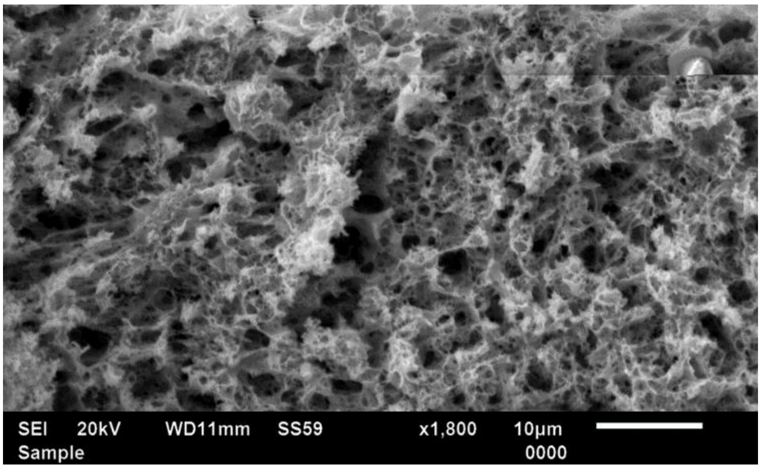

Fig. 3.5 Morphological (SEM) image for fresh $LaNi_{0.5}Co_{0.5}O_3$ perovskite catalyst

The surface morphology of the calcined $LaNi_{0.5}Co_{0.5}O_3$ catalyst is presented by SEM image as illustrated in Fig. 3.5. It shows uniform distribution of porous like structure. Mousavi and Pour have also observed that macroporisity of perovskite catalysts were increased by substituting the Co with Ni [83]. The elemental compositions of different regions on the surface of calcined catalysts using SEM-EDS technique are being displayed in Table 3.2. The composition of all prepared catalyst samples is very close to their stoichiometry ratio, which clearly demonstrates the homogenous distribution of elements in prepared catalyst samples.

Table 3.2 Elemental analysis of $LaNi_xCo_{1-x}O_3$ catalyst by EDS analysis

Catalyst Samples	Atom%			
	La	Ni	Co	O
$LaNiO_3$	26.15	8.95	0	64.90
$LaNi_{0.8}Co_{0.2}O_3$	26.17	7.03	1.83	64.97
$LaNi_{0.6}Co_{0.4}O_3$	25.51	5.48	3.35	65.66
$LaNi_{0.5}Co_{0.5}O_3$	25.02	5.05	4.92	65.01
$LaNi_{0.4}Co_{0.6}O_3$	25.75	3.21	5.78	65.26
$LaNi_{0.2}Co_{0.8}O_3$	26.12	1.75	6.98	65.15
$LaCoO_3$	25.83	0	9.21	64.96

3.2.4. Temperature Programmed Reduction (TPR)

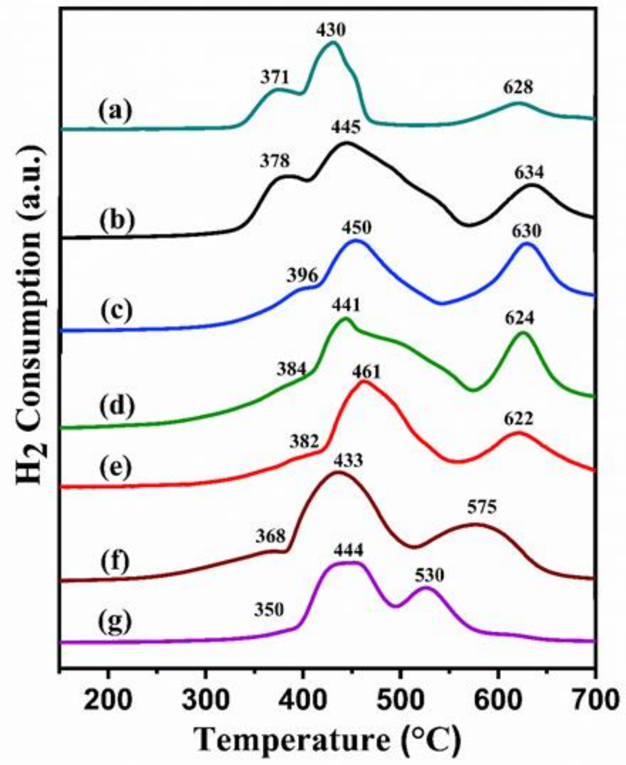

Fig. 3.6 TPR profiles of (a) $LaCoO_3$ (b) $LaNi_{0.2}Co_{0.8}O_3$, (c) $LaNi_{0.4}Co_{0.6}O_3$, (d) $LaNi_{0.5}Co_{0.5}O_3$, (e) $LaNi_{0.6}Co_{0.4}O_3$, (f) $LaNi_{0.8}Co_{0.2}O_3$ (g) $LaNiO_3$ catalysts.

TPR profiles of the prepared $LaNi_xCo_{1-x}O_3$ catalysts (x=0, 0.2, 0.4, 0.5, 0.6, 0.8, 1.0) are displayed in Fig. 3.6, where each catalyst sample has shown a similar trend for the reduction profiles. The peaks obtained from TPR analysis can be categorized into three reduction zones, i.e., low (below 400 ºC), moderate (400-500 ºC) and high temperature (greater than 500 ºC) zones. In each curve, the peak intensities indicate the amount of hydrogen (reducing gas) consumed during each reduction process.

The first reduction peak in the low-temperature zone is correspond to the reduction of NiO and Co_3O_4 (formed in very small amount) get reduced into Ni^0 and Co^0, which are weekly bounded in the perovskite structures [89,90]. The second reduction peak at moderate temperature zone is ascribed to the reduction of Ni^{3+} and Co^{3+} to Ni^{2+} and Co^{2+} respectively [87,91]. Further, the reduction peak at high-temperature zone is related to the reduction of Ni^{2+} and Co^{2+} to Ni^0 and Co^0 respectively and formation of La_2O_3, which is in good agreement with reported work [83,92]. However, these reduction peaks shifted slightly to higher temperatures on increasing the Co content. After complete reduction, Ni and Co metal species forms a very strong interaction with metals and oxides, especially in perovskite and spinel catalysts [63,81–83].

Moreover, the hydrogen consumption amount was calculated for each reaction step for all catalyst samples and displayed in the Table 3.3. The total amount of hydrogen consumed is increased with the Ni amount, which confirm that Ni is more reducible than Co [83]. The hydrogen consumption amount for first reduction step is minimum for all the catalyst samples, which confirms the imperceptible formation of NiO and Co_3O_4. However, for Ni/Co=1, the hydrogen consumption during first reduction step is minimum which signifies that most of the Ni and Co species were well incorporated in the perovskite structure. Furthermore, it was also observed that $LaNi_{0.5}Co_{0.5}O_3$ had shown the highest hydrogen consumption in the moderate and high temperature zone among different $LaNi_xCo_{1-x}O_3$ catalysts, which indicates the strongest interaction of different atoms present in this perovskite structure. Incidentally, Ni and Co species are evenly mixed in the perovskite structure because of their similar ionic radii, resulting formation of bimetallic Ni-Co alloy [87,92]. The XRD analysis of reduced catalyst sample (as displayed in Fig. 3.4) also confirms the formation of Ni-Co alloy. The similar type of reduction behaviour and formation of metallic alloys of different perovskite material for SR process has already been reported by other researchers [75,86,87,93]. These results concluded that the equimolar concentration of Ni and Co species provide a more stable perovskite structure among all the prepared perovskite catalysts.

Table 3.3 Hydrogen consumption for $LaNi_xCo_{1-x}O_3$ during H_2-TPR analysis

Catalyst	Reduction Temperature (°C)[a]	H_2 Consumption [mL H_2/g_{cat}]	H_2 Consumption [mmol H_2/g_{cat}]
$LaCoO_3$	371(20), 430(52), 628 (28)	301	13.53
$LaNi_{0.2}Co_{0.8}O_3$	378(9), 445(64), 634 (27)	291	13.07
$LaNi_{0.4}Co_{0.6}O_3$	396(9), 450(52), 630(39)	301	13.53
$LaNi_{0.5}Co_{0.5}O_3$	384(4), 441(61), 624(35)	315	14.16
$LaNi_{0.6}Co_{0.4}O_3$	382(8), 461(57), 622(35)	361	16.25
$LaNi_{0.8}Co_{0.2}O_3$	368(11), 433(55), 575(35)	377	16.96
$LaNiO_3$	350(9), 444(56), 530(34)	392	17.62

[a] Numbers in the bracket represents the H_2 consumption percentage for each reduction step (peak)

3.3 Steam reforming of simulated bio-oil (SB1) over $LaNi_xCo_{1-x}O_3$ catalysts

After studying the different properties of the synthesized perovskite catalyst, the steam reforming experiments were conducted to test the different composition of perovskite catalyst $LaNi_xCo_{1-x}O_3$ (x=0, 0.2, 0.4, 0.5, 0.6, 0.8 and 1). The steam reforming of single model compound (acetic acid) had been explored by many researchers [49,71,94–97]. However, rigorous study on steam reforming of real bio-oil is yet to be explored. Therefore, the present study aims to explore the steam reforming of mixture (representative of main functional group present in bio-oil) of bio-oil model compounds, which is a step further to understand complexity of real bio-oil. The model compound composition of simulated bio-oil have been chosen to meet the property of real bio-oil, such as pH (2.6-3.0), density (1052-1065 kg/m^3) and kinematic viscosity (1.4-1.7) as well as the major functional group present in the real bio-oil [98]. The simulated bio-oil used in the present study is acidic in nature and possesses the following properties as presented in Table 3.4.

Table 3. 4 Properties of Simulated Bio-oil 1

Property	Value
pH	2.8
density(kg/m^3)	1054
kinematic viscosity(cst)	1.7

3.3.1 Influence of Ni and Co content

The effect of Ni and Co species present in $LaNi_xCo_{1-x}O_3$ (x=0, 0.2, 0.4, 0.5, 0.6, 0.8 and 1) catalysts on gaseous products and simulated bio-oil conversion was studied and shown in Fig. 3.7. The results displayed that the simulated bio-oil conversion was found similar (>90%) for all catalyst samples. However, the maximum hydrogen yield of 83% was observed on $LaNi_{0.5}Co_{0.5}O_3$ catalyst, where B position was substituted by an equimolar amount of Ni and Co elements. The $LaNi_{0.5}Co_{0.5}O_3$ catalyst exhibited the best catalytic activity among all the prepared catalysts because of its strong interaction of atomic species inside the perovskite lattice and formation of Ni-Co alloy (after reduction), which was also in agreement with the reported work [74,87]. Furthermore, the maximum specific surface area (6.1 m^2/g), pore volume (0.0152 cm^3/g) and minimum crystallite size (47.6 nm) also confirmed that the $LaNi_{0.5}Co_{0.5}O_3$ catalyst is the best catalyst among all $LaNi_xCo_{1-x}O_3$ catalysts.

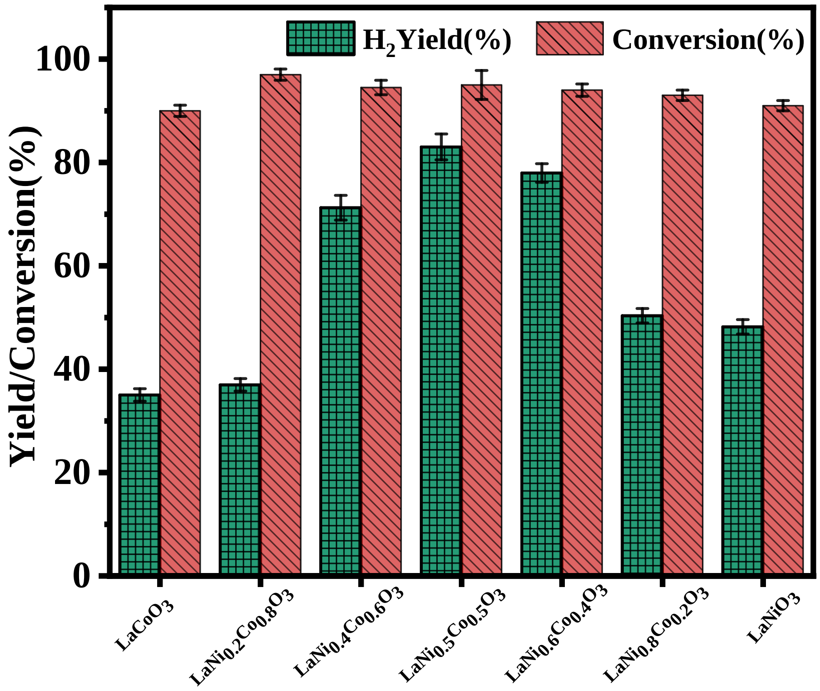

Fig. 3.7 Effect of different Ni and Co content on hydrogen yield and bio-oil conversion for $LaNi_xCo_{1-x}O_3$ perovskite catalyst (W/F_{AO} =18.4 $kg_{cat}.h/kgmol_{bio\text{-}oil}$, S/C = 2.7, T=650 ^oC and P=1 atm)

3.3.2. Effect of reaction temperature (RT)

The effect of reaction temperature (RT) was studied on simulated bio-oil conversion and yield of the gaseous products in the range of 600-800 ^oC as displayed in Fig. 3.8. The results revealed that the conversion of bio-oil model compounds increased with temperature as the SR reaction is favoured at high temperature because of its endothermic nature. As the temperature increased from 600 to 650 ^oC, H_2 yield increased from 45% to 83%. This sharp change in H_2 yield was observed because of a sudden increment in carbon conversion at 650 ^oC. At 700 ^oC, the maximum H_2 yield of 87% was found, but further increasing the temperature, it decreased to 53% at 800^oC because of the equilibrium shift favouring reverse WGS reaction. The same pattern was noted for CO_2 yield, as it increased from 64% to 76% with an increase in temperature from 600 to 650 ^oC, maximize at 81% at 700 ^oC, and it dropped subsequently beyond 700 ^oC. Moreover, the increasing trends of CO (8-

27%) and CH_4 (1-4%) evidently proves the occurrence of reverse WGS and thermal decomposition reactions, respectively.

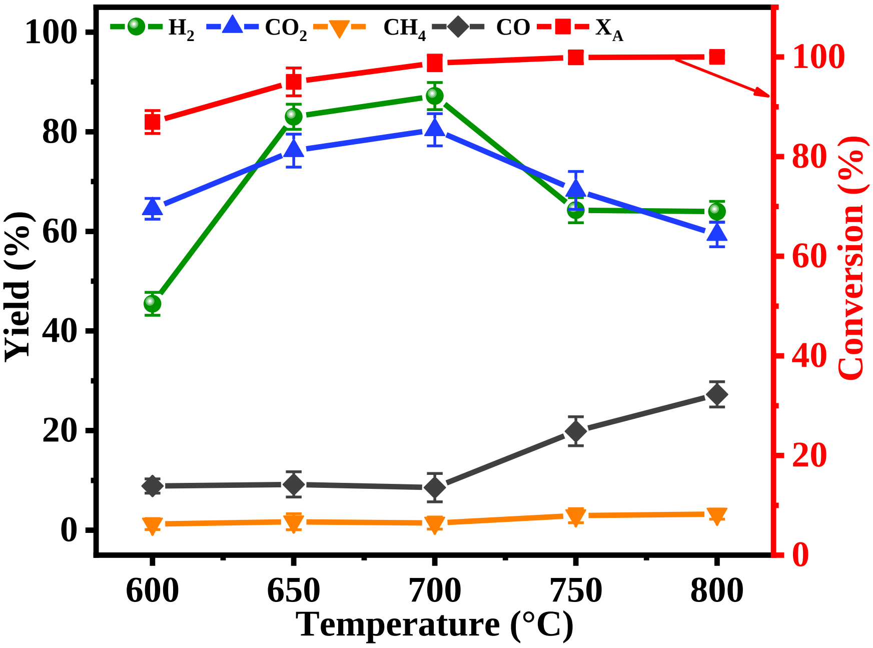

Fig. 3.8 Effect of temperature on gaseous products and bio-oil conversion for $LaNi_{0.5}Co_{0.5}O_3$ perovskite catalyst (W/F_{AO} =18.4 $kg_{cat}.h/kgmol_{bio-oil}$, S/C= 2.7 and P=1 atm)

3.3.3. Effect of steam to carbon molar ratio (SCMR)

The effect of SCMR on simulated bio-oil conversion and gaseous products yield was studied at 650 °C for space-time 18.4 $kg_{cat}.h/kgmol_{bio-oil}$ using $LaNi_{0.5}Co_{0.5}O_3$ catalyst and presented in Fig.3.9. It was observed from the experiments that on increasing the SCMR from 1.6 to 2.7, simulated bio-oil conversion increased from 71% to 95% while the hydrogen yield increased from 65% to 83%. This trend clearly demonstrated that an increase in the amount of steam in the feed mixture favoured SR and WGS reactions, which was also confirmed by the increase in CO_2 yield. However, on further increasing the SCMR to 3.26, the bio-oil conversion and H_2 yield both remain almost unchanged, whereas the reduction in CO and increase in CO_2 was recorded. The WGS and carbon gasification reactions could be the possible reasons for this, which was also in agreement with other researchers [79]. Moreover, the methane steam reforming (MSR) reaction is also favoured at higher SCMR [62]. In the present study, the slight decrease in CH_4 was observed on increasing the SCMR (1.6-3.2), which confirms the occurrence of MSR reaction.

Therefore, a steam to carbon ratio of 2.7 is found to be optimum for SR of simulated bio-oil on $LaNi_{0.5}Co_{0.5}O_3$ catalyst at 650ºC w ith space-time of 18.4 kg_{cat}.h/$kgmol_{bio-oil}$.

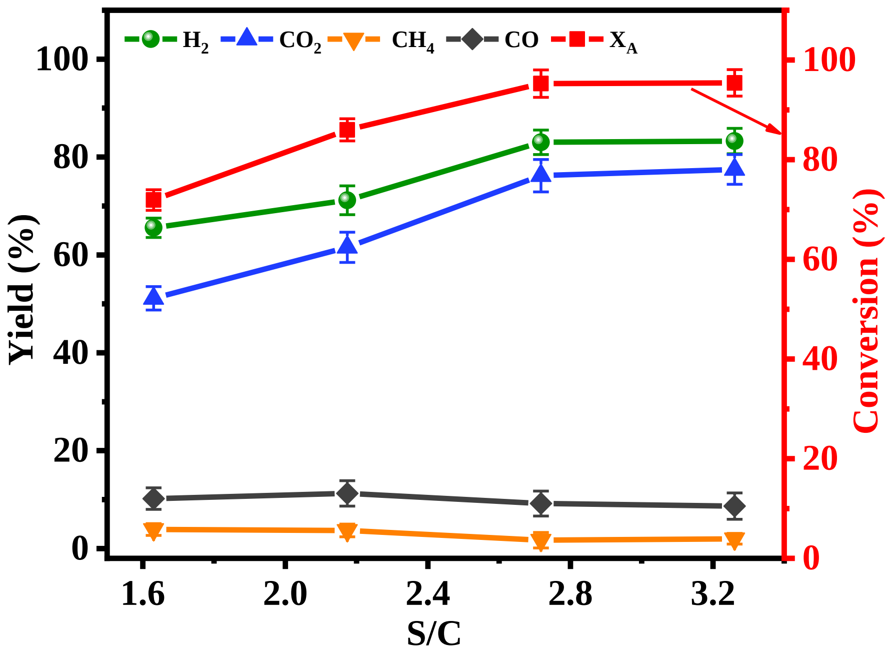

Fig. 3.9 Effect of steam to carbon ratio on gaseous products and bio-oil conversion for $LaNi_{0.5}Co_{0.5}O_3$ perovskite catalyst (W/F_{AO} =18.4 kg_{cat}.h/$kgmol_{bio-oil}$, T = 650 ºC and P=1 atm)

3.3.4. Effect of weight hourly space-time (WHST)

The product yields and simulated bio-oil conversion were studied by varying WHST from 7.14 to 18.36 kg_{cat}.h/$kmol_{bio-oil}$ at 650ºC for a fixed SCMR of 2.7 using $LaNi_{0.5}Co_{0.5}O_3$ catalyst. As demonstrated in Fig. 3.10, H_2 yield and simulated bio-oil conversion showed an increasing trend from 74 to 95% and 46 to 83%, respectively by changing WHST from 7.14 to 18.36 kg_{cat}.h/$kmol_{bio-oil}$ at 650 ºC with SCMR of 2.7 on $LaNi_{0.5}Co_{0.5}O_3$ catalyst. Meanwhile, the other gaseous products yield was also demonstrated the same trend and found to be maximum at a WHST of 18.36 kg_{cat}.h/$kmol_{bio-oil}$. The obtained results revealed that higher space-time is favourable for SR as on increasing the space-time reactants get more contact time with the catalyst, which promotes SR as well as WGS reactions. Therefore, a space-time of 18.36 kg_{cat}.h/$kmol_{bio-oil}$ was chosen optimum for further TOS studies.

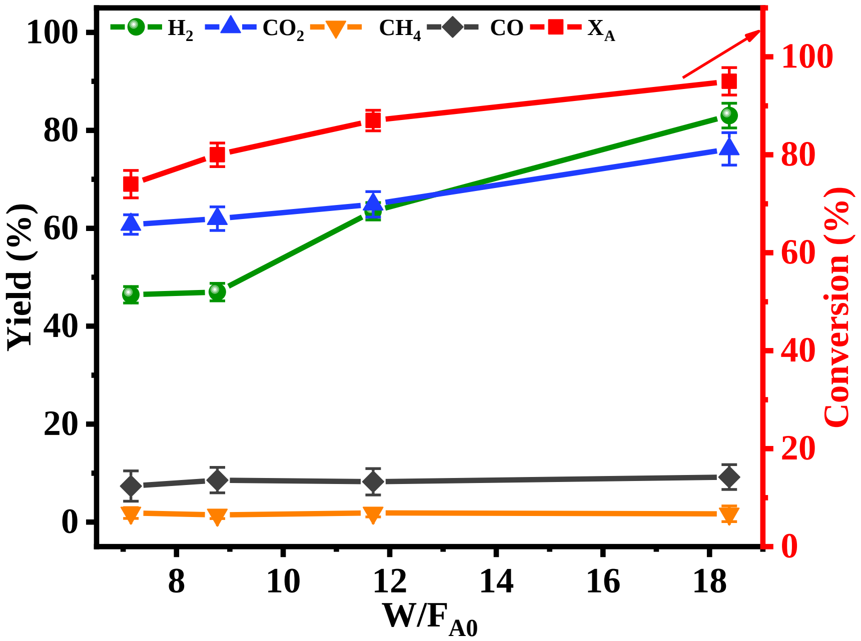

Fig. 3.10 Effect of weight hourly space time on gaseous products and bio-oil conversion for $LaNi_{0.5}Co_{0.5}O_3$ perovskite catalyst (S/C=2.7, T = 650 ^oC and P=1 atm)

3.3.5 Time on stream (TOS) study

TOS study was executed for $LaNi_{0.5}Co_{0.5}O_3$ catalyst at 650 ^oC and 700 ^oC for a fixed SCMR and space-time of 2.7 and 18.36 $kg_{cat}.h/kmol_{bio\text{-}oil}$, respectively, to monitor the catalyst stability in terms of gaseous products yield and simulated bio-oil conversion with respect to time.

Firstly, the time on steam (TOS) experiments were executed at 700 ^oC temperature as the highest hydrogen yield, and feed conversion was obtained at this temperature. The results (Fig. 3.11(a)) revealed that hydrogen yield and simulated bio-oil conversion was constant for initial 2 h, and then started decreasing and reached 90.7% and 50%, respectively, after 6 h. The observed deactivation at 700^{o}C was attributed to carbon species deposited on active sites of the catalyst. The carbon formation was observed in a large amount due to massive cracking of the bio-oil molecules, which was also confirmed by TG analysis. Further, the product gases obtained after this massive cracking may undergo via Boudouard reaction, and methane decomposition reaction, which are responsible for the coke formation. It was also indicated from slight decrease in CO_2 and constant CO and CH_4 yield throughout the run time. Moreover, the reactor blockage was observed which occurred due to excessive coke formation abolishing the porosity of the catalyst bed after 6 h of the experiment.

Similarly, the time on steam (TOS) experiments were performed separately at 650 ^{o}C, keeping other process parameters the same as the TOS study at 700 ^{o}C. The results displayed excellent catalyst stability for 12 h, as demonstrated in Fig. 3.11(b). The carbon conversion was found to be nearly constant (~95%) up to 12 h, while the H_2 yield was constant up to 9 h in the range of 83 ($\pm 2\ to$ 3)%. However, H_2 yield started decreasing afterwards (beyond 9 h) and reached 76% after 12 h because of slight catalyst deactivation. Furthermore, CO_2 yield demonstrated the same trend as H_2 yield, whereas a small increase in CH_4 and CO gas yield was observed because of catalyst deactivation which supresses both SR and WGS reactions [46].

Along with gaseous products yield, coke deposition yield was also calculated after the TOS experiments for both the temperatures (650 ^{o}C and 700 ^{o}C). The percentage yield of carbon deposited on catalyst surface was calculated by TGA method using equation 18 and found 0.94% and 1.62% for SR process at 650 ^{o}C and 700 ^{o}C, respectively.

Therefore, it was concluded from the TOS study that LaNi$_{0.5}$Co$_{0.5}$O$_3$ catalyst was more stable at 650 ^{o}C rather than 700 ^{o}C.

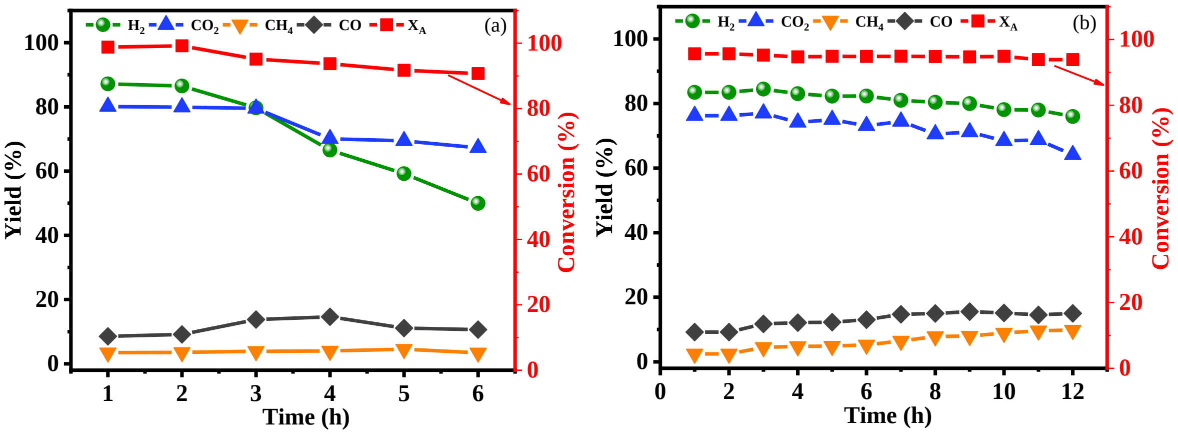

Fig. 3.11 Effect of time on steam on gaseous products and bio-oil conversion for LaNi$_{0.5}$Co$_{0.5}$O$_3$ perovskite catalyst (W/F$_{AO}$ =18.4 kg$_{cat}$.h/kmol$_{bio\text{-}oil}$, S/C = 2.7 and P=1 atm) (a) Temperature = 700 ^{o}C, (b) Temperature = 650 ^{o}C.

Chapter 4: Effect of Partial substitution at A and B site of $La_yA_{1-y}Ni_xM_{1-x}O_3$ catalysts

The present chapter delves into the examination of the synergistic effect that results from partial substitution at the A and B positions in LaNiO3 with alternate metal elements (Ce, Ca, Zr for the A position, and Co, Fe, Cu for the B position) during the SR process for the generation of green hydrogen from simulated bio-oil. As presented in Table 4.1, the simulated bio-oil used here is a mixture of major organic groups present in the bio-oil obtained from rice husk pyrolysis[98,99]. These organic groups are acids, ketones, furans and phenolic compounds and their respective representative are acetic acid (35 mol %), hydroxyacetone (22 mol%), furfural (11 mol%) and phenol (32 mol%). The elemental composition of the simulated bio-oil also constitutes a similar composition as real bio-oil used by other researchers[76,79]. The different $LaNi_{0.5}M_{0.5}O_3$ (M = Ni, Co, Cu, and Fe) catalysts were synthesized and their performance was evaluated in a tubular fixed bed reactor for simulated bio-oil steam reforming process. The process parameters temperature and space-time were optimized for steam to carbon molar ratio of 2.7. The fresh and spent catalysts were characterized via different characterization techniques, for instance, XRD, FTIR, TPD, TGA, BET, XPS, RAMAN spectroscopy and FESEM etc.

Table 4.1 Comparison of simulated bio-oil used for the present work with the literature

Chemical groups	**Pyrolysis bio-oil composition (wt.%)**[98]	**Pyrolysis bio-oil composition (wt.%)**[99]	**Simulated Bio-oil2 (SB2)**
Organic acids	25-28	18-25	27
Phenols	35-40	35-45	38
Furans	12-15	10-12	14
Ketone	18-21	10-15	21

4.1 Catalyst characterization

4.1.1 X-ray diffraction (XRD)

4.1.1.1 B-site substitution

Fig. 4.1. displays the XRD diffraction patterns of $LaNi_{0.5}M_{0.5}O_3$ catalysts (M = Cu, Fe, Co, and Ni) synthesized via sol-gel method. The diffractogram of $LaNiO_3$ exhibited peaks at 2θ values of 23.2°, 32.8°, 33.2°, 40.6°, 47.4°, 53.5°, 58.8°, and 68.7° that can be indexed to the (012), (110), (104), (202), (024), (116), (214), (018), and (220) lattice planes of rhombohedral $LaNiO_3$ perovskite phase[77,81,83,100]. The presence of these characteristic peaks indicates the successful formation of perovskite phase. Besides these, additional peaks were observed at 37.2°, 43.3°, and 62.8°, which could be indexed to the (101), (012) and (110) lattice planes of NiO, respectively, and at 31.4°, which corresponds to the (004) lattice plane of La_2O_3[70,77,81,83]. In addition, a small intensity diffraction peak corresponding to the (111) plane of La_2NiO_4 perovskite phase, possibly arising from the decomposition of $LaNiO_3$, was also observed at 24.1°[101]. Partially substituting Ni with Co and/or Cu did not result in any shifting of the characteristic peaks belonging to the perovskite phase, as observed in the diffraction patterns of $LaNi_{0.5}Co_{0.5}O_3$ and $LaNi_{0.5}Cu_{0.5}O_3$. However, when Ni was partially substituted with Fe, the two most intense peaks belonging to the perovskite phase at 32.8° and 33.2° were observed to have merged and shifted to a lower 2θ value of 32.3°. A similar shift towards lower 2θ values was observed for other characteristic peaks of perovskite structure as well, which can be attributed to the difference in ionic radii of Ni^{3+} and Fe^{3+} ions [101–103]. In addition to the characteristic peaks of perovskite phase, the diffraction patterns of all the synthesized $LaNi_{0.5}M_{0.5}O_3$ catalysts exhibited peaks at 37.2°, 43.3°, and 62.8°, which could be attributed to NiO. For the case of $LaNi_{0.5}Cu_{0.5}O_3$ catalyst, peaks corresponding to CuO were observed at 35.6°¸38.7°, and 48.9°[77,81,83,104]. Furthermore, two small intensity peaks which could be indexed to La_2O_3 were observed at 25.4° and 30.4° in the pattern of $LaNi_{0.5}Cu_{0.5}O_3$. Similarly, the diffractogram of $LaNi_{0.5}Fe_{0.5}O_3$ also exhibited peaks corresponding to Fe_2O_3 at 2θ = 35.6°. In addition, the peaks at 37.2°, and 43.3° could also correspond to Fe_2O_3 (ICSD collection code – 96075). The presence of peaks corresponding to the oxides of Cu, Fe, and Ni is indicative of the incomplete incorporation of these metals into the perovskite structure.

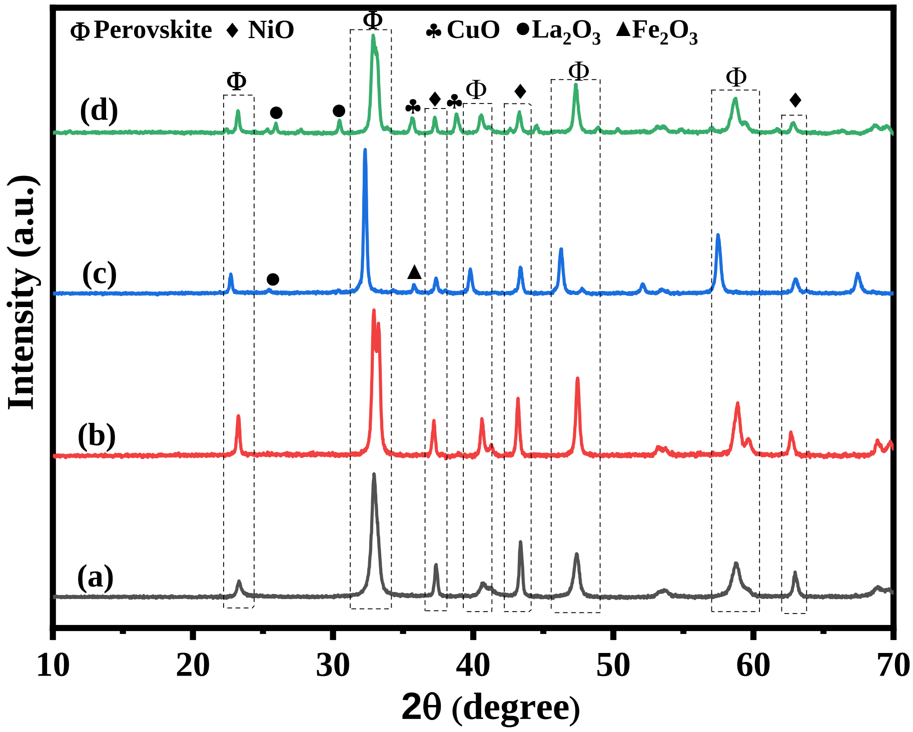

Fig. 4.1 XRD diffraction patterns of reduced (a) $LaNiO_3$, (b) $LaNi_{0.5}Co_{0.5}O_3$, (c) $LaNi_{0.5}Fe_{0.5}O_3$ and (d) $LaNi_{0.5}Cu_{0.5}O_3$

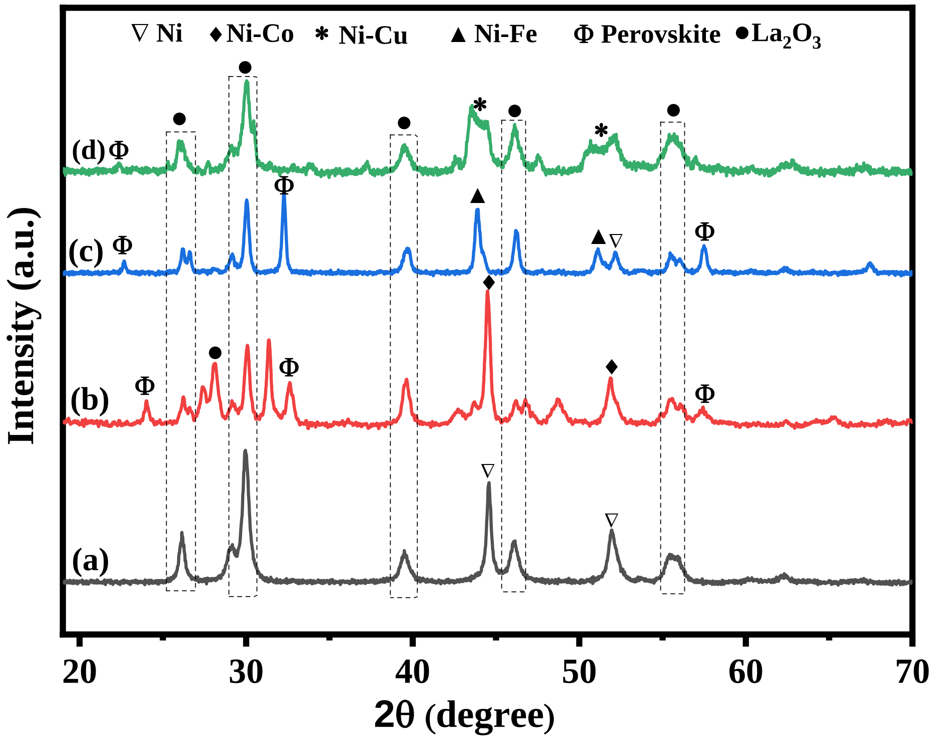

Fig. 4.2 XRD diffraction patterns of fresh (a) $LaNiO_3$, (b) $LaNi_{0.5}Co_{0.5}O_3$, (c) $LaNi_{0.5}Fe_{0.5}O_3$ and (d) $LaNi_{0.5}Cu_{0.5}O_3$

Fig. 4.2 displays the XRD patterns for reduced $LaNi_{0.5}M_{0.5}O_3$ catalysts (M = Ni, Co, Cu, and Fe). Post-reduction, the characteristic diffraction peaks of $LaNiO_3$ structure were observed to have completely disappeared from its XRD pattern. Instead, peaks corresponding to just La_2O_3 (2θ = 26.2°, 29°, 30°, 39.7°, 46.3°, and 55.5°) and Ni metal (2θ = 44.5° and 51.8°) were observed [83,105], confirming that the perovskite structure disintegrated completely under the reduction conditions used, giving way to metallic Ni dispersed on La_2O_3 support. The XRD patterns of perovskite catalysts where Ni had been partially substituted with Co, Cu and Fe not only exhibited peaks corresponding to La_2O_3 but also some of those characteristics of the perovskite phase, signifying its incomplete decomposition. Besides these peaks, diffraction peaks corresponding to Ni-Co alloy (ICSD collection code-108308) at 2θ = 44.5°, 51.8°, Ni-Cu alloy (ICSD collection code-103063) at 2θ = 44 °, 51.2° and Ni-Fe alloy ((ICSD collection code-103555) at 43.8°, 50.9° in the diffractograms of reduced $LaNi_{0.5}Co_{0.5}O_3$, $LaNi_{0.5}Cu_{0.5}O_3$ and $LaNi_{0.5}Fe_{0.5}O_3$catalysts, respectively. The presence of peaks corresponding to La_2O_3 alloys confirms the strong interactions between Ni and the substituted metals, as well as the formation of La_2O_3, supported bimetallic Ni-M (M = Co, Cu and Fe) catalysts after reduction. Interestingly, the peaks corresponding to Ni-Fe alloy were noted to have shifted slightly from those of Ni metal towards lower 2θ values, indicating that only part of Fe undergoes reduction under the conditions used and that the Ni-Fe bimetallic alloys formed as a result are rich in Ni [75]. Furthermore, the textural properties such as BET surface area, which was obtained by N_2 adsorption desorption isotherm, pore volume and average pore size of catalyst samples were displayed in Table 4.2. The crystallite size of fresh and reduced catalyst samples was also calculated using the Scherrer equation and found to be maximum for $LaNi_{0.5}Co_{0.5}O_3$ catalyst.

Table 4.2 Textural properties of LaNi$_{0.5}$M$_{0.5}$O$_3$ (M = Ni, Co, Cu, and Fe) catalyst samples

Catalyst	**Specific surface area**[a] **(m^2/g)**	**Pore volume**[b] **(cm^3/g)**	**Avg. pore size**[b] **(nm)**	**Crystallite size**[c]	
				Fresh[#] **(nm)**	**Reduced*** **(nm)**
LaNiO$_3$	5.7	0.028	18.2	28.8	35.7
LaNi$_{0.5}$Co$_{0.5}$O$_3$	7.4	0.015	10.8	42.1	44.7
LaNi$_{0.5}$Fe$_{0.5}$O$_3$	5.1	0.012	17.3	36.7	22.3
LaNi$_{0.5}$Cu$_{0.5}$O$_3$	4.3	0.011	20.4	33.1	17.8

[a] *calculated using BET method*
[b] *calculated using BJH method*
[c] *calculated by the Scherrer equation* [#] *(2θ =perovskite characteristic peak at 32.8)*
**(2θ = Ni-M alloy characteristic peak)*

4.1.1.2 A-site substitution

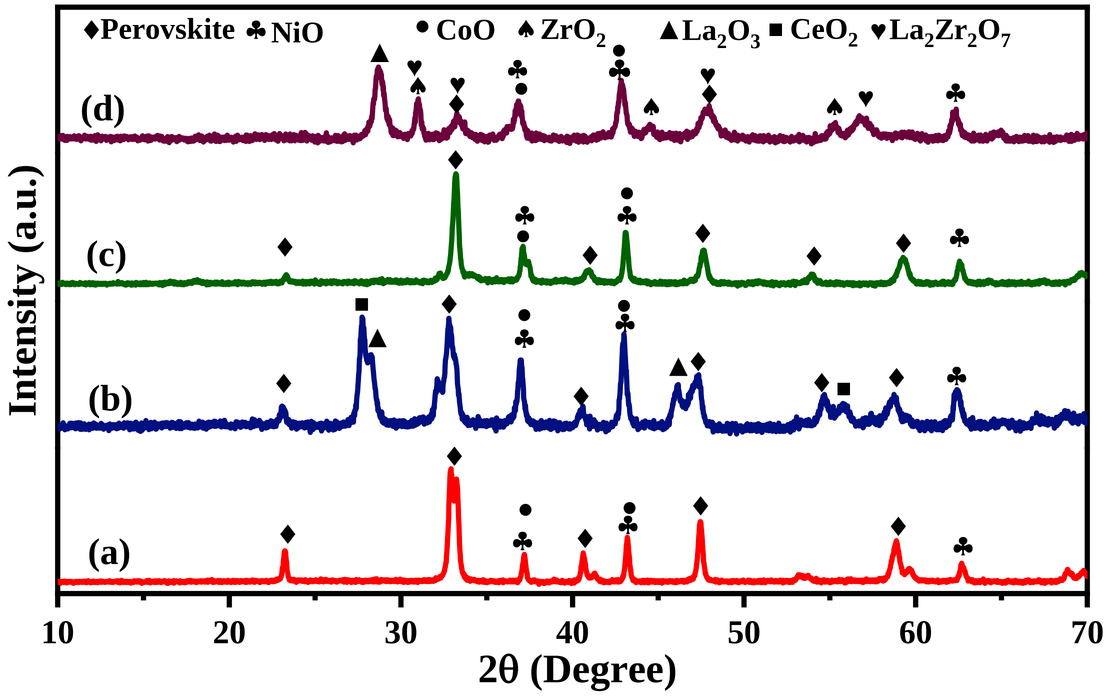

Fig. 4.3 XRD patterns of (a) LaNi$_{0.5}$Co$_{0.5}$O$_3$, (b) La$_{0.5}$Ce$_{0.5}$Ni$_{0.5}$Co$_{0.5}$O$_3$, (c) La$_{0.5}$Ca$_{0.5}$Ni$_{0.5}$Co$_{0.5}$O$_3$ and (d) La$_{0.5}$Zr$_{0.5}$Ni$_{0.5}$Co$_{0.5}$O$_3$

Fig. 4.3 shows the XRD diffractogram of the calcined La$_{1-x}$M$_x$Ni$_{0.5}$Co$_{0.5}$O$_3$ catalysts. For the case of LaNi$_{0.5}$Co$_{0.5}$O$_3$ catalyst, diffraction peaks corresponding to the rhombohedral perovskite phase were observed at 2θ values of 23.2°, 33°, 40.6°, 47.4°, 53.1°, 58.8°, and

68.7° [40,77,81]. Additionally, peaks were also observed at 2θ values of 37°, 43°, and 62.5° which could correspond to the presence of either NiO (ICSD collection code – 53930) or CoO (ICSD collection code – 53057) phases, signifying that the metals were not completely incorporated into the perovskite structure [40,77,81]. No peaks corresponding to any La oxide phase was not observed in the diffraction pattern, indicating complete incorporation into the perovskite structure. When La was partially substituted with Ce, the resulting $La_{0.5}Ce_{0.5}Ni_{0.5}Co_{0.5}O_3$ catalyst did not exhibited any shift in the peaks corresponding to the perovskite structure, which is expected as La^{3+} and Ce^{3+} ions have similar ionic radius [71,81,106]. Diffraction peaks belonging to the cubic phase of CeO_2 were observed at 2θ values of 28°, and 55.8° (ICSD Code – 155608) [81] and those belonging to NiO were noted at 37.1°, 43.2°, and 62.5° [40,77,81]. Additionally, the peaks at 46.3° and 66.9° could be ascribed to La_2O_3 (ICSD Code – 154586). Partially replacing La with Ca did not lead to any shifting in the characteristic peaks of perovskite did not exhibit any shift owing to the very similar sizes of La^{3+} and Ca^{2+} ions [71,107]. While peaks corresponding to NiO and/or Co_3O_4 were observed in the diffractogram, those corresponding to CaO were not detected, which indicates complete incorporation of Ca in the perovskite structure [108]. Finally, when La was partially with Zr, only two peaks corresponding to perovskite phase was observed at 2θ values of 33.1° and 47.6°. Furthermore, their intensity was observed to have reduced remarkably as compared to that in the diffractograms of other synthesized $La_{1-x}M_xNi_{0.5}Co_{0.5}O_3$ catalysts. Simultaneously, an intense peak belonging to La_2O_3 emerged at 28.8° (ICSD collection code – 154588) as well as those belonging to ZrO_2 were noted at 31.1°, 44.5°, 55.4°, 61.9° and 64.9° (ICSD collection code – 92092). Peaks corresponding to NiO (ICSD collection code – 53930) and/or CoO (ICSD collection code – 53057) also emerged at 36.9 ° and 42.9°, as seen for the other three catalysts. Additionally, the peaks at 28.8°, 33.1 °, 47.6°, and 56.5° could also possibly be attributed to the formation of a mixed $La_2Zr_2O_7$ phase (ICSD collection code – 15165). The appearance of peaks corresponding to single and mixed oxides of La and Zr suggest that partially replacing La with Zr does not favor the formation of perovskite structure due to the large difference in the ionic radius of the La^{3+} and Zr^{4+} ions [71].

4.1.2. Temperature programmed reduction (TPR)

4.1.2.1. B-site substitution

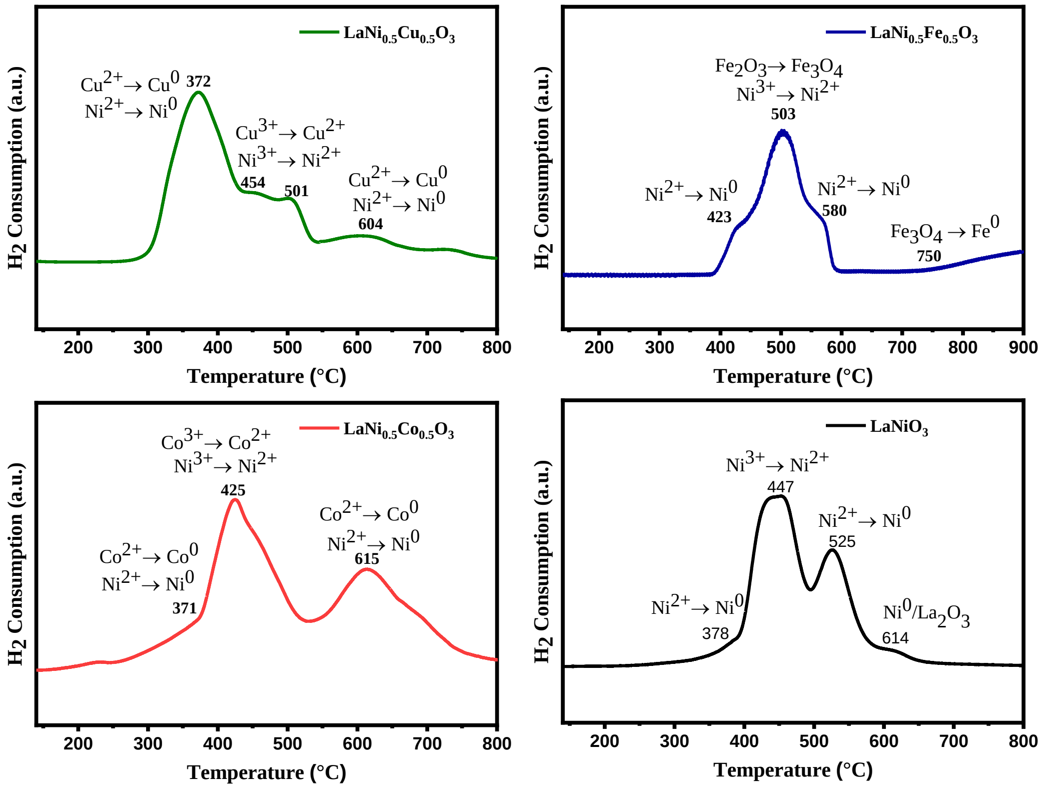

Fig. 4.4 H_2-TPR profiles of $LaNi_{0.5}M_{0.5}O_3$ perovskite catalysts

TPR profiles of $LaNi_{0.5}M_{0.5}O_3$ (M= Cu, Fe, Co, and Ni) catalysts are presented in Fig. 4.4 All perovskite catalyst samples have shown quite similar type of reduction profiles. The reduction profile of $LaNiO_3$ exhibited peaks in three temperature ranges – low (< 400 °C), moderate (400 to 500 °C) and high (> 500 °C). The small shoulder reduction peak at low-temperature zone can be ascribed to the reduction of NiO species exhibiting weak interactions with the perovskite structure to Ni^0 species [70]. The existence of reduction peaks in the moderate and high-temperature zones is indicative of a two-step reduction process of the perovskite phase. These observations are in good agreement with the available literature [75,105,109,110], according to which the reduction reaction may be proposed to occur as follows:

$$2LaNiO_3 + H_2 \rightarrow La_2Ni_2O_5 + H_2O \qquad (4.1)$$

$$La_2Ni_2O_5 + 2H_2 \rightarrow 2Ni^0 + La_2O_3 + 2H_2O \qquad (4.2)$$

The peak between 400-500 °C may be attributed to the reduction of the $LaNiO_3$ perovskite phase, wherein its Ni^{3+} species gets reduced to Ni^{2+} species, resulting in the concomitant formation of La_2NiO_5 phase [75,105,109,110]. Meanwhile, the peak between 500 to 600 °C can be allocated to the reduction of Ni^{2+} species to Ni^0, which get dispersed on La_2O_3 [75,109–111]. It can therefore be concluded that the perovskite structure formed after calcination is completely demolished after reduction, producing metallic Ni^0 dispersed on La_2O_3.

The reduction profile of $LaNi_{0.5}Co_{0.5}O_3$ catalyst was nearly similar to that of pure $LaNiO_3$, exhibiting peaks in the low, moderate and high-temperature regimes. While the reduction peak in the low temperature could be ascribed to the reduction of NiO and Co_3O_4 phases weakly interacting with the perovskite structure to their respective metallic states, the peaks in the moderate zone correspond to the reduction of Ni^{3+} and Co^{3+} species present in the perovskite phase to Ni^{2+} and Co^{2+}, respectively [70,83]. The third peak, lying in the high-temperature region, can be ascribed to the reduction of Ni^{2+} and Co^{2+} species to Ni^0 and Co^0, respectively and the formation of La_2O_3 [70,83]. This peak was observed to have shifted from between 500-600 °C for unsubstituted $LaNiO_3$ to above 600 °C for the $LaNi_{0.5}Co_{0.5}O_3$, which could be attributed to the partial replacement of Ni by Co in the perovskite structure resulting the formation of Ni-Co bimetallic alloy on La_2O_3 surface [70,83].

When Ni was partially replaced with Fe, all of the peaks corresponding to the reduction of different Ni species ($Ni^{3+} \rightarrow Ni^0$ and $Ni^{2+} \rightarrow Ni^0$) exhibited a significant shift towards higher temperatures. Furthermore, a new, broad hump-shaped peak beyond 750 °C was also noted to emerge. This shifting of Ni reduction peaks towards higher temperatures and the emergence of a broad peak at such a high temperature may be attributed to the strong interaction of Fe in perovskite structure. [75,110–113]. The reports available in literature suggest that reduction of Fe-based catalysts proceeds in two steps : reduction of Fe_2O_3 to Fe_3O_4 which exhibits peak between 300-450 °C and that of Fe_3O_4 to Fe^0 during which a peak can be observed in 500-900 °C range [75]. Moreover, the shifting of reduction at higher temperatures has often been ascribed to the existence of strong interactions between Fe and La_2O_3. Partially substituting Ni with Fe has been observed to lead to a similar enhancement in stability towards reduction, particularly at larger loadings of Fe [75,110–113]. The existence of a reduction peak at such elevated temperatures in Ni and

Fe-containing perovskites has been assigned to the reduction of a fraction of Fe, aided by Ni and the subsequent formation of Ni-Fe bimetallic alloys [75,110–113]. Furthermore, the reduction profile for $LaNi_{0.5}Cu_{0.5}O_3$ catalyst presented little shift of first peak towards lower temperature stating the reduction of NiO and CuO together and formation of Ni-Cu alloy[79,104]. However, the slight shift of second and third reduction peaks was noted, which may be because of the reduction of Ni^{2+} to $Ni^{0,}$ which was difficult after the substitution of Cu while compared with $LaNiO_3$.

Thus, the observed shifting of reduction peaks to higher temperatures could be concluded to emanate from and confirm the presence of strong interaction of Ni with other transition metals (Co, Fe, and Cu) and the formation of bimetallic alloys. These results are in good agreement with the results obtained from XRD analysis of the reduced catalyst, where diffraction peaks of bimetallic Ni-Co, Ni-Fe and Ni-Cu alloys were observed.

4.1.2.2. A-site substitution

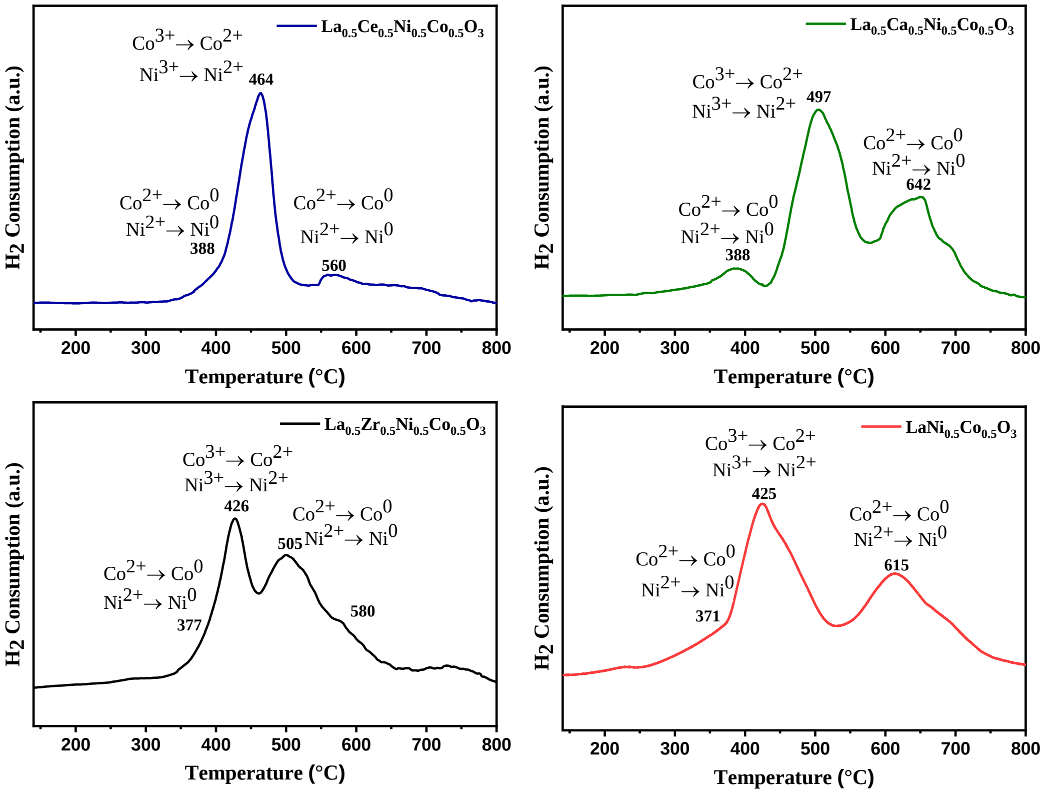

Fig. 4.5 H_2-TPR profiles of $La_{0.5}A_{0.5}Ni_{0.5}Co_{0.5}O_3$ perovskite catalysts

Fig. 4.5 shows the H_2-TPR profiles of $La_{1-x}M_xNi_{0.5}Co_{0.5}O_3$ catalysts. The reduction profile of $LaNi_{0.5}Co_{0.5}O_3$ catalyst exhibited three peaks, one each in the low (< 400 °C), medium (400-500 °C) and high (> 500 °C) temperature regions (Fig. d). Here, the peak in the low temperature zone corresponds to the reduction of the segregated Ni and Co oxide species interacting very weakly with the perovskite phase to Ni^0 and Co^0 species [40,83]. Similarly, the peak in the moderate zone corresponds to the Ni^{3+} and Co^{3+} species of the perovskite phase undergoing reduction to Ni^{2+} and Co^{2+} species, respectively [40,83]. Lastly, the peak in the high temperature zone emerges because of the formation of Ni^0 and Co^0 species from the reduction of Ni^{2+} and Co^{2+} species and the concomitant formation of La_2O_3 [40,83]. The partial substitution of La with Ce and Zr induced a significant change in the reduction profiles of the resulting catalysts (Fig. a and c). For the case of $La_{0.5}Ce_{0.5}Ni_{0.5}Co_{0.5}O_3$ catalyst, the peak corresponding to the reduction of segregated oxides was moved to a slightly higher temperature. The peak belonging to the reduction of Ni^{3+} and Co^{3+} in perovskite phase moved to a higher temperature while showing an increased intensity. On the other hand, the peak corresponding to the formation of Ni^0 and La_2O_3 species was shifted emerged at a significantly temperature while also having undergone a significant reduction in intensity. Soongprasit et. al. [114] and Podila et. [115] have reported that partial substitution of La by Ce boosts the reducibility of the catalysts due to the movement of the lattice oxygen towards area deficient in oxygen. Consequently, the behaviours exhibited by the peaks in the medium and high temperature zones could be ascribed to the increased reducibility brought about by Ce substitution, because of which the Ni^{3+} and Co^{3+} present in the perovskite structure were reduced to Ni^0 and Co^0 species at lower temperatures. On a similar note, partial replacement of La with Zr also led to a significant change in the reduction characteristics. The reduction peak attributed to the reduction of Co^{2+} and Ni^{2+} species, formed by the reduction of Co^{3+} and Ni^{3+} species present in perovskite structure, saw a drastic shift to a lower temperature (505 °C) as compared to its position for $LaNi_{0.5}Co_{0.5}O_3$ catalyst. As such, this broad peak could correspond to the formation of metal Ni and Co species and that of La_2O_3-ZrO_2 support. The peaks in the low and medium temperature zone, meanwhile, only saw a minor shift. Finally, for the case of $La_{0.5}Ca_{0.5}Ni_{0.5}$ $Co_{0.5}O_3$ catalyst, the peaks exhibited a notable shift towards higher temperatures as compared to their positions for $LaNi_{0.5}$ $Co_{0.5}O_3$ catalyst. The results are in agreement with those reported by Junior et. al. [116] and Onrubia-Calvio et. al. [108] who noted that Ca incorporation into the perovskite structure not only boosted the resistance to reduction for the perovskite phase as well as the segregated Ni and Co oxides.

4.1.3. Surface Acidity and Basicity

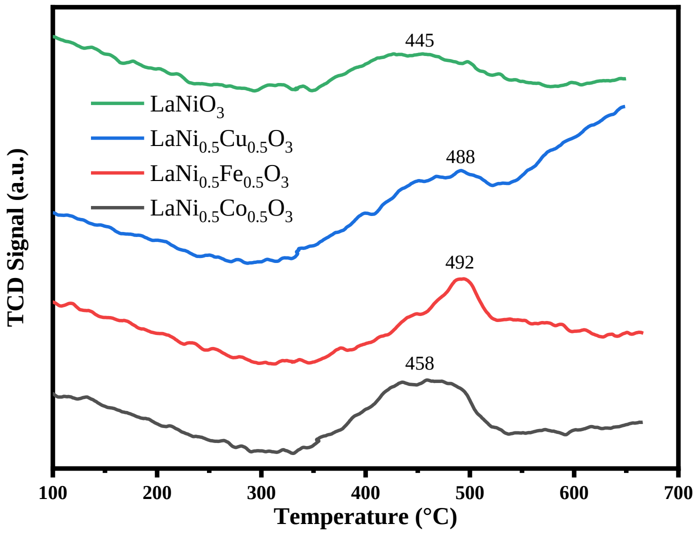

Fig. 4.6 NH_3- TPD profile of $LaNi_{0.5}M_{0.5}O_3$ (M= Ni, Co, Fe, and Cu) perovskite catalysts

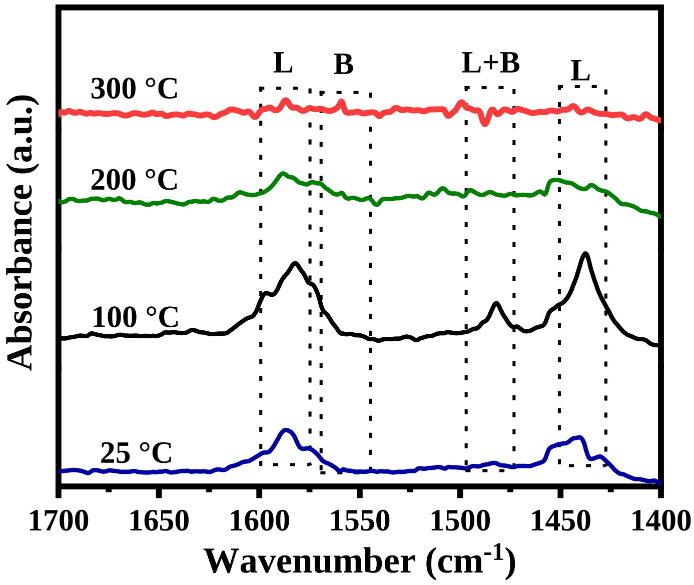

Fig. 4.7 Infrared spectra of Pyridine molecules absorbed on $LaNi_{0.5}Co_{0.5}O_3$ perovskite catalyst surface

The surface acidity of all synthesized perovskite material was characterized by NH_3-temperature programmed desorption (TPD) as displayed in Fig. 4.6. Depending on the desorption temperature, the observed surface-active sites can be broadly classified into three categories: (i) low acidic strength (less than 200 ºC) (ii) medium acidic strength (300-500 ºC) (iii) high acidic strength (More than 500 ºC). It could be clearly understood from

Fig. 4.6, that all fresh catalysts exhibit acidic sites of medium strength, which are accountable for promoting the formation of carbon during the steam reforming reactions. The total acidic site concentration of $LaNi_{0.5}Co_{0.5}O_3$ was found to be 44.6 µmol/g_{cat} from NH_3-TPD experiment. In order to shed further light on the type of surface acidity present in the synthesized perovskite catalyst samples, pyridine-FTIR experiments (Fig.4.7) were performed. Bands corresponding to the presence of Lewis (L) acidic sites were observed at 1437 and 1582 cm^{-1} [117]; additionally, a minor band that may be attributed to Brønsted (B) acidity was observed at about 1550 cm^{-1}. Another minor band that may possibly be ascribed to both Lewis as well as Brønsted acidic sites was observed at 1482 cm^{-1}. In order to test the strength of these acidic sites, the analysis temperature was elevated from 100 °C to 300 °C. As the temperature rose to 200 °C, a marked reduction in the intensity of the bands was noted, signaling the desorption of a significant amount of the adsorbed pyridine.

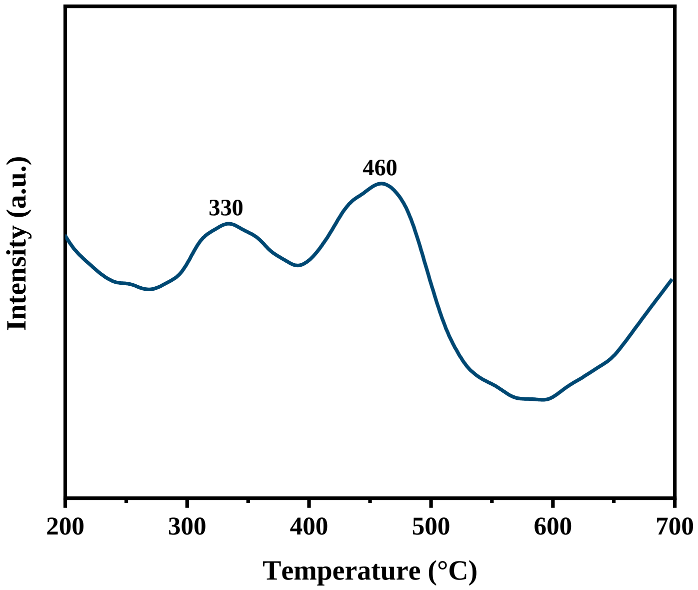

Fig. 4.8 CO_2- TPD profile of $LaNi_{0.5}Co_{0.5}O_3$ perovskite catalysts

Further raising the temperature to 300 °C led to a nearly complete disappearance of the bands, which corroborates results of NH_3-TPD analysis that the catalysts are home to surface sites of medium acidic strength.

The surface basicity of $LaNi_{0.5}Co_{0.5}O_3$ was determined by CO_2- TPD experiments, as shown in Fig. 4.8. Like the case of NH_3-TPD, the desorption peaks in CO_2-TPD can also be broadly classified into three categories of strength depending upon the temperature at which they appear: (i) weakly basic (below 200 °C), (ii) medium strength (200-500 °C) and (iii) strongly basic sites (above 500 °C). The TPD profile of $LaNi_{0.5}Co_{0.5}O_3$ exhibited two broad peaks between 300 and 500 °C, signifying CO_2 desorption from basic sites of medium strength and the total basic site concentration was found 8.75 µmol/g_{cat}. In addition, a peak began to emerge as the temperature rose above 600 °C, which may be attributed to the decomposition of bulk carbonates and/or lanthanum oxycarbonates, which originate from the adsorption of CO_2 on basic La_2O_3 [118].

4.1.4 X-ray photoelectron spectroscopy (XPS)

4.1.4.1 B-site substitution

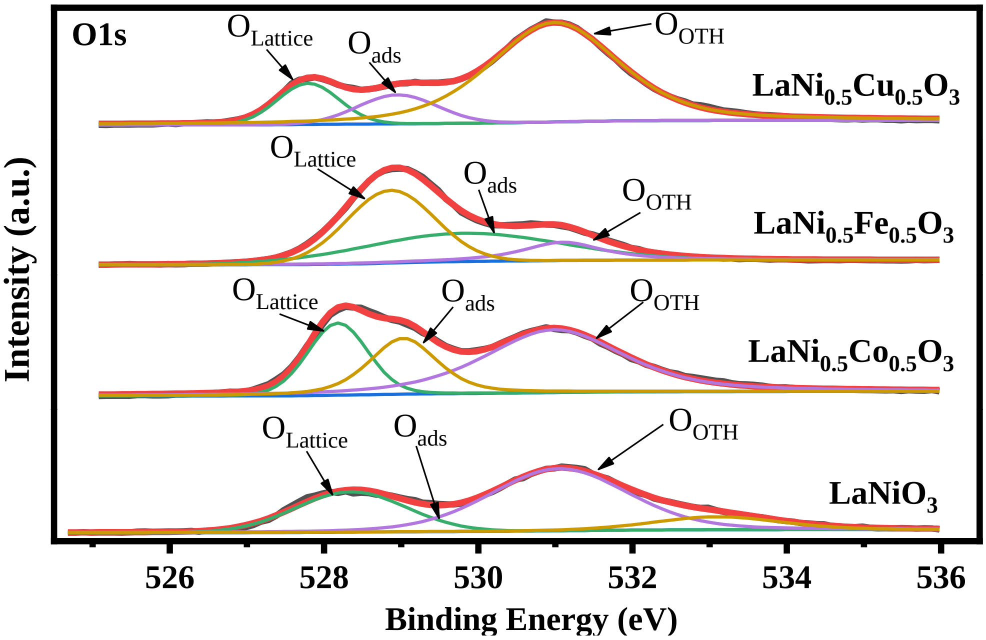

Fig. 4.9 XPS O1s profiles of $LaNi_{0.5}M_{0.5}O_3$ (M= Cu, Fe, Co, and Ni) perovskite catalysts

The XPS profile of O 1s (Fig. 4.9) presented three peaks at 527-528.5 eV, 529-530 eV and 531-533 eV representing lattice oxygen ($O_{Lattice}$), adsorbed oxygen (O_{ads}) and other oxygen (O_{OTH} : adsorbed water/hydroxyl/carbonated species) vacancies, respectively [71,75,102]. Perovskite-type catalysts are well known to possess oxygen vacancies and/or oxygen mobility, which, according to several reports available in literature, can be enhanced by partial and/or complete substitution of metals at A and B sites[71,77,119]. Oxygen vacancies have been noted to play an influential role in the activation and evolution of oxygen from the lattice, allowing it to participate in reactions [71,77,120]. Therefore, their presence in a catalyst provides a boost to catalytic reactions, with Da et. al[121] reporting that perovskite catalysts having higher oxygen vacancies are capable of accelerating catalytic reactions and providing enhanced performances. In this context, the evaluation of the availability of oxygen vacancies on catalysts' surface is crucial, which can be accomplished by evaluating, in turn, the adsorbed oxygen species O_{ads}. The general consensus is that for oxide-type catalysts such as perovskites, greater the number of oxygen vacancies on the catalysts' surface, the greater are the surface adsorbed oxygen species O_{ads} [71,121].In this context, the obtained O1s profiles were deconvoluted to $O_{ads}/O_{Lattice}$ ratios for $LaNiO_3$ as well as each of the $LaNi_{0.5}M_{0.5}O_3$ catalysts so as to shed light on the variation in oxygen mobility/vacancies produced by partially substituting Ni with Co, Cu and Fe. The values for $LaNiO_3$, $LaNi_{0.5}Co_{0.5}O_3$, $LaNi_{0.5}Fe_{0.5}O_3$, and $LaNi_{0.5}Cu_{0.5}O_3$ were determined to be 0.81, 1.01, 0.86 and 0.90, respectively. The results demonstrate that while the $LaNi_{0.5}Cu_{0.5}O_3$ catalyst exhibited the highest O_{ads}, it was the $LaNi_{0.5}Co_{0.5}O_3$ catalyst that had the highest $O_{ads}/O_{Lattice}$ ratio and, consequently, the highest concentration of surface oxygen vacancies. This may explain the enhanced catalytic performance as well as coke suppression observed during the evaluation of catalytic activity. [71,75,121]. However, O1s peak corresponds to 531-533 eV binding energy representing the physically adsorbed oxygen and found maximum for $LaNi_{0.5}Cu_{0.5}O_3$ on comparing with all calcined perovskites.

4.1.4.2 A-site substitution

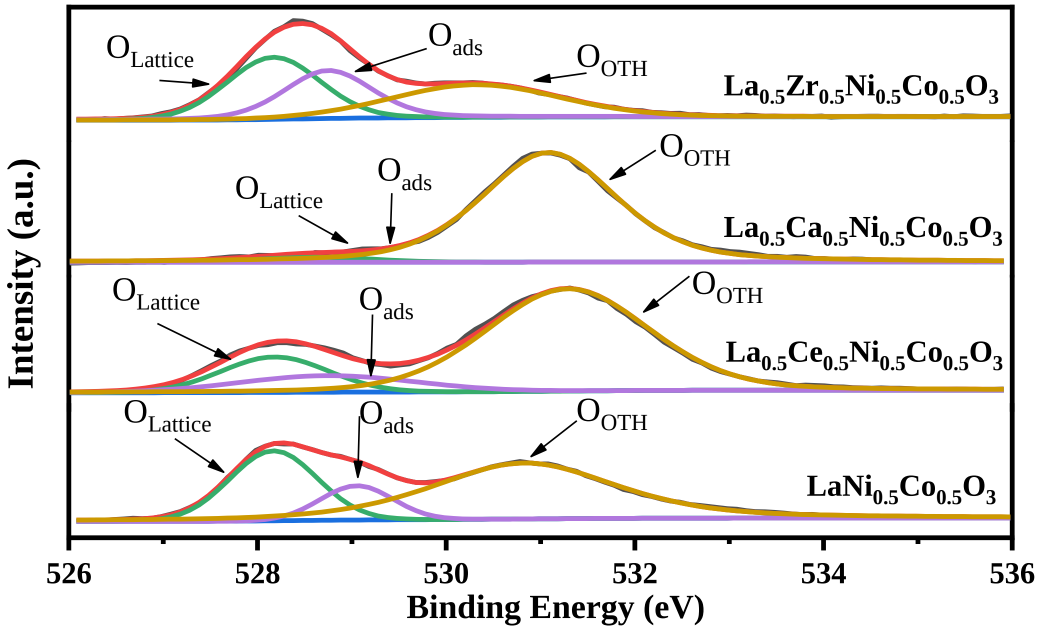

Fig. 4.10 XPS O1s profiles of $La_{0.5}A_{0.5}Ni_{0.5}Co_{0.5}O_3$ (A= La, Ce, Ca, and Zr) perovskite catalysts

Fig. 4.10 displays the O1s spectra for the synthesized $La_{1-x}M_xNi_{0.5}Co_{0.5}O_3$ catalysts. The existence of three peaks in the O1s spectrum points towards the existence of three different types of oxygen species on the surface of the catalysts. While the peak at a binding energy of ~528 eV corresponds to the lattice oxygen ($O_{lattice}$), the peaks at binding energy values of 529-530 eV and 530-531 eV correspond to adsorbed oxygen (O_{ads}) and other oxygen species (O_{oth}) such as hydroxyl or carbonated and/or adsorbed water, respectively [71,75,102]. Perovskite catalysts are known for possessing significant amounts of oxygen vacancies [71,77,120], whose presence has been known to accelerate catalytic reactions and result in improved performances [71,77,119,121]. It is widely accepted that for metal oxides, oxygen vacancies on the oxides' surface influence the adsorbed oxygen species (O_{ads}). Thus, the greater the content of O_{ads} species, the greater would be oxygen vacancies presently [71,121] and consequently, catalytic activity would also be higher. It has been noted by several studies available in literature that modifying perovskite catalysts by partial substitution at either A or B-site can result in increased surface oxygen vacancies [71,77,120]. Accordingly, to evaluate the changes in oxygen mobility induced by partial substitution of La at A site by Ca, Ce and Zr, the O1s spectra obtained were deconvoluted to determine the $O_{ads}/O_{lattice}$ ratio. The values of this ratio were found to be 1.01, 0.63, 0.41 and 0.0001 for $LaNi_{0.5}Co_{0.5}O_3$, $La_{0.5}Ce_{0.5}Ni_{0.5}Co_{0.5}O_3$, $La_{0.5}Ca_{0.5}Ni_{0.5}Co_{0.5}O_3$, and $La_{0.5}Zr_{0.5}Ni_{0.5}Co_{0.5}O_3$, respectively. As such, the results demonstrate that partially substituting La with these Ce, Ca and Zr decreased the extent of oxygen vacancies in the catalysts, which would explain the reduced catalytic stability encountered later during the evaluation of catalytic activity.

4.1.5 TG Analysis

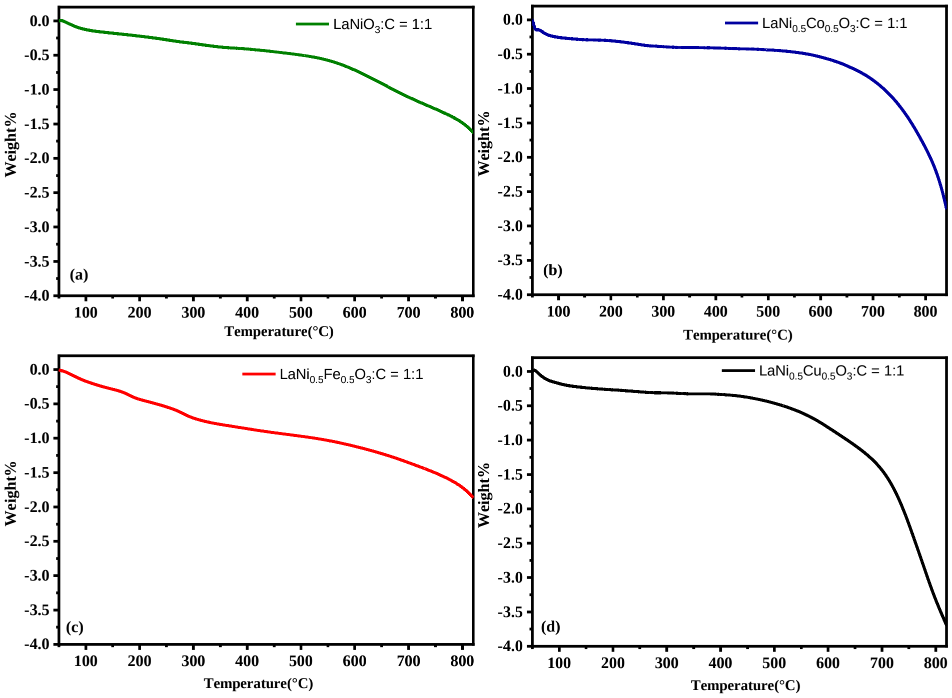

Fig. 4.11 TGA plot for mixture of fresh perovskite and carbon (a) $LaNiO_3$, (b) $LaNi_{0.5}Co_{0.5}O_3$, (c) $LaNi_{0.5}Fe_{0.5}O_3$ and (d) $LaNi_{0.5}Cu_{0.5}O_3$

In order to gain further insight into the changes in the oxygen evolution behaviour brought about by the partial substitution of Ni with other first-row transition metals (Cu, Fe, and Co) on the availability of the mobile oxygen species, TG analysis was performed. The results of the TG analysis of $LaNi_{0.5}M_{0.5}O_3$ (M= Cu, Fe, Co, and Ni) catalysts and carbon mixture are presented in Fig.4.11, with the total weight loss was found 3.5%, 1.8%, 2.8% and 1.6% respectively. Weight loss was noted to have occurred primarily in three regions i.e., (i) up to 200 ºC (ii) 200-600 ºC and (iii) beyond 600 ºC. The weight loss in the first region was noted due to the moisture adsorbed on the surface, while that in the second region may be assigned to α-oxygen, which corresponds to surface oxygen vacancies [77]. The weight loss in the third region represents the reduction in weight because of the lattice oxygen (β-oxygen) present in the perovskite structure[77]. Additionally, the results of the TG analysis revealed that $LaNi_{0.5}Cu_{0.5}O_3$ catalyst exhibited the maximum amount of physically adsorbed oxygen (O_{ads}), which is in good agreement with the observations made in the XPS analysis.

4.1.6. Surface Morphology

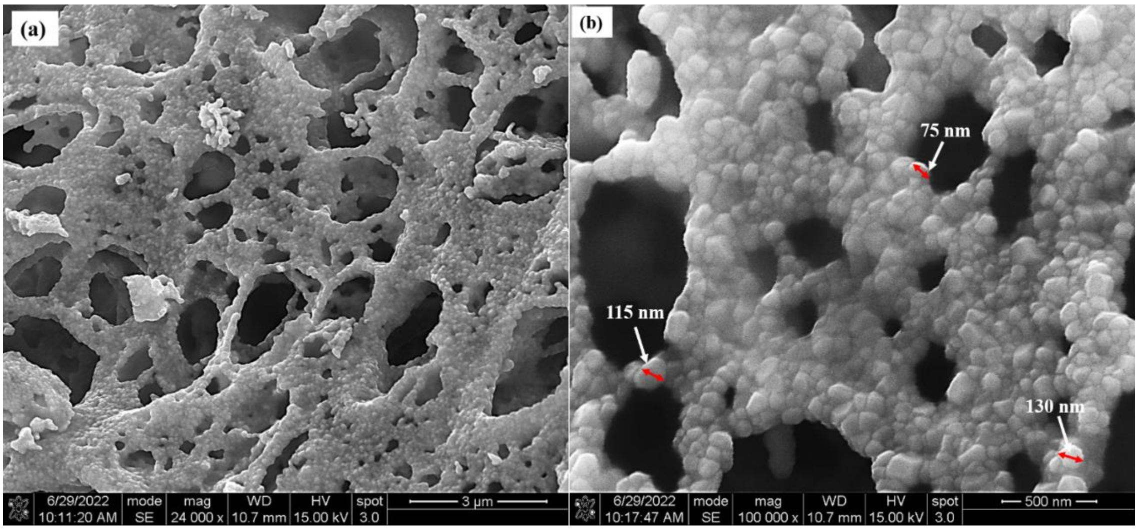
(a)
(b)
75 nm
115 nm
130 nm
6/29/2022 10:11:20 AM
mode SE
mag 24 000 x
WD 10.7 mm
HV 15.00 kV
spot 3.0
3 μm
6/29/2022 10:17:47 AM
mode SE
mag 100 000 x
WD 10.7 mm
HV 15.00 kV
spot 3.0
500 nm

Fig. 4.12 FESEM images of fresh perovskite $LaNi_{0.5}Co_{0.5}O_3$ catalyst captured at magnification of (a) 24000x(b) 100,000x

The FESEM images of $LaNi_{0.5}Co_{0.5}O_3$ catalyst were captured at two different magnifications (24000x and 100000x) to visualize the surface morphology and crystal size of the synthesized $LaNi_{0.5}Co_{0.5}O_3$ catalyst and the results are displayed in Fig.4.12. It could be clearly seen from the FESEM image taken at 24000x (Fig.4.12(a)) that the catalyst possesses large void spaces which confirm its highly porous nature. The porous nature of the catalyst material is usually desired for good catalytic activity for heterogeneous catalytic reaction systems. In addition to this, the image taken at 100,000x (Fig.4.12(b)) clearly demonstrates the catalyst contains nanoparticles having crystal size of 75-150 nm.

4.2 Steam reforming of simulated bio-oil (SB2) over $La_yA_{1-y}Ni_xM_{1-x}O_3$ catalysts

The steam reforming experiments were performed to evaluate the effectiveness of perovskite catalysts synthesized through partial substitution of metal elements at the A and B positions in LaNiO3. The metal elements used for substitution were Ce, Ca, Zr for the A position and Co, Fe, Cu for the B position. The goal was to determine the impact of these substitutions on the properties and performance of the perovskite catalysts in steam reforming. The simulated bio-oil (SB2) used in the experiment is a mixture of the major organic groups found in real bio-oil obtained from rice husk pyrolysis [98]. The organic groups included in the SB2 are acetic acid (35%), hydroxyacetone (22%), furfural (11%) and phenol (32%). The elemental composition of the simulated bio-oil is similar to that of real bio-oil used by other researchers, as referenced in [76,79].

4.2.1 Effect of partial substitution at A and B – site of perovskite catalyst

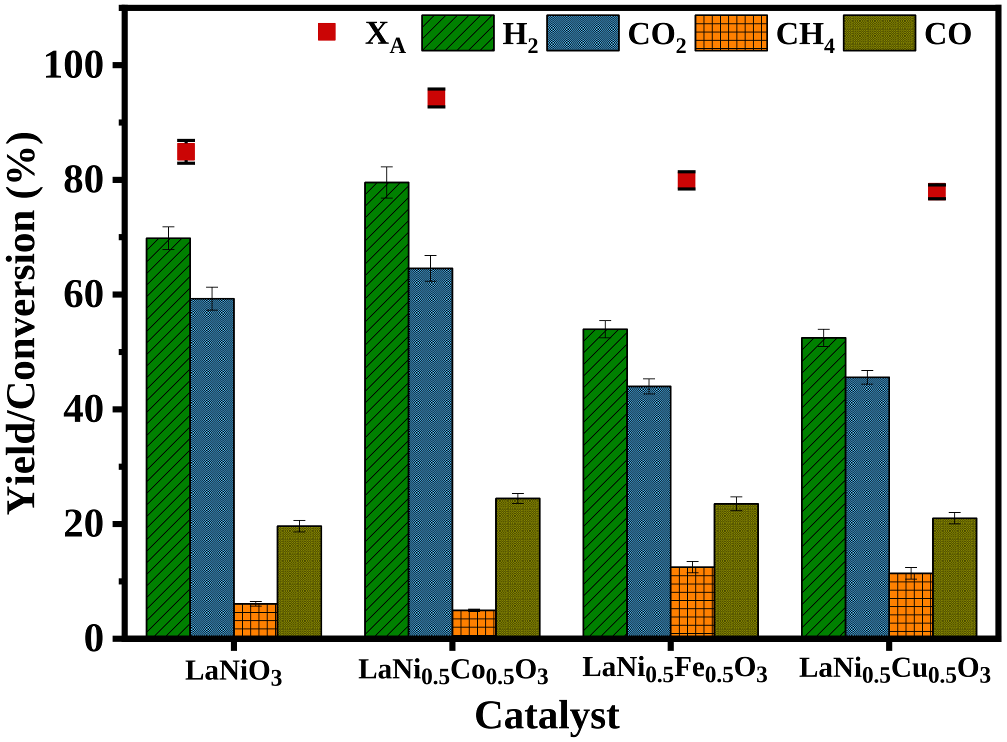

Fig. 4.13 Effect of different perovskite catalysts $LaNi_{0.5}M_{0.5}O_3$ on gaseous products yield and bio-oil conversion (W/F_{AO} =17.4 kg_{cat}.h/$kgmol_{bio-oil}$, S/C = 2.7, T=700 ^oC and P=1 atm)

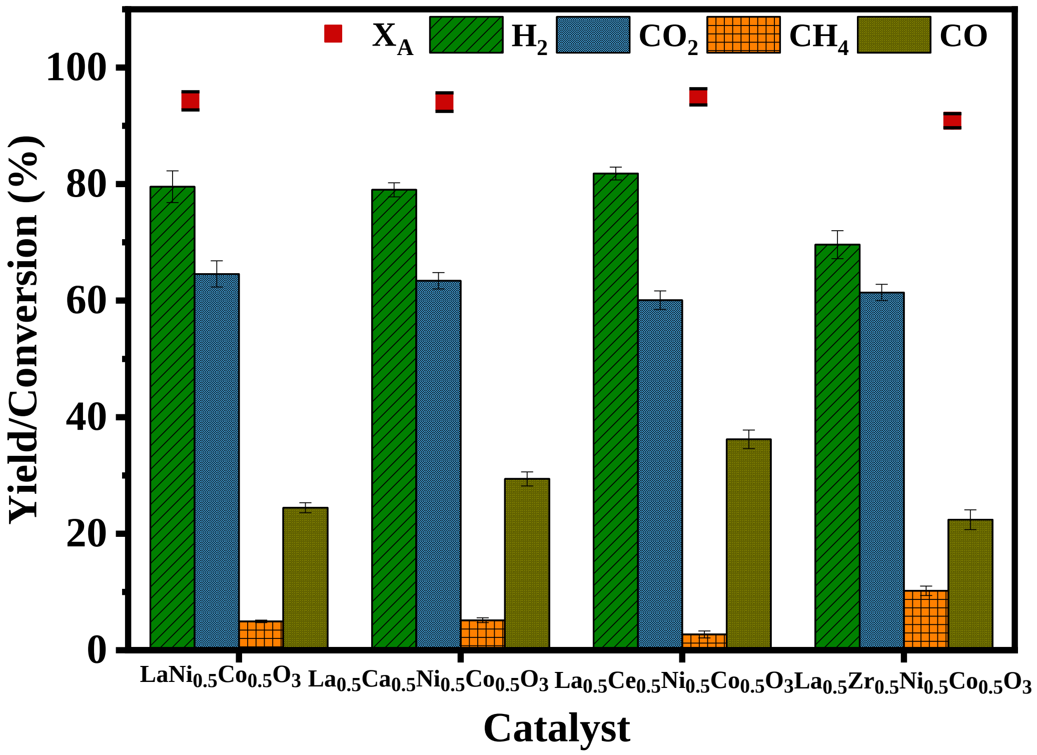

Fig. 4.14 Effect of different perovskite catalysts $La_{0.5}A_{0.5}Ni_{0.5}Co_{0.5}O_3$ on gaseous products yield and bio-oil conversion (W/F_{AO} =17.4 kg_{cat}.h/$kgmol_{bio\text{-}oil}$, S/C = 2.7, T=700 °C and P=1 atm)

The evaluation of the catalytic activity of the synthesized $LaNi_{0.5}M_{0.5}O_3$ (M= Cu, Fe, Co, and Ni) perovskite catalysts for bio-oil steam reforming was started by assessing the role of the metal substituted in B site on conversion and product yields at specified process conditions (WHST =17.4 kg_{cat}.h/$kgmol_{bio\text{-}oil}$, S/C = 2.7, T=700 °C and P=1 atm). The results obtained, as shown in Fig. 4.13, revealed that the values of conversion and H_2 yield over unsubstituted $LaNiO_3$ perovskite were 87% and 70%, respectively. Among the catalysts with Ni partially replaced by Co, Cu and Fe, the $LaNi_{0.5}Co_{0.5}O_3$ exhibited the best performance, with the values of bio-oil conversion (94%) and H_2 yield (79%) obtained over it being higher than those for $LaNiO_3$ as well. The yield of CO_2 was also found to be the highest for this particular combination. $LaNi_{0.5}Cu_{0.5}O_3$ and $LaNi_{0.5}Fe_{0.5}O_3$ catalysts, on the other hand, exhibited lower conversion (78% and 80%, respectively) and H_2 yield (52.4% and 54%, respectively) values than $LaNiO_3$. Moreover, these catalysts were exhibited notably higher CH_4 yields (11.4% and 12.4%, respectively). The obtained results are in good agreement with those reported by Hu and Lu [53] for acetic acid steam reforming over first-row transition metals for instance, Cu, Fe, Co, and Ni. They noted that Ni and Co were active for the scission of both C-C as well as C-H bonds, making SR and WGS reactions highly favourable over them and explaining the high values of conversion as well as H_2 and CO_2 yields obtained over $LaNi_{0.5}Co_{0.5}O_3$. Fe and Cu, meanwhile, were found to be selective for C-C bond activation and C-H bond cleavage, respectively, thereby explaining the low values of conversion and H_2 yield and higher CH_4 formation obtained over $LaNi_{0.5}Cu_{0.5}O_3$ and $LaNi_{0.5}Fe_{0.5}O_3$ catalysts. Another reason for the observed superior performance of $LaNi_{0.5}Co_{0.5}O_3$ catalyst could be the formation of a Ni-Co alloy after reduction owing to the existence of strong interactions among Ni and Co, confirmed by the XRD analysis of reduced samples. Usually, such alloys are known to possess smaller crystallite sizes, which would play a positive role in boost the catalytic activity towards reforming [70,75].

As displayed in Fig. 4.14, the effect of partial substitution at A- site of $La_{0.5}A_{0.5}Ni_{0.5}Co_{0.5}O_3$ (A= Ce, Ca, and Zr) on the SB2 conversion and hydrogen gas yield was evaluated for SB2 steam reforming process. The results of the steam reforming reaction show that the conversion of SB2 is nearly constant for all combinations of the catalyst. This observation indicates that the partial substitution of metal elements at the A-site does not have a significant impact on the conversion of SB2. Additionally, the results show that the hydrogen yield is nearly constant (80% ± 3%) when La is partially substituted with Ca and Ce metals, and similar results were obtained for CO_2, CO, and CH_4 gas yields. However, the hydrogen yield for $La_{0.5}Zr_{0.5}Ni_{0.5}Co_{0.5}O_3$ decreased to 70%. This decrease is attributed to an increase in CH_4 production, which is related to the pro-methanation nature of Zr.

Based on the results, it can be concluded that the $LaNi_{0.5}Co_{0.5}O_3$ catalyst is the optimal catalyst for the bio-oil steam reforming process. The improved performance of $LaNi_{0.5}Co_{0.5}O_3$ is likely due to the high concentration of oxygen vacancies on its surface. Additionally, the results show that CO, a by-product of the reforming reaction, is formed in similar amounts over all tested catalysts. As a result, $LaNi_{0.5}Co_{0.5}O_3$ was chosen for further study [70,75].

4.2.2 Influence of reaction temperature

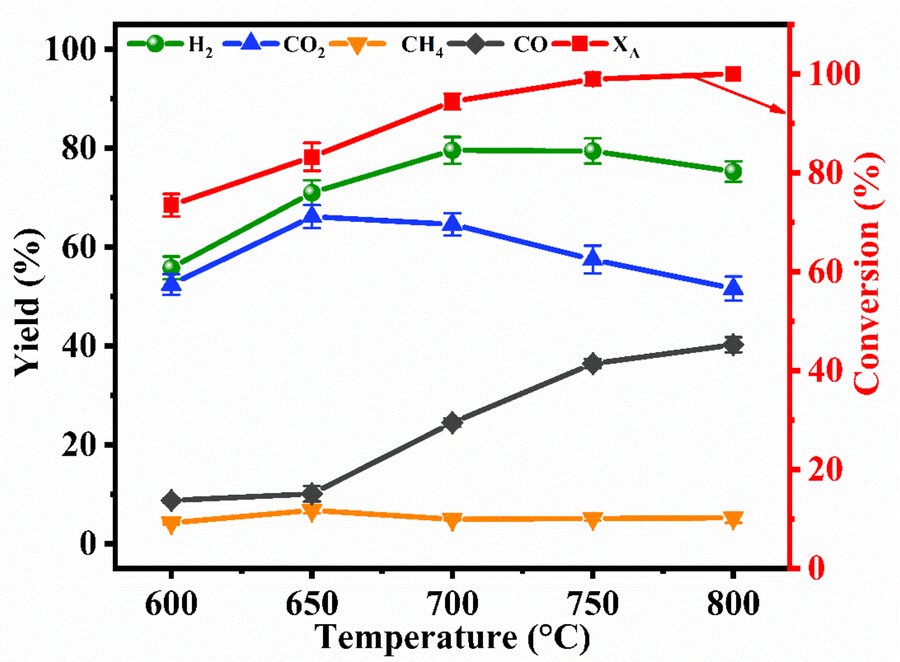

Fig. 4.15 Influence of reaction temperature on gaseous products yield and bio-oil conversion for $LaNi_{0.5}Co_{0.5}O_3$ perovskite catalyst (W/F_{AO} =17.4 kg_{cat}.h/$kgmol_{bio-oil}$, S/C = 2.7, and P=1 atm)

The influence of reaction temperature on bio-oil conversion and product gas distribution was evaluated over $LaNi_{0.5}Co_{0.5}O_3$ catalyst was studied in the range of 600-800 ºC, the results of which are displayed in Fig.4.15. It is clearly evident that the bio-oil conversion and gaseous products yield increases on increasing the temperature owing to endothermic nature of thermal cracking and steam reforming reactions. Because of this, H_2 yield also increased significantly from 55% to 79% on raising the temperature from 600 ºC to 700 ºC. Further raising the temperature to 750 ºC did not produce any appreciable increment in H_2 yield; however, on further increasing the temperature, a slight decrease in H_2 yield was noted. A similar pattern was observed for CO_2 yield, which jumped from 52% to a maximum value of 65% with an increase in temperature from 600 ºC to 700 ºC, and dropped subsequently as the reaction temperature rose beyond 700 ºC. The yield of CO witnessed a significant upward trend (8-40%) as the reaction temperature varied from 600 ºC to 800 ºC, which may be attributed to the increased favourability of reverse WGS reaction at such elevated temperatures. Additionally, the increasing values of CH_4 (3-6%) point toward the occurrence of methanation and thermal decomposition reactions at high temperatures. These results are in good agreement with the studies performed in this direction [76,79,122].

4.2.3 Influence of weight hourly space-time (WHST)

The influence of weight hourly space time (WHST) was investigated in terms of gaseous product yields and simulated bio-oil conversion at 700 ^{0}C and a fixed SCMR of 2.7 over $LaNi_{0.5}Co_{0.5}O_3$ perovskite catalyst. The WHST was varied from 7.04 to 17.4 kg_{cat}.h/$kmol_{bio-oil}$ by changing the volumetric flow rate of the reactants. As displayed in Fig.4.16, the gaseous product yield and simulated bio-oil conversion increase with WHST, signalling the requirement of sufficient and/or high residence time for the reaction to be happen. The highest gaseous products yield (H_2 = 79% , CO_2 = 64% , CO = 24% and CH_4 = 6%) and simulated bio-oil conversion (94%) were obtained at a space-time value of 17.44 kg_{cat}.h/$kmol_{bio-oil}$. The obtained results show that the steam reforming process is favourable at high residence time, which is also in synchronization with our previous study [70].

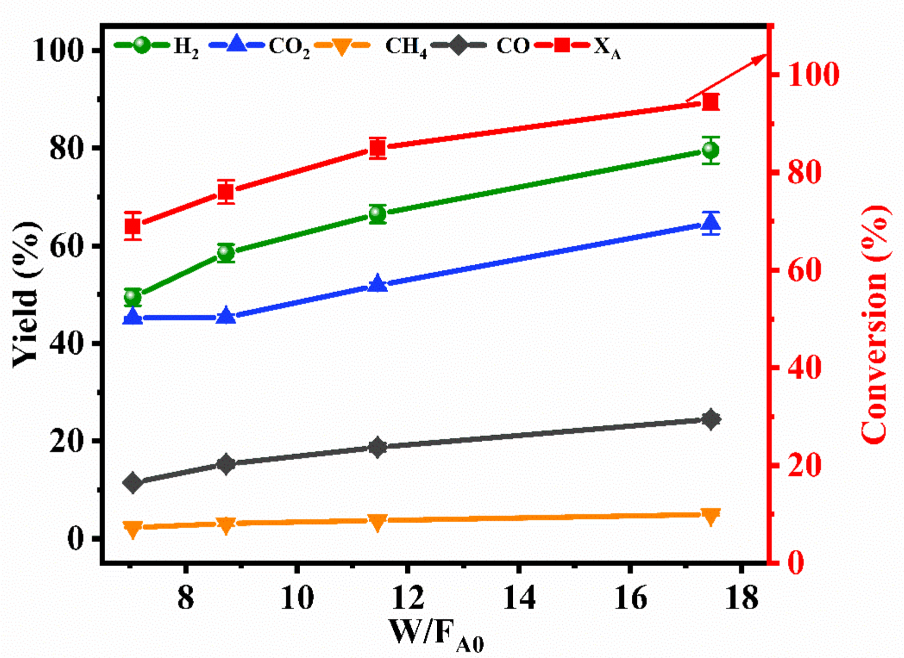

Fig. 4.16 Influence of weight hourly space time on gaseous products and bio-oil conversion for $LaNi_{0.5}Co_{0.5}O_3$ perovskite catalyst (S/C=2.7, T = 700 ^{0}C and P=1 atm)

4.2.4. Time on stream (TOS) study

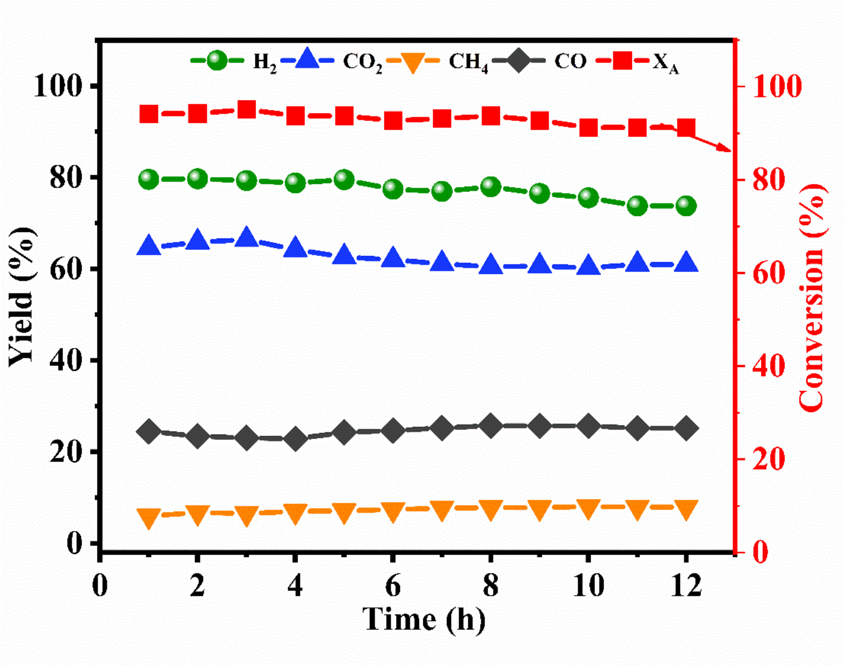

Fig. 4.17 Influence of time on steam on gaseous products and bio-oil conversion for $LaNi_{0.5}Co_{0.5}O_3$ perovskite catalyst (W/F_{AO} =17.4 $kg_{cat}.h/kgmol_{bio\text{-}oil}$, S/C = 2.7, T=700 ºC and P=1 atm)

The time on stream (TOS) tests were conducted to evaluate the catalyst stability over extended time periods at the optimum process conditions (T = 700 ºC, SCMR= 2.7, and WHST = 17.44 $kg_{cat}.h/kmol_{bio\text{-}oil}$) over $LaNi_{0.5}Co_{0.5}O_3$ catalyst with regard to gaseous products yield and simulated bio-oil conversion, as shown in Fig.4.17. It is evident that the catalyst exhibited excellent performance over a period of 12 h, with the value of H_2 yield remaining nearly constant (79% ± 3 %) for up to 8 h and then declining very slowly and reached to 74% at 12th h. A similar pattern was noted for the conversion (94%) and the CO_2 yield (64%). However, a slight increase in the formation of CO and CH_4 was observed. It could be possible because of the deposition of coke on catalyst surface, which may decrease the catalytic activity towards the dissociation of C-H and C-C bonds. Coke deposition on the catalyst surface was confirmed by thermogravimetric analysis of the spent catalyst. Even though the simulated bio-oil used in this study is a mixture of complex model compounds instead of the single model compound-containing oil used in literature, we found that the catalyst activity is not much effected by coke deposition as has been reported by other researchers for steam reforming experiments [123–125]. From the XPS and TG analysis it is clearly evident that synthesized perovskite has a good amount of oxygen vacancy, favouring coke suppression by in-situ oxidation during the process. Finally, from

TOS study, it can be concluded that $LaNi_{0.5}Co_{0.5}O_3$ catalyst is highly stable for bio-oil steam reforming process and could play an important role while designing an efficient catalytic system for steam reforming of bio-oil to produce green hydrogen.

Chapter 5: Kinetic Study

The development of a kinetic model is a crucial step for the commercialization of the steam reforming process. The model is based on the optimum process conditions that have been determined through experimentation. This model is essential for the design and optimization of the reactor used in the SR process.

The kinetic model describes the rate at which the reactants are converted into products and is typically represented by a set of mathematical equations. These equations can be derived from the experimental data obtained under the optimum process conditions. The kinetic model can be used to predict the performance of the reactor under different operating conditions, such as varying the temperature, pressure, or reactant concentrations [126–129].

Furthermore, this model can be used to optimize the reactor design by identifying the most favourable conditions that maximize the yield of the desired product while minimizing the formation of unwanted by-products. Additionally, the kinetic model can be used to identify the rate-limiting step in the reaction, which can provide important insights into the underlying mechanisms of the SR process.

In summary, the kinetic model developed using the optimum process conditions is a crucial step in the commercialization of the SR process. The model enables the design and optimization of the reactor, which can improve the performance of the process, increase the yield of the desired product, and reduce the formation of unwanted by-products. Additionally, the kinetic model can provide valuable insights into the underlying mechanisms of the SR process.

Before developing the kinetic model for the phenol steam reforming process, a thorough study on process parameter optimization was conducted. The focus of this study was to identify the optimum process conditions for the reaction by varying parameters such as reaction temperature, steam to carbon molar ratio (SCMR), and space-time. By conducting this study, the most favourable conditions for the phenol steam reforming process were determined, which were then used as the basis for developing the kinetic model. This optimization study is critical for achieving the highest conversion efficiency and products yield in the phenol steam reforming process, and it lays the foundation for the kinetic model development.

5.1 Process parameter optimization

5.1.1 Effect of temperature

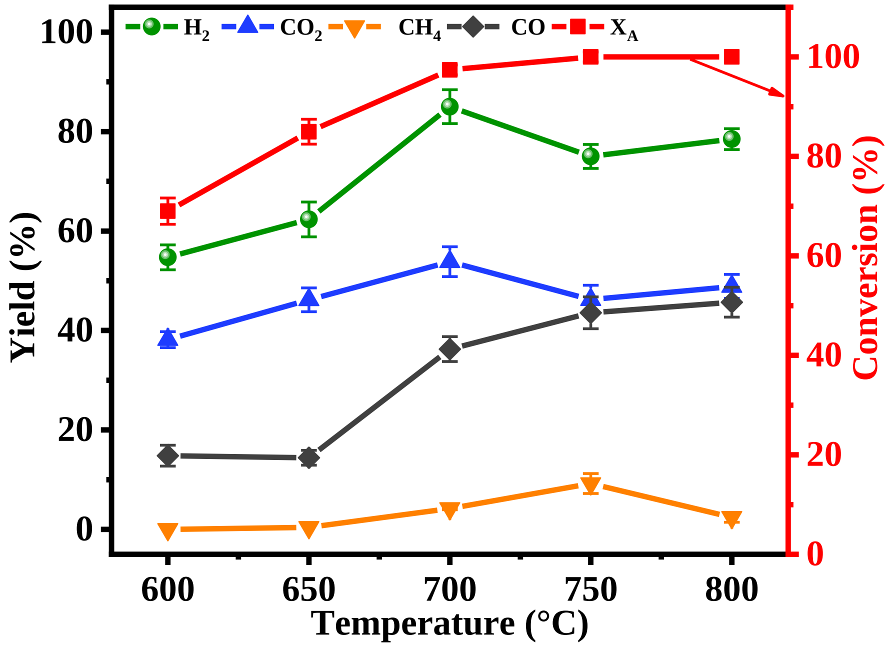

Fig. 5.1 Effect of reaction temperature on gaseous products and phenol conversion for LaNi$_{0.5}$Co$_{0.5}$O$_3$ perovskite catalyst (W/F$_{AO}$ =30.14 kg$_{cat}$.h/kgmol$_{phenol}$, S/C = 2.7 and P=1 atm)

The impact of reaction temperature on the conversion of phenol and the distribution of gaseous products over a LaNi$_{0.5}$Co$_{0.5}$O$_3$ catalyst was thoroughly investigated in the range of 600-800 °C. The results, depicted in Fig. 5.1, demonstrate a clear correlation between increasing reaction temperature and the phenol conversion and gaseous product yields, which is a direct consequence of the endothermic nature of thermal cracking and steam reforming reactions [130,131]. More specifically, the H_2 yield increases significantly from 54% to 85% as the temperature increases from 600 °C to 700 °C. However, it is important to note that further increases in temperature above 700 °C do not result in a significant increment in H_2 yield and may even cause a slight decrease (79%). A similar trend was observed for CO_2 yield, where the maximum value of 54% was reached at 700 °C before decreasing at higher temperatures. Additionally, the yield of CO showed a significant upward trend (14-45%) as the reaction temperature varied from 600 °C to 800 °C, which can be attributed to the increased thermodynamic favorability of the reverse water-gas shift reaction at elevated temperatures. Furthermore, these results also indicate an increase in CH_4 yield (1-9%) as the reaction temperature increases, which can be attributed to the occurrence of methanation and thermal decomposition reactions at high temperatures (750 °C). However, as the temperature is further increased to 800 °C, a slight decrease in CH_4 yield is observed in conjunction with an increase in H_2 and CO_2 yields. This suggests the occurrence of methane steam reforming reaction at this elevated temperature. This confirms that the reaction mechanism is influenced by the temperature and it is important to consider this factor in the optimization of the process.

5.1.2 Effect of SCMR

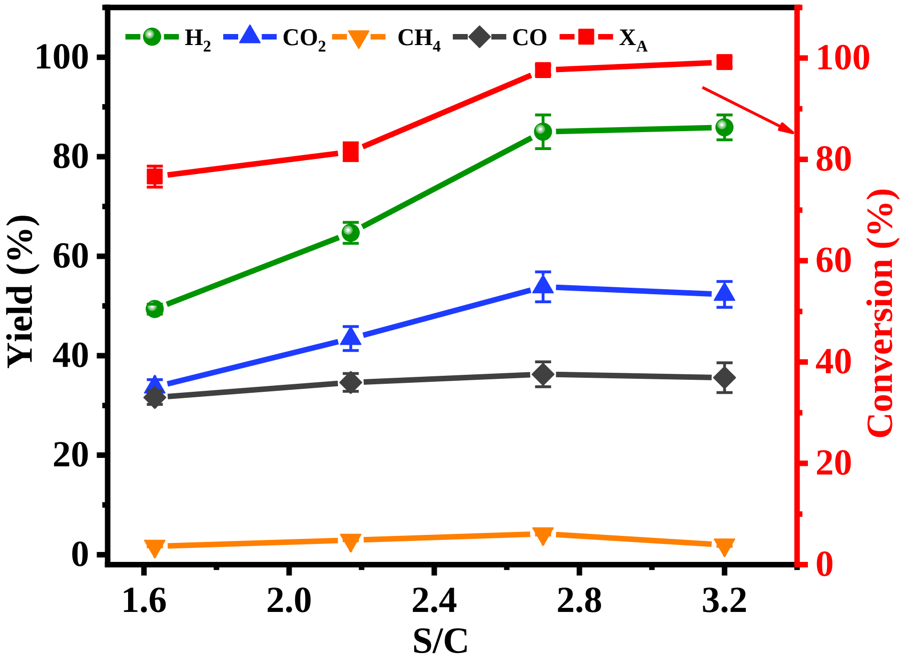

Fig. 5.2 Effect of SCMR on gaseous products and phenol conversion for $LaNi_{0.5}Co_{0.5}O_3$ perovskite catalyst (W/F_{AO} =30.14 $kg_{cat}.h/kgmol_{phenol}$, T = 700 °C and P=1 atm)

The effect of steam to carbon molar ratio (SCMR) on the conversion of phenol and the distribution of gaseous products was studied using a $LaNi_{0.5}Co_{0.5}O_3$ catalyst at a reaction temperature of 700 °C and a space-time of 30.14 $kg_{cat}.h/kgmol_{phenol}$. The results, as illustrated in the corresponding Fig. 5.2, demonstrate that as the SCMR increases from 1.6 to 2.7, the conversion of phenol also increases from 76% to 97%, and the yield of hydrogen increases from 49% to 85%. This trend illustrates that an increase in the amount of steam in the feed mixture enhances the steam reforming (SR) reactions (eq. 1) and water-gas shift (WGS) reactions (eq. 2), as supported by the increase in CO_2 yield. However, when the

SCMR is further increased to 3.26, there is no significant change in the phenol conversion as well as the yield of gaseous products (H2, CO, and CO_2). However, the slight decrease in CH_4 yield as SCMR increases (1.6-3.2) confirms the occurrence of methane steam reforming (MSR) reactions, which are usually favored at higher SCMR [53,132]. Therefore, it can be concluded that an SCMR of 2.7 is the optimal value for phenol steam reforming using $LaNi_{0.5}Co_{0.5}O_3$ catalyst at a reaction temperature of 700 °C and a space-time of 30.14 kg_{cat}.h/$kgmol_{phenol}$.

5.1.3 Effect of space time

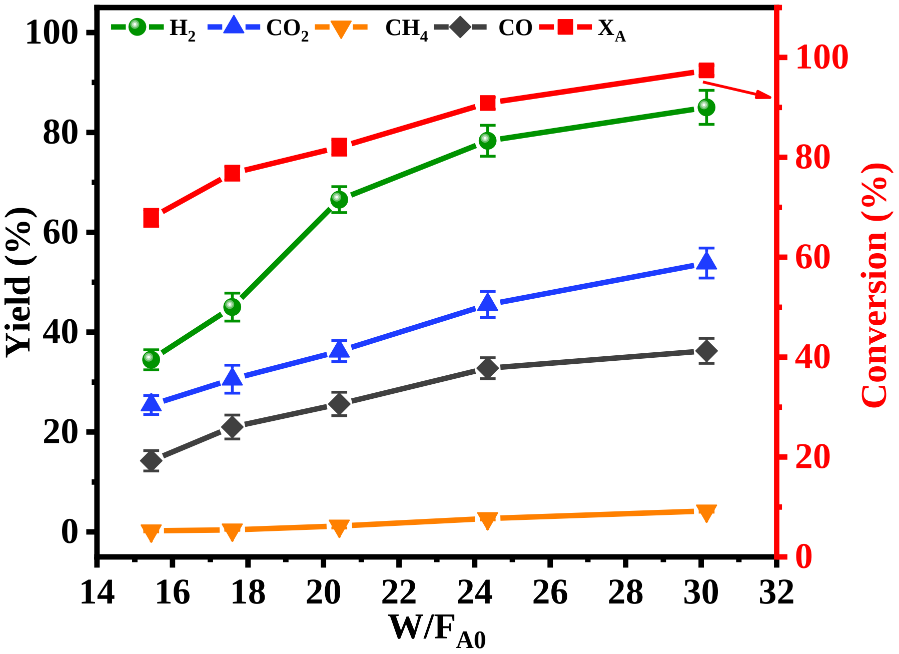

Fig. 5.3 Effect of space time on gaseous products and phenol conversion for $LaNi_{0.5}Co_{0.5}O_3$ perovskite catalyst (T = 700 ºC, S/C = 2.7 and P=1 atm)

The influence of weight hourly space time (WHST) on the conversion of simulated bio-oil and the distribution of gaseous products was studied using a $LaNi_{0.5}Co_{0.5}O_3$ catalyst at a reaction temperature of 700 °C and a fixed steam to carbon ratio (SCMR) of 2.7. The results, as depicted in Figure 5.3, demonstrate that as the WHST increases from 15.43 to 30.14 kg_{cat}.h/$kmol_{phenol}$, the conversion of phenol also increases from 67% to 97%, and the yield of hydrogen increases from 34% to 85%. This trend illustrates that an increase in the contact time of the reactants with the catalyst by increasing the WHST is favorable for steam reforming (SR) reactions as well as water-gas shift (WGS) reactions [124,125]. The higher space-time allows for more extended interactions between the reactants and the catalyst surface, which results in a more efficient utilization of the catalyst, promoting both

SR and WGS reactions. Furthermore, the yield of other gaseous products such as CO and CO_2 also showed a similar trend, reaching maximum values at a WHST of 30.14 $kg_{cat}.h/kmol_{phenol}$. These results indicate that increasing the WHST is a crucial factor in optimizing the process, as it improves the conversion of phenol and increases the yield of hydrogen and other gaseous products.

5.1.4 Time on stream study

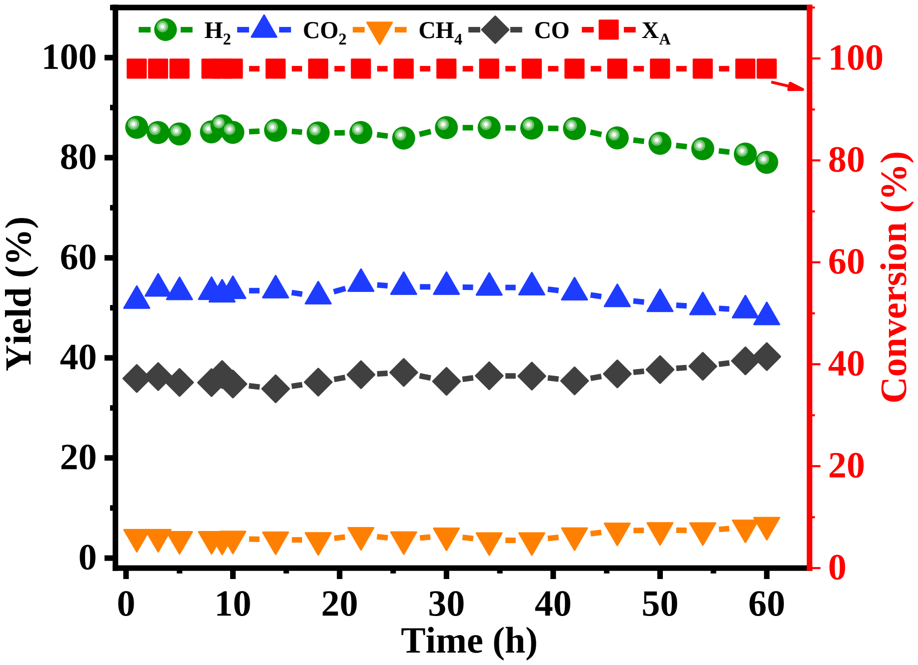

Fig. 5.4 Time on stream study on gaseous products yield and phenol conversion for $LaNi_{0.5}Co_{0.5}O_3$ perovskite catalyst (W/F_{AO} =30.14 $kg_{cat}.h/kmol_{phenol}$, T = 700 ºC, S/C = 2.7 and P=1 atm)

The stability of the $LaNi_{0.5}Co_{0.5}O_3$ catalyst for phenol steam reforming (PSR) was evaluated over an extended period of time using time on stream (TOS) tests. These tests were conducted under optimal process conditions of 700 °C, steam-to-carbon molar ratio (SCMR) of 2.7, and weight hourly space velocity (WHST) of 30.14 $kg_{cat}.h/kmol_{phenol}$. The results, as depicted in Fig.5.4, indicate that the catalyst performance remained exceptional for a duration of 60 hours. The yield of hydrogen (H_2) was observed to be nearly constant at 85% for the initial 45 hours before a slow decline to 79% at the 60th hour. A similar trend was observed for the yield of carbon dioxide (CO_2), which remained at 54% for the initial 45 hours before a decline to 48% at the 60th hour. However, the phenol conversion remained constant throughout the stability test. Additionally, a slight increase in the formation of carbon monoxide (CO) and methane (CH_4) was observed. This increase could be attributed to the deposition of coke on the catalyst surface, which decreases the catalytic activity towards the dissociation of C-H and C-C bonds [46,133]. The presence of coke on the catalyst surface was confirmed via thermogravimetric analysis of the spent catalyst.

Moreover, the X-ray photoelectron spectroscopy (XPS) and thermogravimetric analysis (TG) revealed that the synthesized perovskite had a significant amount of oxygen vacancies, which favor coke suppression via in-situ oxidation during the process. Based on the TOS study results, it can be concluded that the $LaNi_{0.5}Co_{0.5}O_3$ catalyst is highly stable for the PSR process and could play an important role in the design of an efficient catalytic system for steam reforming process to produce green hydrogen. The stability of the catalyst is a crucial factor in the design of catalytic systems, as it ensures the longevity and consistency of the process. The results of this study demonstrate the potential of $LaNi_{0.5}Co_{0.5}O_3$ as a highly active catalyst for PSR and the production of green hydrogen.

Furthermore, the above optimum process conditions were utilized to develop the kinetic model, which is important step required for reactor design and optimization to promote the commercialization viability of the SR process.

5.2 Development of kinetic model

The kinetics of the phenol steam reforming reaction can be modeled using a power law model, which is an empirical equation that describes the reaction rate as a function of the reactant concentrations [134,135]. The power law model for the phenol steam reforming reaction can be expressed as:

$$-r_A = k * p_{Ph}^n * p_w^m \qquad (5.1)$$

where $-r_A$ is the reaction rate, k is the rate constant, p_{ph} and p_w are the partial pressure of phenol and water, respectively, and n and m are the reaction order with respect to phenol and water.

The reaction order with respect to phenol (n) and water (m) can be determined experimentally by performing a series of experiments at different reactant concentrations/partial pressure and measuring the reaction rate. The values of n and m can then be determined by fitting the experimental data to the power law model using a least-squares regression analysis.

The rate constant k can be determined by measuring the reaction rate at a specific temperature and reactant concentrations and then using the Arrhenius equation, which relates the rate constant to temperature. It can be represented as:

$$k = k_0 * \mathrm{e}^{\frac{-E_A}{RT}} \qquad (5.2)$$

where k_0 is the pre-exponential factor, Ea is the activation energy, R is the ideal gas constant and T is the temperature in Kelvin.

Design equation for catalytic fixed bed reactor can be written as:

$$\frac{w}{F_{AO}} = \int \frac{\mathrm{d}x_A}{(-r_A)} \qquad (5.3)$$

Where, w is weight of catalyst, F_{A0} is the reactant molar flow rate, x_A is the conversion and $-r_A$ is the rate of reaction.

The presented data describes the results of an experimental study on the conversion for phenol steam reforming using $LaNi_{0.5}Co_{0.5}O_3$ catalyst at various temperatures and space times. The conversion of phenol was measured at 600 ºC, 650 ºC, and 700 ºC and the results were recorded in Table 5.1-5.3. The results showed that as the temperature increased, the phenol conversion also increased. Additionally, an increase in space time resulted in a higher phenol conversion. The experimental rate of reaction and corresponding partial pressure data for each run were also recorded in Table 5.1-5.3.

Table 5.1 Reaction results at 600 ºC

p_{ph} (atm)	p_w (atm)	Reaction rate ($kmol/kg_{cat}.h$)	Phenol conversion (%)	w/F_{A0} ($kg_{cat}.h/kmol$)
0.017	0.428	0.0229	69	30.14
0.019	0.449	0.0251	61	24.35
0.021	0.483	0.0260	53	20.42
0.024	0.502	0.0267	47	17.58
0.025	0.530	0.0272	42	15.44

Table 5.2 Reaction results at 650 ºC

p_{ph} (atm)	p_w (atm)	Reaction rate ($kmol/kg_{cat}.h$)	Phenol conversion (%)	w/F_{A0} ($kg_{cat}.h/kmol$)
0.011	0.370	0.0282	84.97	30.14
0.015	0.402	0.0311	75.66	24.35
0.018	0.432	0.0321	65.55	20.42
0.020	0.452	0.0349	61.33	17.58
0.022	0.480	0.0357	55.08	15.44

Table 5.3 Reaction results at 700 ºC

p_{ph} (atm)	p_w (atm)	Reaction rate ($kmol/kg_{cat}.h$)	Phenol conversion (%)	w/F_{A0} ($kg_{cat}.h/kmol$)
0.005	0.303	0.0323	97.40	30.14
0.007	0.358	0.0373	90.86	24.35
0.011	0.389	0.0402	82.04	20.42
0.015	0.391	0.0437	76.83	17.58
0.017	0.420	0.0440	67.90	15.44

The kinetic parameter (k) and the order of reaction with respect to phenol and water (m, n) were evaluated by using non-linear regression analysis based on the Levenberg-Marquart algorithm. This method was implemented in the software program POLYMATH, and was used to minimize the sum of residual squares of the reaction rates. The function to be minimized in this study is a residual sum of squares function, represented by the equation provided. It is commonly used in non-linear regression analysis and optimization, and it is calculated by taking the difference between the calculated rate of reaction (r_{cal}) and the experimental rate of reaction (r_{exp}) at each data point. The calculated difference is then squared and summed over all data points (i = 1 to N) to give the total residual sum of squares (F). This function is used to determine the best-fit kinetic parameters (k) and reaction order (m,n) by minimizing the value of F. Mathematically it can be presented in the following form:

$$F = \sum_{i=1}^{N} (r_{cal_i} - r_{exp_i})^2 \qquad (5.4)$$

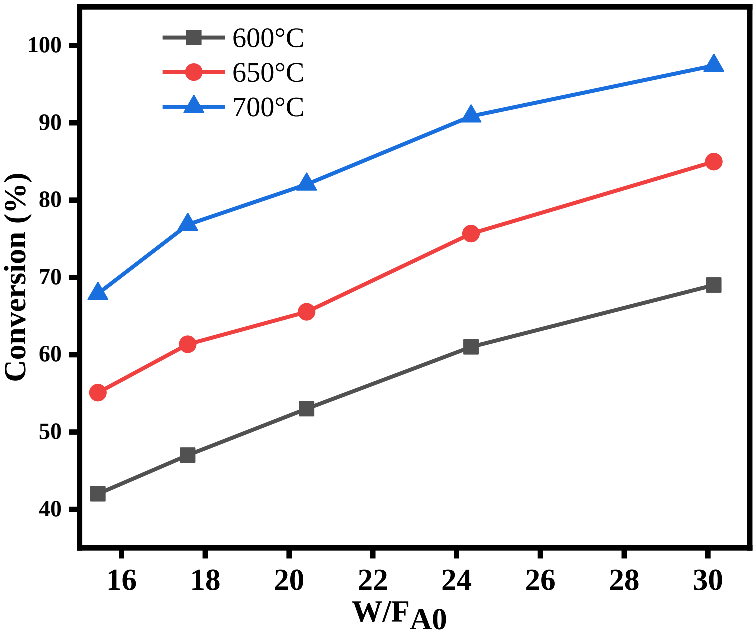

Fig. 5.5 Effect of space time on phenol conversion for $LaNi_{0.5}Co_{0.5}O_3$ perovskite catalyst (W/F_{AO} =30.14 $kg_{cat}.h/kmol_{phenol}$, S/C = 2.7 and P=1 atm)

Fig. 5.5 presents the phenol conversion data at different temperatures (600 ºC, 650 ºC, and 700 ºC), which was used to calculate the kinetic parameters via power law model as per the method described above. The kinetic parameters, including the rate constant k and the calculated reaction orders (m, n), were determined for three different temperatures (600 ºC, 650 ºC, and 700 ºC). It was observed that the values for these parameters (k =

0.112, n = 0.14, and m = 0.38) were consistent across the temperature range of 600 ºC-700 ºC, leading to the conclusion that the power law model for the phenomenon of interest can be effectively applied in this temperature range. Hence the power law model for PSR at 700 ºC can be written as

$$-r_A = 0.112 * p_{Ph}^{0.14} * p_w^{0.38} \qquad (5.5)$$

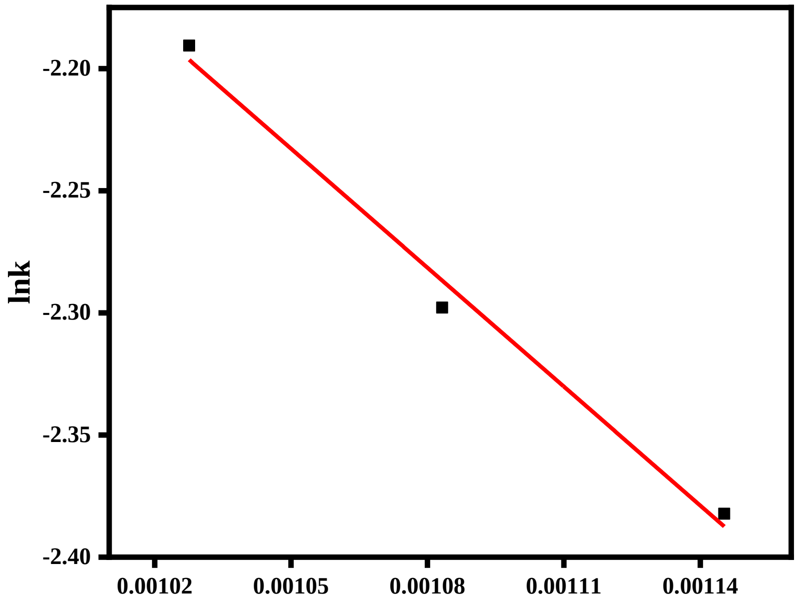

Fig. 5.6 Arrhenius plot based on power law model for phenol steam reforming using $LaNi_{0.5}Co_{0.5}O_3$ perovskite catalyst

Furthermore, the activation energy and the frequency factor of the reaction were determined by utilizing the Arrhenius equation (eq.2). This was achieved by plotting the logarithm of the rate constant against the inverse of the absolute reaction temperature, as depicted in Fig. 5.6. The activation energy and frequency factor are important parameters in understanding the kinetics of a chemical reaction. The activation energy (E_A) of the reaction was determined to be 13495 KJ/kmol, which is a measure of the energy required for the reaction to occur. The pre-exponential factor, also known as the frequency factor, was found to be 0.59 $kmol_{phenol}/kg_{cat}.h.atm^{0.51}$. This value is a measure of how likely the reaction is to occur at a given temperature and is often used in combination with the activation energy to predict the rate of a chemical reaction. By employing these kinetic parameters, the rate equation for phenol steam reforming using $LaNi_{0.5}Co_{0.5}O_3$ perovskite catalyst can be written as

$$\boldsymbol{-r_A = 0.59 * e^{\frac{-13495}{RT}} * p_{Ph}^{0.14} * p_w^{0.38}} \qquad (5.6)$$

Chapter 6: Catalytic steam reforming of agricultural residue derived bio-oil

The present chapter aims to explore the potential of catalytic steam reforming as a means of producing hydrogen from bio-oil which is derived from a blend of different types of biomass feedstocks, particularly rice husk, wheat straw, corn cob, and sugarcane bagasse. These feedstocks have been selected as they represent the waste generated by the primary crops grown in the northern region of India, particularly in the state of Punjab.

This study involves the pyrolysis of an agricultural residue blend, followed by the catalytic steam reforming of the resulting bio-oil to produce green hydrogen. Firstly, various process parameters such as temperature, ramp rate, effect of feed stocks, were studied to maximize the bio-oil yield. Then, the produced bio-oil was subjected to catalytic steam reforming process, utilizing the most effective $LaNi_{0.5}Co_{0.5}O_3$ perovskite catalyst, which was previously determined through separate investigations. The catalytic steam reforming experiments were executed at the optimized process conditions established in previous studies.

The results of the study have the potential to provide valuable insights into the feasibility of using biomass waste as a sustainable source of hydrogen, thereby contributing to the development of cleaner and more sustainable energy solutions.

6.1 Pyrolysis of agricultural blend to produce bio-oil

The agricultural waste materials collected from the vicinity of the Indian Institute of Technology Ropar in the Rupnagar district underwent a pre-treatment procedure prior to utilization in the pyrolysis experiments. This pre-treatment methodology is described in detail in Chapter 2. The treated agricultural waste materials, including rice husk, wheat straw, corn cob, and sugarcane bagasse, were blended in equal weight ratios to form a homogeneous mixture, which was then used in the pyrolysis experiments. The objective of the pyrolysis experiments was to maximize the production of bio-oil as the primary product.

6.1.1 Effect of temperature

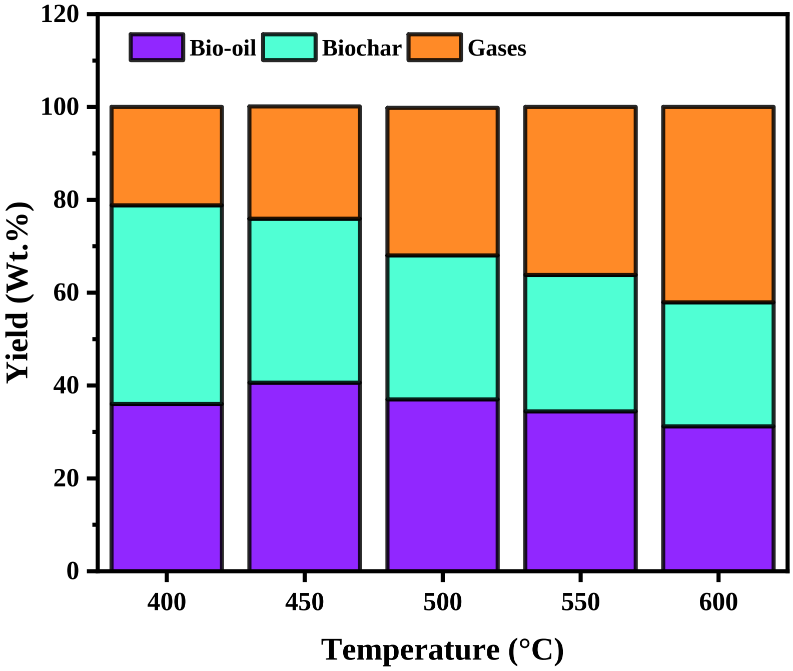

Fig. 6.1 Effect of temperature on products yield (Ramp Rate = 10 °C/min, N_2 flowrate = 50 mL/min, Feed: Agricultural residues blend)

The temperature effect was evaluated and presented in Fig. 6.1 for the pyrolysis of a blend of agricultural residues at temperatures ranging from 400-600 ºC with the aim of maximizing bio-oil production. The weight percentages of the three products produced (bio-oil, biochar, and gases) are documented in Table 6.1. At 400 ºC, the highest yield was observed for biochar (42.8%), while the yields of bio-oil and gases were 36% and 21.2%, respectively. The maximum bio-oil yield (40.6%) was recorded at 450 ºC, with biochar and gas yields of 35.3% and 24.2%, respectively. With further increase in temperature to 600 ºC, the bio-oil and biochar yields decreased, while the gas yield increased, which could be attributed to the prevalence of gasification reactions at higher temperatures. These results are consistent with previous studies in this direction [136–139].

Table 6.1 Pyrolysis products yield at different temperature (Ramp Rate = 10 °C/min, N_2 flowrate = 50 mL/min, Feed: Agricultural residues blend)

Temperature (°C)	Bio-oil (wt%)	Biochar (wt%)	Gases (wt%)
400	36	42.8	21.2
450	40.6	35.3	24.2
500	37	31	31.8
550	34.4	29.4	36.2
600	31.2	26.7	42.1

6.1.2 Effect of ramp rate

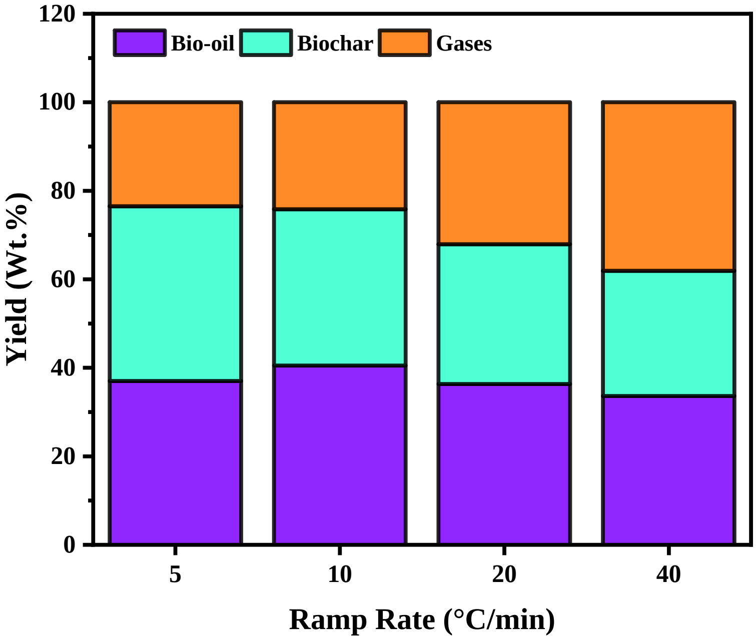

Fig. 6.2 Effect of ramp rate on products yield (Temperature = 450 °C/min, N_2 flowrate = 50 mL/min, Feed: Agricultural residues blend)

The impact of heating rate (ramp rate) on the production of pyrolysis products was investigated at a constant temperature of 450 °C and N2 flow rate of 50 mL/min. Four different heating rates of 5, 10, 20, and 40 °C/min were employed, under slow pyrolysis condition. The results, as presented in Table 6.2, demonstrate that an increase in heating rate from 5 to 10 °C/min led to an increase in bio-oil yield, followed by a decrease. At a slow heating rate of 5 °C/min, a lower bio-oil yield and a higher biochar yield (39.5%) were observed due to the slower decomposition of the volatile component of biomass. Conversely, with increasing heating rate from 5 to 40 °C/min, the yield of gases increased, with a maximum yield of 38.1% gases being recorded at a heating rate of 40 °C/min. This was attributed to the rapid decomposition of biomass and secondary decomposition of volatile components, as well as excessive decomposition of char [140]. Thus, it can be concluded that the maximum yield of bio-oil was obtained at a heating rate of 10 °C/min.

Table 6.2 Pyrolysis products yield at various heating/ramp rate (Temperature = 450 °C/min, N_2 flowrate = 50 mL/min, Feed: Agricultural residues blend)

Ramp rate (°C/min)	Bio-oil (wt%)	Biochar (wt%)	Gases (wt%)
5	37	39.5	23.5
10	40.5	35.3	24.2
20	36.3	31.6	32.1
40	33.6	28.3	38.1

6.1.3 Effect of feed stocks

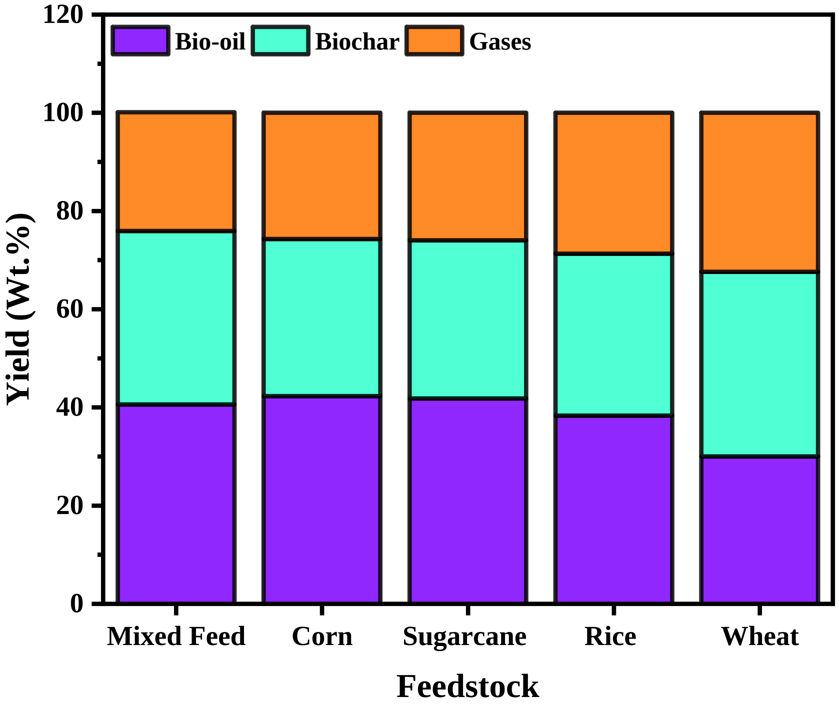

Fig. 6.3 Effect of feed stocks on products yield (Ramp Rate = 10 °C/min, N_2 flowrate = 50 mL/min, Temperature = 450 °C/min)

The results of pyrolysis processing on various agricultural residues are presented in Fig. 6.3 and Table 6.3. The process conditions were optimized with a ramp rate of 10 °C/min, N_2 flowrate of 50 mL/min, and a temperature of 450 °C/min. The yields of bio-oil, biochar, and gases were determined for individual agricultural residues as well as a blend of all four residues. The highest bio-oil yields were obtained from corn cob (42.3%) and sugarcane bagasse (41.8%). Rice husk and wheat straw had lower yields at 38.3% and 30% respectively. The bio-oil yield for the blend was 40.6%, while the yields of biochar and gases were 35.3% and 24.2%. These results indicate that the composition of agricultural residues has a significant impact on the yield of bio-oil and other products obtained through pyrolysis processing.

Table 6.3 Pyrolysis products yield for different feed stocks (Ramp Rate = 10 °C/min, N_2 flowrate = 50 mL/min, Temperature = 450 °C/min)

Feed	**Bio-oil (wt%)**	**Biochar (wt%)**	**Gases (wt%)**
Mixed Feed	40.6	35.3	24.2
Corn Cob	42.3	32	25.7
Sugarcane Bagasse	41.8	32.2	26
Rice Husk	38.3	33	28.7
Wheat Straw	30	37.6	32.4

6.1.4 Effect of temperature on bio-oil composition

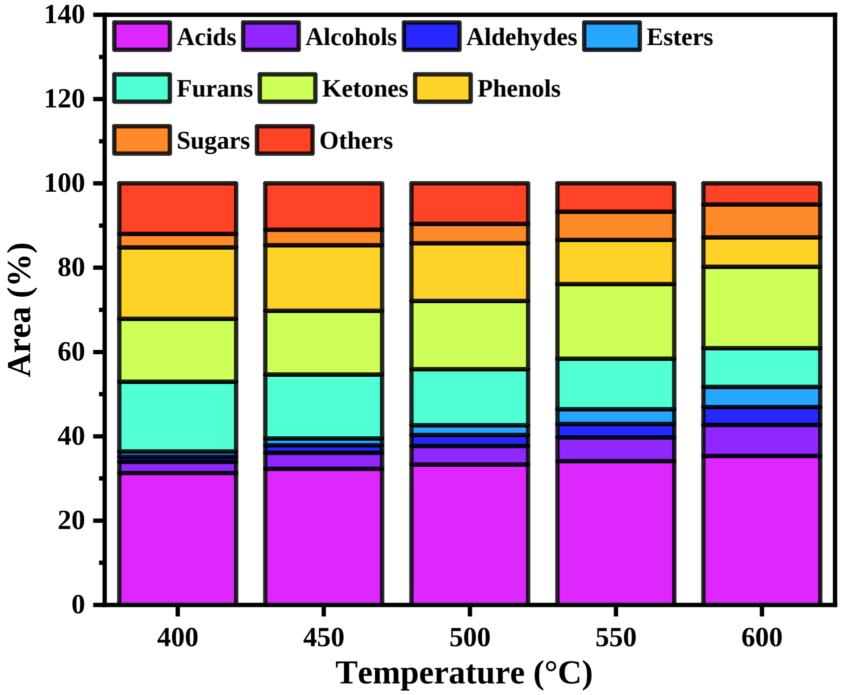

Fig. 6.4 Effect of temperature on bio-oil composition (Ramp Rate = 10 °C/min, N_2 flowrate = 50 mL/min, Feed: Agricultural residues blend)

The study of the effect of temperature (400-600 °C) on the composition of bio-oil produced from a blend of agricultural residues via pyrolysis was performed using a ramp rate of 10 °C/min. The bio-oil was analyzed using Gas Chromatography-Mass Spectrometry (GCMS) to determine the chemical compounds present. The resulting data was then classified into 9 functional groups, including acids, alcohols, aldehydes, esters, furans, ketones, phenols, sugars, and others. The bio-oils were found to be a complex mixture of organic compounds with a high concentration of oxygenated species such as phenols, ketones, and carboxylic acids. The study showed that bio-oils produced at different temperatures had similar compositions. The major constituents of the bio-oils were identified as phenolic compounds, such as phenol, cresols, guaiacols, and benzendiols, in addition to acetic acid and ketones.[98,141–143] It was concluded that the acids, ketones, furans, and phenols made up a significant portion of the bio-oil, contributing 70-85% of its composition. However, the obtained bio-oil has several limitations, including instability over time and a low heating value compared to petroleum products. These drawbacks highlight the need for further upgrading of the bio-oil into biofuels, chemicals, or other value-added products to enhance its commercial viability. One possible solution is to perform catalytic steam reforming of the bio-oil, which can significantly improve its quality and generate carbon-neutral green hydrogen. This process holds significant potential for the development of sustainable energy sources and the reduction of greenhouse gas emissions.

Table 6.4 Bio-oil composition at different temperatures

Temperature(°C) →	**400**	**450**	**500**	**550**	**600**
Compounds	**GCMS Area (%)**				
Acids	31.3	32.3	33.3	34.1	35.3
Alcohols	2.65	3.8	4.4	5.6	7.4
Aldehydes	1.2	1.8	2.6	3.2	4.2
Esters	1.2	1.6	2.3	3.5	4.8
Furans	16.6	15.2	13.3	12	9.2
Ketones	14.9	15.1	16.2	17.7	19.3
Phenols	16.9	15.6	13.7	10.5	7
Sugars	3.2	3.6	4.6	6.7	7.8
Others	12	11	9.6	6.7	5

6.2 Catalytic steam reforming of raw bio-oil

Bio-oil produced via pyrolysis of a agricultural residue blend was used as a feed stock for catalytic steam reforming experiments. The production of bio-oil was carried out via pyrolysis of a blend of agricultural residues and its elemental composition was determined through CHNS analysis. The results indicated that the bio-oil consisted of 43.4% carbon, 6.2% hydrogen, and 50.4% oxygen, yielding a molecular formula of $C_{3.6}H_{6.2}O_{3.2}$. The overall steam reforming reaction is as follows:

$$\boldsymbol{CH_{1.69}O_{0.86} + 1.13H_2O \rightarrow 1.98H_2 + CO_2}$$

In order to investigate the hydrogen production potential from bio-oil, the TOS experiments were performed utilizing $LaNi_{0.5}Co_{0.5}O_3$ catalyst for steam reforming process at optimized process parameters. The temperature was set at 700 °C, the steam-to-carbon mole ratio was established at 2.7, and the flow rate of the bio-oil feed was maintained at 12 ml/h (to maintain same space time of previous studies). As displayed in Fig. 6.5, the performance of the $LaNi_{0.5}Co_{0.5}O_3$ catalyst in the steam reforming of bio-oil was evaluated over a 12 h period. The results showed that the catalyst exhibited high activity in producing hydrogen, with a yield of 74% (±3%) at 5th h that gradually decreased to 60% at 12th h. The conversion rate of bio-oil to gaseous products followed a similar trend, decreasing from 94% at 5th h to 80% at 12th h. The CO_2 and CO yields also declined, from 64% and 38% at 5th h to 55% and 35% at 12th h, respectively. This decrease in catalytic activity was attributed to the accumulation of coke on the catalyst surface, which reduced the ability of the catalyst to dissociate the C-H and C-C bonds in bio-oil and suppressed the steam reforming and water-gas shift reactions. However, the CH_4 yield increased from 5% to 8% over the course of the experiment, likely due to reverse methane decomposition and/or methanation reactions [46,144,145]. Overall, the results demonstrate the excellent activity of the $LaNi_{0.5}Co_{0.5}O_3$ catalyst to efficiently produce green and renewable hydrogen through the steam reforming of bio-oil.

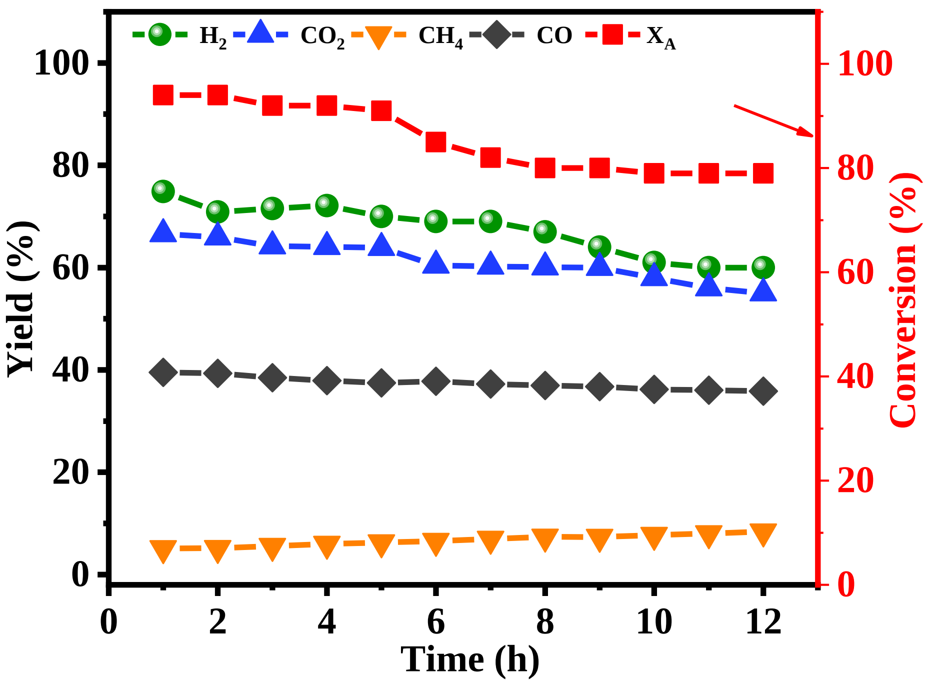

Fig. 6.5 Influence of time on stream on gaseous products and bio-oil conversion for $LaNi_{0.5}Co_{0.5}O_3$ perovskite catalyst (feed flow rate= 12mL/h, S/C = 2.7, T=700 °C and P=1 atm)

6.3 Comparison of raw bio-oil steam reforming processes

Only a limited number of studies have investigated the raw bio-oil as a reactant in steam reforming process. The finding of these studies are being summarized in Table 6.5 and compared with the findings of the present study. The primary source material for these studies was typically pine wood or sawdust, which was converted into bio-oil and subsequently utilized in a catalytic steam reforming process for hydrogen production. Upon comparison with other studies in this area, it becomes apparent that the $LaNi_{0.5}Co_{0.5}O_3$ catalyst exhibited remarkable stability, with a maximum operational duration of 12 hours and the highest yield of hydrogen, reaching up to 60%.

Table 6. 5 Comparison of raw bio-oil steam reforming processes

Biomass source	**Catalyst**	**Process conditions**	**Conversion & H_2 yield**	**TOS**	**Reference**
Pine wood	$La_{0.8}Ce_{0.2}FeO_3$	T = 800ºC SCMR = 2	X_A = 65.57% H_2 yield = 53%	5h	G. Chen et al. 2015 [80]
Pine wood saw dust	$La_{0.8}K_{0.2}MnO_3$	T = 800ºC SCMR = 3	X_A = 76.6% H_2 yield = 49%	9 h	G. Chen et al. 2016 [76]
Pine wood saw dust	$LaCo_{0.9}Cu_{0.1}O_3$	T = 800ºC SCMR = 2	X_A = 80% H_2 yield = 54%	9 h	J. Yao et al 2016 [146]
Pine saw dust	Ni/La_2O_3-αAl_2O_3	T = 700ºC SCMR = 1.5	X_A = 90% H_2 yield = 48%	6 h	B. Valle et al. 2018 [144]
Agricultural biomass blend	**$LaNi_{0.5}Co_{0.5}O_3$**	**T = 700ºC** **SCMR = 2.7**	**X_A = 80% H_2 yield = 60%**	**12 h**	**Present study**

Chapter 7: Catalyst deactivation study

This chapter focuses on studying how catalysts used in steam reforming processes lose their activity over time, a process known as deactivation. It presents a detailed analysis of the coke deposits on the spent catalysts, which is the main cause of deactivation, by using various techniques such as X-ray diffraction (XRD), Raman spectroscopy, thermal gravimetric analysis (TGA), and field emission scanning electron microscopy (FESEM). The analysis was performed on spent catalysts obtained from steam reforming studies using different reactant feeds.

7.1 Catalyst deactivation study for simulated bio-oil 1 (SB1)

The catalyst deactivation behavior of spent catalysts obtained from the steam reforming TOS experiments of SB1 at temperatures of 650 °C and 700 °C was investigated in order to comprehend the underlying mechanisms responsible for the decline in catalytic activity. An in-depth analysis of the spent catalysts was performed to elucidate the causes of deactivation.

7.1.1 Raman spectroscopy

The qualitative analysis or nature of coke deposited on the catalyst surface after SR process was confirmed by Raman spectroscopic technique. The Raman spectra were deconvoluted into two characteristic peaks mainly as follows: (i) G band (1575-1600 cm^{-1}) represents graphitic layers with ordered aromatic structure and (ii) D band (~1350 cm^{-1}) corresponds to amorphous carbon material with disordered aromatic structure, which confirms the presence of microcrystalline graphite or multilayer filamentous carbon fibers [77,147]. Fig. 7.1 represents the Raman spectra of fresh and spent $LaNi_{0.5}Co_{0.5}O_3$ catalyst at temperature 650 ^oC and 700 ^oC.

Raman spectra of spent catalysts obtained after experiments at temperature 650 °C and 700 °C, have shown D and G bands, which confirms the deposition of coke on the catalyst surface. The intensity of D and G bands for spent catalyst at 700 °C are greater than the spent catalyst obtained at 650 °C, which confirms that the coke deposition was more during reaction at 700 °C. Furthermore, the ratios of the intensity (I_D/I_G) of D and G bands ascribed to the dominance of deposited coke type on the catalyst surface. The I_D/I_G ratio was found 1.03 for spent catalyst obtained from the reaction at 650 °C, which indicated the dominance of less structured carbon material deposited on the catalyst surface. While, the I_D/I_G ratio for spent catalyst obtained from the reaction at 700 °C was 0.97, which confirmed the deactivation occurred mainly due to deposition of large amount of filamentous or graphitic carbon.

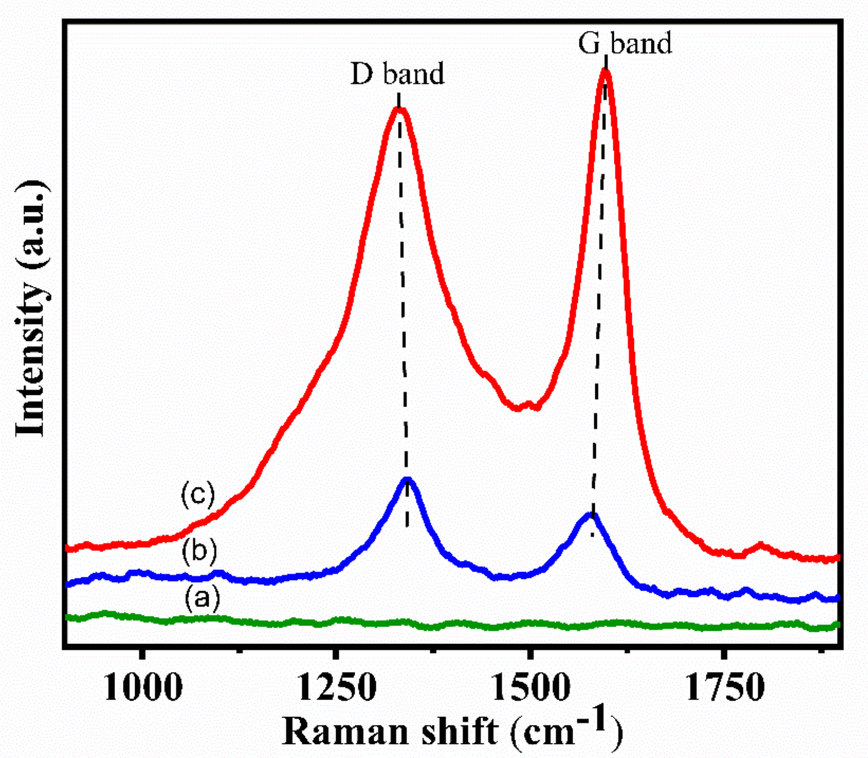

Fig. 7.1 Raman spectra of (a) fresh and spent $LaNi_{0.5}Co_{0.5}O_3$ perovskite catalyst at (b) 650 °C and (c) 700 °C reaction temperature

7.1.2 Surface morphology

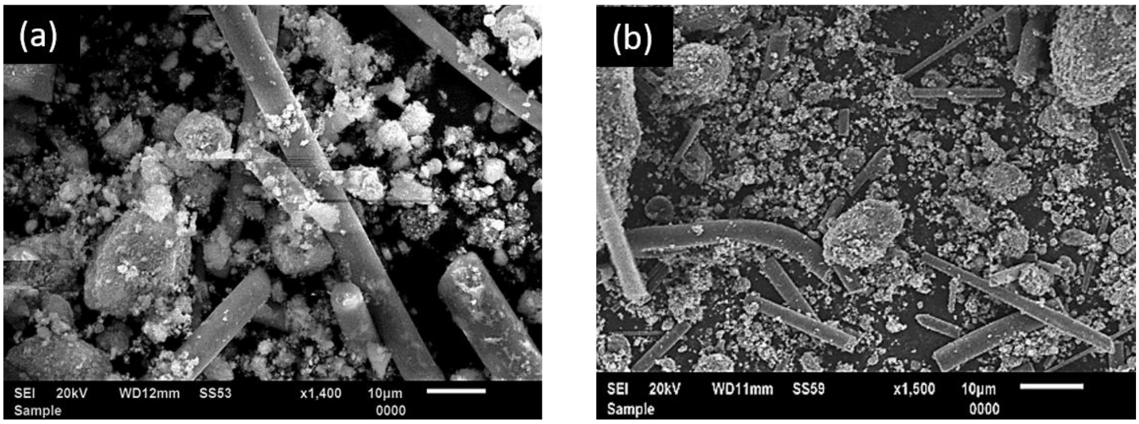
(a)
SEI 20kV WD12mm SS53 x1,400 10µm
Sample 0000
(b)
SEI 20kV WD11mm SS59 x1,500 10µm
Sample 0000

Fig. 7. 2 SEM images of spent perovskite $LaNi_{0.5}Co_{0.5}O_3$ catalyst (a) spent catalysts at 650 °C (b) spent catalyst at 700 °C

Further, the surface topology of the spent catalyst after SR process was analyzed by SEM technique. SEM images of the deactivated catalyst after SR process at 650 °C and 700 °C were shown in Fig. 7.2 (a) & (b). Coherently with Raman analysis, the SEM image of deactivated catalyst at 650 °C revealed the dominance of amorphous or less structured coke formation. In addition, the formation of filamentous carbon (small amount) with rod-like structure (diameter = 5-8 μm) on the catalyst surface was also observed, which does not fully cover surface of the active sites and hence porosity of the bed remains unaffected during the deactivation process [148]. These type of rods are also known as carbon-fibers; few researchers reported the formation of carbon fiberss during the catalytic SR of acetic acid and biomass tar using Ni-based catalyst [148–153]. However, the morphological image of used catalyst at 700 °C displayed the formation of large amount of structured/filamentous carbon along with formation of agglomerated coke distributed on catalyst surface, which covered the active sites and make it inaccessible for further reaction [7,46,133,152,154]. Moreover, the excess deposition of coke destroyed the porosity of the catalytic bed resulting in blockage of the reactor [95,155].

7.1.3 Thermogravimetric analysis

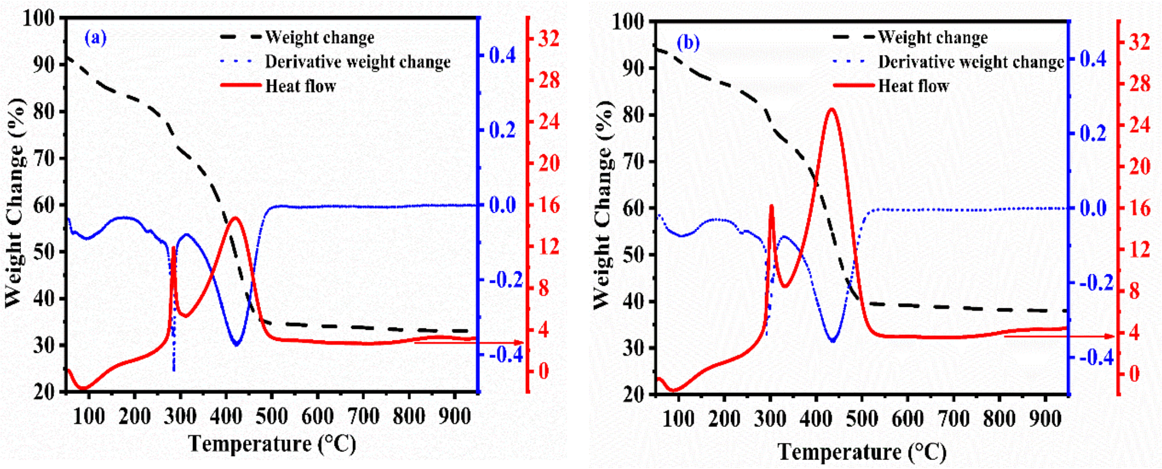

Fig. 7. 3 TG analysis of spent perovskite $LaNi_{0.5}Co_{0.5}O_3$ catalyst; (a) spent catalyst after 12 h TOS study at 650 °C, (b) spent catalyst after 6 h TOS study at 700 °C

The amount of coke deposited on the catalyst surface was calculated by TG analysis in the presence of air. TGA results revealed that major weight loss of spent catalyst was occurred in the temperature range of 200 °C to 500 °C as shown in Fig. 7.3 (a) & (b), which correspond to the formation of CO_2 gas, further confirming the presence of carbonaceous species. The coke deposition rate was found 125 $mg_{carbon}/(g_{cat}.h)$ for SR process at 650 °C temperature, whereas, at 700 °C, the massive increase in the rate of coke deposition (215 $mg_{carbon}/g_{cat}.h$) was observed. In addition, the same can be concluded from the increased rate of heat flow during TG analysis of spent catalyst at 700 °C because of the exothermic nature of carbon oxidation reaction (Fig. 8.3). Moreover, Nogueira *et al.* stated that the amorphous carbon oxidizes in the presence of air at low temperature (~300 °C) while graphitic carbon oxidizes at high temperature (~500 °C) [73]. Thus, from heat flow curves of TG analysis, it was observed that the formation of amorphous and structured/graphitic carbon was lesser for spent catalyst at 650 °C in comparison with spent catalyst at 700 °C, which is supported by the fact that a massive cracking of bio-oil compounds occurs at high temperature (700 °C).

Therefore, it can be concluded that the coke formation during SR process at 650 °C do not deactivate the whole catalyst rather partially covered the active sites. Whereas, the excessive coke formation at 700 °C (dominated by graphitic carbon) resulting in deactivation of the whole catalyst and hence, abolishing the porosity of the catalytic bed.

7.2 Catalyst deactivation study for simulated bio-oil 2 (SB2)

The spent catalyst obtained from the TOS study of the steam reforming of SB2 (discussed in section…, Chapter5), underwent a comprehensive analysis to ascertain the characteristics and quantity of deposits, as well as their effect on the catalyst bed and its activity in the steam reforming process. Ni based catalyst have been reported to prone to coke formation because of its acidic nature, which reduces the catalytic bed porosity as well as activity for steam reforming reactions. Therefore, for understanding the nature, amount and its effect on catalytic bed various analysis, XRD, TG, SEM and RAMAN analyses of the spent catalyst were performed.

7.2.1 RAMAN spectroscopy

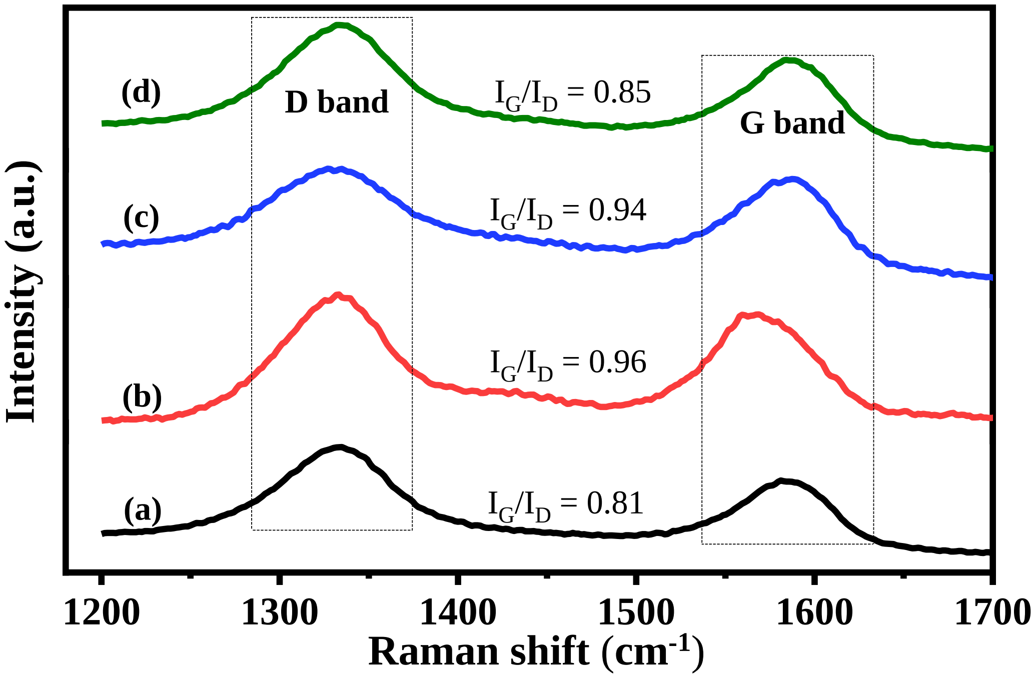

Fig. 7.4 Raman spectra of spent (a) $LaNiO_3$, (b) $LaNi_{0.5}Co_{0.5}O_3$, (c) $LaNi_{0.5}Fe_{0.5}O_3$ and (d) $LaNi_{0.5}Cu_{0.5}O_3$

The nature of coke was predicted from the Raman spectroscopy technique of spent perovskite catalysts. As shown in Fig.7.4, the Raman analysis was performed for the spent $LaNi_{0.5}M_{0.5}O_3$ (M= Ni, Co, Fe, and Cu) catalysts. All samples have shown two significant peaks located at: (a) 1350 cm^{-1} and (b) 1580cm^{-1} representing D and G bands, respectively. The D band in Raman analysis confirms the presence of less structured or amorphous carbonaceous species, whereas the G band is evidence of the formation of more structured or graphitic carbon [154]. Along with this, the degree of graphitization I_G/I_D (ratio of the intensity of G and D bands) was also computed to understand the dominance of the two different types of coke in the spent catalysts. The I_G/I_D was minimum for $LaNiO_3$ and after partial substitution of B- site element, an increasing trend was observed, and found to be a maximum 0.96 for $LaNi_{0.5}Co_{0.5}O_3$ catalyst. These results signify that the formation of structured graphitic carbon was maximum for $LaNi_{0.5}Co_{0.5}O_3$ catalyst, among other synthesized catalysts.

7.2.2 Surface morphology

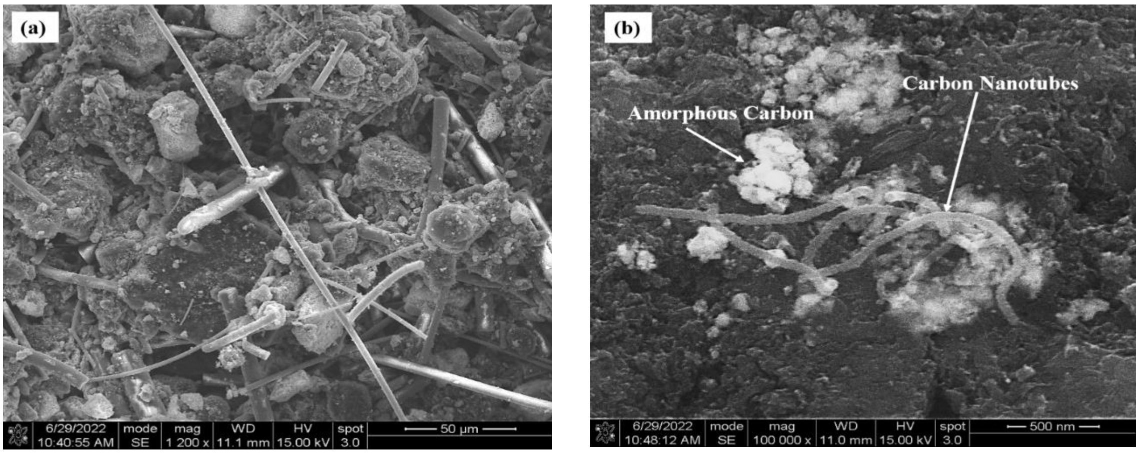

Fig. 7.5 FESEM images of spent perovskite $LaNi_{0.5}Co_{0.5}O_3$ catalyst captured at magnification of (a) 1200x(b) 100,000x

The FESEM analysis of spent $LaNi_{0.5}Co_{0.5}O_3$ catalyst obtained after 12 h TOS study was performed (Fig.7.5) at two different magnifications (1200x and 100,000x) to visualize the surface morphology as well as the coke. The formation of a large amount of graphitic or filamentous carbon and agglomerated amorphous carbon can be observed in Fig.7.5 (a). Furthermore, on increasing the magnification, the formation of carbon nanotubes (CNTs) of 80-90 nm also became evident (Fig. 7.5(b)). Researchers have reported that amorphous coke plays a major role in reducing the catalyst bed porosity as comparable to CNTs or graphitic coke [60,156,157]. Moreover, the amorphous coke blocks the metal active sites and leads to catalyst deactivation and resulting decrease in conversion and products yield. However, the filamentous coke grows as a tip growth which partially cover the active site and less affect the catalytic activity as compare with amorphous coke. The coke generated during the bio-oil steam reforming reactions is mainly responsible for the catalyst deactivation which may lead to reactor blockage after long hour run. However, there was no blockage observed in the present study during TOS.

7.2.3 XRD analysis

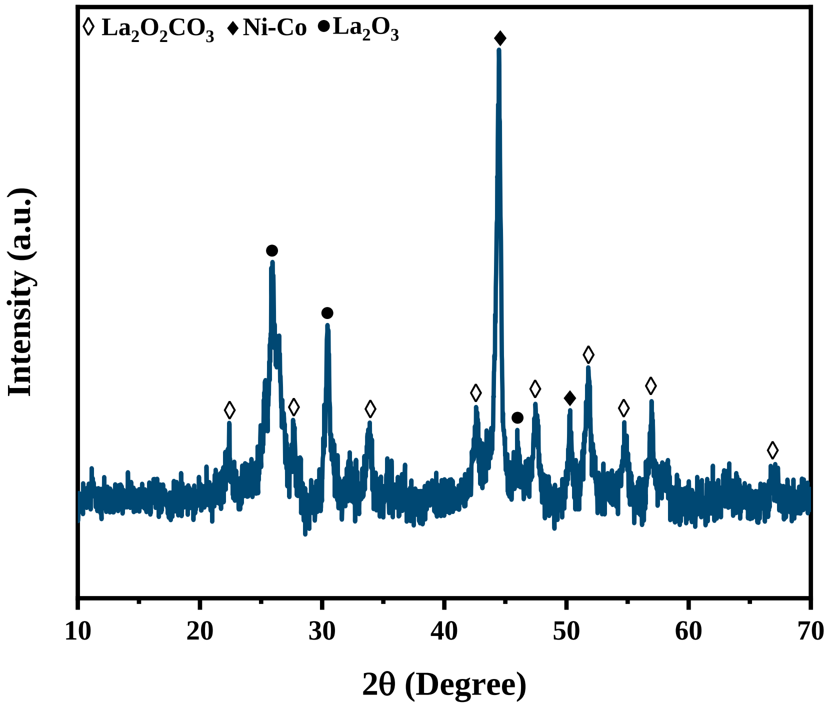

Fig. 7.6 XRD diffractogram of spent perovskite $LaNi_{0.5}Co_{0.5}O_3$ catalyst

Fig. 7.6 displays the XRD pattern of the spent $LaNi_{0.5}Co_{0.5}O_3$ catalyst obtained after TOS study. The diffractogram exhibited peaks corresponding to Ni-Co bimetallic alloy at 2θ values of 44.5° and 51.4°, as well as those corresponding to La_2O_3, which is in good agreement with the XRD analysis of freshly reduced $LaNi_{0.5}Co_{0.5}O_3$ Besides these, peaks corresponding to the hexagonal phase of $La_2O_2CO_3$ at 2θ values of 22.3°, 27.6°, 33.8°, 42.6°, 47.5°, 51.8°, 54.7°, 57° and 67° were noted to have emerged [118,158]. The emergence of peaks corresponding to this phase can be attributed to the ability of rare earth metal oxides such as La_2O_3 to maintain catalyst structure and react with the CO_2 being generated to form $La_2O_2CO_3$. In turn, this new phase plays an important role in suppressing coke formation on active metal sites by providing oxygen species to the deposited carbon, which gets removed as CO_2, while $La_2O_2CO_3$ gets reduced to La_2O_3 [77,159]. Besides Ni metal, the acidity and/or basic nature of the support material has also been known to play an important role in coke formation. While supports such as Al_2O_3 actively promote the formation of coke owing to the presence of highly acidic sites, materials such as La_2O_3, CeO_2, MgO, etc. retard coke formation due to their inherently basic nature and the presence of oxygen vacancies [160]. Consequently, the prolonged stability displayed by the catalyst over the course of the TOS study indicates reduced coke formation which in turn could ascribed to the basic nature of La_2O_3 and the presence of oxygen vacancies.

7.2.4 Thermogravimetric analysis

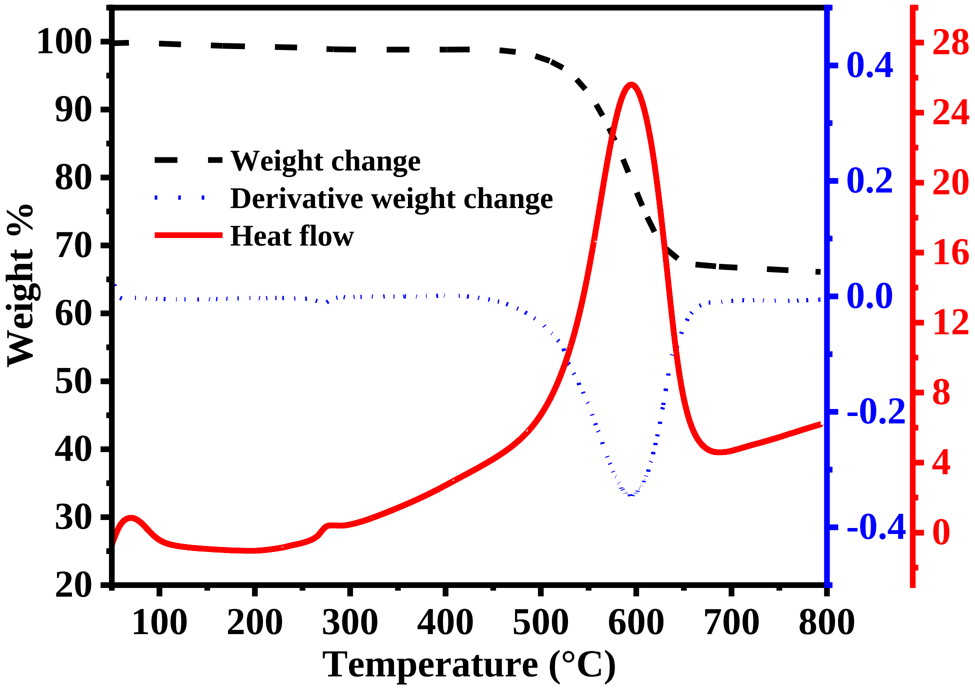

Fig. 7.7 TG analysis of spent perovskite $LaNi_{0.5}Co_{0.5}O_3$ catalyst

Furthermore, the quantitate analysis of coke deposited on the catalyst surface was performed by TG analysis of spent catalyst under constant air flow. He et al.[152] discussed in detail about the coke deposited on catalytic surface in reforming reaction. The carbonaceous species present in the spent catalyst is of different types such as amorphous/disordered coke and graphitic/structured coke. These carbonaceous species start oxidizing under air at 300-700 °C and the oxidizing temperature depends on the nature of the coke. Li et al.[153] also discussed the nature of coke and the temperature required for its oxidization for different bio-oil model compounds in reforming reactions. In our previous study [70], a comparative evaluation was conducted to gain insight about the nature and amount of coke for simulated bio-oil steam reforming reaction at different temperatures. Valle et al.[157] reported that the amorphous carbon oxidize at low temperature (less than 500 °C), while the filamentous carbon oxidize at higher temperature (above 500 °C). Here, as displayed in the Fig. 7.7 it can be observed that the major weight loss occurred at 450 – 650 °C, which is slightly higher than the previous study (section 7.1.3). This increase in coke oxidation temperature signifies the formation of more structured carbonaceous species. Furthermore, the coke deposition rate was also computed and found to be 41.9 mg_{carbon} $(g_{cat}.h)^{-1}$, with the rate of formation of amorphous coke being 8.03 mg_{carbon} $(g_{cat}.h)^{-1}$ and that of graphitic coke being 33.87 mg_{carbon} $(g_{cat}.h)^{-1}$. Thereby, it can also be concluded that the bio-oil model compounds and the reaction temperature both play an important role on nature of the coke formed during reforming reaction.

7.3 Catalyst deactivation study for raw bio-oil reforming

Following the catalyst deactivation study for simulated bio-oil (SB1 & SB2) steam reforming, the spent catalyst obtained after steam reforming with raw bio-oil was also analysed. This investigation aimed to provide insights into the underlying mechanisms of catalyst deactivation and to inform strategies for mitigating coke formation and improving catalyst performance for scaling up this process.

7.3.1 RAMAN spectroscopy

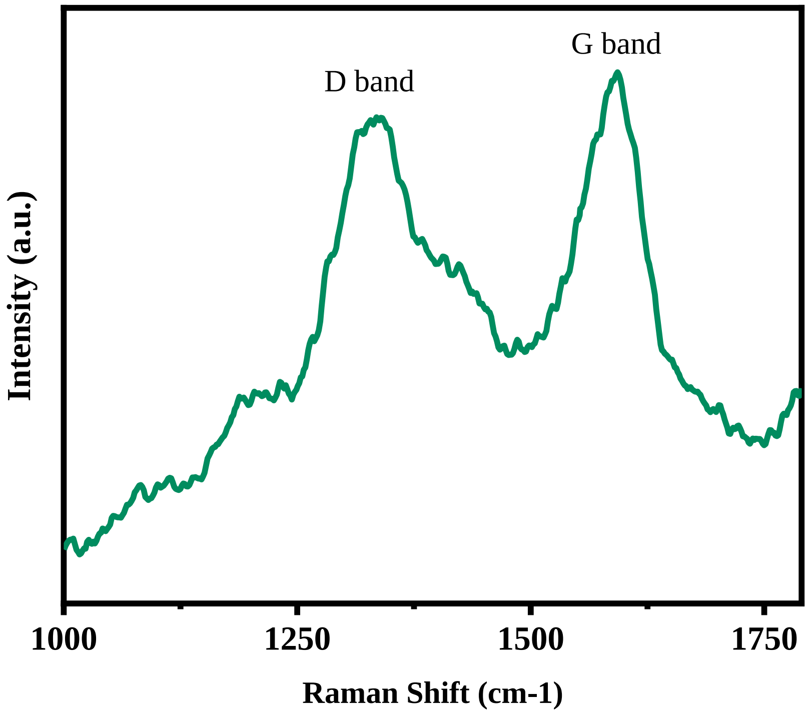

Fig. 7.8 Raman spectra of spent $LaNi_{0.5}Co_{0.5}O_3$ catalyst after raw bio-oil reforming

Figure 7.8 presents the Raman spectra of the spent LaNi0.5Co0.5O3 catalyst, obtained from the study of the deactivation behaviour (TOS) of this catalyst. The purpose of this analysis was to investigate the nature of the coke deposits on the catalyst surface. The results showed that the presence of graphitic carbon was more abundant than encapsulating or disordered coke on the catalyst surface. Additionally, the degree of graphitization (I_G/I_D), which measures the relative proportion of graphitic and disordered carbon in the coke deposits, was calculated and found to be 1.05, indicating that graphitic or more structured carbon was dominant. These results are in good agreement with the other studies performed in this direction [46,124,133].

7.3.2 Surface morphology

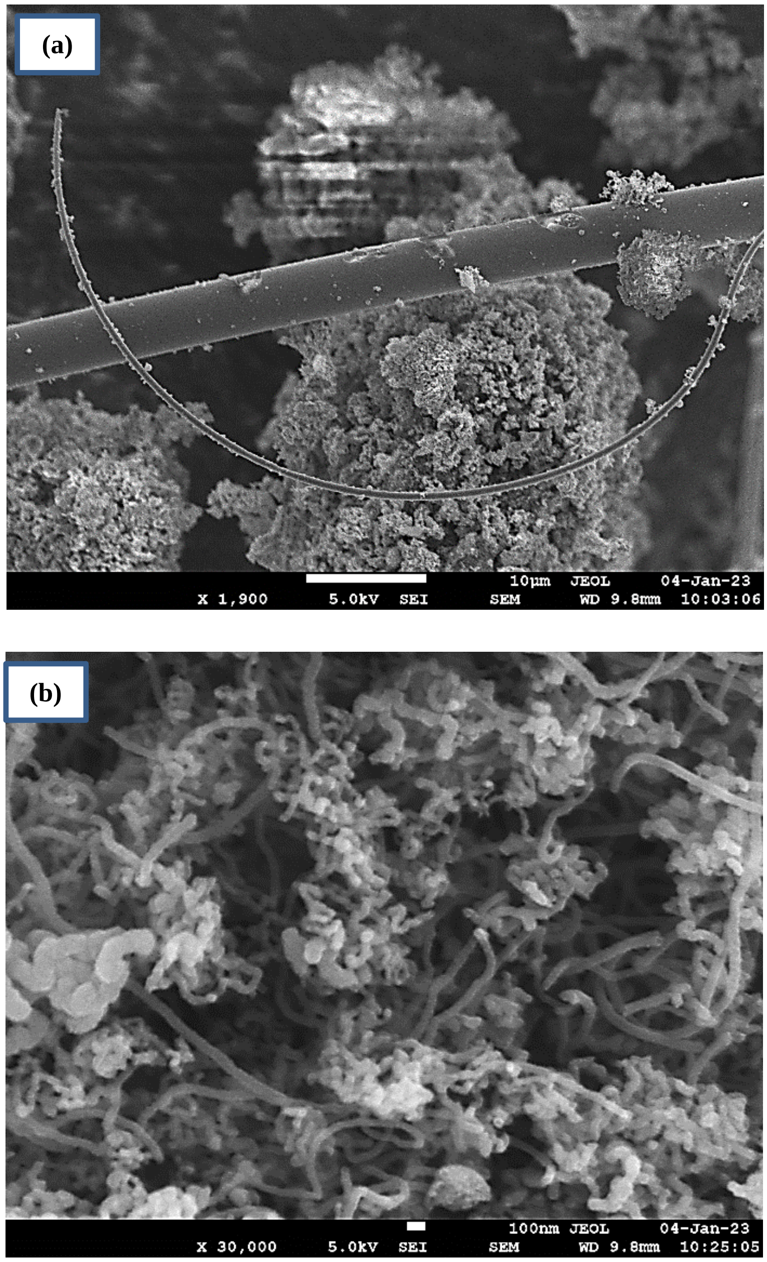
(a)
10µm JEOL 04-Jan-23
X 1,900 5.0kV SEI SEM WD 9.8mm 10:03:06
(b)
100nm JEOL 04-Jan-23
X 30,000 5.0kV SEI SEM WD 9.8mm 10:25:05

Fig. 7.9 FESEM images of spent perovskite $LaNi_{0.5}Co_{0.5}O_3$ catalyst captured at magnification of (a) 1900x(b) 30,000x

The morphology and composition of the coke deposits on the spent $LaNi_{0.5}Co_{0.5}O_3$ catalyst were analysed in detail using FESEM analysis. The analysis was conducted after a 12 h steam reforming experiment with raw bio-oil. As shown in Figure 7.9, the analysis was performed at two different magnifications (1900x and 30,000x). The results showed that the catalyst surface was covered with a significant amount of graphitic or filamentous carbon and agglomerated amorphous carbon. The results of the Raman analysis, as presented in Fig. 7.8, showed that the majority of the coke deposits on the spent catalyst was graphitic in nature. This was further confirmed by the observation of a large number of carbon nanotubes (CNTs) in the FESEM analysis, as shown in Fig. 7.9(b). The presence of CNTs is an indication of graphitic coke, which has a well-ordered, crystalline structure. This result highlights the importance of understanding the nature of coke deposits and their impact on catalyst performance, as different types of coke can have varying effects on catalyst activity and stability. The presence of graphitic coke, in particular, is significant as it is known to have a lesser impact on catalytic activity as compared to other forms of coke. This information can be useful for developing strategies to mitigate coke formation and improve catalyst performance for bio-oil steam reforming processes.

In conclusion, the FESEM and RAMAN analysis provide valuable insights into the nature and amount of coke deposits on the spent catalyst, which can inform strategies for mitigating coke formation and improving catalyst performance. A better understanding of the mechanisms of catalyst deactivation will be critical for the scaling-up of steam reforming processes for bio-oil upgrading.

Chapter 8: Advanced steam reforming processes

This chapter presents the thermodynamic potential of H_2 production via different bio-oil steam reforming processes. The purpose of the study was to assess the conventional bio-oil steam reforming process and identify areas for improvement. In this regard, two potential avenues for intensification were identified. First was the utilisation of a simulated bio-oil mixture comprising model compounds from major oxygenate families in order to take into account the chemical complexity of actual bio-oil. The second was incorporating advanced technologies – in-situ CO_2 capture, chemical looping and combined CO_2 capture-looping – into conventional technology. Here, CaO was selected as the sorbent while NiO was the selected oxygen carrier. A thorough evaluation was carried out for the three advanced reforming processes and the results obtained were compared against those of conventional steam reforming, which served as the benchmark. The performance of all four processes were compared in terms of H_2 yield and selectivity as well as required energy for each process. The results obtained were subsequently used to throw light on the most appealing features and drawbacks of each process. In the end, some possible avenues for future work were also mentioned. Given the highly endothermic nature and significant carbon footprint of the current steam reforming process, by far the most important issue addressed in this study is how H_2 could be produced from bio-oil economically with minimal environmental footprint.

8.1 Simulation Methodology

The bio-oil obtained from the pyrolysis of agricultural residues such as rice husk and straw contains oxygenates like acids, phenols, ketones, furans etc., resulting a very complex and unstable mixture. The simulated bio-oil used in the present study is a mixture of representative of major oxygenates present in the bio-oil, as reported by several pyrolysis studies [98,141]. The selected model compounds and their mass fraction in the simulated bio-oil are reported in Table 1.

Table 8.1 List of model compounds, oxygenates family and their mass fraction used in the present study

Model Compound	Oxygenate Family	Mass Fraction in Bio-oil (%)
Acetic Acid	Acids	22.53
Hydroxyacetone	Ketones	18.30
Levoglucosan	Anhydrosugars	4.22
Vanillin	Substituted phenols	7.04
p-Cresol	Substituted phenols	7.04
Furfural	Furans	14.08
Guaiacol	Methoxyphenols	9.85
Phenol	Phenols	14.08
Toluene	Hydrocarbons	2.86

Here, the four different processes for hydrogen production from bio-oil were modeled and/or explored: conventional steam reforming (CSR), and three advanced reforming processes namely sorption-enhanced steam reforming (SESR), chemical looping steam reforming (CLSR), and sorption-enhanced chemical looping steam reforming (SE-CLSR). The simulation of the processes was carried out using the Aspen Plus simulation package. For CSR process, Soave-Redlich-Kwong (SRK) equation of state was used as the thermodynamic package. Meanwhile, for SESR, CLSR, and CL-SESR processes, a SOLIDS model with ESSRK as the thermodynamics package was used due to the presence of solids. Heating and/or cooling of reactants and/or product streams were modeled using a HEATER model. RGIBBS model was used for simulating reforming reactor as well as SORBENT and OTM regeneration reactors while fluid-solid separation was simulated by a CYCLONE model.

H_2, CO, CO_2, CH_4, H_2O, CaO, NiO, $CaCO_3$, Ni, N_2 and O_2 were considered as possible products for the processes under consideration. To account for coke formation during reforming, graphite was considered as one of the possible products. Formation of any other compounds was assumed to be unfavourable from a thermodynamic viewpoint at the relevant operating conditions. It was assumed that the reactivity and structure of the sorbent and the oxygen carrier remained unchanged with recurring cyclic operation.

Additionally, particle size distribution was assumed to have no bearing on the activity of the solids. Lastly, it was assumed that there was no pressure and heat loss in any of the units.

8.1.1 Process description of conventional and advanced reforming processes

In the CSR process (Fig. 8.1), bio-oil and water streams were first mixed (MX-01) to generate a feed stream which was then heated to the reaction temperature using a heat exchanger (HE-01). Following this, the vaporised feed stream was fed to the reforming reactor (RCTR) where the bio-oil was converted to an H_2-rich gaseous mixture via reactions mentioned in Eq. 8.1-8.4. While these equations represent the major reactions taking place during the process, some side reactions such as methanation, Boudard and coke formation reactions may also take place alongside them [161–163]. Subsequently, the produced gas was cooled down by passing it through a heat exchanger (HE-02).

For advanced reforming processes, besides the feed stream containing bio-oil and water, a second input stream consisting of solids – SORBENT for SESR, OTM for CLSR and a combined SORBENT + OTM for SE-CLSR - was also fed to the reforming reactor RCTR after being heated to reaction temperature using a heat exchanger. The presence of CaO results in in-situ CO_2 capture during the reaction, shifting the chemical equilibrium and resulting in enhanced H_2 selectivity and purity. Moreover, CO_2 capture also releases some heat which lowers the energy demand of the reforming reactor. Meanwhile, OTM (NiO) acts as a source of oxygen for partial oxidation of the feed, releasing heat and again lowering the energy demand for reforming. In the reforming reactor, steam reforming reactions take place alongside those involving CaO and/or NiO. Following the reaction, the gaseous and solid products were separated using a cyclone separator (CYCLONE). The gaseous products were passed through a heat exchanger to obtain cooled products (PRODUCTS). The solid products consisting of spent sorbent and/or reduced oxygen carrier were transported to CALCINE and OXIDISE reactors, respectively, where they underwent regeneration. For SE-CLSR process, the solid stream containing spent solids was first separated into two separate streams containing the spent sorbent and oxygen carrier, which were then regenerated in two separate reactors. In CALCINE reactor, the spent SORBENT present in the form of $CaCO_3$ was heated at high temperature, resulting in the desorption of CO_2 and the formation of CaO. Meanwhile, the reduced OTM was regenerated by oxidation using air as the oxidant in the OXIDIZE reactor. The regenerated solids were then heated and/or cooled down to the reformer temperature using a heat exchanger and were then recycled back to the reformer. The WASTE GAS generated during the regeneration of the solids was cooled down before being discharged. Fig. 8.2,8.3 and 8.4 represent the process flow diagrams for the proposed SESR, CLSR and SE-CLSR processes, respectively [161–163].

Bio-oil Steam Reforming Reaction

$$C_nH_mO_k + (n-k)H_2O \rightarrow n\,CO + \left(n + \frac{m}{2} - k\right)H_2 \qquad (8.1)$$

Water Gas Shift (WGS) Reaction

$$CO + H_2O \leftrightarrow CO_2 + H_2 \qquad (8.2)$$

Global Steam Reforming Reaction

$$C_nH_mO_k + (2n-k)H_2O \rightarrow \left(2n + \frac{m}{2} - k\right)H_2 + nCO_2 \qquad (8.3)$$

Methane Steam Reforming Reaction

$$CH_4 + H_2O \leftrightarrow CO + 3H_2 \qquad (8.4)$$

Methanation Reactions

$$CO + 3H_2 \leftrightarrow CH_4 + H_2O \qquad (8.5)$$

$$CO_2 + 4H_2 \leftrightarrow CH_4 + 2H_2O \qquad (8.6)$$

Boudard Reaction

$$2CO \leftrightarrow C\ (s)\ + CO_2 \qquad (8.7)$$

Methane Decomposition Reaction

$$CH_4 \leftrightarrow C\ (s) + 2H_2 \qquad (8.8)$$

Carbon Oxides Decomposition Reactions

$$CO + H_2 \leftrightarrow C + H_2O \qquad (8.9)$$

$$CO_2 + 2H_2 \leftrightarrow C + 2H_2O \tag{8.10}$$

Carbonation Reaction

$$CaO\ (s) + CO_2 \rightarrow CaCO_3\ (s) \qquad \Delta H_r^{298} = -177.8\ kJ\ mol^{-1} \tag{8.11}$$

Sorption-Enhanced Steam Reforming (SESR)

$$C_nH_mO_k + (2n-k)H_2O + nCaO \rightarrow \left(2n + \frac{m}{2} - k\right)H_2 + nCaCO_3 \tag{8.12}$$

Oxidation of Hydrogen

$$NiO\ (s) + H_2 \leftrightarrow Ni(s) + H_2O \qquad \Delta H_r^{298} = -1.83\ kJ\ mol^{-1} \tag{8.13}$$

Oxidation of Carbon Monoxide

$$NiO\ (s) + CO \leftrightarrow Ni(s) + CO_2 \qquad \Delta H_r^{298} = -42.98\ kJ\ mol^{-1} \tag{8.14}$$

Oxidation of Methane

$$CH_4 + NiO \leftrightarrow CO + Ni + 2H_2 \qquad \Delta H_r^{298} = 204\ kJ\ mol^{-1} \tag{8.15}$$

Partial Oxidation of Bio-oil

$$C_nH_mO_k + (n-k)NiO \rightarrow (n-k)Ni + nCO + \frac{m}{2}H_2 \tag{8.16}$$

Complete Oxidation of Bio-oil

$$C_nH_mO_k + \left(2n + \frac{m}{2} - k\right)NiO \rightarrow \left(2n + \frac{m}{2} - k\right)Ni + nCO_2 + \frac{m}{2}H_2O \tag{8.17}$$

Chemical Looping Steam Reforming (CLSR)

$$C_nH_mO_k + \left(n - \frac{2k}{3}\right)NiO + \left(n - \frac{k}{3}\right)H_2O \rightarrow \left(n - \frac{2k}{3}\right)Ni + nCO_2$$

$$+ (n + \frac{m}{2} - \frac{k}{3})H_2 \tag{8.18}$$

Sorption-Enhanced Chemical Looping Steam Reforming (SE-CLSR)

$$C_nH_mO_k + \left(n - \frac{2k}{3}\right)NiO + \left(n - \frac{k}{3}\right)H_2O + nCaO \rightarrow \left(n - \frac{2k}{3}\right)Ni + nCaCO_3$$

$$+(n+\frac{m}{2}-\frac{k}{3})H_2 \qquad (8.19)$$

Sorbent Regeneration/Calcination

$$CaCO_3(s) \rightarrow CaO\ (s) + CO_2 \qquad \Delta H_r^{298} = 177.8\ kJ\ mol^{-1} \qquad (8.20)$$

OTM Regeneration/Oxidation

$$Ni\ (s) + 0.5O_2 \rightarrow NiO\ (s) \qquad \Delta H_r^{298} = -240\ kJ\ mol^{-1} \qquad (8.21)$$

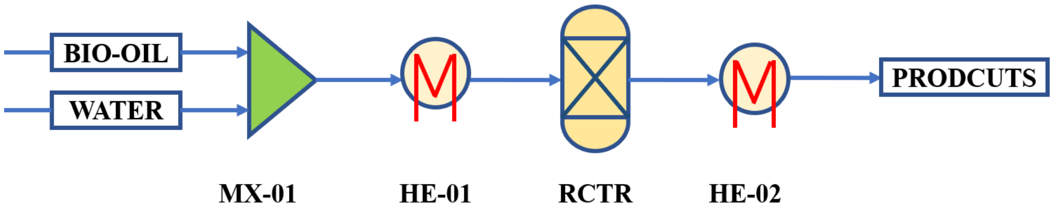
BIO-OIL
WATER
PRODCUTS
MX-01
HE-01
RCTR
HE-02

Fig. 8.1 Process flowsheet for the proposed CSR process

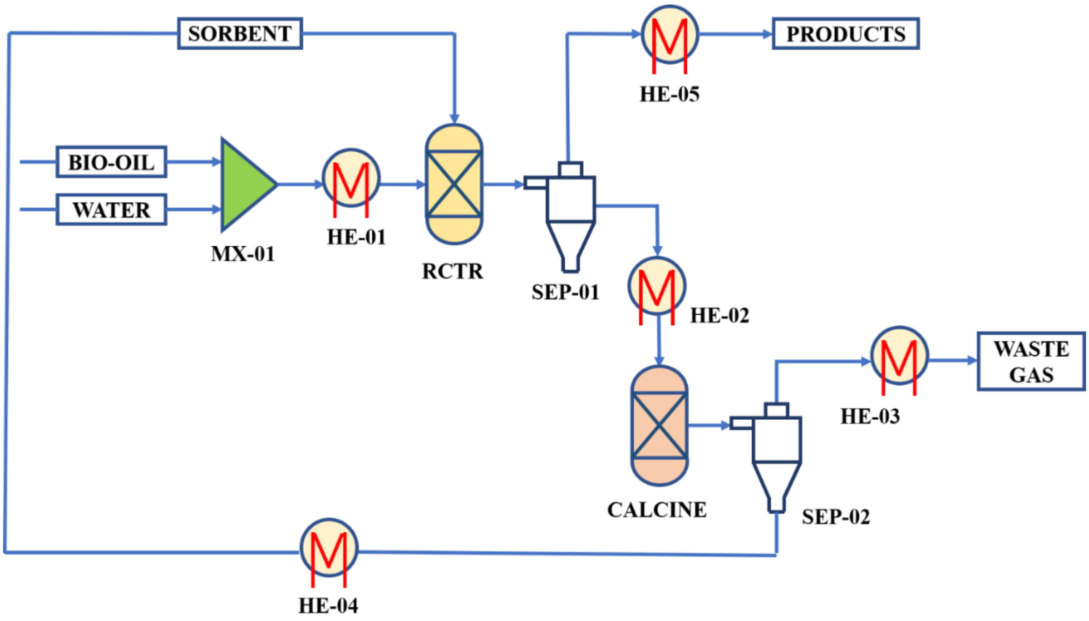
SORBENT
PRODUCTS
HE-05
BIO-OIL
WATER
MX-01
HE-01
RCTR
SEP-01
HE-02
WASTE GAS
HE-03
CALCINE
SEP-02
HE-04

Fig. 8.2 Process flowsheet for the proposed SESR process

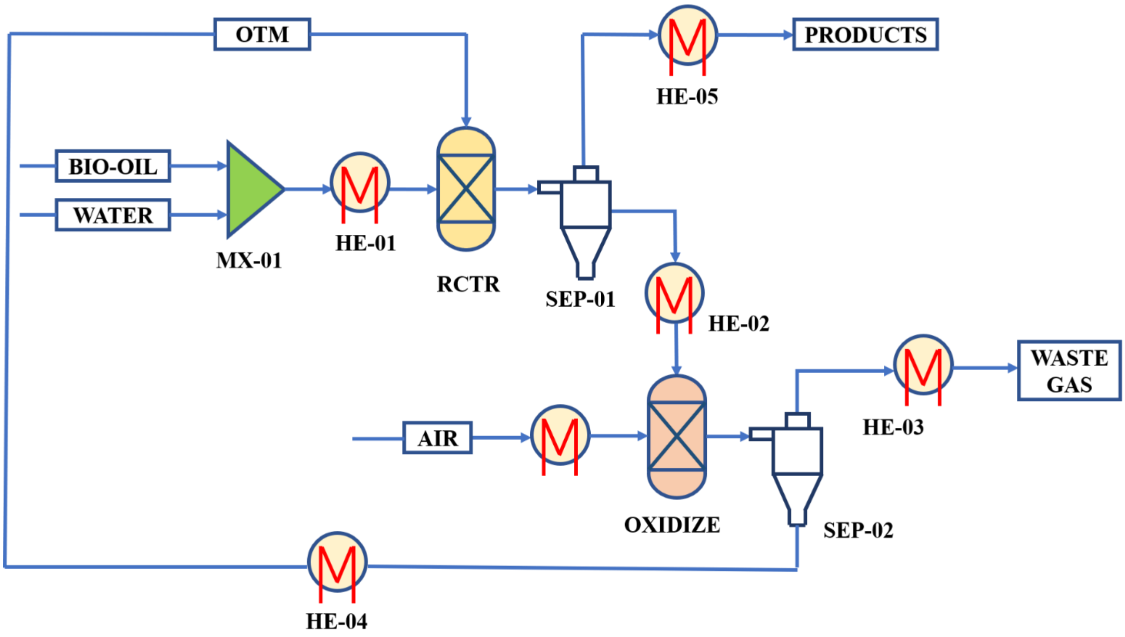
OTM
PRODUCTS
HE-05
BIO-OIL
WATER
MX-01
HE-01
RCTR
SEP-01
HE-02
WASTE GAS
HE-03
AIR
OXIDIZE
SEP-02
HE-04

Fig. 8.3 Process flowsheet for the proposed CLSR process

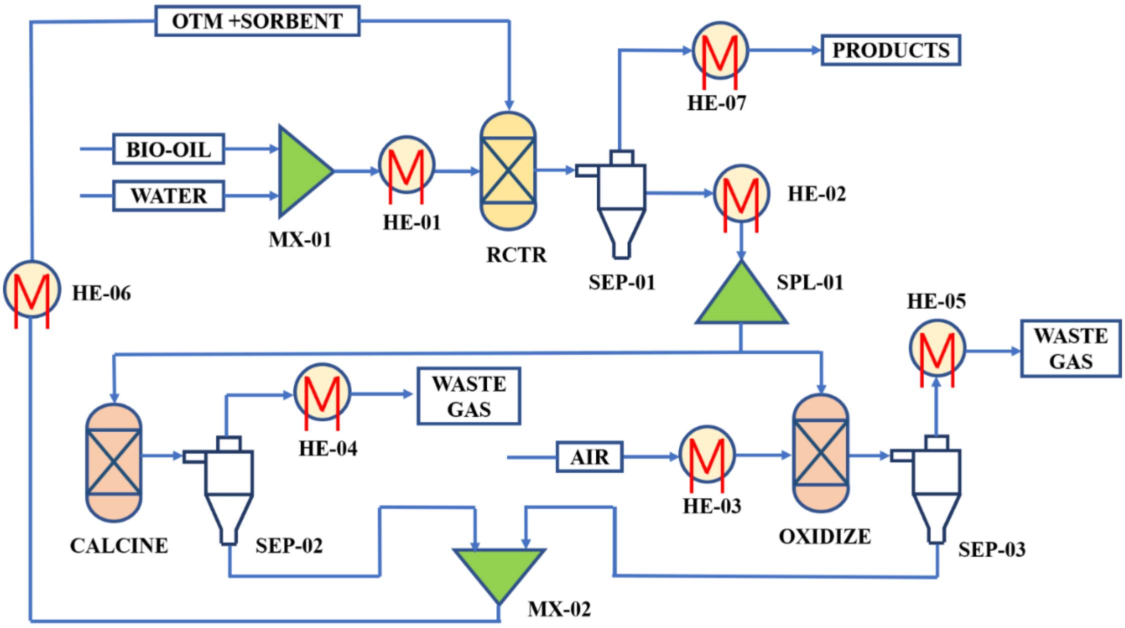
OTM +SORBENT
PRODUCTS
HE-07
BIO-OIL
WATER
MX-01
HE-01
RCTR
SEP-01
HE-02
SPL-01
HE-06
HE-05
WASTE GAS
WASTE GAS
HE-04
AIR
HE-03
OXIDIZE
CALCINE
SEP-02
SEP-03
MX-02

Fig. 8.4 Process flowsheet for the proposed SE-CLSR process

8.1.2 Methods of data processing

To evaluate and compare the performance of conventional as well as advanced reforming processes, the following parameters were utilised:

Product Selectivity and/or Concentration

$$\text{Selectivity and/or concentration of species i (mol\%, dry basis)} = \frac{\text{moles of product i formed}}{\text{Total moles of gaseous products formed}} \text{ x } 100 \qquad (8.22)$$

Where, the term gaseous products refer to CO, CO_2, CH_4 and H_2.

Hydrogen Yield

$$\text{Hydrogen Yield} = \frac{\text{Mass of Hydrogen produced}}{\text{Mass of bio-oil fed}} \left(\frac{kg_{H_2}}{kg_{bio-oil}}\right) \qquad (8.23)$$

Energy Demand

$$Q_{D,RR/Bio-oil} = \frac{\text{Heat duty of reforming reactor}}{\text{Moles of bio-oil fed}} \left(\frac{MJ}{kmol}\right) \qquad (8.24)$$

$$Q_{D,net/Bio-oil} = \frac{\text{Net heat duty of the process}}{\text{Moles of bio-oil fed}} \left(\frac{MJ}{kmol}\right) \qquad (8.25)$$

$$Q_{D,net/H2} = \frac{\text{Net heat duty of the process}}{\text{Moles of Hydrogen produced}} \left(\frac{MJ}{kmol}\right) \qquad (8.26)$$

For the purpose of determining the net energy demand of a process, only the heat duties of the major equipment such as reforming reactor, heat exchangers to heat and/or cool the reactant and product streams and the solids, and regeneration reactors was considered. Accordingly, the energy demand for equipment separating solids and gases and downstream H_2 purification unit was ignored.

8.2 Thermodynamic evaluation of different SR processes

In the present study, CSR process serves as the benchmark against which the advanced reforming processes – SESR, CLSR and SE-CLSR - were compared. Accordingly, the effect of important process parameters such as steam to carbon molar ratio (SCMR), reforming temperature, sorbent to carbon ratio and oxygen carrier to carbon ratio was investigated to arrive at a set of process conditions that provided the highest H_2 yield and selectivity. In addition, the energy demand of the proposed processes was also taken into consideration. In all the processes under consideration, bio-oil was observed to have undergo complete conversion. As a result, the outlet stream from the reactor consisted of H_2, CO, CO_2, CH_4, and spent sorbent and oxygen carrier.

8.2.1 Conventional steam reforming (CSR) process

Fig. 8.5 displays the effect of steam to carbon molar ratio (SCMR and/or S/C) on product distribution as well as energy demand and H_2 yield. At low S/C values, particularly at SCMR = 1, significant amount of coke formation was noted. Moreover, CH_4 and CO formation was also observed in significant amount, as a consequence of which the selectivity of H_2 and CO_2 in the product stream was smaller (Fig. 8.5(a)). However, on increasing the SCMR, the concentration of coke, and CH_4 start decreasing due to domination of bio-oil steam reforming, and methane steam reforming reactions, respectively over decomposition reaction [164]. Subsequently, the CO formed reacts with steam via WGS reaction (Eq. 2) to yield H_2 and CO_2, which explains the low final CO selectivity. These observations suggest that low S/C values were not conducive for SR reactions but were instead favourable for decomposition reactions [161,162,164–166]. It can be seen from Fig. 5(a) that H_2 selectivity rises initially as the S/C value is increased from 1 to 5 and then plateaus beyond this value. A similar trend was also observed for CO_2 selectivity, which also became nearly constant at S/C > 5. However, increasing the SCMR beyond 5 didn't result in much change in the selectivity of H_2, which was found to increase by just 1.5% as the S/C ratio doubled from 5 to 10. The selectivities of CO_2 and CO also exhibited a similar trend, remaining nearly constant at S/C values greater than 5. While increasing SCMR value beyond 5 had little effect on H_2 selectivity, the same cannot be said for the overall energy demand of the process. It is clear from Fig. 5(b) that $Q_{D,\ net/Bio\text{-}oil}$ and $Q_{D,\ net/H2}$, which represent the net energy demand of the process per unit mole of bio-oil feed fed and per unit mole of H_2 produced respectively, exhibited an almost linear increasing trend with SCMR values. Doubling the S/C ratio from 5 to 10 led to $Q_{D,\ net/Bio\text{-}oil}$ and $Q_{D,\ net/H2}$ values increasing from 1328.5 MJ $kmol_{Bio\text{-}oil}^{-1}$ and 159.5 MJ $kmol_{H2}^{-1}$ to 2335.8 MJ $kmol_{Bio\text{-}oil}^{-1}$ and 262.3 MJ $kmol_{H2}^{-1}$ respectively, which corresponds to an increment of 75.8% and 64.5%, respectively. Such a large increase in energy consumption could be ascribed to the huge amount of energy required for heating the reactants. Meanwhile, the H_2 yield, which denotes the amount of H_2 produced per kg of bio-oil fed, only rose by 6.9% from 0.194 $kg_{H2}\ kg_{Bio\text{-}oil}^{-1}$ to 0.208 $kg_{H2}\ kg_{Bio\text{-}oil}^{-1}$. Consequently, it is safe to conclude that using SCMR values results in a massive energy demand, outweighing the increment in amount of H_2 that can be produced and thereby, making the process inviable from an economic standpoint. Accordingly, an SCMR value of 5 was used for carrying out further studies.

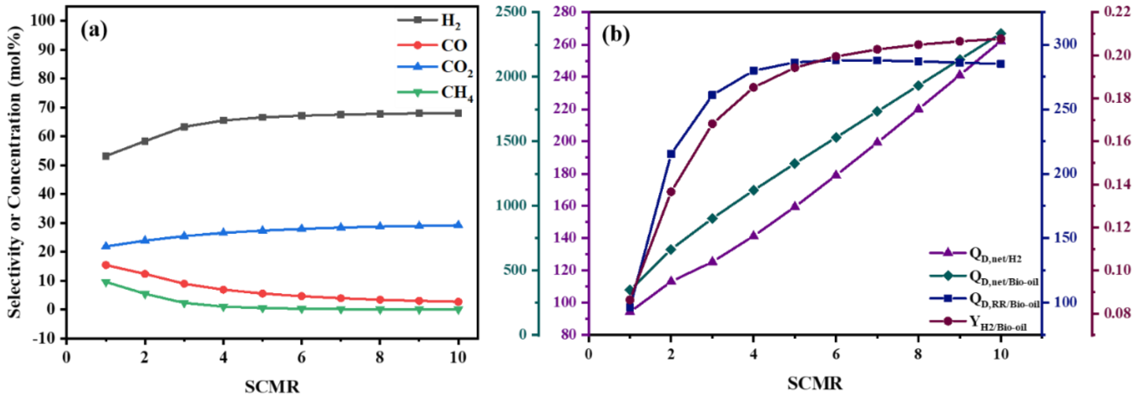

Fig. 8.5 Effect of SCMR on (a) product selectivity and (b) energy demands (MJ kmol$_{H2}$-1 and MJ kmol$_{Bio\text{-}oil}$-1) and H_2 yield (kg$_{H2}$ kg$_{Bio\text{-}oil}$-1) in CSR process

Much like the SCMR value, the reaction temperature also has a huge effect on the product distribution, as can be seen from Fig. 8.6. At the lower end of the investigated temperature range, H_2 selectivity was found to be quite low (42.1%). CH_4 was found to be present in significant amount in the product stream with a 21.5% selectivity, while CO formation was negligible. At temperatures on the lower end of the investigated range (~ 400 °C), methanation reactions (Eq. 4 and 5) which consume H_2 are favoured [162,164], explaining the low H_2 yield and selectivity. H_2 selectivity increased as the temperature rose from 400 °C and flattened out at 600 °C; simultaneously, CH_4 selectivity started declining and became zero at 600 °C. Increased formation of H_2 was accompanied by CO formation in increasingly larger amounts as the temperature rose from 400 to 600 °C, as can be seen in Fig. 6. Increasing the temperature beyond 600 °C did not lead to any increase in H_2 selectivity; instead, it remained nearly constant until 650 °C and then started decreasing as the temperature rose further beyond 700 °C [162,166]. On the other hand, CO formation was noted to have accelerated, with its selectivity increasing rapidly as temperature increased beyond 600 °C. The above observations can be explained by the fact that with increasing temperatures, H_2 consumption via methanation reaction is diminished; however, H_2 production from WGS reaction is also diminished since it is exothermic in nature [162,164,166]. The H_2 saved from reduced methane formation compensates the reduced H_2 formation from WGS reaction, as a result of which H_2 selectivity continued to increase and reach a maximum at a certain temperature (600 °C). However, beyond this temperature, methane formation is practically negligible while reverse WGS reaction becomes more and more favourable, resulting in H_2 consumption and thereby leading to reduced selectivity. With respect to the energy demands, it is evident from Fig. 6b that utilisation of high temperatures in the reformer resulted in higher energy demands ($Q_{D, net/Bio-oil}$ and $Q_{D, RR/Bio-oil}$). The high energy demands are obvious given that massive amounts of energy would be required to raise the reactants to reformer temperature. Meanwhile, the energy demand per mole of H_2 produced ($Q_{D, net/H2}$) was the highest at lower temperatures and decreased to a minimum with increasing temperatures in the range of 550-600 °C. With further increase in reformer temperature beyond 600 °C, the value of $Q_{D, net/H2}$ again rose sharply. This can be attributed to the fact that H_2 yield is quite low at lower temperatures due to methanation reaction (Fig. 6b), as a result of which $Q_{D, net/H2}$ is very high. With increasing temperatures, the H_2 yield rises rapidly, bringing down the energy required to produce a single mole of H_2. At very high temperatures, the H_2 yield falls again due to its consumption in reverse WGS reaction, as a consequence of which the energy demand $Q_{D, net/H2}$ rises once again. It can be inferred from the above discussion that neither very low temperatures nor very high temperatures are conducive for H_2 production and that the highest yields are obtained at moderate temperatures. Consequently, the reaction temperature of 600 °C was used for carrying out further investigations since highest H_2 yield was obtained at this temperature with the lowest energy demands.

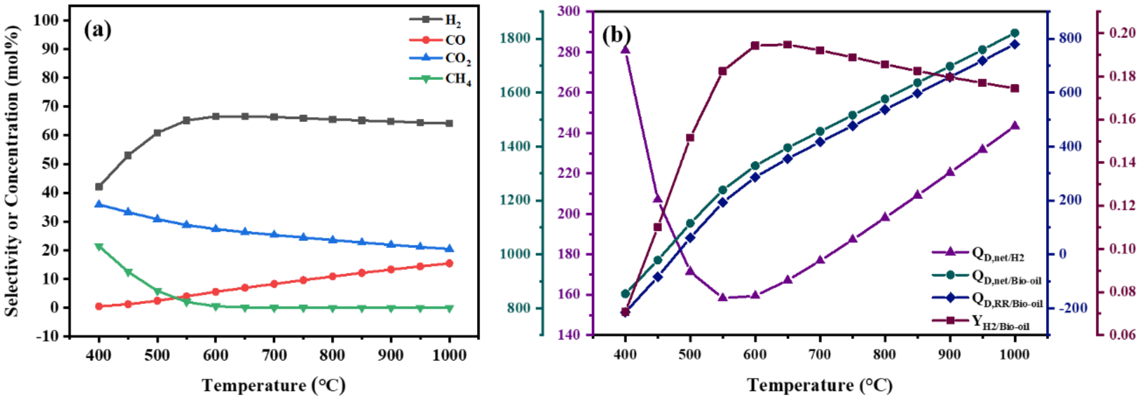

Fig. 8.6 Effect of temperature on (a) product selectivity and (b) energy demands (MJ kmol$_{H2}$-1 and MJ kmol$_{Bio-oil}$-1) and H_2 yield (kg$_{H2}$ kg$_{Bio-oil}$-1) in CSR process

8.2.2 Advanced reforming processes

Previously for the case of CSR process, it was noted that the highest H_2 selectivity and yield were obtained at an SCMR value of 5 and reaction temperature of 600 °C. Accordingly, these conditions were used as the base case for evaluating the H_2 production potential of the three advanced processes under consideration.

8.2.2.1 SESR process

SESR process is an intensified process that results from combining the traditional steam reforming process (CSR) with the simultaneous sorption of CO_2 using a solid sorbent, which in this case is CaO. CO_2 can be continuously and selectively removed during the reforming reaction itself in SESR, which shifts the equilibrium position of the reactions towards greater H_2 yields as well as purity. The sorbent gets converted to $CaCO_3$ and is regenerated by heating at high temperature in calcination reactor. Consequently, the molar ratio of sorbent to carbon in the bio-oil is an important factor when it comes to achieving maximum H_2 selectivity. Fig. 8.7(a) represents the results obtained from varying the molar ratio of CaO to C (CaO/C MR) on the product selectivities and energy demand at a SCMR value of 5 and temperature 600 °C. As the CaO to C MR increased from 0, CO_2 concentration in the product gases leaving the reforming reactor dropped rapidly owing to its capture by reaction with CaO (Eq. 11). CO_2 capture shifted the equilibrium of WGS reaction in the forward direction (Eq. 2), leading to a rapid increase in the H_2 concentration [162] while that of CO dropped to zero. The low concentration could be explained by the fact that CO_2-sorption pulls the equilibrium position of WGS reaction in the forward reaction, thereby resulting in the consumption of CO. Also, greater the amount of sorbent fed, the greater is the amount of CO_2 captured and CO consumption is also equally large [162,164]. Owing to the low CO and CO_2 concentrations, the equilibrium positions of side reactions such as methanation and/or decomposition reactions are shifted backwards, as a result of which they are inhibited [161,167]. The H_2 concentration continued to increase with increasing CaO/C MR until eventually stabilising for values ≥ 1, reaching a maximum concentration of 98.72 mol% in the product gases, marking an increment of about 32.5% over the maximum concentration for CSR process. H_2 yield also exhibited a similar trend, increasing rapidly as the CaO/C ratio rose from 0 and then peaked out as the latter approached values > 1, with an increment of about 11% over the base case yield (optimum

CSR yield) (Fig. 8.7(b)). Further increasing the sorbent loading would only contribute to increased energy requirement without any effect on H_2 yield [166].

For the case of energy demands (Fig. 8.7(b)), the trend observed was different from that noted for CSR process. In SESR, the energy demand of the reforming reactor $Q_{D,\ RR/bio\text{-}oil}$ exhibited a steep decline with increasing CaO/C ratios, becoming negative and stabilising at CaO/C > 1. The negative energy demand suggests that the energy liberated via CO_2 sorption in the reactor was much larger than the energy to be supplied externally for carrying out the steam reforming reaction. Consequently, the reforming reactor could essentially be operated without supplying any external heat; in fact, the heat generated could be put to use somewhere else in the plant for generating utilities such as steam. At CaO/C MR value of 1, where highest H_2 yield was obtained, a staggering 253% reduction in the energy demand of the reforming reactor was noted over that for CSR process. For CSR process, however, the $Q_{D,\ RR/bio\text{-}oil}$ had displayed an increasing trend (Fig. 5b). This could be attributed to the fact that due to the endothermic nature of the overall reforming process, heat has to be supplied externally to overcome the thermodynamic limitations [162,166]. The greater the SCMR value and/or reforming temperature, greater is the energy required to process a mole of bio-oil; consequently, the CSR process involves greater energy demand. Meanwhile, in SESR, heat is liberated when CO_2 is captured during the reforming process due to the exothermic nature of the sorption process (Eq 11). The amount of heat liberated increases as the amount of sorbent fed increases, which results in a greatly reduced energy demand for the reformer. $Q_{D,\ net/bio\text{-}oil}$ was reduced very slightly (~3.5 %), while $Q_{D,\ net/H2}$ for SESR saw a slight increase (~7.1%) over the values obtained for the base case (CSR at optimum conditions). This is because of the addition of a regeneration unit for converting the spent sorbent back to its original form. Due to the highly endothermic nature of the regeneration step (Eq. 20), the regeneration reactor requires a large amount of energy, which is why the overall energy demand for the process only changed minimally.

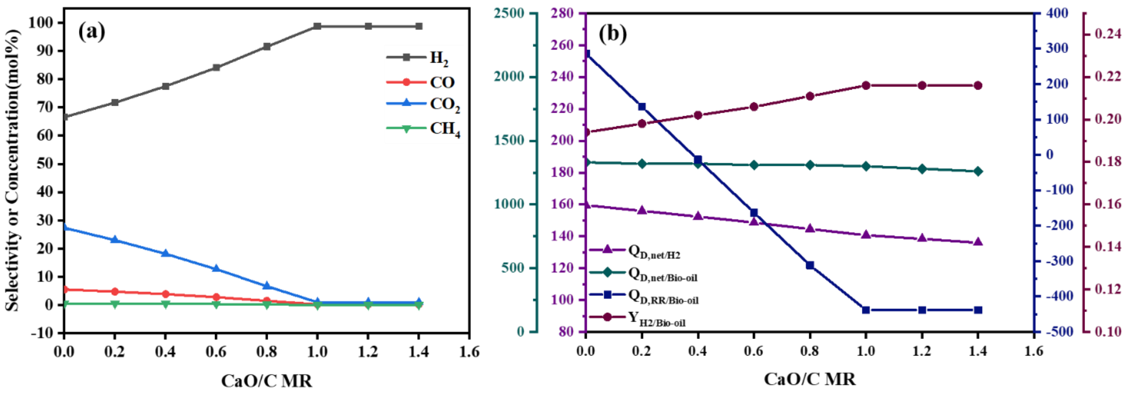

Fig. 8.7 Effect of CaO/C MR on (a) product selectivity and (b) energy demands (MJ $kmol_{H2}$-1 and MJ kmolBio-oil-1) and H_2 yield (kg_{H2} $kg_{Bio\text{-}oil}$-1) in SESR process

Fig. 8.8 displays the effect of reformer temperature on the product distribution and energy demand for SESR process. It was observed for CSR process that low temperatures in the reformer favour methanation and WGS reaction and this behaviour is expected to remain the same for SESR process as well. However, in this case, low temperatures also favour the CO_2 sorption process which is a strongly exothermic reaction (Eq. 11). As a result, at the lower end of the investigated temperature range, CO_2 concentration in the product gases is negligible (Fig. 8.8(a)). Furthermore, the complete removal of CO_2 in turn pulls the equilibrium of WGS reaction in the forward direction, ensuring complete conversion of CO to CO_2. The absence of CO and CO_2 inhibits methanation, due to which CH_4 concentration in the product gases is much lower than that observed for CSR process at the same temperature range (Fig. 8.6(a) and Fig. 8.8(a)). The concentrations of CO and CO_2 remained negligible until 600 °C, beyond which their values increased notably. Accordingly, H_2 selectivity and yield were also the highest and almost constant from 400 to 600 °C (99.94% and 0.216, respectively) (Fig. 8.8). A particularly sharp rise in CO_2 concentration was observed as the temperature soared above 700 °C and thereafter, it decreased again as temperature rose further. Correspondingly, the H_2 yield and selectivity started declining rapidly as temperature surged beyond 600 °C before eventually stabilising at 750 °C. The decreased H_2 formation could be attributed to the fact that the CO_2 sorption reaction is most favourable at temperatures up to 600 °C [162]. As the temperature increases beyond 600 °C, the reverse of the sorption reaction (CO_2 desorption) becomes increasingly favourable. Consequently, CO_2 is no longer captured, which in turn slows down WGS reaction and lowers H_2 production. At temperatures above 750 °C, no CO_2

capture was observed; also, at such high temperatures, reverse WGS reaction is more favourable, which explains the increased CO formation [162,164,166].

The energy demands also exhibited a very similar trend (Fig. 8.8(b)), wherein their values were at their lowest and almost constant up to 600 °C. The heat liberated during CO_2 capture and WGS reaction greatly compensates the energy required for carrying out reforming, thereby keeping the net energy demand low. At higher temperatures, however, CO_2 capture is greatly reduced, which in turn reduces the liberated heat; similarly, WGS reaction also slows down. Consequently, the heat now has to be supplied externally to meet the energy requirements that were earlier being compensated by in-situ generated heat. Also, in high-temperature regimes, the highly endothermic reverse WGS reaction takes over. These factors lead to a massive surge in both the reforming energy demand and the overall energy demand, as seen in Fig. 8.8(b).

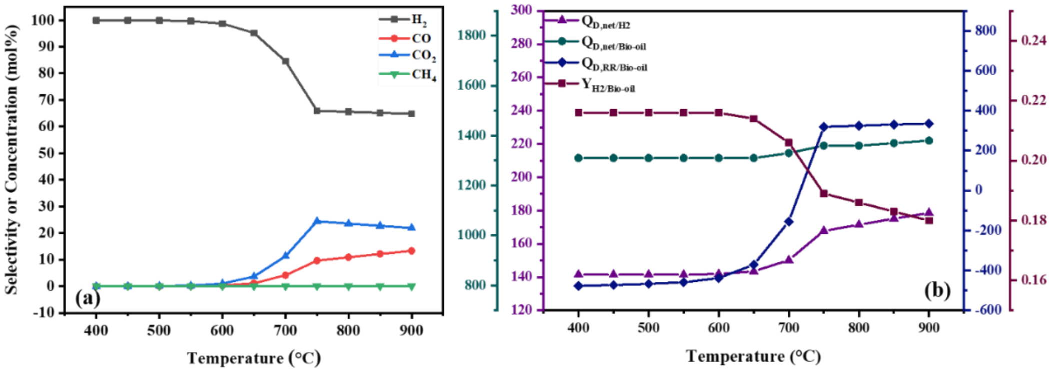

Fig. 8.8 Effect of temperature on (a) product selectivity and (b) energy demands (MJ $kmol_{H2}$-1 and MJ $kmol_{Bio\text{-}oil}$-1) and H_2 yield (kg_{H2} $kg_{Bio\text{-}oil}$-1) in SESR process

8.2.2.2 CLSR process

Like the SESR process, CLSR is an intensified process which combines the two processes of steam reforming and partial oxidation inside the reforming reactor. The partial oxidation is carried out by the transfer of oxygen from the lattice of a solid material (oxygen carrier). In this way, the feed is partially oxidised, liberating heat in the process, which greatly lowers the energy requirement of the reformer. The oxygen carrier, on the other hand, gets reduced in this process, is separated from the products and then regenerated back in an oxidiser with air as an oxidant. Using OTMs as sources of oxygen instead of air prevents the outlet gaseous stream from being diluted with huge amounts of N_2, saving significant capital investment in downstream H_2 purification. Consequently, the molar ratio of oxygen carrier and/or OTM to the carbon the bio-oil feedstock (NiO/C MR) is an important parameter to consider given that that the presence of NiO in the reforming reactor is likely to promote several reactions (Eq. 13-17), which in turn will lead to a markedly different product distribution. Fig. 8.9 displays the effect of NiO/C MR on product distribution and energy demand of the process at SCMR = 5 and 600 °C. Additionally, CO_2 concentration in the product gases was noted to have climbed up rapidly as the NiO/C MR increased from 0 to 1 while H_2 concentration in the product gas diminished equally rapidly from 66.58 mol% obtained in traditional CSR process to 53 mol% at NiO/C value of 1, corresponding to a reduction of 20.5% of CO concentration also underwent a slight decrease and CH_4 concentration remained almost negligible through the entire range of NiO/C MR values. The H_2 yield was hit more badly, declining by 43.2% as compared to the H_2 yield for CSR at optimum conditions. The massively reduced H_2 selectivity and yield in CLSR process could be attributed to the fact that a lesser amount of H_2 is generated from Eq. 16 and 17 as compared to Eq. 1. Additionally, some of the generated H_2 could also get oxidised by the oxygen carrier via Eq. 13. The low concentrations of CH_4 and CO could be explained by their oxidation to CO and CO_2 respectively via Eq. 14 and 15. The oxidation of CO is also partially responsible for reduced H_2 formation since its oxidation to CO_2 lowers its concentration in the reformer, preventing the WGS reaction from occurring [162].

With respect to the energy requirements of the process, the energy demand of the reforming reactor only decreased slightly with increasing the oxygen carrier to carbon ratio. On the other hand, $Q_{D,\ net/bio\text{-}oil}$ and $Q_{D,\ net/H2}$, which represent the overall energy demand, were greatly reduced - 74.8% and 55.6%, respectively - as the NiO/C MR was varied from 0 to 1. This could be attributed to the heat liberated during – (i) the partial oxidation of bio-oil feedstock and the product gases in the reforming reactor and (ii) the regeneration of the spent oxygen carrier in the oxidiser reactor (Eq. 21). Cerqueira et. al. [162] noted a similar large reduction in H_2 yield with increasing feed rates of oxygen carrier (NiO) while investigating steam reforming of olive mill wastewater. It is amply clear from the obtained results that the addition of an oxygen carrier and/or OTM is advantageous from the point of view of energy efficiency, and the greater the amount of the OTM fed, the greater is the reduction in the energy demand of the process. Technically, at high enough values of NiO/C molar ratios, both the reforming reactor as well as the entire process could theoretically be operated in autothermal mode. However, its addition is also directly responsible for a reduction in the amount of H_2 that can be produced from bio-oil, with the reduction being drastic at high NiO/C mola ratios. Consequently, the oxygen carrier material should be added in such a way that a maximum possible reduction in energy demand is achieved while keeping the reduction in H_2 yield as low as possible. Accordingly, it was decided that for further investigations, the NiO/C molar ratio would be selected in such a way to ensure the reduction in H_2 yield is as low as possible. At a NiO/C ratio of 0.2, a 7.3% and ~15% reduction was observed in the values of $Q_{D,\ net/Bio\text{-}oil}$ and $Q_{D,\ net/H2}$, respectively over those of the base case while the reforming energy demand $Q_{D,\ /Bio\text{-}oil}$ saw a mere ~2% reduction. The H_2 yield, meanwhile, was around 8% lower than that obtained from CSR process. Accordingly, this value was selected for carrying out further studies.

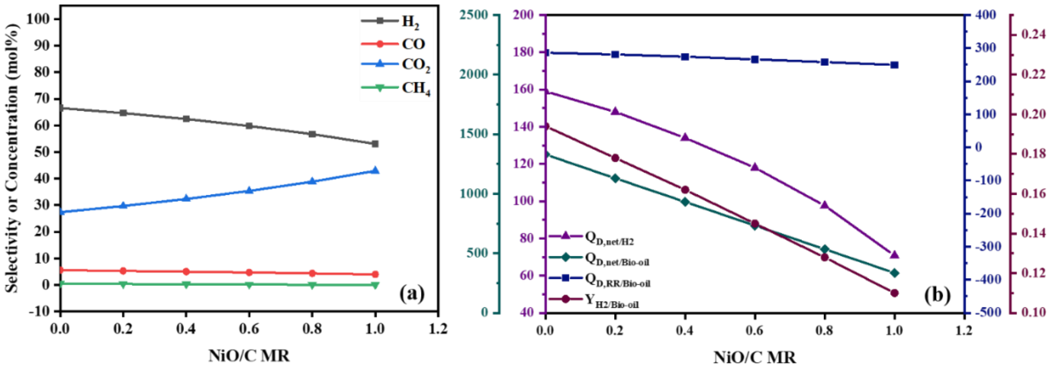

Fig. 8.9 Effect of NiO/C MR on (a) product selectivity and (b) energy demands (MJ $kmol_{H2}$-1 and MJ $kmol_{Bio\text{-}oil}$-1) and H_2 yield (kg_{H2} $kg_{Bio\text{-}oil}$-1) in CLSR process

Fig. 8.10 represents the effect of temperature on the product distribution and energy yield of CLSR process at a NiO/C molar ratio of 0.2. It can be observed from Fig. 10a that the product distribution for CLSR process was almost identical to the one obtained for CSR process (Fig. 6a). Throughout the investigated temperature range, the H_2 and CH_4 concentrations obtained with CLSR were only slightly smaller than those obtained with CSR while the CO_2 concentration was just a bit higher than the CSR values. The rather small difference in the product concentrations obtained with CSR and CLSR is due to the fact that since the oxygen carrier is only present in a small amount, the extent of oxidation is also quite small. The trend observed for H_2 yield and overall energy demand per mole of H_2 produced $Q_{D,\ net/H2}$ was also almost similar to their trend for CSR process. The value of $Q_{D,\ net/H2}$ reduced sharply as the temperature rose, and reached a minimum at 600 °C, which corresponds to maximum H_2 production (Fig. 8.10(a)). Subsequently, the value of $Q_{D,\ net/H2}$ slowly increased as the temperature was increased further. The reforming energy demand

$Q_{D, RR/Bio\text{-}oil}$ and overall energy demand per mole of bio-oil processed $Q_{D, net/Bio\text{-}oil}$, however, exhibited a trend quite different from that for CSR process. For CSR process, the values of these parameters had been increasing in an almost linear manner as the temperature increased. However, for CLSR, $Q_{D, RR/Bio\text{-}oil}$ and $Q_{D, net/Bio\text{-}oil}$ initially increased with temperature before essentially stabilising at temperatures above 600 °C. As such, this difference in trends of energy demands could probably be ascribed to the compensation of external energy requirements by the heat liberated during the partial oxidation of bio-oil feedstock and product gases. Overall, it can be safely concluded that 600 °C was the optimum temperature for obtaining the highest possible H_2 yields.

8.2.2.3 SE-CLSR process

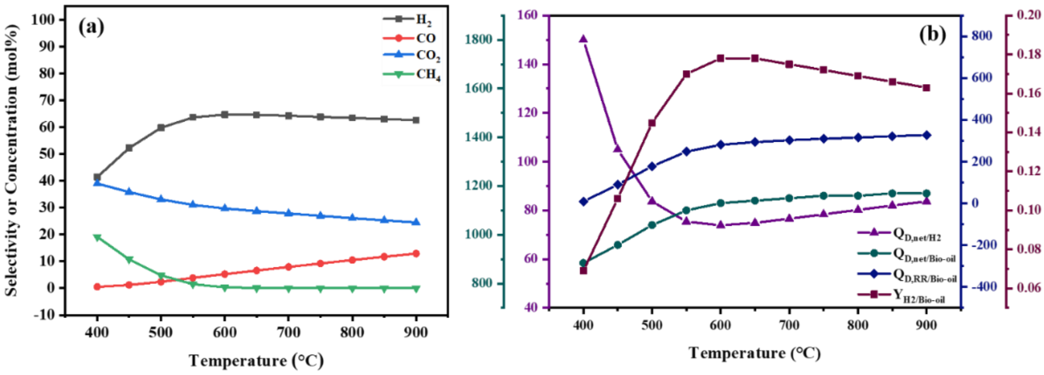

Fig. 8.10 Effect of temperature on (a) product selectivity and (b) energy demands (MJ $kmol_{H2}$-1 and MJ $kmol_{Bio\text{-}oil}$-1) and H_2 yield (kg_{H2} $kg_{Bio\text{-}oil}$-1) in CLSR process

The SE-CLSR process can be thought of a hybrid intensified process that combines traditional, sorption-enhanced and chemical looping-enhanced reforming into a single process. The idea behind combining sorption with chemical looping is to bring together the benefits obtained from CO_2 capture in sorption reforming with the increased energy efficiency provided by chemical looping reforming. The combined process would then generate H_2 in higher purity and yield as well as at lower energy requirements. With this is mind, a combined sorption-enhanced chemical looping reforming (SE-CLSR) process was proposed, whose flowsheet is presented in Fig. 8.4. In the previous investigations on SESR and CLSR process, it was observed that highest H_2 yields and lowest energy demands were obtained at CaO/C and NiO/C molar ratios equal to 1 and 0.2, respectively. Consequently, the same molar ratios of sorbent to carbon and OTM to carbon were selected for evaluating the performance of the combined process displayed in Fig. 8.4. Since the temperature has a huge influence on the CO_2 capture ability of the sorbent as well as the variety of reactions that take place during reforming, it was considered worthwhile to explore how its effect on product distribution and energy demand of the intensified SE-CLSR process (Fig. 8.11).

It can be seen from Fig. 8.11(a) that the product distribution obtained with SE-CLSR over the entire investigated range of temperatures is almost identical to that obtained with SESR. The apparent similarity in product distribution could be ascribed to the presence of CaO and NiO. Due to the presence of NiO in the reactor, bio-oil feedstock as well as products such as CH_4, CO and H_2 get oxidised. Additionally, the presence of CaO results in near complete CO_2 capture, which in turn pulls the WGS reaction and CH_4 oxidation reactions in the forward direction. Consequently, the product gas leaving the reformer consists of just the excess steam and H_2. As the CO_2 sorption reaction is an exothermic reaction, it is highly favoured at low-temperature conditions. Similarly, the oxidation reactions of CO, CH_4 and H_2 are also exothermic and, therefore, favoured at low temperatures. As a result, H_2 is obtained in extremely high purity at temperatures between 400 and 600 °C, with its concentration in the outlet gas being $\geq 99\%$ in the above-mentioned range. Similarly, H_2 yield was also noted to be the highest at 400 °C and remained constant up to 600 °C (Fig. 8.11(b)), following a sharp reduction was noted in both yield and concentration in the outlet gas. The reduction could be assigned to the fact that as temperatures, CO_2-sorption onto the sorbent becomes increasingly unfavourable, and above 750 °C, CO_2-sorption completely ceases (Fig. 8.11(a)). The CO_2 concentration in the reformer rises rapidly, which slows the WGS reaction and in consequence, H_2 formation. Furthermore, high temperatures favour the reverse WGS reaction, which results in the consumption of CO_2 and H_2 and explains the increasing CO concentration (Fig. 8.11(a)).

With regards to the energy demand, it can be noted from Fig. 8.11(b) that the values of $Q_{D,\ net/H2}$ and $Q_{D,\ RR/Bio\text{-}oil}$ were the lowest at 400 °C and remained nearly stable at these values for temperatures up to 400 °C, which is in line with the observations made for H_2 yield and concentration in the outlet gas. At low temperatures, the WGS, CO_2-sorption and oxidation reactions liberated heat that is much larger than the energy requirement of the reformer, which can be seen from the net negative value of its energy demand in Fig. 8.11(b). With increasing temperatures, these reactions are slowed down, in turn limiting the amount of heat liberated and raising the amount to be supplied externally. As temperatures reach the higher end of the investigated range, heat is no longer available from CO_2 capture, and endothermic reactions such as reverse WGS reaction take over. With the in-situ heat generation already diminished, the amount of energy to be supplied externally increases tremendously. The value of $Q_{D,\ net/Bio\text{-}oil}$ also remains practically constant up to 600 °C, following which a small increase was observed. The relatively small change in $Q_{D,\ net/Bio\text{-}oil}$ is due to the heat liberated from exothermic oxygen carrier regeneration balancing the heat required for sorbent regeneration. Since the amount of heat generated in the reformer is quite large and vastly outweighs the energy required to maintain the temperature, the reactor could be operated in an autothermal mode, i.e., without supplying any energy externally. The excess heat left behind after that required for sustaining autothermal operation could then be utilised for generating utilities and/or electricity, and bringing down the operational cost of the proposed process.

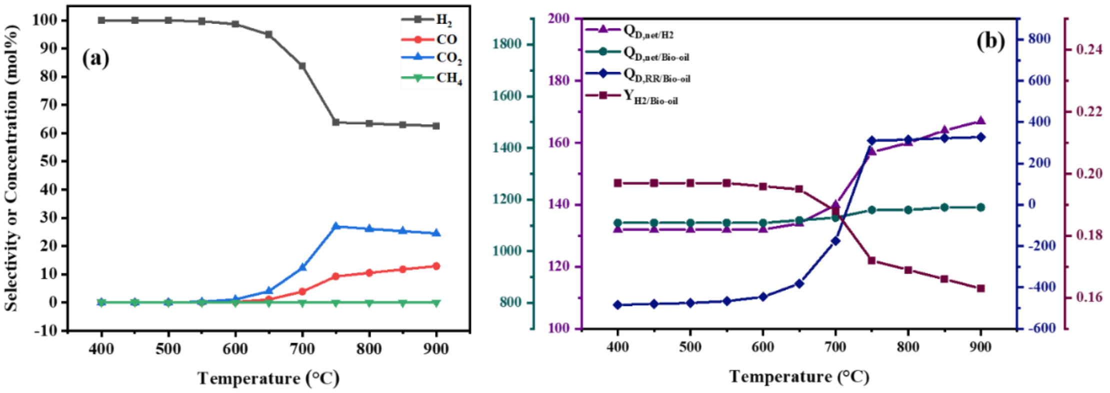

Fig. 8.11 Effect of temperature on (a) product selectivity and (b) energy demands (MJ $kmol_{H2}$-1 and MJ $kmol_{Bio\text{-}oil}$-1) and H_2 yield (kg_{H2} $kg_{Bio\text{-}oil}$-1) in combined SE-CLSR process

8.3 Comparing conventional and advanced reforming process

In the previous section, a thorough thermodynamic investigation was carried out to evaluate the potential of H_2 production via steam reforming of bio-oil and four processes were considered: traditional (CSR), sorption-enhanced (SESR), chemical looping enhanced (CLSR), and sorption and chemical looping enhanced (SE-CLSR). During the course of the investigations, the effect of important process variables was evaluated in-depth and a set of optimum process conditions which yielded the highest H_2 yields were arrived upon, as shown in Fig. 8.5-8.11. Given that both H_2 yield and purity as well as the energy requirement, are equally crucial when a new process technology is being developed. It was considered worthwhile to how the four proposed processes under consideration fare against one another (Table 8.2 and Fig. 8.12). It could be noted that the highest H_2 was obtained for SESR process (0.216 kg_{H2} $kg_{Bio\text{-}oil}^{-1}$), owing to the enhancement of WGS reaction produced by the in-situ capture of CO_2 in the reforming reactor. The second highest yield was obtained with the combined SE-CLSR process (0.197 kg_{H2} $kg_{Bio\text{-}oil}^{-1}$), though it must be mentioned that the yield for the combined sorption and looping enhanced process was only ~1.5% higher than that of CSR process (0.194 kg_{H2} $kg_{Bio\text{-}oil}^{-1}$). The rather small increase in H_2 yield in the SE-CLSR can be ascribed to the oxidation of some of the produced H_2. CLSR provided the smallest H_2 yield among all the process (0.178 kg_{H2} $kg_{Bio\text{-}oil}^{-1}$), which could be ascribed to the fact that the smaller amount of H_2 produced during the process as a result of the partial oxidation of some of the produced H_2 and increased favourability of CO oxidation over the WGS reaction.

When comparing these processes, the energy requirements play a crucial role as the SR process is highly endothermic. If the energy requirements of the proposed processes are high, the operating costs would also be equally high, which in turn would adversely affect the economic viability of the proposed. In this context, the CSR process had particularly high energy demands stemming from the need to supply heat for the endothermic steam reforming reactions. While it provided the highest H_2 yield, the SESR process also boasted high overall energy demands, as seen in Fig. 8.12. The net energy required to process one mole of bio-oil ($Q_{D,\ net/Bio\text{-}oil}$) was higher for SESR than that for CSR. The energy requirement per mole of H_2 produced $Q_{D,\ net/H2}$ was only slightly smaller than that for CSR. This is because the energy requirement saved via CO_2-sorption is eventually almost balanced out by the heat that has to be supplied externally to regenerate the spent sorbent. However, it should be mentioned that the immense amount of heat generated during CO_2-sorption in the reforming reactor could be utilised elsewhere, driving down the energy requirements of the process on the whole to some extent. Despite the drawback of high energy requirements, what makes SESR particularly appealing is the fact that it produces a very high yield of high purity H_2, which saves a lot of capital investment in designing a downstream processing unit for purification. The energy demands for CLSR process were almost the opposite of that observed for SESR. It had nearly the same heat demand for reforming reactor as the CSR process due to the limited extent of oxidation. The energy demands over the whole process were significantly reduced because of the heat liberated during the exothermic OTM regeneration. In theory, there exists an excellent potential to carry out the entire process in essentially autothermal mode by using higher values of NiO/C molar ratios. However, the drastically improved energy efficiency will be achieved at the cost of severely lowered H_2 yield. In conclusion, while the increased energy efficiency makes the CLSR process hugely attractive from an economic standpoint, H_2 production is considerably reduced. Consequently, a larger amount of bio-oil feedstock would be required if the H_2 production is to be at par with that from CSR or SESR processes, which is a major downside as it will result in increased costs for raw material procurement. Additionally, a downstream purification unit will be needed since the outlet stream also contains substantial amounts of CO and CO_2. As a result, for CLSR, the disadvantages associated with increased capital investments elsewhere in the process outweigh the cost benefits achieved with increased energy efficiency and dent its potential as a possible candidate for H_2 production.

Lastly, when CO_2-sorption and bio-oil partial oxidation were combined to have a highly intensified SE-CLSR process, a major improvement was observed in terms of the energy efficiency. The reforming reactor had a highly negative energy demand, just like the SESR process, signalling that the in-situ heat generation is orders of magnitude larger than the energy required to carry out reforming. As such, it provides an opportunity that the reforming reactor could potentially be operated in autothermal mode. Also, any excess heat left behind after ensuring autothermal operation could be utilised elsewhere for in the process for generating useful utilities. As for the overall energy demands of the process - $Q_{D,\ net/H2}$ and $Q_{D,\ net/Bio\text{-}oil}$ – a substantial reduction (> 10%) was observed for SE-CLSR as compared to both CSR and SESR. This is because the heat liberated during the highly exothermic regeneration of oxygen carrier compensates for the high energy demands of the endothermic sorbent regeneration process. Furthermore, a large amount of heat can also be recuperated from the cooling of sorbent and oxygen carrier post-regeneration and from cooling the waste gases, which would also contribute greatly to reducing the net energy load. The fact that SE-CLSR process offers high yields of H_2 in very high purity and at considerably lower energy requirements is a major advantage that none of the other processes have. The above-mentioned factors make SE-CLSR process by the most appealing both from a technological and economic standpoint among the four processes considered here in this study.

Table 8.2 Comparison of H_2 yield and energy demands of the four processes under consideration

Process	H_2 Yield (kg_{H2} $kg_{Bio\text{-}oil}^{-1}$)	$Q_{D, net/H2}$ (MJ $kmol_{H2}^{-1}$)	$Q_{D, net/Bio\text{-}oil}$ (MJ $kmol_{Bio\text{-}oil}^{-1}$)	$Q_{D, RR/Bio\text{-}oil}$ (MJ $kmol_{Bio\text{-}oil}^{-1}$)
CSR	0.194	159.5	1328.5	286.3
SESR	0.216	150.1	1389.3	-477.4
CLSR	0.178	74	1131	280.7
SE-CLSR	0.197	132	1112	-484.6

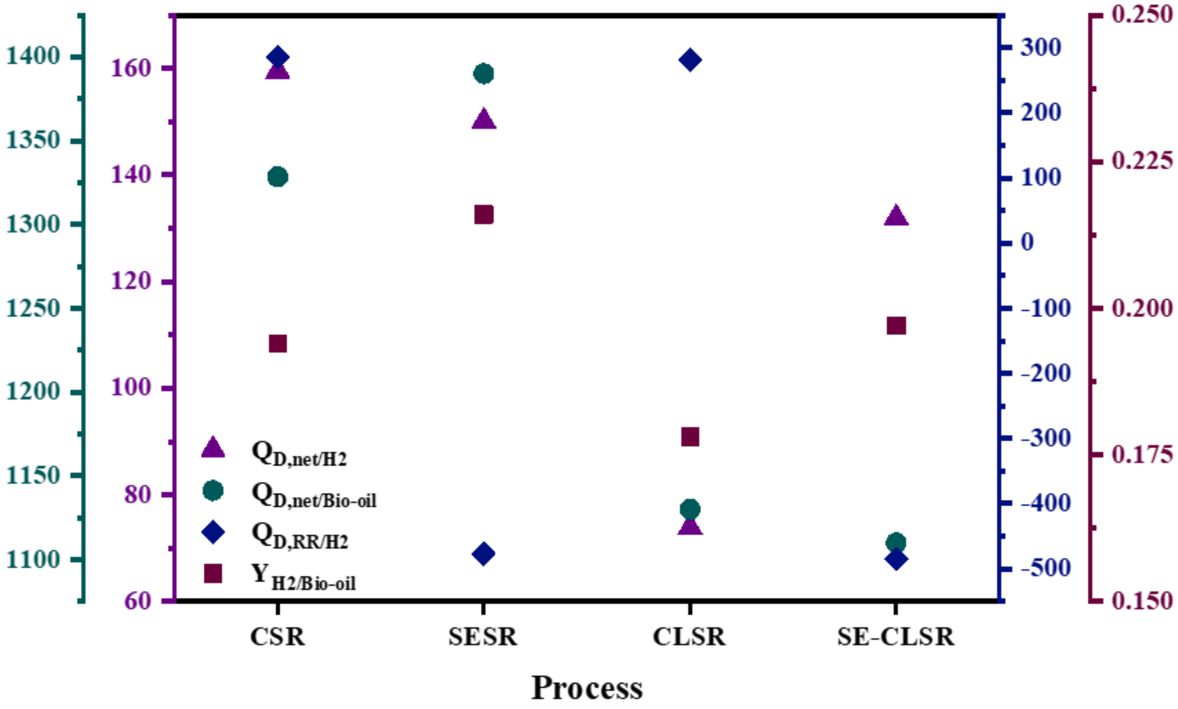

Fig. 8.12 A comparison of the H_2 yield (kg_{H2} $kg_{Bio\text{-}oil}$-1) and energy demands (MJ $kmol_{H2}$-1 and MJ $kmol_{Bio\text{-}oil}$-1) for the four processes at their optimum conditions.

8.4.5 Concluding remarks

This work was aimed at evaluating the potential of H_2 production from pyrolysis bio-oil through steam reforming. In this regard, two opportunities were identified to understand conventional reforming and suggest strategies for intensification. First was the modelling of bio-oil as a mixture of model compounds as opposed to using single model compounds so as to have a much closer resemblance with actual bio-oil. The second was the investigation of three advanced reforming processes – SESR, CLSR and SE-CLSR whose performance was compared with that of the conventional steam reforming (CSR) process. To this end, a thorough thermodynamic evaluation was carried out to assess the potential of the four processes for H_2 production. The effect of important process parameters such as steam to carbon (SCMR), sorbent to carbon (CaO/C) and oxygen carrier to carbon (NiO/C) ratios and reforming temperature was investigated to arrive at a set of optimum process conditions that provided the highest H_2 yield. For the purpose of assessing and comparing the performance of the four processes, 3 parameters were taken into consideration: H_2 concentration and/or purity, and yield and the energy demands ($Q_{D,\ RR/Bio\text{-}oil}$, $Q_{D,\ net/Bio\text{-}oil}$, and $Q_{D,\ net/H2}$).

The conventional reforming process provided a relatively high yield of 0.194 $kg_{H2}\ kg_{Bio\text{-}oil}^{-1}$ with high external energy requirements. An enhancement in process performance in the form of improved H_2 yield and/or reduced energy demands were observed in the case of advanced reforming processes. Sorption-enhanced process provided the highest H_2 yield (0.216 $kg_{H2}\ kg_{Bio\text{-}oil}^{-1}$) among all the processes, albeit at the cost of increased consumption of energy. Chemical looping, on the other hand, led to reduced energy consumption at the expense of H_2 yield. Combining CO_2 sorption and chemical looping in the SE-CLSR process led to a high purity H_2 yield of 0.197 $kg_{H2}\ kg_{Bio\text{-}oil}^{-1}$ with markedly lower energy demands as compared to all the other processes. H_2 was obtained in very high purity, doing away the need for an expensive downstream product purification unit. Additionally, a large amount of heat generation was noted in the reforming reactor which could potentially be used to operate the reactor under autothermal condition while the excess heat could be utilised elsewhere in the process for heating purposes. Consequently, the above-mentioned factors make SE-CLSR an exciting and promising route for sustainable hydrogen production.

Overall, the results obtained in this study demonstrate that advanced reforming processes such as SE-CLSR could strengthen the technological and economic viability of bio-oil as an alternative and renewable feedstock for hydrogen production. While thermodynamic analysis is an extremely informative tool that is a first step towards developing dynamic and realistic models of actual processes, further work is required in process development to carefully assess the feasibility of a real advanced reforming process. In this direction, heat integration is likely to be a major consideration given that there is a huge potential to recover heat from solids (sorbent and oxygen carrier) and waste gases. Economic constraints are also likely to be a crucial parameter; furthermore, optimisation could also be carried out to look for areas with scope for further intensification. In conclusion, a techno-economic analysis could provide a real time idea of a proposed process's technological and economic viability and suggest any remedial steps to boost the prospects.

Chapter 9: Conclusion and future recommendations

9.1 Conclusions

The catalytic steam reforming of bio-oil represents a promising avenue towards the generation of environmentally friendly hydrogen from renewable resources. By utilizing a catalyst, the bio-oil - a derivative of biomass transformation processes - is transformed into hydrogen gas. This methodology is deemed to be "green" as it harnesses the potential of renewable biomass as its feedstock, generating hydrogen that serves as a clean energy source. The hydrogen produced through this method can be utilized in a range of applications, including transportation and electricity generation, thus reducing greenhouse gas emissions and dependence on finite fossil fuels. Furthermore, the employment of catalysts elevates the process's efficiency and helps to mitigate its cost, making it a highly desirable option for hydrogen production. Additionally, following observations were noted via a systematic study performed in the direction of setting a stable catalytic system for green hydrogen production from agricultural residue.

- The catalytic steam reforming of simulated bio-oil (SB1) using $LaNi_xCo_{1-x}O_3$ perovskite catalysts was investigated in a tubular fixed-bed reactor to evaluate their catalytic performance for hydrogen production. Results showed that the $LaNi_{0.5}Co_{0.5}O_3$ catalyst had the best catalytic activity among the various synthesized catalysts. Further H_2-TPR analysis confirmed the strong interaction between the metal species at the B position and other metals and oxygen atoms in the perovskite structure for the $LaNi_{0.5}Co_{0.5}O_3$ catalyst. The highest hydrogen yield of 87% and simulated bio-oil conversion of 98% were obtained at 700 °C, with a steam-to-carbon molar ratio of 2.7 and a weight hourly space time of 18.4 $kg_{cat}.h/kgmol_{bio\text{-}oil}$. These results highlight the importance of identifying the optimal catalyst and reaction conditions for the steam reforming of bio-oil in order to maximize the production of green hydrogen.
- The synergistic effect of partial substitution at the A and B positions in $LaNiO_3$ with alternate metal elements (Ce, Ca, Zr for the A position, and Co, Fe, Cu for the B position) during the SR process for the generation of green hydrogen from

simulated bio-oil (SB2) was evaluated. Moreover, the catalytic properties of partial substitution on $LaNiO_3$ were assessed via a series of characterizations such as XRD, H_2-TPR, TPD (NH_3 and CO_2), Py-FTIR, XPS, TG and FESEM analyses. The XRD analysis of reduced catalysts revealed the formation of bimetallic Ni-M alloys supported on La_2O_3, which was also confirmed from H_2-TPR analysis. The XPS and TG analysis of the catalysts confirmed the availability of oxygen vacancies on the surface of the catalysts, with the maximum concentration being observed for $LaNi_{0.5}Co_{0.5}O_3$. As a result, $LaNi_{0.5}Co_{0.5}O_3$ catalyst exhibited excellent activity and stability during TOS study over a period of 12 h.

- The bio-oil was produced via the pyrolysis of a blend of different types of biomass feedstocks, particularly rice husk, wheat straw, corn cob, and sugarcane bagasse (primary crops Punjab state). The produced bio-oil was then utilized for the catalytic steam reforming to produce green hydrogen at optimized process conditions and catalyst. The TOS results showed that the $LaNi_{0.5}Co_{0.5}O_3$ catalyst exhibited high activity in producing hydrogen, with a yield of 74% (±3%) at 5th h that gradually decreased to 60% at 12th h. In conclusion, the average H_2 yield was found 65% over the course of the stability experiments
- Catalyst deactivation study was performed to comprehend the nature of the coke precursors deposited on catalyst surface, by using various techniques like XRD, TGA, FESEM, RAMAN etc. The results indicated that the formation of $La_2O_2CO_3$ phase validated the catalyst's ($LaNi_{0.5}Co_{0.5}O_3$) high ability to suppress the formation of coke. Furthermore, the appearance of graphitic carbon and/or CNTs along with the amorphous carbon was observed through Raman and FESEM analyses. It was also noted that the reaction temperature played a crucial role in determining the nature of the coke formed and that an increase in temperature led to an increase in the formation of CNTs.
- The phenol steam reforming experiments were performed with optimum catalyst to identify the optimized process parameters for the kinetic study of phenol steam reforming process. The Kinetic parameters ($k_0 = 0 \cdot 59 \frac{kmol_{bio-oil}}{kg_{cat}.h.atm^{0.51}}$ & $E_A = 13495 \frac{KJ}{kmol}$) were obtained using the power law model and rate equation is found to be $-r_A = 0.59 * \mathrm{e}^{\frac{-13495}{RT}} * p_{Ph}^{0.14} * p_w^{0.38}$.

- Thermodynamic study of advanced steam reforming processes – SESR, CLSR, and SECLSR, were performed and compared with CSR process. The results revealed that the SESR process may improve the purity of hydrogen by capturing CO_2 gas, which can help to reduce greenhouse gas emissions and combat climate change. It's worth noting that while these processes have potential benefits, more research is needed to further optimize and commercialize them, including improving the efficiency of the sorbent materials, reducing the costs associated with carbon capture, and optimizing the reaction conditions for maximum hydrogen production.

9.2 Future recommendations

- Sorption enhanced steam reforming experiments may provide more insight for improving the purity of hydrogen gas.
- Combined pyrolysis and steam reforming process may also improve the process efficiency.
- A pilot plant study can provide valuable information and insights into the process being studied and help to identify any challenges that may need to be addressed when scaling up to an industrial scale.
- The utilization of the bio-refinery concept enables the full utilization of all by-products generated during the process. For instance, biochar produced as a by-product from the pyrolysis process can be transformed into a profitable component during the scaling up of the process. Another example is the conversion of carbon dioxide into valuable chemicals.
- The study on techno-economic viability of the biomass to green hydrogen production process is also required for scaling up this process to industrial scale.

References:

[1] I.E. Agency, W.E. Outlook, World Energy Outlook 2019, World Fig. (2019) 32–32. https://www.iea.org/reports/world-energy-outlook-2019%0Ahttp://files/4079/International Energy Agency - 2015 - World Energy Outlook 2015.pdf%0Ahttp://files/3681/International Energy Agency - 2011 - World Energy Outlook 2011.pdf%0Ahttp://files/3685/Interna.

[2] EIA, Country analysis executive summary: India, Indep. Stat. Anal. (2021) 9. https://www.eia.gov/international/content/analysis/countries_long/Libya/pdf/libya.pdf%0Ahttps://www.eia.gov/international/content/analysis/countries_long/India/india.pdf.

[3] Air BP, BP Annual Report and Form 20-F 2020, (2021) 1–352. https://www.bp.com/content/dam/bp/business-sites/en/global/corporate/pdfs/investors/bp-annual-report-and-form-20f-2020.pdf.

[4] M. Foston, A.J. Ragauskas, Biomass characterization: Recent progress in understanding biomass recalcitrance, Ind. Biotechnol. 8 (2012) 191–208. https://doi.org/10.1089/ind.2012.0015.

[5] K. Alper, K. Tekin, S. Karagöz, A.J. Ragauskas, Sustainable energy and fuels from biomass: A review focusing on hydrothermal biomass processing, Sustain. Energy Fuels. 4 (2020) 4390–4414. https://doi.org/10.1039/d0se00784f.

[6] A. Tursi, A review on biomass: importance, chemistry, classification, and conversion, Biofuel Res. J. 6 (2019) 962–979. https://doi.org/10.18331/BRJ2019.6.2.3.

[7] D. Li, X. Li, J. Gong, Catalytic Reforming of Oxygenates: State of the Art and Future Prospects, Chem. Rev. 116 (2016) 11529–11653. https://doi.org/10.1021/acs.chemrev.6b00099.

[8] A. Tagade, N. Kirti, A.N. Sawarkar, Pyrolysis of agricultural crop residues: An overview of researches by Indian scientific community, Bioresour. Technol. Reports. 15 (2021) 2589–2603. https://doi.org/10.1016/j.biteb.2021.100761.

[9] M. Ahiduzzaman, A.K.M.A. Islam, Z. Yaakob, J.A. Ghani, N. Anuar, Agricultural residues from crop harvesting and processing: A renewable source of bio-energy, in: K.R. Hakeem, M. Jawaid, U. Rashid (Eds.), Biomass Bioenergy Appl., Springer International Publishing, Cham, 2015: pp. 323–337. https://doi.org/10.1007/978-3-319-07578-5_16.

[10] F.H. Isikgor, C.R. Becer, Lignocellulosic biomass: a sustainable platform for the production of bio-based chemicals and polymers, Polym. Chem. 6 (2015) 4497–4559. https://doi.org/10.1039/c5py00263j.

[11] J.N. Putro, F.E. Soetaredjo, S.Y. Lin, Y.H. Ju, S. Ismadji, Pretreatment and conversion of lignocellulose biomass into valuable chemicals, RSC Adv. 6 (2016) 46834–46852. https://doi.org/10.1039/c6ra09851g.

[12] M. Ayyachamy, F.E. Cliffe, J.M. Coyne, J. Collier, M.G. Tuohy, Lignin: Untapped biopolymers in biomass conversion technologies, Biomass Convers. Biorefinery. 3 (2013) 255–269. https://doi.org/10.1007/s13399-013-0084-4.

[13] R. Yukesh Kannah, S. Kavitha, Preethi, O. Parthiba Karthikeyan, G. Kumar, N.V. Dai-Viet, J. Rajesh Banu, Techno-economic assessment of various hydrogen production methods – A review, Bioresour. Technol. 319 (2021) 124175. https://doi.org/10.1016/j.biortech.2020.124175.

[14] G. Kumar, A.P. Eswari, S. Kavitha, M.D. Kumar, R.Y. Kannah, L.C. How, G. Muthukaruppan, J.R. Banu, Thermochemical conversion routes of hydrogen production from organic biomass: processes, challenges and limitations, Biomass Convers. Biorefinery. (2020) 1–26. https://doi.org/10.1007/s13399-020-01127-9.

[15] S. Fremaux, S.M. Beheshti, H. Ghassemi, R. Shahsavan-Markadeh, An experimental study on hydrogen-rich gas production via steam gasification of biomass in a research-scale fluidized bed, Energy Convers. Manag. 91 (2015) 427–432. https://doi.org/10.1016/j.enconman.2014.12.048.

[16] M. Ni, D.Y.C. Leung, M.K.H. Leung, K. Sumathy, An overview of hydrogen production from biomass, Fuel Process. Technol. 87 (2006) 461–472. https://doi.org/10.1016/j.fuproc.2005.11.003.

[17] A. Demirbaş, Hydrogen production from biomass by the gasification process, Energy Sources. 24 (2002) 59–68. https://doi.org/10.1080/00908310252712307.

[18] J.J. Hernández, G. Aranda, G. San Miguel, A. Bula, Gasification of grapevine pruning waste in an entrained-flow reactor: Gas products, energy efficiency and gas conditioning alternatives, Glob. Nest J. 12 (2010) 215–227. https://doi.org/10.30955/gnj.000679.

[19] T. Ogi, S.Y. Yokoyama, Liquid Fuel Production from Woody Biomass by Direct Liquefaction, Sekiyu Gakkaishi (Journal Japan Pet. Institute). 36 (1993) 73–84. https://doi.org/10.1627/jpi1958.36.73.

[20] A. Demirbaş, Mechanisms of liquefaction and pyrolysis reactions of biomass, Energy Convers. Manag. 41 (2000) 633–646. https://doi.org/10.1016/S0196-8904(99)00130-2.

[21] A. V. Bridgwater, Production of high grade fuels and chemicals from catalytic pyrolysis of biomass, Catal. Today. 29 (1996) 285–295. https://doi.org/10.1016/0920-5861(95)00294-4.

[22] O. Onay, O.M. Koçkar, Fixed-bed pyrolysis of rapeseed (Brassica napus L.), Biomass and Bioenergy. 26 (2004) 289–299. https://doi.org/10.1016/S0961-9534(03)00123-5.

[23] A. V. Bridgwater, Review of fast pyrolysis of biomass and product upgrading, Biomass and Bioenergy. 38 (2012) 68–94. https://doi.org/10.1016/j.biombioe.2011.01.048.

[24] R.C. Saxena, D. Seal, S. Kumar, H.B. Goyal, Thermo-chemical routes for hydrogen rich gas from biomass: A review, Renew. Sustain. Energy Rev. 12 (2008) 1909–1927. https://doi.org/10.1016/j.rser.2007.03.005.

[25] P. McKendry, Energy production from biomass (part 1): Overview of biomass, Bioresour. Technol. 83 (2002) 37–46. https://doi.org/10.1016/S0960-8524(01)00118-3.

[26] S. Czernik, A. V. Bridgwater, Overview of applications of biomass fast pyrolysis oil, Energy and Fuels. 18 (2004) 590–598. https://doi.org/10.1021/ef034067u.

[27] A. V. Bridgwater, Production of high grade fuels and chemicals from catalytic pyrolysis of biomass, Catal. Today. 29 (1996) 285–295. https://doi.org/10.1016/0920-5861(95)00294-4.

[28] A. Kumar, J.P. Chakraborty, R. Singh, Bio-oil: the future of hydrogen generation, Biofuels. 8 (2017) 663–674. https://doi.org/10.1080/17597269.2016.1141276.

[29] H. Wang, J. Male, Y. Wang, Recent advances in hydrotreating of pyrolysis bio-oil and its oxygen-containing model compounds, ACS Catal. 3 (2013) 1047–1070. https://doi.org/10.1021/cs400069z.

[30] P.M. Mortensen, J.D. Grunwaldt, P.A. Jensen, K.G. Knudsen, A.D. Jensen, A review of catalytic upgrading of bio-oil to engine fuels, Appl. Catal. A Gen. 407 (2011) 1–19. https://doi.org/10.1016/j.apcata.2011.08.046.

[31] D. Wang, S. Czernik, E. Chornet, Production of hydrogen from biomass by catalytic steam reforming of fast pyrolysis oils, 1998. https://doi.org/10.1021/ef970102j.

[32] H. Lee, Y.M. Kim, I.G. Lee, J.K. Jeon, S.C. Jung, J. Do Chung, W.G. Choi, Y.K. Park, Recent advances in the catalytic hydrodeoxygenation of bio-oil, Korean J. Chem. Eng. 33 (2016) 3299–3315. https://doi.org/10.1007/s11814-016-0214-3.

[33] L. Zhang, R. Liu, R. Yin, Y. Mei, Upgrading of bio-oil from biomass fast pyrolysis in China: A review, Renew. Sustain. Energy Rev. 24 (2013) 66–72. https://doi.org/10.1016/j.rser.2013.03.027.

[34] K. Sahoo, A. Kumar, J.P. Chakraborty, A comparative study on valuable products: bio-oil, biochar, non-condensable gases from pyrolysis of agricultural residues, J. Mater. Cycles Waste Manag. 23 (2021) 186–204. https://doi.org/10.1007/s10163-020-01114-2.

[35] R. Nava, B. Pawelec, P. Castaño, M.C. Álvarez-Galván, C. V. Loricera, J.L.G. Fierro, Upgrading of bio-liquids on different mesoporous silica-supported CoMo catalysts, Appl. Catal. B Environ. 92 (2009) 154–167. https://doi.org/10.1016/j.apcatb.2009.07.014.

[36] J. Ancheyta, J.G. Speight, Hydroprocessing of heavy oils and residua, CRC press, 2007. https://doi.org/10.1179/174602208x330293.

[37] C. Xu, T. Etcheverry, Hydro-liquefaction of woody biomass in sub- and super-critical ethanol with iron-based catalysts, Fuel. 87 (2008) 335–345. https://doi.org/10.1016/j.fuel.2007.05.013.

[38] S. Yaman, Pyrolysis of biomass to produce fuels and chemical feedstocks, Energy Convers. Manag. 45 (2004) 651–671. https://doi.org/10.1016/S0196-8904(03)00177-8.

[39] S. Xiu, A. Shahbazi, Bio-oil production and upgrading research: A review, Renew.

Sustain. Energy Rev. 16 (2012) 4406–4414. https://doi.org/10.1016/j.rser.2012.04.028.

[40] P.P. Singh, N. Nirmalkar, T. Mondal, Catalytic steam reforming of simulated bio-oil for green hydrogen production using highly active LaNixCo1−xO3 perovskite catalysts, Sustain. Energy Fuels. 6 (2022) 1063–1074. https://doi.org/10.1039/d1se01786a.

[41] T. Mondal, N. Kaul, R. Mittal, K.K. Pant, Catalytic Steam Reforming of Model Oxygenates of Bio-oil for Hydrogen Production Over La Modified Ni/CeO2–ZrO2 Catalyst, Top. Catal. 59 (2016) 1343–1353. https://doi.org/10.1007/s11244-016-0662-3.

[42] J. Rostrup-Nielsen, Steam reforming of hydrocarbons. A historical perspective, Stud. Surf. Sci. Catal. 147 (2004) 121–126. https://doi.org/10.1016/s0167-2991(04)80038-7.

[43] J. Chen, J. Sun, Y. Wang, Catalysts for Steam Reforming of Bio-oil: A Review, Ind. Eng. Chem. Res. 56 (2017) 4627–4637. https://doi.org/10.1021/acs.iecr.7b00600.

[44] A.G. Adeniyi, K.S. Otoikhian, J.O. Ighalo, Steam Reforming of Biomass Pyrolysis Oil: A Review, Int. J. Chem. React. Eng. 17 (2019) 20180328. https://doi.org/10.1515/ijcre-2018-0328.

[45] B. Dou, H. Zhang, Y. Song, L. Zhao, B. Jiang, M. He, C. Ruan, H. Chen, Y. Xu, Hydrogen production from the thermochemical conversion of biomass: Issues and challenges, Sustain. Energy Fuels. 3 (2019) 314–342. https://doi.org/10.1039/c8se00535d.

[46] C. Montero, A. Remiro, B. Valle, L. Oar-Arteta, J. Bilbao, A.G. Gayubo, Origin and Nature of Coke in Ethanol Steam Reforming and Its Role in Deactivation of Ni/La2O3-αAl2O3 Catalyst, Ind. Eng. Chem. Res. 58 (2019) 14736–14751. https://doi.org/10.1021/acs.iecr.9b02880.

[47] S.D. Davidson, H. Zhang, J. Sun, Y. Wang, Supported metal catalysts for alcohol/sugar alcohol steam reforming, Dalt. Trans. 43 (2014) 11782–11802. https://doi.org/10.1039/c4dt00521j.

[48] S. Ayalur Chattanathan, S. Adhikari, N. Abdoulmoumine, A review on current status of hydrogen production from bio-oil, Renew. Sustain. Energy Rev. 16 (2012) 2366–2372. https://doi.org/10.1016/j.rser.2012.01.051.

[49] J. Román Galdámez, L. García, R. Bilbao, Hydrogen production by steam reforming of bio-oil using coprecipitated Ni-Al catalysts. Acetic acid as a model compound, Energy and Fuels. 19 (2005) 1133–1142. https://doi.org/10.1021/ef049718g.

[50] Z. Wang, Y. Pan, T. Dong, X. Zhu, T. Kan, L. Yuan, Y. Torimoto, M. Sadakata, Q. Li, Production of hydrogen from catalytic steam reforming of bio-oil using C12A7-O--based catalysts, Appl. Catal. A Gen. 320 (2007) 24–34. https://doi.org/10.1016/j.apcata.2006.12.003.

[51] E.C. Vagia, A.A. Lemonidou, Hydrogen production via steam reforming of bio-oil components over calcium aluminate supported nickel and noble metal catalysts, Appl. Catal. A Gen. 351 (2008) 111–121.

https://doi.org/10.1016/j.apcata.2008.09.007.

[52] M. Pouralamdari Meibod, Bio-oil from Wheat Straw and Hydrogen from Aqueous Phase of Bio-oil, UNIVERSITY OF CALGARY, 2013. https://doi.org/10.11575/PRISM/25133.

[53] X. Hu, G. Lu, Comparative study of alumina-supported transition metal catalysts for hydrogen generation by steam reforming of acetic acid, Appl. Catal. B Environ. 99 (2010) 289–297. https://doi.org/10.1016/j.apcatb.2010.06.035.

[54] E.C. Vagia, A.A. Lemonidou, Thermodynamic analysis of hydrogen production via steam reforming of selected components of aqueous bio-oil fraction, Int. J. Hydrogen Energy. 32 (2007) 212–223. https://doi.org/10.1016/j.ijhydene.2006.08.021.

[55] G. Chen, J. Tao, C. Liu, B. Yan, W. Li, X. Li, Hydrogen production via acetic acid steam reforming: A critical review on catalysts, Renew. Sustain. Energy Rev. 79 (2017) 1091–1098. https://doi.org/10.1016/j.rser.2017.05.107.

[56] X. Hu, L. Zhang, G. Lu, Steam reforming of acetic acid over Cu[sbnd]Zn[sbnd]Co catalyst for hydrogen generation: Synergistic effects of the metal species, Int. J. Hydrogen Energy. 41 (2016) 13960–13969. https://doi.org/10.1016/j.ijhydene.2016.05.066.

[57] S. Goicoechea, E. Kraleva, S. Sokolov, M. Schneider, M.M. Pohl, N. Kockmann, H. Ehrich, Support effect on structure and performance of Co and Ni catalysts for steam reforming of acetic acid, Appl. Catal. A Gen. 514 (2016) 182–191. https://doi.org/10.1016/j.apcata.2015.12.025.

[58] X. Hu, L. Zhang, G. Lu, Pruning of the surface species on Ni/Al 2O 3 catalyst to selective production of hydrogen via acetone and acetic acid steam reforming, Appl. Catal. A Gen. 427–428 (2012) 49–57. https://doi.org/10.1016/j.apcata.2012.03.029.

[59] X. Yang, Y. Weng, M. Li, B. Sun, Y. Li, Y. Wang, Enhanced Hydrogen Production by Steam Reforming of Acetic Acid over a Ni Catalyst Supported on Mesoporous MgO, Energy and Fuels. 30 (2016) 2198–2203. https://doi.org/10.1021/acs.energyfuels.5b02615.

[60] T. Mondal, K.K. Pant, A.K. Dalai, Oxidative and non-oxidative steam reforming of crude bio-ethanol for hydrogen production over Rh promoted Ni/CeO2-ZrO2 catalyst, Appl. Catal. A Gen. 499 (2015) 19–31. https://doi.org/10.1016/j.apcata.2015.04.004.

[61] S. Mahamulkar, Anti-Coking Materials for Steam Crackers, (2017).

[62] A. Arandia, A. Remiro, B. Valle, J. Bilbao, A.G. Gayubo, Deactivation of Ni spinel derived catalyst during the oxidative steam reforming of raw bio-oil, Fuel. 276 (2020) 117995. https://doi.org/10.1016/j.fuel.2020.117995.

[63] Y. Wang, C. Wang, M. Chen, J. Hu, Z. Tang, D. Liang, W. Cheng, Z. Yang, J. Wang, H. Zhang, Influence of CoAl2O4 spinel and Co-phyllosilicate structures derived from Co/sepiolite catalysts on steam reforming of bio-oil for hydrogen production, Fuel. 279 (2020) 118449. https://doi.org/10.1016/j.fuel.2020.118449.

[64] L. Landa, A. Remiro, J. Valecillos, B. Valle, J. Bilbao, A.G. Gayubo, Unveiling the deactivation by coke of NiAl2O4 spinel derived catalysts in the bio-oil steam

reforming: Role of individual oxygenates, Fuel. 321 (2022). https://doi.org/10.1016/j.fuel.2022.124009.

[65] N. García-Gómez, J. Valecillos, A. Remiro, B. Valle, J. Bilbao, A.G. Gayubo, Effect of reaction conditions on the deactivation by coke of a NiAl2O4 spinel derived catalyst in the steam reforming of bio-oil, Appl. Catal. B Environ. 297 (2021). https://doi.org/10.1016/j.apcatb.2021.120445.

[66] N.G. Saeidabad, Y.S. Noh, A.A. Eslami, H.T. Song, H.D. Kim, A. Fazeli, D.J. Moon, A review on catalysts development for steam reforming of biodiesel derived glycerol; promoters and supports, Catalysts. 10 (2020) 1–22. https://doi.org/10.3390/catal10080910.

[67] Z. Bian, Z. Wang, B. Jiang, P. Hongmanorom, W. Zhong, S. Kawi, A review on perovskite catalysts for reforming of methane to hydrogen production, Renew. Sustain. Energy Rev. 134 (2020) 110291. https://doi.org/10.1016/j.rser.2020.110291.

[68] S. Bhattar, M.A. Abedin, S. Kanitkar, J.J. Spivey, A review on dry reforming of methane over perovskite derived catalysts, Catal. Today. 365 (2021) 2–23. https://doi.org/10.1016/j.cattod.2020.10.041.

[69] L. Cao, I.K.M. Yu, X. Xiong, D.C.W. Tsang, S. Zhang, J.H. Clark, C. Hu, Y.H. Ng, J. Shang, Y.S. Ok, Biorenewable hydrogen production through biomass gasification: A review and future prospects, Environ. Res. 186 (2020) 109547. https://doi.org/10.1016/j.envres.2020.109547.

[70] P.P. Singh, N. Nirmalkar, T. Mondal, Catalytic steam reforming of simulated bio-oil for green hydrogen production using highly active LaNi x Co 1− x O 3 perovskite catalysts, Sustain. Energy Fuels. 6 (2022) 1063–1074. https://doi.org/10.1039/D1SE01786A.

[71] C. Liu, D. Chen, J. Ashok, P. Hongmanorom, W. Wang, T. Li, Z. Wang, S. Kawi, Chemical looping steam reforming of bio-oil for hydrogen-rich syngas production: Effect of doping on LaNi0.8Fe0.2O3 perovskite, Int. J. Hydrogen Energy. 45 (2020) 21123–21137. https://doi.org/10.1016/j.ijhydene.2020.05.186.

[72] Q. Yang, G. Liu, Y. Liu, Perovskite-Type Oxides as the Catalyst Precursors for Preparing Supported Metallic Nanocatalysts: A Review, Ind. Eng. Chem. Res. 57 (2018) 1–17. https://doi.org/10.1021/acs.iecr.7b03251.

[73] F.G.E. Nogueira, P.G.M. Assaf, H.W.P. Carvalho, E.M. Assaf, Catalytic steam reforming of acetic acid as a model compound of bio-oil, Appl. Catal. B Environ. 160–161 (2014) 188–199. https://doi.org/10.1016/j.apcatb.2014.05.024.

[74] Z. Ou, Z. Zhang, C. Qin, H. Xia, T. Deng, J. Niu, J. Ran, C. Wu, Highly active and stable Ni/perovskite catalysts in steam methane reforming for hydrogen production, Sustain. Energy Fuels. 5 (2021) 1845–1856. https://doi.org/10.1039/d1se00082a.

[75] U. Oemar, P.S. Ang, K. Hidajat, S. Kawi, Promotional effect of Fe on perovskite LaNixFe 1-xO3 catalyst for hydrogen production via steam reforming of toluene, Int. J. Hydrogen Energy. 38 (2013) 5525–5534. https://doi.org/10.1016/j.ijhydene.2013.02.083.

[76] G. Chen, J. Yao, J. Liu, B. Yan, R. Shan, Biomass to hydrogen-rich syngas via catalytic steam reforming of bio-oil, Renew. Energy. 91 (2016) 315–322. https://doi.org/10.1016/j.renene.2016.01.073.

[77] C. Liu, S. Li, Dong chen, Y. Xiao, T. Li, W. Wang, Hydrogen-rich syngas production by chemical looping steam reforming of acetic acid as bio-oil model compound over Fe-doped LaNiO3 oxygen carriers, Int. J. Hydrogen Energy. 44 (2019) 17732–17741. https://doi.org/10.1016/j.ijhydene.2019.05.148.

[78] J. Alvarez, G. Lopez, M. Amutio, J. Bilbao, M. Olazar, Bio-oil production from rice husk fast pyrolysis in a conical spouted bed reactor, Fuel. 128 (2014) 162–169. https://doi.org/10.1016/j.fuel.2014.02.074.

[79] J. Yao, J. Liu, H. Hofbauer, G. Chen, B. Yan, R. Shan, W. Li, Biomass to hydrogen-rich syngas via steam gasification of bio-oil/biochar slurry over LaCo1-xCuxO3 perovskite-type catalysts, Energy Convers. Manag. 117 (2016) 343–350. https://doi.org/10.1016/j.enconman.2016.03.043.

[80] G. Chen, J. Yao, J. Liu, B. Yan, R. Shan, Biomass to hydrogen-rich syngas via catalytic steam gasification of bio-oil/biochar slurry, Bioresour. Technol. 198 (2015) 108–114. https://doi.org/10.1016/j.biortech.2015.09.009.

[81] S.M. De Lima, A.M. Da Silva, L.O.O. Da Costa, J.M. Assaf, L. V. Mattos, R. Sarkari, A. Venugopal, F.B. Noronha, Hydrogen production through oxidative steam reforming of ethanol over Ni-based catalysts derived from La 1-xCe xNiO 3 perovskite-type oxides, Appl. Catal. B Environ. 121–122 (2012) 1–9. https://doi.org/10.1016/j.apcatb.2012.03.017.

[82] D. Phadtare, S. Kondawar, A. Athawale, C. Rode, Crystalline LaCoO3 perovskite as a novel catalyst for glycerol transesterification, Mol. Catal. 475 (2019) 110496. https://doi.org/10.1016/j.mcat.2019.110496.

[83] M. Mousavi, A. Nakhaei Pour, Performance and structural features of LaNi0.5Co0.5O3 perovskite oxides for the dry reforming of methane: Influence of the preparation method, New J. Chem. 43 (2019) 10763–10773. https://doi.org/10.1039/c9nj01805k.

[84] A. Khan, R. Hussain, A.M. Toufiq, A. Shah, B.A. Khan, Z. Niaz, S. ur Rahman, Fabrication of cryptomelane FexMn1-xO2 with enhanced antibacterial activity and specific heat capacity, Mater. Charact. 169 (2020) 110661. https://doi.org/10.1016/j.matchar.2020.110661.

[85] A.M. Toufiq, F. Wang, Q.U.A. Javed, Y. Li, Magnetic properties of MnO2 shrimps-like nanostructures synthesized by hydrothermal route, Mod. Phys. Lett. B. 27 (2013) 1–8. https://doi.org/10.1142/S0217984913502151.

[86] E.H. Yang, Y.S. Noh, S. Ramesh, S.S. Lim, D.J. Moon, The effect of promoters in La0.9M0.1Ni0.5Fe0.5O3 (M = Sr, Ca) perovskite catalysts on dry reforming of methane, Fuel Process. Technol. 134 (2015) 404–413. https://doi.org/10.1016/j.fuproc.2015.02.023.

[87] F. Liu, Y. Qu, Y. Yue, G. Liu, Y. Liu, Nano bimetallic alloy of Ni-Co obtained from LaCoxNi1-xO3 and its catalytic performance for steam reforming of ethanol, RSC Adv. 5 (2015) 16837–16846. https://doi.org/10.1039/c4ra14131h.

[88] S.H. Hong, S.H. Ahn, I. Choi, S.G. Pyo, H.J. Kim, J.H. Jang, S.K. Kim, Fabrication and evaluation of nickel cobalt alloy electrocatalysts for alkaline water splitting, Appl. Surf. Sci. 307 (2014) 146–152. https://doi.org/10.1016/j.apsusc.2014.03.197.

[89] J. Li, G. Lu, G. Wu, D. Mao, Y. Wang, Y. Guo, Promotional role of ceria on cobaltosic oxide catalyst for low-temperature CO oxidation, Catal. Sci. Technol. 2 (2012) 1865–1871. https://doi.org/10.1039/c2cy20118f.

[90] T. Mondal, K.K. Pant, A.K. Dalai, Catalytic oxidative steam reforming of bio-ethanol for hydrogen production over Rh promoted Ni/CeO2-ZrO2 catalyst, Int. J. Hydrogen Energy. 40 (2015) 2529–2544. https://doi.org/10.1016/j.ijhydene.2014.12.070.

[91] M. Ao, G.H. Pham, V. Sage, V. Pareek, Structure and activity of strontium substituted LaCoO3 perovskite catalysts for syngas conversion, J. Mol. Catal. A Chem. 416 (2016) 96–104. https://doi.org/10.1016/j.molcata.2016.02.020.

[92] X. Gao, J. Ashok, S. Kawi, N. Yang, Steam reforming of toluene as model compound of biomass tar over Ni–Co/La2O3 nano-catalysts: Synergy of Ni and Co, Int. J. Hydrogen Energy. 46 (2021) 30926–30936. https://doi.org/10.1016/j.ijhydene.2021.04.047.

[93] S.M. de Lima, J.M. Assaf, Synthesis and Characterization of LaNiO3, LaNi(1-x)Fe xO3 andLaNi(1-x)Co xO3 Perovskite Oxides for Catalysis Application, Mater. Res. 5 (2002) 329–335. https://doi.org/10.1590/s1516-14392002000300018.

[94] S.D. Davidson, K.A. Spies, D. Mei, L. Kovarik, I. Kutnyakov, X.S. Li, V. Lebarbier Dagle, K.O. Albrecht, R.A. Dagle, Steam Reforming of Acetic Acid over Co-Supported Catalysts: Coupling Ketonization for Greater Stability, ACS Sustain. Chem. Eng. 5 (2017) 9136–9149. https://doi.org/10.1021/acssuschemeng.7b02052.

[95] F. Zhang, M. Wang, L. Zhu, S. Wang, J. Zhou, Z. Luo, A comparative research on the catalytic activity of La2O3 and Γ-Al2O3 supported catalysts for acetic acid steam reforming, Int. J. Hydrogen Energy. 42 (2017) 3667–3675. https://doi.org/10.1016/j.ijhydene.2016.06.264.

[96] X. Hu, D. Dong, X. Shao, L. Zhang, G. Lu, Steam reforming of acetic acid over cobalt catalysts: Effects of Zr, Mg and K addition, Int. J. Hydrogen Energy. 42 (2017) 4793–4803. https://doi.org/10.1016/j.ijhydene.2016.12.033.

[97] K.A. Resende, C.N. Ávila-Neto, R.C. Rabelo-Neto, F.B. Noronha, C.E. Hori, Hydrogen production by reforming of acetic acid using La-Ni type perovskites partially substituted with Sm and Pr, Catal. Today. 242 (2015) 71–79. https://doi.org/10.1016/j.cattod.2014.07.013.

[98] M.S. Abu Bakar, J.O. Titiloye, Catalytic pyrolysis of rice husk for bio-oil production, in: J. Anal. Appl. Pyrolysis, Elsevier B.V., 2013: pp. 362–368. https://doi.org/10.1016/j.jaap.2012.09.005.

[99] W. Cai, L. Dai, R. Liu, Catalytic fast pyrolysis of rice husk for bio-oil production, Energy. 154 (2018) 477–487. https://doi.org/10.1016/j.energy.2018.04.157.

[100] H.R. Vergara, M.H. Brijaldo, J.J. Martinez, H.A. Rojas, J. Pedraza, F.B. Passos, L.P. da Costa, D. Gonzalez-Vera, P. Osorio-Vargas, Effect of metal content on ethanol

decomposition over Ni-Co catalysts supported on La-Ce oxides, Materials (Basel). 13 (2020). https://doi.org/10.3390/ma13030759.

[101] J. Yan, W. Liu, R. Sun, S. Jiang, S. Wang, L. Shen, Chemical looping catalytic gasification of biomass over active LaNixFe1-xO3 perovskites as functional oxygen carriers, Chinese J. Chem. Eng. 36 (2021) 146–156. https://doi.org/10.1016/j.cjche.2020.09.038.

[102] L. Zeng, T. Peng, H. Sun, J. Yang, Y. Li, Y. Qin, Fe-doped LaNi1-xFexO3 perovskite oxides for enhanced visible-light-driven photocatalytic activity, J. Solid State Chem. 297 (2021) 122033. https://doi.org/10.1016/j.jssc.2021.122033.

[103] Y. Luo, X. Wang, Q. Qian, Q. Chen, Studies on B sites in Fe-doped LaNiO3 perovskite for SCR of NOx with H2, Int. J. Hydrogen Energy. 39 (2014) 15836–15843. https://doi.org/10.1016/j.ijhydene.2014.07.135.

[104] S. Ramesh, E.H. Yang, J.S. Jung, D.J. Moon, Copper decorated perovskite an efficient catalyst for low temperature hydrogen production by steam reforming of glycerol, Int. J. Hydrogen Energy. 40 (2015) 11428–11435. https://doi.org/10.1016/j.ijhydene.2015.02.013.

[105] S.M. de Lima, A.M. da Silva, L.O.O. da Costa, J.M. Assaf, G. Jacobs, B.H. Davis, L. V. Mattos, F.B. Noronha, Evaluation of the performance of Ni/La2O3 catalyst prepared from LaNiO3 perovskite-type oxides for the production of hydrogen through steam reforming and oxidative steam reforming of ethanol, Appl. Catal. A Gen. 377 (2010) 181–190. https://doi.org/10.1016/j.apcata.2010.01.036.

[106] L. Li, B. Jiang, D. Tang, Q. Zhang, Z. Zheng, Hydrogen generation by acetic acid steam reforming over Ni-based catalysts derived from La1−xCexNiO3 perovskite, Int. J. Hydrogen Energy. 43 (2018) 6795–6803. https://doi.org/10.1016/j.ijhydene.2018.02.128.

[107] G. Pecchi, M.G. Jiliberto, E.J. Delgado, L.E. Cadús, J.L.G. Fierro, Effect of B-site cation on the catalytic activity of La1-xCaxBO3 (B = Fe, Ni) perovskite-type oxides for toluene combustion, J. Chem. Technol. Biotechnol. 86 (2011) 1067–1073. https://doi.org/10.1002/jctb.2611.

[108] J.A. Onrubia-Calvo, A. Bermejo-López, B. Pereda-Ayo, J.A. González-Marcos, J.R. González-Velasco, Ca doping effect on the performance of La1−xCaxNiO3/CeO2-derived dual function materials for CO2 capture and hydrogenation to methane, Appl. Catal. B Environ. 321 (2023). https://doi.org/10.1016/j.apcatb.2022.122045.

[109] T. Maneerung, K. Hidajat, S. Kawi, LaNiO3 perovskite catalyst precursor for rapid decomposition of methane: Influence of temperature and presence of H2 in feed stream, Catal. Today. 171 (2011) 24–35. https://doi.org/10.1016/j.cattod.2011.03.080.

[110] H. Provendier, C. Petit, A. Kiennemann, Steam reforming of methane on LaNixFe1-xO3 (0≤x≤1) perovskites. Reactivity and characterisation after test, Comptes Rendus l'Academie Des Sci. - Ser. IIc Chem. 4 (2001) 57–66. https://doi.org/10.1016/S1387-1609(00)01212-3.

[111] S.M. de Lima, J.M. Assaf, Ni–Fe Catalysts Based on Perovskite-type Oxides for Dry Reforming of Methane to Syngas, Catal. Letters. 108 (2006) 63–70.

https://doi.org/10.1007/s10562-006-0026-x.

[112] H. Provendier, C. Petit, C. Estournès, S. Libs, A. Kiennemann, Stabilisation of active nickel catalysts in partial oxidation of methane to synthesis gas by iron addition, Appl. Catal. A Gen. 180 (1999) 163–173. https://doi.org/10.1016/S0926-860X(98)00343-3.

[113] H. Arandiyan, J. Li, L. Ma, S.M. Hashemnejad, M.Z. Mirzaei, J. Chen, H. Chang, C. Liu, C. Wang, L. Chen, Methane reforming to syngas over LaNi xFe 1-xO 3 (0≤x≤1) mixed-oxide perovskites in the presence of CO 2 and O 2, J. Ind. Eng. Chem. 18 (2012) 2103–2114. https://doi.org/10.1016/j.jiec.2012.06.004.

[114] K. Soongprasit, D. Aht-Ong, V. Sricharoenchaikul, D. Atong, Synthesis and catalytic activity of sol-gel derived La-Ce-Ni perovskite mixed oxide on steam reforming of toluene, Curr. Appl. Phys. 12 (2012) S80–S88. https://doi.org/10.1016/j.cap.2012.02.025.

[115] S. Podila, H. Driss, A.M. Ali, A.A. Al-Zahrani, M.A. Daous, Influence of Ce substitution in LaMO3 (M = Co/Ni) perovskites for COx-free hydrogen production from ammonia decomposition, Arab. J. Chem. 15 (2022) 103547. https://doi.org/10.1016/j.arabjc.2021.103547.

[116] R.B.S. Junior, R.C. Rabelo-Neto, R.S. Gomes, F.B. Noronha, R. Fréty, S.T. Brandão, Steam reforming of acetic acid over Ni-based catalysts derived from La1−xCaxNiO3 perovskite type oxides, Fuel. 254 (2019). https://doi.org/10.1016/j.fuel.2019.115714.

[117] J. Yang, S. Hu, L. Shi, S. Hoang, W. Yang, Y. Fang, Z. Liang, C. Pan, Y. Zhu, L. Li, J. Wu, J. Hu, Y. Guo, Oxygen Vacancies and Lewis Acid Sites Synergistically Promoted Catalytic Methane Combustion over Perovskite Oxides, Environ. Sci. Technol. 55 (2021) 9243–9254. https://doi.org/10.1021/acs.est.1c00511.

[118] S. Das, S. Bhattar, L. Liu, Z. Wang, S. Xi, J.J. Spivey, S. Kawi, Effect of Partial Fe Substitution in La0.9Sr0.1NiO3Perovskite-Derived Catalysts on the Reaction Mechanism of Methane Dry Reforming, ACS Catal. 10 (2020) 12466–12486. https://doi.org/10.1021/acscatal.0c01229.

[119] A. Safakas, G. Bampos, S. Bebelis, Oxygen reduction reaction on La0.8Sr0.2CoxFe1-xO3-Δ perovskite/carbon black electrocatalysts in alkaline medium, Appl. Catal. B Environ. 244 (2019) 225–232. https://doi.org/10.1016/j.apcatb.2018.11.015.

[120] A. Grimaud, O. Diaz-Morales, B. Han, W.T. Hong, Y.L. Lee, L. Giordano, K.A. Stoerzinger, M.T.M. Koper, Y. Shao-Horn, Activating lattice oxygen redox reactions in metal oxides to catalyse oxygen evolution, Nat. Chem. 9 (2017) 457–465. https://doi.org/10.1038/nchem.2695.

[121] Y. Da, L. Zeng, C. Wang, T. Mao, R. Chen, C. Gong, G. Fan, Catalytic oxidation of diesel soot particulates over Pt substituted LaMn 1-x Pt x O 3 perovskite oxides, Catal. Today. 327 (2019) 73–80. https://doi.org/10.1016/j.cattod.2018.06.007.

[122] C. Quan, S. Xu, C. Zhou, Steam reforming of bio-oil from coconut shell pyrolysis over Fe/olivine catalyst, Energy Convers. Manag. 141 (2017) 40–47. https://doi.org/10.1016/j.enconman.2016.04.024.

[123] J.A. Calles, A. Carrero, A.J. Vizcaíno, L. García-Moreno, P.J. Megía, Steam reforming of model bio-oil aqueous fraction using Ni-(Cu, Co, Cr)/SBA-15 catalysts, Int. J. Mol. Sci. 20 (2019). https://doi.org/10.3390/ijms20030512.

[124] M. Artetxe, M.A. Nahil, M. Olazar, P.T. Williams, Steam reforming of phenol as biomass tar model compound over Ni/Al2O3 catalyst, Fuel. 184 (2016) 629–636. https://doi.org/10.1016/j.fuel.2016.07.036.

[125] S. Wang, Q. Cai, F. Zhang, X. Li, L. Zhang, Z. Luo, Hydrogen production via catalytic reforming of the bio-oil model compounds: Acetic acid, phenol and hydroxyacetone, Int. J. Hydrogen Energy. 39 (2014) 18675–18687. https://doi.org/10.1016/j.ijhydene.2014.01.142.

[126] A. Arregi, G. Lopez, M. Amutio, I. Barbarias, L. Santamaria, J. Bilbao, M. Olazar, Kinetic study of the catalytic reforming of biomass pyrolysis volatiles over a commercial Ni/Al2O3 catalyst, Int. J. Hydrogen Energy. 43 (2018) 12023–12033. https://doi.org/10.1016/j.ijhydene.2018.05.032.

[127] I. Llera, V. Mas, M.L. Bergamini, M. Laborde, N. Amadeo, Bio-ethanol steam reforming on Ni based catalyst. Kinetic study, Chem. Eng. Sci. 71 (2012) 356–366. https://doi.org/10.1016/j.ces.2011.12.018.

[128] T.Y. Ahmed, A. Tanksale, A.F.A. Hoadley, A kinetic model for air-steam reforming of bio-oil over Rh–Ni/γ-Al2O3 catalyst: Acetol as a model compound, Int. J. Hydrogen Energy. 45 (2020) 24300–24311. https://doi.org/10.1016/j.ijhydene.2020.06.219.

[129] T. Mondal, K.K. Pant, A.K. Dalai, Mechanistic Kinetic Modeling of Oxidative Steam Reforming of Bioethanol for Hydrogen Production over Rh-Ni/CeO2-ZrO2 Catalyst, Ind. Eng. Chem. Res. 55 (2016) 86–98. https://doi.org/10.1021/acs.iecr.5b03828.

[130] S. Wang, F. Zhang, Q. Cai, X. Li, L. Zhu, Q. Wang, Z. Luo, Catalytic steam reforming of bio-oil model compounds for hydrogen production over coal ash supported Ni catalyst, Int. J. Hydrogen Energy. 39 (2014) 2018–2025. https://doi.org/10.1016/j.ijhydene.2013.11.129.

[131] Y. Xu, Y. Zhu, P. Shen, G. Chen, X. Li, Production of hydrogen by steam reforming of phenol over Ni/Al2O3-ash catalysts, Int. J. Hydrogen Energy. 47 (2022) 13592–13603. https://doi.org/10.1016/j.ijhydene.2022.02.097.

[132] P.J. Megía, M. Cortese, C. Ruocco, A.J. Vizcaíno, J.A. Calles, A. Carrero, V. Palma, Catalytic behavior of co-based catalysts in the kinetic study of acetic acid steam reforming, Ind. Eng. Chem. Res. 59 (2020) 19531–19538. https://doi.org/10.1021/acs.iecr.0c03599.

[133] A. Ochoa, J. Bilbao, A.G. Gayubo, P. Castaño, Coke formation and deactivation during catalytic reforming of biomass and waste pyrolysis products: A review, Renew. Sustain. Energy Rev. 119 (2020) 109600. https://doi.org/10.1016/j.rser.2019.109600.

[134] O. Levenspiel, Chemical reaction engineering, 2008. https://doi.org/10.1201/9781420087567-13.

[135] H.S. Fogler, Elements of Chemical Reaction Engineering, 2004.

[136] H.S. Heo, H.J. Park, J.I. Dong, S.H. Park, S. Kim, D.J. Suh, Y.W. Suh, S.S. Kim, Y.K. Park, Fast pyrolysis of rice husk under different reaction conditions, J. Ind. Eng. Chem. 16 (2010) 27–31. https://doi.org/10.1016/j.jiec.2010.01.026.

[137] Z. Ji-lu, Bio-oil from fast pyrolysis of rice husk: Yields and related properties and improvement of the pyrolysis system, J. Anal. Appl. Pyrolysis. 80 (2007) 30–35. https://doi.org/10.1016/J.JAAP.2006.12.030.

[138] J. Alvarez, G. Lopez, M. Amutio, J. Bilbao, M. Olazar, Bio-oil production from rice husk fast pyrolysis in a conical spouted bed reactor, Fuel. 128 (2014) 162–169. https://doi.org/10.1016/J.FUEL.2014.02.074.

[139] S.H. Chang, Rice Husk and Its Pretreatments for Bio-oil Production via Fast Pyrolysis: a Review, Bioenergy Res. 13 (2020) 23–42. https://doi.org/10.1007/s12155-019-10059-w.

[140] S. Şensöz, I. Demiral, H.F. Gerçel, Olive bagasse (Olea europea L.) pyrolysis, Bioresour. Technol. 97 (2006) 429–436. https://doi.org/10.1016/j.biortech.2005.03.007.

[141] B. Biswas, N. Pandey, Y. Bisht, R. Singh, J. Kumar, T. Bhaskar, Pyrolysis of agricultural biomass residues: Comparative study of corn cob, wheat straw, rice straw and rice husk, Bioresour. Technol. 237 (2017) 57–63. https://doi.org/10.1016/j.biortech.2017.02.046.

[142] V. Dhyani, T. Bhaskar, A comprehensive review on the pyrolysis of lignocellulosic biomass, Renew. Energy. 129 (2018) 695–716. https://doi.org/10.1016/j.renene.2017.04.035.

[143] H.S. Heo, H.J. Park, J.I. Dong, S.H. Park, S. Kim, D.J. Suh, Y.W. Suh, S.S. Kim, Y.K. Park, Fast pyrolysis of rice husk under different reaction conditions, J. Ind. Eng. Chem. 16 (2010) 27–31. https://doi.org/10.1016/J.JIEC.2010.01.026.

[144] B. Valle, B. Aramburu, P.L. Benito, J. Bilbao, A.G. Gayubo, Biomass to hydrogen-rich gas via steam reforming of raw bio-oil over Ni/La2O3-AAl2O3 catalyst: Effect of space-time and steam-to-carbon ratio, Fuel. 216 (2018) 445–455. https://doi.org/10.1016/j.fuel.2017.11.151.

[145] Z. Zhao, Y.A. Situmorang, P. An, N. Chaihad, J. Wang, X. Hao, G. Xu, A. Abudula, G. Guan, Hydrogen Production from Catalytic Steam Reforming of Bio-Oils: A Critical Review, Chem. Eng. Technol. 43 (2020) 625–640. https://doi.org/10.1002/ceat.201900487.

[146] W. Chen, S. Shi, J. Zhang, M. Chen, X. Zhou, Co-pyrolysis of waste newspaper with high-density polyethylene: Synergistic effect and oil characterization, Energy Convers. Manag. 112 (2016) 41–48. https://doi.org/10.1016/j.enconman.2016.01.005.

[147] U. Oemar, M.L. Ang, K. Hidajat, S. Kawi, Enhancing performance of Ni/La2O3 catalyst by Sr-modification for steam reforming of toluene as model compound of biomass tar, RSC Adv. 5 (2015) 17834–17842. https://doi.org/10.1039/c4ra16983b.

[148] A. Ochoa, B. Aramburu, B. Valle, D.E. Resasco, J. Bilbao, A.G. Gayubo, P. Castaño,

Role of oxygenates and effect of operating conditions in the deactivation of a Ni supported catalyst during the steam reforming of bio-oil, Green Chem. 19 (2017) 4315–4333. https://doi.org/10.1039/c7gc01432e.

[149] D. Zeng, Y. Qiu, S. Zhang, L. Ma, M. Li, D. Cui, J. Zeng, R. Xiao, Synergistic effects of binary oxygen carriers during chemical looping hydrogen production, Int. J. Hydrogen Energy. 44 (2019) 21290–21302. https://doi.org/10.1016/j.ijhydene.2019.06.118.

[150] D. Cui, Y. Qiu, M. Li, L. Ma, S. Zhang, D. Zeng, R. Xiao, Cu–Fe–Al–O mixed spinel oxides as oxygen carrier for chemical looping hydrogen generation, Int. J. Hydrogen Energy. 45 (2020) 11908–11915. https://doi.org/10.1016/j.ijhydene.2020.02.145.

[151] A. Sadezky, H. Muckenhuber, H. Grothe, R. Niessner, U. Pöschl, Raman microspectroscopy of soot and related carbonaceous materials: Spectral analysis and structural information, Carbon N. Y. 43 (2005) 1731–1742. https://doi.org/10.1016/j.carbon.2005.02.018.

[152] L. He, G. Liao, H. Li, Q. Ren, S. Hu, H. Han, J. Xu, L. Jiang, S. Su, Y. Wang, J. Xiang, Evolution characteristics of different types of coke deposition during catalytic removal of biomass tar, J. Energy Inst. 93 (2020) 2497–2504. https://doi.org/10.1016/j.joei.2020.08.009.

[153] X. Li, Z. Zhang, L. Zhang, H. Fan, X. Li, Q. Liu, S. Wang, X. Hu, Investigation of coking behaviors of model compounds in bio-oil during steam reforming, Fuel. 265 (2020) 116961. https://doi.org/10.1016/j.fuel.2019.116961.

[154] P. Lu, Q. Huang, A.C. Bourtsalas, Y. Chi, J. Yan, Effect of Operating Conditions on the Coke Formation and Nickel Catalyst Performance During Cracking of Tar, Waste and Biomass Valorization. 10 (2019) 155–165. https://doi.org/10.1007/s12649-017-0044-5.

[155] H.D. Setiabudi, M.A.A. Aziz, S. Abdullah, L.P. Teh, R. Jusoh, Hydrogen production from catalytic steam reforming of biomass pyrolysis oil or bio-oil derivatives: A review, Int. J. Hydrogen Energy. 45 (2020) 18376–18397. https://doi.org/10.1016/j.ijhydene.2019.10.141.

[156] N. García-Gómez, J. Valecillos, B. Valle, A. Remiro, J. Bilbao, A.G. Gayubo, Combined effect of bio-oil composition and temperature on the stability of Ni spinel derived catalyst for hydrogen production by steam reforming, Fuel. 326 (2022). https://doi.org/10.1016/j.fuel.2022.124966.

[157] B. Valle, B. Aramburu, M. Olazar, J. Bilbao, A.G. Gayubo, Steam reforming of raw bio-oil over Ni/La2O3-αAl2O3: Influence of temperature on product yields and catalyst deactivation, Fuel. 216 (2018) 463–474. https://doi.org/10.1016/j.fuel.2017.11.149.

[158] J.P.P. Attfield, G. Férey, Structure determinations of La2O2CO3-II and the unusual disordered phase La2O2.52(CO3)0.74Li0.52 using powder diffraction, J. Solid State Chem. 82 (1989) 132–138. https://doi.org/10.1016/0022-4596(89)90232-6.

[159] Y. Ruan, Y. Zhao, Y. Lu, D. Guo, Y. Zhao, S. Wang, X. Ma, Mesoporous LaAl0.25Ni0.75O3 perovskite catalyst using SBA-15 as templating agent for

methane dry reforming, Microporous Mesoporous Mater. 303 (2020) 110278. https://doi.org/10.1016/J.MICROMESO.2020.110278.

[160] L. Santamaria, G. Lopez, A. Arregi, M. Amutio, M. Artetxe, J. Bilbao, M. Olazar, Stability of different Ni supported catalysts in the in-line steam reforming of biomass fast pyrolysis volatiles, Appl. Catal. B Environ. 242 (2019) 109–120. https://doi.org/10.1016/j.apcatb.2018.09.081.

[161] J. Spragg, T. Mahmud, V. Dupont, Hydrogen production from bio-oil: A thermodynamic analysis of sorption-enhanced chemical looping steam reforming, Int. J. Hydrogen Energy. 43 (2018) 22032–22045. https://doi.org/10.1016/j.ijhydene.2018.10.068.

[162] P. Cerqueira, M.A. Soria, L.M. Madeira, Hydrogen production through chemical looping and sorption-enhanced reforming of olive mill wastewater: Thermodynamic and energy efficiency analysis, Energy Convers. Manag. 238 (2021) 114146. https://doi.org/10.1016/j.enconman.2021.114146.

[163] T. Udomchoke, S. Wongsakulphasatch, W. Kiatkittipong, A. Arpornwichanop, W. Khaodee, J. Powell, J. Gong, S. Assabumrungrat, Performance evaluation of sorption enhanced chemical-looping reforming for hydrogen production from biomass with modification of catalyst and sorbent regeneration, Chem. Eng. J. 303 (2016) 338–347. https://doi.org/10.1016/j.cej.2016.05.115.

[164] H. Xie, Q. Yu, H. Lu, Y. Zhang, J. Zhang, Q. Qin, Thermodynamic study for hydrogen production from bio-oil via sorption-enhanced steam reforming: Comparison with conventional steam reforming, Int. J. Hydrogen Energy. 42 (2017) 28718–28731. https://doi.org/10.1016/j.ijhydene.2017.09.155.

[165] Y.A. Situmorang, Z. Zhao, P. An, T. Yu, J. Rizkiana, A. Abudula, G. Guan, A novel system of biomass-based hydrogen production by combining steam bio-oil reforming and chemical looping process, Appl. Energy. 268 (2020) 115122. https://doi.org/10.1016/j.apenergy.2020.115122.

[166] P. Wang, H. Xie, J. Zhang, L. Jia, Z. Yu, R. Li, Optimization of two bio-oil steam reforming processes for hydrogen production based on thermodynamic analysis, Int. J. Hydrogen Energy. 47 (2022) 9853–9863. https://doi.org/10.1016/j.ijhydene.2022.01.055.

[167] A. Lima Da Silva, I.L. Müller, Hydrogen production by sorption enhanced steam reforming of oxygenated hydrocarbons (ethanol, glycerol, n-butanol and methanol): Thermodynamic modelling, Int. J. Hydrogen Energy. 36 (2011) 2057–2075. https://doi.org/10.1016/j.ijhydene.2010.11.051.

Appendix

Catalyst Synthesis

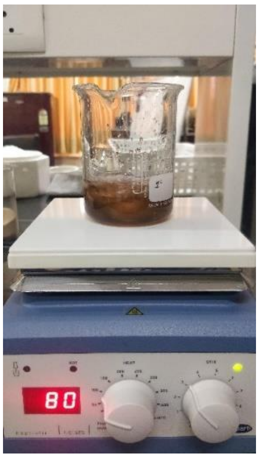

Mixing of metal' precursors

Prepared gel

Calcined sample

Grounded precalcined sample

Different catalyst samples

Fixed bed reactor unit with online GC

Pyrolysis Experimental setup

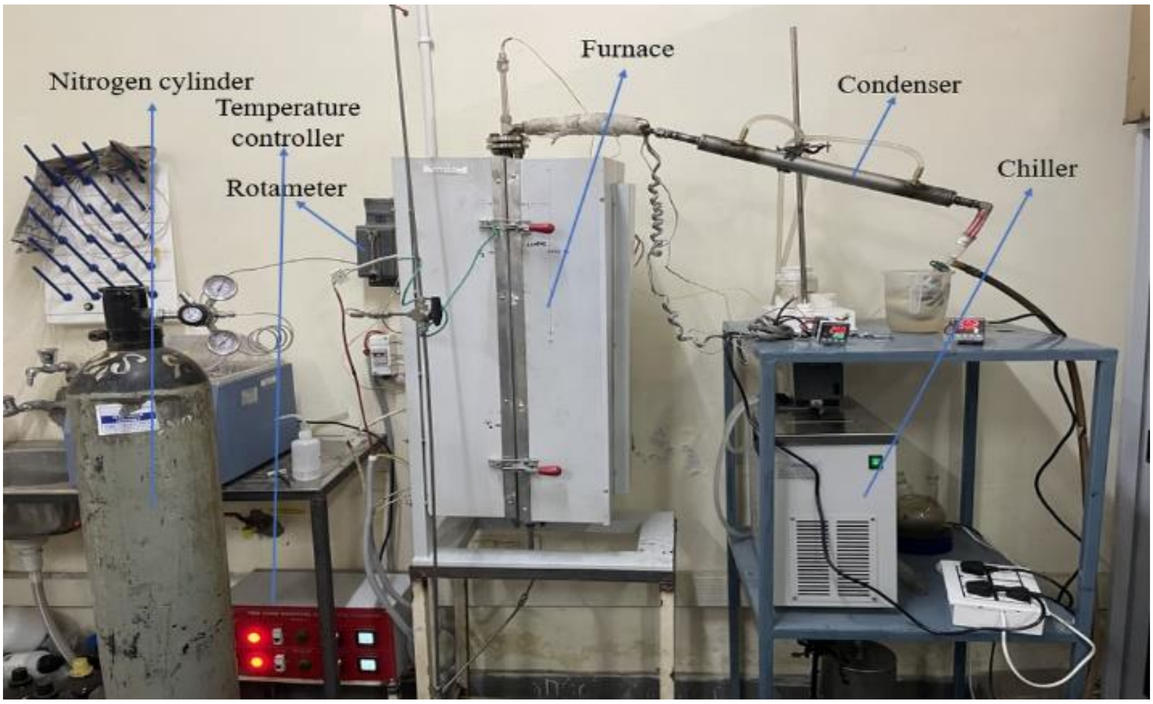
Nitrogen cylinder
Temperature controller
Rotameter
Furnace
Condenser
Chiller

Agricultural residue & Bio-oil

DURAN
500 ml
Mixed Feed
Bio-oil
APPROX. VOL.
Made in Germany
Retrace Code
10090588
www.duran-group.com

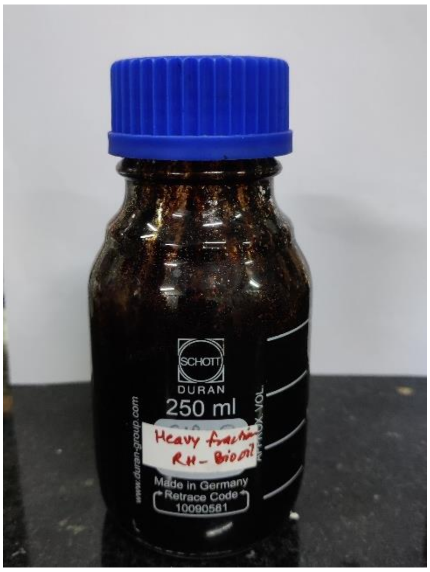
SCHOTT
DURAN
250 ml
Heavy fraction
RH-Bio oil
APPROX. VOL.
Made in Germany
Retrace Code
10090581
www.duran-group.com

Gas chromatograph of gas samples

Page 1 of 1

Area % Report

Data File: F:\Piyush\Result\March 2022\8March22_T_700_0.2ml_10.rslt\8March22_T_700_0.2ml_10.dat
Method: F:\Piyush\Method\Gas Analysis_argon_01.met
Acquired: 3/9/2022 3:59:14 PM (GMT +05:30)
Printed: 5/7/2022 11:16:12 PM (GMT +05:30)

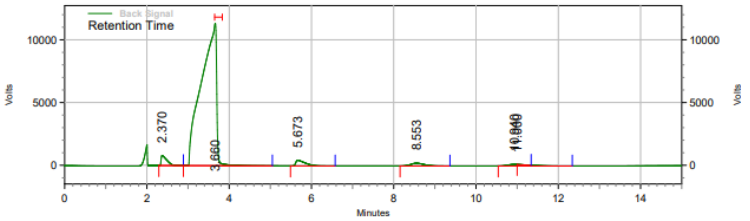

Back Signal
Results

Retention Time	Area	Area %	Height	Height %
2.370	59438175	2.45	6185562	6.22
3.660	2237231463	92.25	87135160	87.56
5.673	54812407	2.26	3488263	3.51
8.553	38781416	1.60	1718728	1.73
10.940	34699160	1.43	984633	0.99
11.000	210303	0.01	0	0.00
Totals	2425172924	100.00	99512346	100.00

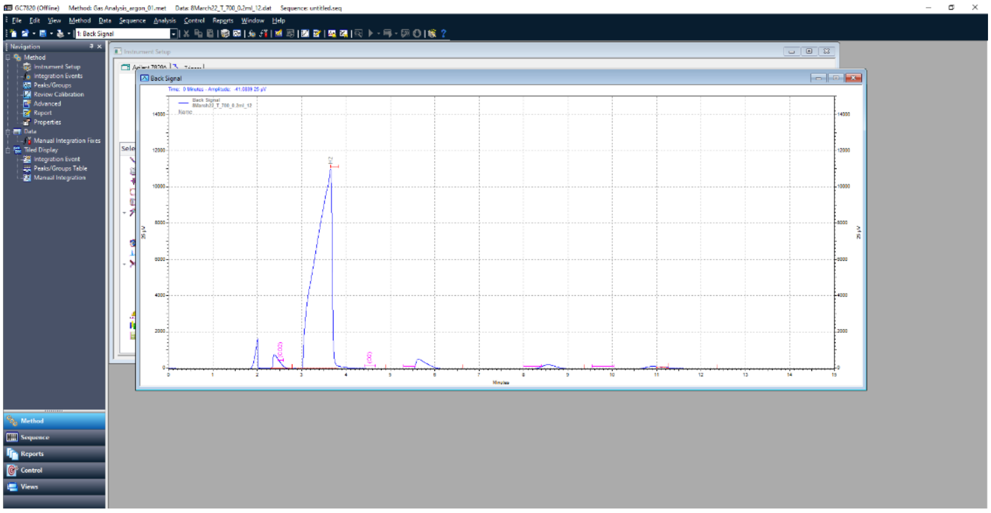
GC7820 (Offline) Method: Gas Analysis_argon_01.met Data: 8March22_T_700_0.2ml_12.dat Sequence: untitled.seq

Time: 0 Minutes - Amplitude: -41.0889 25 µV

File
Edit
View
Method
Data
Sequence
Analysis
Control
Reports
Window
Help
1: Back Signal
Navigation
Method
Instrument Setup
Integration Events
Peaks/Groups
Review Calibration
Advanced
Report
Properties
Data
Manual Integration Fixes
Tiled Display
Integration Event
Peaks/Groups Table
Manual Integration
Instrument Setup
Back Signal
Back Signal
8March22_T_700_0.2ml_12
H2
14000
12000
10000
8000
6000
4000
2000
0
25 µV
Minutes
Method
Sequence
Reports
Control
Views

List of Publications

Journal Publications

- **P. P. Singh**, A. Jaswal, N. Nirmalkar, and T. Mondal, “Synergistic effect of transition metals substitution on the catalytic activity of LaNi0.5M0.5O3 (M = Co, Cu, and Fe) perovskite catalyst for steam reforming of simulated bio-oil for green hydrogen production,” Renew. Energy, vol. 207, pp. 575–587, May 2023, doi: 10.1016/j.renene.2023.03.057.
- **P. P. Singh**, N. Nirmalkar, and T. Mondal, “Catalytic steam reforming of simulated bio-oil for green hydrogen production using highly active LaNi x Co 1− x O 3 perovskite catalysts,” Sustain. Energy Fuels, vol. 6, no. 4, pp. 1063–1074, 2022, doi: 10.1039/D1SE01786A.
- **P. P. Singh**, M. Trivedi, T. Mondal, and N. Nirmalkar, “A novel strategy to enhance the cooling effectiveness in a confined porous jet impingement using non-Newtonian fluids,” Int. Commun. Heat Mass Transf., vol. 126, no. June, p. 105362, 2021, doi: 10.1016/j.icheatmasstransfer.2021.105362.
- A. Jaswal, **P. P. Singh**, A. K. Kar, T. Mondal, and R. Srivastava, “Production of 2-methyl furan, a promising 2nd generation biofuel, by the vapor phase hydrodeoxygenation of biomass-derived furfural over TiO2 supported Cu Ni bimetallic catalysts,” Fuel Process. Technol., vol. 245, no. March, p. 107726, Jun. 2023, doi: 10.1016/j.fuproc.2023.107726.
- A. Jaswal, **P. P. Singh**, and T. Mondal, “Furfural-a versatile, biomass-derived platform chemical for the production of renewable chemicals,” Green Chem., vol. 24, no. 2, pp. 510–551, 2022, doi: 10.1039/d1gc03278j.
- A. Goyal, **P. P. Singh**, and T. Mondal, Abstracts of the International Chemical Engineering Conference 2021: 100 Glorious Years of Chemical Engineering &amp; Technology, vol. 3, no. 001. AIJR Publisher, 2022. doi: 10.21467/abstracts.146.
- **P. P. Singh,** A. Jaswal, R. Singh, T. Mondal, and K. K. Pant, “Green hydrogen production from biomass – An assessment of the potential of conventional and advanced bio-oil steam reforming processes”. *International Journal of Hydrogen Energy (Elsevier)* **(Under review)**

- **P. P. Singh**, A. Jaswal, and T. Mondal, "Kinetic study of Phenol Steam Reforming to produce renewable hydrogen using $LaNi_{0.5}Co_{0.5}O_3$ perovskite catalyst". **(Under preparation)**
- **P. P. Singh**, A. Jaswal, and T. Mondal, "Catalytic steam reforming of raw bio-oil derived from blended agricultural residues using perovskite catalyst". **(Under preparation)**

Book Chapter

- **P. P. Singh**, A. Goyal, A. Jaswal and T. Mondal, 'Catalytic pyrolysis & reforming of agro-waste for hydrogen production' in "Biohydrogen fuel: recent insights & modelling (approach in thermochemical and biological track)" *Apple Academic Press (Taylor and Francis Group)* **(Accepted)**

Conference presentation

- Delivered a talk under ‘young scientist category’ at ‘4th National Conference on Advances in Chemical Engineering and Science’ held on 31st March-1st April 2023 at IISER Bhopal.

- Presented a poster at ‘International Union of Materials Research Society-International Conference in Asia (IUMRS-ICA 2022)’ held on December 19-23, 2022 at IIT Jodhpur.

- Presented a poster at ‘Conference on Advances in Catalysis for Energy and Environment (CACEE-2022)’ held on October 30 to November 4, 2022 at TIFR Mumbai.

- Presented a paper at ‘International Conference on Chemical Engineering Enabling Transition Towards Sustainable Future (ChemTSF 2022)’ held on September 8-10, 2022 at IIT Roorkee. (Invited for publication in Special issue of Biomass Conversion and Biorefinery Journal)

- Presented a paper at ‘2021 MRS Fall Meeting and Exhibit (Advanced materials for Hydrogen and Fuel Cell Technologies)’ held on December 6-9, 2021 at Boston, Massachusetts, USA.

- Presented a paper at ‘Chemical Engineering Congress (CHEMCON 2018)’ held on December 26-30, 2018 at NIT Jalandhar.

- Presented a poster at ‘Complex Fluid Symposium (COMPFLU-2018)’ held on December 6-8, 2018 at IIT Roorkee.

Biodata

Piyush Pratap Singh

Education:

M.Tech: Chemical Engineering with specialization in ‘Chemical Process Design’ from Maulana Azad National Institute of Technology Bhopal, Madhya Pradesh, India **(2014)**
Performance/CGPA: 9.05/10

B.Tech: Chemical Engineering from AKTU Lucknow, India (formerly UPTU/GBTU Lucknow) **(2012)**
Performance/Percentage: 71.04%

Work experience:

Assistant Professor: Chemical Engineering, Chandigarh University, Mohali, India (July 2014- January 2018)

Project Intern: CSIR- Indian Institute of Chemical Technology Hyderabad, India (July 2013- April 2014)

Research interest:

- ✓ Heterogeneous catalysis
- ✓ Biomass conversion to value-added chemicals and fuels
- ✓ Techno-economic evaluation of biomass conversion processes
- ✓ Waste water treatment
- ✓ Bio-fertilizer

Technical skills:

Handling and analysing the data using the following sophisticated analytical instruments:

- ✓ XRD (room temperature and high temperature with inert and ambient atmosphere)
- ✓ FTIR and In-situ DRIFT Spectroscopy
- ✓ Gas Chromatography with MS, FID and TCD
- ✓ SEM
- ✓ TGA

Softwares: ASPEN+, COMSOL, Origin, Xpert-plus highscore etc.

LEADERSHIP/MANAGERIAL SKILLS:

- Convenor, Student Legislative Council, IIT Ropar (AY 2022-23)
- PhD Representative/ Research Secretary, IIT Ropar (September 2020- September 2022)
- Covid-Task Force committee member, IIT Ropar (2020-22)
- Academic coordinator, Chandigarh University (2016-2017)
- Placement coordinator, Chandigarh University (2014-2017)
- President-CChE-AITH Kanpur (2011-12)
- Student Secretary, AITH Kanpur (2010-11)

AWARD / HONOURS / Memberships:

- ✓ Won first prize for Innovative Idea for Energy and Sustainability organized by PEDA, Govt of Punjab.
- ✓ Life Associate Member- Indian Institute of Chemical Engineers (IIChE) LAM-54721
- ✓ Won Best Poster Presenter in National Conference on 'Technical Advances in Chemical, Petroleum and Natural Gas Engineering' (ACPNe 2015)
- ✓ Awarded as Best Paper Presentation in "International conference on Global Scenario in Environment and Energy" (ICGSE2 2013)
- ✓ Qualified GATE 2012 (Graduate Aptitude Test in Engineering) conducted by IIT-Delhi
- ✓ Won 1st prize in Model Presentation in intercollegiate Technical festival in "UDAYAYA 2011"
- ✓ Won 1st prize in Chemical Quiz in intercollegiate Technical festival in "UDAYAYA 2011"
- ✓ Received scholarship from 'President of India' during Intermediate Education (2005-2007)
- ✓ Awarded as a State Children Scientist by National Children's Science Congress in 2003-2004